

THE STARK EFFECTS ON GROUP II-VI SEMICONDUCTOR NANOPARTICLES  
(NP) DURING SYNTHESIS IN SOLUTION AND ON NP EMBEDDED IN A GLASS  
MATRIX AND IN NANOSTRUCTURED THIN FILMS



by

Fatma Melda Patan Alper

Submitted to Graduate School of Natural and Applied Sciences  
in Partial Fulfillment of the Requirements  
for the Degree of Doctor of Philosophy in  
Physics

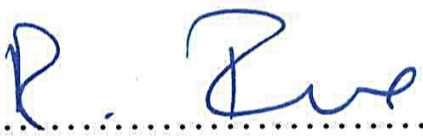
Yeditepe University

2017

THE STARK EFFECTS ON GROUP II-VI SEMICONDUCTOR NANOPARTICLES  
(NP) DURING SYNTHESIS IN SOLUTION AND ON NP EMBEDDED IN A GLASS  
MATRIX AND IN NANOSTRUCTURED THIN FILMS

APPROVED BY:

Prof. Dr. Rabia İnce  
(Thesis Supervisor)

  
.....

Prof. Dr. Avadis Hacınlıyan

  
.....

Prof. Dr. Hikmet Yükselici

  
.....

Prof. Dr. Yani Skarlatos

  
.....

Assoc. Prof. Dr. İpek Karaaslan

  
.....

DATE OF APPROVAL: ...../...../.....

## ACKNOWLEDGEMENTS

I would like to express my appreciation to my PhD supervisor Professor Dr. Rabia Ince for her guidance, encouragement, support and patience during the thesis process. Foremost, I want to thank Professor Dr. Ahmet Ince who believed in me with all my work and who always supported me.

I also own thanks to my husband Barış Özgür Alper who is my mentor, my everything. He always motivated me, has been with me and showed me patience with my son Barış Mete Alper.

I thank my parents, Ali and Cahide Patan, my sister Seda, İlhan and Selin Karaağaç, my uncle Hamdi Patan for guiding me, raising me and always being there through everything. I would like to thank them for their endless love and support. Also thanks to my extended family İsmet, Ahmet and Ata Alper.

I would also like to thank my co-supervisor Professor Doctor Hikmet Yükselici for his support and help. He gave great support for my work by allowing me to use Yıldız Technical University Physics Department Photonic Laboratory facilities.

A very special thank to Assist. Prof. Dr. Cem Levent Altan Chemistry Department in Yeditepe University. I thank my dearest friends and colleagues Dr. Mehmet Torun and Dr. Ekrem Sınır.

I would like to express my appreciation to my other teachers Assist. Prof. Dr. Ercüment Akat, Prof. Dr. Avadis Hacınılyan, Prof. Dr. Yani Skarlatos, Doc. Dr. İpek Karaaslan, Doc. Dr. Vildan Üstoğlu Ünal, Doc. Dr. Ertan Akşahin, Prof. Dr. Necdet Aslan, Assist. Prof. Dr. Alexandre Titov for their motivation, support and encouragement throughout my PhD studies and also very special thanks for Maria Aiordachioaiei, Mehmet Nacar and Burcu Ebeler.

This thesis is dedicated to my husband Barış Özgür Alper and my son Barış Mete Alper.

## **ABSTRACT**

### **THE STARK EFFECTS ON GROUP II-VI SEMICONDUCTOR NANOPARTICLES (NP) DURING SYNTHESIS IN SOLUTION AND ON NP EMBEDDED IN A GLASS MATRIX AND IN NANOSTRUCTURED THIN FILMS**

The main purpose in the thesis is to change the dimensions of the various compositions of quantum dots and investigate their optical and electro-optical properties. This investigation was divided into three main parts: 1- preliminary studies starting with thin films, preparation of the sample and design set up, taking absorption spectra measurements. Changes in optical absorption and electro-absorption properties were observed in multilayer CdTe nanoparticle thin films especially when the amount of sample, annealing time, temperature and coating method (layer by layer technique with spincoater) were changed. 2- The preparation of CdTe nanoparticles embedded in glass matrix sandwiched between ITO glasses was also investigated depending on the heat treatment time and temperature to control the size and to optimize the optical and electro-optical properties of the nanoparticles. 3- Synthesis and characterization water soluble CdTe quantum dots with different sizes. Mercaptopropionic acid was used as capping agent which is important for reducing toxicity and controlling the size of the nanoparticles.

UV-Vis absorption, electro-absorption and Raman spectra were carried out to characterize the optical properties of these nanoparticles.

Investigations and development were made during the synthesis and production by varying the heat-treatment time, temperature, pH of the solution and capping agent.

Effects of electro modulation on the nanoparticles, nano structured thin films, glass matrix and solution were studied and the results analysed with spectroscopic techniques.

## ÖZET

### **GRUP II-VI YARIİLETKEN NANOPARÇACIKLARIN (NP) ÇÖZELTİDE VE CAM MATRİS İÇİNDE GÖMÜLÜ VE İNCE FİLM NANOYAPILARDA SENTEZİ SIRASINDA STARK ETKİSİ**

Bu tezin ana amacı, çeşitli kuantum noktalarının kompozisyonlarının boyutlarını değiştirmek ve bunların optik ve elektro-optik özelliklerini araştırmaktır. Bu araştırma üç ana bölüme ayrılmıştır: 1- İnce filmlerden başlayan ön hazırlık çalışması, örneğin hazırlanması ve deney düzeneğinin tasarlanması, emilim spektrumu ölçümlerinin gerçekleşmesi. Özellikle örnek miktarı, tavlama süresi, sıcaklık ve kaplama metodu (spincoater ile katman-tabaka tekniği) değiştirildiğinde CdTe nanoparçacıklar ince tabakanın çok tabakalı optik soğurma ve elektro-emilim özelliklerinde değişiklikler gözlenmiştir. 2- ITO kaplı camlar arasına sıkıştırılmış cam matris içine gömülü CdTe nanoparçacıkların hazırlanması, ısıtım işlem süresine ve sıcaklığa bağlı olarak boyutu kontrol etmek ve nanoparçacıkların optik ve elektro-optik özelliklerinin optimize edilmesi araştırılmıştır. 3- Farklı büyüklükteki suda çözünebilen CdTe kuantum noktalarının sentezlenip karakterize edilmesi. Mercaptopropionic asit, toksikliğin azaltılması ve nanoparçacıkların boyutunun kontrol edilmesi için önemli olan bir kapak oluşturucu madde olarak kullanılmıştır.

Bu nanoparçacıkların optik özelliklerini karakterize etmek için UV-Vis, elektro-absorpsiyon ve Raman spektrumları kullanılmıştır.

Isıtım işlem süresi, sıcaklık, çözeltinin Ph değeri ve kapak ajanının değiştirilmesi ile sentez ve üretim sırasında inceleme ve geliştirme yapılmıştır.

Elektro modülasyonun nano yapıları ince filmler, cam matris ve çözeltiler için nanoparçacıklar üzerindeki etkileri araştırılmış ve sonuçlar spektroskopik teknikler ile analiz edilmiştir.

## TABLE OF CONTENTS

ACKNOWLEDGEMENTS.....	iii
ABSTRACT.....	iv
ÖZET .....	v
LIST OF FIGURES .....	viii
LIST OF TABLES.....	xix
LIST OF SYMBOLS/ABBREVIATIONS.....	xxi
1. INTRODUCTION.....	1
1.1. OVERVIEW SEMICONDUCTOR QUANTUM DOTS AND QUANTUM CONFINEMENT IN SEMICONDUCTORS .....	1
1.2. QUANTUM DOT DIMENSIONS AND BOHR RADIUS .....	2
1.3. METHODS OF SYNTHESIS FOR SEMICONDUCTOR NANOMATERIALS .....	5
1.4. STAGES DURING GROWTH OF QD IN SOLUTION .....	5
2. SPECTROSCOPIC CHARACTERIZATION TECHNIQUES FOR SEMICONDUCTOR NANOPARTICLES .....	8
2.1. UV-VIS ABSORPTION SPECTROSCOPY.....	8
2.2. RAMAN SPECTROSCOPY .....	9
3. ELECTROABSORPTION IN SEMICONDUCTOR.....	13
3.1. ELECTROABSORPTION IN SEMICONDUCTOR.....	13
3.2. THE QUANTUM CONFINED STARK EFFECT (QCSE).....	13
3.3. FRANZ-KELDYSH EFFECT .....	14
3.4. TIME-INDEPENDENT SCHRODINGER EQUATION.....	16
3.5. PERTURBATIONAL METHOD .....	16
4. EXPERIMENTAL SECTION.....	22
4.1. PRELIMINARY EXPERIMENTS .....	22
4.1.1. PREPARATION OF THE SAMPLE .....	22
4.1.2. OPTICAL MEASUREMENTS .....	22
4.1.3. OPTICAL MEASUREMENT RESULTS.....	26

4.2.	MAIN EXPERIMENTS.....	30
4.2.1.	SOLID SAMPLE.....	30
4.2.2.	AQUEOUS SAMPLES .....	34
4.2.3.	SYNTHESIS OF WATER SOLUABLE CDTE QUANTUM DOTS .....	37
5.	METHOD.....	41
5.1.	ABSORPTION SPECTRUM MEASUREMENT .....	41
5.2.	RAMAN SPECTROSCOPY MEASUREMENT .....	45
5.3.	ELECTRO-ABSORPTION SPECTRUM MEASUREMENT .....	48
5.4.	REPEATABILITY OF THE MEASUREMENT (HYSTERISIS).....	50
5.5.	CALCULATION OF THE MEASUREMENT UNCERTAINTY.....	51
6.	RESULTS.....	53
6.1.	UV-VIS RESULTS FOR BOTH SOLID AND AQUEOUS SAMPLES.....	53
6.2.	DIELECTRIC PERMITTIVITY RESULTS .....	61
6.3.	PARTICLE SIZE DISTRIBUTION ANALYSIS .....	67
6.4.	ELECTRO-ABSORPTION SPECTRUM MEASUREMENT RESULTS .....	81
6.4.1.	SOLID SAMPLE 1: 3 HOURS ANNEALED .....	83
6.4.2.	SOLID SAMPLE 2: 8 HOURS ANNEALED .....	99
6.4.3.	SOLID SAMPLE 3: 12 HOURS ANNEALED .....	109
6.4.4.	SOLUTION SAMPLE 1: 15 MINUTES HEAT-TREATED.....	114
6.4.5.	SOLUTION SAMPLE 3: 2 HOURS HEAT-TREATED.....	119
6.4.6.	SOLUTION SAMPLE 4: 3 HOURS HEAT-TREATED.....	125
6.4.7.	SOLUTION SAMPLE 6: 5 HOURS HEAT-TREATED.....	127
6.4.8.	SOLUTION SAMPLE 7: 5 HOURS 15 MINUTES HEAT-TREATED ....	130
7.	CONCLUSION AND FUTURE WORK.....	138
	REFERENCES .....	144
	APPENDIX A.....	154

## LIST OF FIGURES

Figure 1.1. Energy levels and band gaps of a semiconductor from bulk crystals to nanosized crystals .....	3
Figure 1.2. Density of states as a function of energy: bulk (3D), quantum well (2D), quantum wire (1D) and quantum dot (0D) .....	4
Figure 1.3. Schematic graph displaying the relationship between the precursor concentration and the reaction time for the solution phase synthesis process a) LaMer's Diagram (Concentration vs. Time) [34]. .....	6
Figure 2.1. The basic principle of the absorption spectrum.....	8
Figure 2.2. The Rayleigh and Raman Scattering Energy Diagram .....	10
Figure 2.3. Optical and acoustical branches of the dispersion relation for a diatomic lattice .....	11
Figure 3.1. Electron and hole wavefunctions for the infinite potential well without field and with field [50] .....	14
Figure 3.2. The Franz-Keldysh effect and the resulting change in absorption spectrum ....	15
Figure 4.1. Optical absorption spectra for thin film CdSe/ZnS quantum dots before heat treatment .....	22
Figure 4.2. AFM surface topographical image of deposited CdSe/ZnS thin films with spin coater at 500 rpm and 100 rpm .....	24
Figure 4.3. CdSe/ZnS core shell 590 nm quantum dots in solution with the different concentrations .....	24



Figure 4.4. The change in energy shift and with respect to speed of the spin coater .....	26
Figure 4.5. Optical absorption spectra for thin film CdSe/ZnS quantum dots after heat treatment. ....	27
Figure 4.6. The optical density difference before annealing versus speed of the spin coater .....	28
Figure 4.7. (a.b) Dependence of the deposited and annealed (onto glass samples) CdSe/ZnS quantum dots size with respect to speed of the spin coater .....	29
Figure 4.8. Optical absorption spectrum of Sample 4 at different temperatures .....	29
Figure 4.9. Picture of Carbolite 3 zone furnace for heat treatment process .....	32
Figure 4.10. Picture of Hart Scientific S Type Thermocouple to Determine the Temperature of the Furnace .....	32
Figure 4.11. Picture of Solid Samples for high dc. voltage measurement.....	33
Figure 4.12. Sample preparations for stark effect measurement .....	34
Figure 4.13. Preparative HPLC water analyzed in Sartorius Machine.....	35
Figure 4.14. Picture of high dc. voltage source .....	36
Figure 4.15. The NaHTe solution after 24 hours wait in refrigarator.....	37
Figure 4.16. Yellow solution: After 15 minutes NaHTe has been added to Cd ion solution .....	39
Figure 4.17. Orange solution: After 3 hours NaHTe has been added to Cd ion solution....	39

Figure 4.18. CdTe QDs in aqueous solution with different sizes .....	40
Figure 5.1. Optical spectrometer set-up for spectral measurements.....	41
Figure 5.2. FWHM of a Gaussian Distribution .....	45
Figure 5.3. Raman spectra of RG 830 samples: as-received sample, melted sample, heat treated sample .....	46
Figure 6.1. The absorption spectra of $Zn_xCd_{1-x}Te$ semiconductor nanocrystals embedded in glass matrices.....	55
Figure 6.2. Graph of optical absorption spectra for the sample heat treated at 600 °C for 8 hours without field.....	56
Figure 6.3. Graph of optical absorption spectra for the sample heat treated at 600 °C for 12 hours without field.....	56
Figure 6.4. Tauc plot obtained from the optical absorption spectra of as-received sample without field.....	57
Figure 6.5. Tauc plot obtained from the optical absorption spectra of melted sample without field .....	57
Figure 6.6. Tauc plot obtained from the optical absorption spectra of heat-treated sample without field.....	58
Figure 6.7. Tauc plot obtained from the optical absorption spectra of solid sample 2 without field .....	58
Figure 6.8. Tauc plot obtained from the optical absorption spectra of solid sample 3 without field .....	59

Figure 6.9. The absorption spectra of CdTe solution semiconductor nanocrystals without electric field (in Yeditepe uv-vis) .....	60
Figure 6.10. Components of the complex dielectric permittivity of solid sample 1.....	61
Figure 6.11. Components of the complex dielectric permittivity of solid sample 2.....	62
Figure 6.12. Components of the complex dielectric permittivity of solid sample 3.....	62
Figure 6.13. Components of the complex dielectric permittivity of aqueous sample 1 .....	63
Figure 6.14. Components of the complex dielectric permittivity of aqueous sample 2 .....	63
Figure 6.15. Components of the complex dielectric permittivity of aqueous sample 3 .....	64
Figure 6.16. Components of the complex dielectric permittivity of aqueous sample 4 .....	64
Figure 6.17. Components of the complex dielectric permittivity of aqueous sample 5 .....	65
Figure 6.18. Components of the complex dielectric permittivity of aqueous sample 6 .....	65
Figure 6.19. Components of the complex dielectric permittivity of aqueous sample 7 .....	66
Figure 6.20. Particle size distribution curve of solid sample 1 at 0 V .....	67
Figure 6.21. Particle size distribution curve of solid sample 1 at 1000 V .....	68
Figure 6.22. Particle size distribution curve of solid sample 1 at 5500 V .....	68
Figure 6.23. Particle size distribution curve of solid sample 2 at 0 V .....	69
Figure 6.24. Particle size distribution curve of solid sample 2 at 1000 V .....	69

Figure 6.25. Particle size distribution curve of solid sample 2 at 3000 V .....	70
Figure 6.26. Particle size distribution curve of solid sample 3 at 0 V .....	70
Figure 6.27. Particle size distribution curve of solid sample 3 at 1000 V .....	71
Figure 6.28. Particle size distribution curve of solid sample 3 at 1750 V .....	71
Figure 6.29. Particle size distribution curve of solution sample 1 at 0 V .....	72
Figure 6.30. Particle size distribution curve of solution sample 1 at 1000 V .....	72
Figure 6.31. Particle size distribution curve of solution sample 1 at 2500 V .....	73
Figure 6.32. Particle size distribution curve of solution sample 3 at 0 V .....	73
Figure 6.33. Particle size distribution curve of solid sample 3 at 1000 V .....	74
Figure 6.34. Particle size distribution curve of solution sample 3 at 1500 V .....	74
Figure 6.35. Particle size distribution curve of solution sample 4 at 0 V .....	75
Figure 6.36. Particle size distribution curve of solution sample 4 at 1000 V .....	75
Figure 6.37. Particle size distribution curve of solution sample 6 at 0 V .....	76
Figure 6.38. Particle size distribution curve of solution sample 6 at 1000 V .....	76
Figure 6.39. Particle size distribution curve of solution sample 6 at 2000 V .....	77
Figure 6.40. Particle size distribution curve of solution sample 7 at 0 V .....	77
Figure 6.41. Particle size distribution curve of solution sample 7 at 1000 V .....	78

Figure 6.42. Particle size distribution curve of solution sample 7 at 2000 V .....	78
Figure 6.43. Particle size distribution for CdTe quantum dots at 0 V before and after application of electric field .....	80
Figure 6.44. Particle size distribution for CdTe quantum dots at 0 V and 3000 V .....	81
Figure 6.45. Diagram of the electro-optical absorption measurement set-up for solid samples .....	81
Figure 6.46. Illustration of electrical connections to the aqueous solution samples .....	82
Figure 6.47. Picture of quartz tube and electro-absorption measurement set up for solution samples.....	82
Figure 6.48. Plots of $(\alpha h\nu)^2$ versus $h\nu$ for Solid Sample 1 without field.....	85
Figure 6.49. Plots of $(\alpha h\nu)^2$ versus $h\nu$ Solid Sample 1 at 500 V .....	86
Figure 6.50. Plots of $(\alpha h\nu)^2$ versus $h\nu$ for Solid Sample 1 at 1000 V.....	86
Figure 6.51. Plots of $(\alpha h\nu)^2$ versus $h\nu$ Solid Sample 1 at 1500 V .....	87
Figure 6.52. Plots of $(\alpha h\nu)^2$ versus $h\nu$ for Solid Sample 1 at 2000 V.....	87
Figure 6.53. Plots of $(\alpha h\nu)^2$ versus $h\nu$ for Solid Sample 1 at 2500 V .....	88
Figure 6.54. Plots of $(\alpha h\nu)^2$ versus $h\nu$ for Solid Sample 1 at 3000 V.....	88
Figure 6.55. Plots of $(\alpha h\nu)^2$ versus $h\nu$ for Solid Sample 1 at 3500 V.....	89
Figure 6.56. Plots of $(\alpha h\nu)^2$ versus $h\nu$ for Solid Sample 1 at 4000 V.....	89

Figure 6.57. Plots of $(\alpha h\nu)^2$ versus $h\nu$ for Solid Sample 1 at 4500 V.....	90
Figure 6.58. Plots of $(\alpha h\nu)^2$ versus $h\nu$ Solid Sample 1 at 5000 V.....	90
Figure 6.59. Plots of $(\alpha h\nu)^2$ versus $h\nu$ for Solid Sample 1 at 5500 V.....	91
Figure 6.60. Plots of $(\alpha h\nu)^2$ versus $h\nu$ for Solid Sample 1 at 0 V.....	91
Figure 6.61. Plots of $(\alpha h\nu)^2$ versus $h\nu$ for Solid Sample 1 at 500 V.....	92
Figure 6.62. Plots of $(\alpha h\nu)^2$ versus $h\nu$ for Solid Sample 1 at 1000 V.....	92
Figure 6.63. Plots of $(\alpha h\nu)^2$ versus $h\nu$ for Solid Sample 1 at 1500 V.....	93
Figure 6.64. Plots of $(\alpha h\nu)^2$ versus $h\nu$ for Solid Sample 1 at 2000 V.....	93
Figure 6.65. Plots of $(\alpha h\nu)^2$ versus $h\nu$ for Solid Sample 1 at 2500 V.....	94
Figure 6.66. Plots of $(\alpha h\nu)^2$ versus $h\nu$ for Solid Sample 1 at 3000 V.....	94
Figure 6.67. Plots of $(\alpha h\nu)^2$ versus $h\nu$ for Solid Sample 1 at 3500 V.....	95
Figure 6.68. Plots of $(\alpha h\nu)^2$ versus $h\nu$ for Solid Sample 1 at 4000 V.....	95
Figure 6.69. Plots of $(\alpha h\nu)^2$ versus $h\nu$ for Solid Sample 1 at 4500 V.....	96
Figure 6.70. Plots of $(\alpha h\nu)^2$ versus $h\nu$ for Solid Sample 1 at 5000 V.....	96
Figure 6.71. Plots of $(\alpha h\nu)^2$ versus $h\nu$ for Solid Sample 1 at 5500 V.....	97
Figure 6.72. Band gap energies versus electric field of increasing and decreasing measurement with measurement uncertainty bar.....	97

Figure 6.73. Graph of band gap and radius versus electric field .....	98
Figure 6.74. Graph of band gap and radius versus electric field after decreasing order measurement .....	99
Figure 6.75. Plots of $(\alpha h\nu)^2$ versus $h\nu$ for Solid Sample 2 at 0 V .....	100
Figure 6.76. Plots of $(\alpha h\nu)^2$ versus $h\nu$ for Solid Sample 2 at 500 V .....	101
Figure 6.77. Plots of $(\alpha h\nu)^2$ versus $h\nu$ for Solid Sample 2 at 1000 V .....	101
Figure 6.78. Plots of $(\alpha h\nu)^2$ versus $h\nu$ for Solid Sample 2 at 1500 V .....	102
Figure 6.79. Plots of $(\alpha h\nu)^2$ versus $h\nu$ for a Solid Sample 2 at 2000 V .....	102
Figure 6.80. Plots of $(\alpha h\nu)^2$ versus $h\nu$ for Solid Sample at 2500 V .....	103
Figure 6.81. Plots of $(\alpha h\nu)^2$ versus $h\nu$ for Solid Sample 2 at 3000 V .....	103
Figure 6.82. Plots of $(\alpha h\nu)^2$ versus $h\nu$ for Solid Sample 2 at 0 V .....	104
Figure 6.83. Plots of $(\alpha h\nu)^2$ versus $h\nu$ for Solid Sample 2 at 500 V .....	105
Figure 6.84. Plots of $(\alpha h\nu)^2$ versus $h\nu$ for Solid Sample 2 at 1000 V .....	105
Figure 6.85. Plots of $(\alpha h\nu)^2$ versus $h\nu$ for Solid Sample 2 at 1500 V .....	106
Figure 6.86. Plots of $(\alpha h\nu)^2$ versus $h\nu$ for Solid Sample 2 at 2000 V .....	106
Figure 6.87. Plots of $(\alpha h\nu)^2$ versus $h\nu$ for Solid Sample 2 at 2500 V .....	107
Figure 6.88. Band gap energies and radius versus electric field of increasing measurement .....	107

Figure 6.89. Band gap energies and radius versus electric field of decreasing measurement .....	108
Figure 6.90. Band gap energies versus electric field of increasing and decreasing measurement with measurement uncertainty bar .....	108
Figure 6.91. Band gap energies, radius vs. electric field with uncertainty bar .....	109
Figure 6.92. Plots of $(\alpha h\nu)^2$ versus $h\nu$ for Solid Sample 3 at 0 V .....	110
Figure 6.93. Plots of $(\alpha h\nu)^2$ versus $h\nu$ for Solid Sample 3 at 250 V .....	110
Figure 6.94. Plots of $(\alpha h\nu)^2$ versus $h\nu$ for Solid Sample 3 at 500 V .....	111
Figure 6.95. Plots of $(\alpha h\nu)^2$ versus $h\nu$ for Solid Sample 3 at 1000 V .....	111
Figure 6.96. Plots of $(\alpha h\nu)^2$ versus $h\nu$ for Solid Sample 3 at 1500 V .....	112
Figure 6.97. Plots of $(\alpha h\nu)^2$ versus $h\nu$ for Solid Sample 3 at 1750 V .....	112
Figure 6.98. Plots of $(\alpha h\nu)^2$ versus $h\nu$ for Solid Sample 3 at 0 V .....	113
Figure 6.99. Graph of band gap and radius versus electric field .....	113
Figure 6.100. Plots of $(\alpha h\nu)^2$ versus $h\nu$ for Solution Sample 1 at 0 V .....	115
Figure 6.101. Plots of $(\alpha h\nu)^2$ versus $h\nu$ for Solution Sample 1 at 500 V .....	115
Figure 6.102. Plots of $(\alpha h\nu)^2$ versus $h\nu$ for Solution Sample 1 at 750 V .....	116
Figure 6.103. Plots of $(\alpha h\nu)^2$ versus $h\nu$ for Solution Sample 1 at 1000 V .....	116
Figure 6.104. Plots of $(\alpha h\nu)^2$ versus $h\nu$ for Solution Sample 1 at 1250 V .....	117



Figure 6.105. Plots of $(\alpha h\nu)^2$ versus $h\nu$ for Solution Sample 1 at 1500 V.....	117
Figure 6.106. Plots of $(\alpha h\nu)^2$ versus $h\nu$ for Solution Sample 1 at 2500 V.....	118
Figure 6.107. Plots of $(\alpha h\nu)^2$ versus $h\nu$ for Solution Sample 1 at 0 V.....	118
Figure 6.108. Plot of band gap, radius versus applied electric field for aqueous solution sample 1, from table above.....	119
Figure 6.109. Plots of $(\alpha h\nu)^2$ versus $h\nu$ for Solution Sample 3 at 0 V.....	120
Figure 6.110. Plots of $(\alpha h\nu)^2$ versus $h\nu$ for Solution Sample 3 at 250 V.....	121
Figure 6.111. Plots of $(\alpha h\nu)^2$ versus $h\nu$ for Solution Sample 3 at 500 V.....	121
Figure 6.112. Plots of $(\alpha h\nu)^2$ versus $h\nu$ for Solution Sample 3 at 750 V.....	122
Figure 6.113. Plots of $(\alpha h\nu)^2$ versus $h\nu$ for Solution Sample 3 at 1000 V.....	122
Figure 6.114. Plots of $(\alpha h\nu)^2$ versus $h\nu$ for Solution Sample 3 at 1500 V.....	123
Figure 6.115. Plots of $(\alpha h\nu)^2$ versus $h\nu$ for Solution Sample 3 at 2000 V.....	123
Figure 6.116. Plots of $(\alpha h\nu)^2$ versus $h\nu$ for Solution Sample 3 at 0 V.....	124
Figure 6.117. Plot of band gap, radius versus applied electric field for solution sample 3, from table above.....	124
Figure 6.118. Plots of $(\alpha h\nu)^2$ versus $h\nu$ for Solution Sample 4 at 0 V.....	125
Figure 6.119. Plots of $(\alpha h\nu)^2$ versus $h\nu$ for Solution Sample 4 at 1000 V.....	126

Figure 6.120. Plot of band gap, radius versus applied electric field for solution sample 4. .....	126
Figure 6.121. Plots of $(\alpha h\nu)^2$ versus $h\nu$ for Solution Sample 6 at 0 V.....	127
Figure 6.122. Plots of $(\alpha h\nu)^2$ versus $h\nu$ for Solution Sample 6 at 500 V.....	128
Figure 6.123. Plots of $(\alpha h\nu)^2$ versus $h\nu$ for Solution Sample 6 at 1500 V.....	128
Figure 6.124. Plots of $(\alpha h\nu)^2$ versus $h\nu$ for Solution Sample 6 at 2000 V.....	129
Figure 6.125. Plot of band gap, radius versus applied electric field for solution sample 6. .....	129
Figure 6.126. Plots of $(\alpha h\nu)^2$ versus $h\nu$ for Solution Sample 7 at 0 V.....	131
Figure 6.127. Plots of $(\alpha h\nu)^2$ versus $h\nu$ for Solution Sample 7 at 250 V.....	131
Figure 6.128. Plots of $(\alpha h\nu)^2$ versus $h\nu$ for Solution Sample 7 at 500 V.....	132
Figure 6.129. Plots of $(\alpha h\nu)^2$ versus $h\nu$ for Solution Sample 7 at 750 V.....	132
Figure 6.130. Plots of $(\alpha h\nu)^2$ versus $h\nu$ for Solution Sample 7 at 1000 V.....	133
Figure 6.131. Plots of $(\alpha h\nu)^2$ versus $h\nu$ for Solution Sample 7 at 1500 V.....	133
Figure 6.132. Plots of $(\alpha h\nu)^2$ versus $h\nu$ for Solution Sample 7 at 2000 V.....	134
Figure 6.133. Plots of $(\alpha h\nu)^2$ versus $h\nu$ for Solution Sample 7 at 0 V.....	134
Figure 6.134. Plot of band gap, radius versus applied electric field for solution sample 7, from table above .....	135

## LIST OF TABLES

Table 1.1. Parameters of the most common semiconductors .....	4
Table 4.1. Measurement result analysis of the various CdSe/ZnS nanoparticles .....	26
Table 4.2. Elementary analysis of RG830 glass sample .....	30
Table 4.3. Heat Treatment Process of Solid Samples .....	31
Table 4.4. Chemicals to synthesize water soluble CdTe QDs .....	36
Table 4.5. Preparation method of Cadmium Ion Solution .....	38
Table 4.6. Reaction Time of Samples .....	40
Table 5.1. Raman peak values of the samples .....	46
Table 5.2. Strain values from Raman Spectroscopy Measurement .....	47
Table 6.1. Experimental Flow Table .....	53
Table 6.2. Band gaps of $Zn_xCd_{1-x}Te$ semiconductor nanocrystals embedded in glass matrices .....	54
Table 6.3. Table of solution samples absorption wavelength, band gap energies and heating time .....	61
Table 6.4. Dielectric permittivity of the samples .....	66
Table 6.5. Size distribution of the samples .....	79

Table 6.6. Measurement uncertainty of calculation of the particle size distribution.....	80
Table 6.7. Band gap energies and radius of different samples .....	83
Table 6.8. Band gap energies and size of solid sample under different electric fields.....	84
Table 6.9. Repeatability measurement band gap energies and size of solid sample 1 under different electric field.....	85
Table 6.10. Band gap energies and size of solid sample under different electric field .....	99
Table 6.11. Repeatability measurement band gap energies and size of solid sample under different electric field.....	100
Table 6.12. Band gap energies and size of solid sample under different electric field .....	109
Table 6.13. Band gap energies and size of solution sample 1 under different electric field .....	114
Table 6.14. Band gap energies and size of solution sample 3 under different electric field .....	120
Table 6.15. Band gap energies and size of solution sample 4 under different electric field .....	125
Table 6.16. Band gap energies and size of solution sample 6 under different electric field .....	127
Table 6.17. Band gap energies and size of solution sample 7 under different electric field .....	130
Table 6.18. Comparison of Experimental and Theoretical Stark Shift in Band Gap .....	136

## LIST OF SYMBOLS/ABBREVIATIONS

$c$	Speed of Light
$e$	Charge on Electron
$E$	Photon Energy
$E_g$	Band Gap Energy
$h$	Planck's constant
$I$	Intensity of Light
$I_0$	Initial Intensity
$m_e$	Electron Rest Mass
$m_h$	Proton Rest Mass
$m_e^*$	Effective Mass of Excited Electron
$m_h^*$	Effective Mass of Excited Hole
$R$	Radius of the Quantum Dot
$T$	Sampling time
$U$	Coulomb Potential

$\alpha$	Absorption Coefficient
$\epsilon_0$	Permittivity of Free Space
$\epsilon_r$	Relative Permittivity
$\omega$	Angular Frequency

AAS	Atomic Absorption Spectrum
a.u.	Arbitrary Units
CB	Conduction Band
CdTe	Cadmium Telluride
CdSe	Cadmium Selenide
Cys	Cysteine
dc	Direct Current
FWHM	Full Width Half Maximum
ITO	Indium Tin Oxide

LA	Longitudinal Acoustic Phonon
LED	Light Emitting Diode
LO	Longitudinal Optical Phonon
MPA	Mercaptopropionic Acid
NC's	Nanocrystals
NNI	National Nanotechnology Initiative
QCSE	Quantum Confined Stark Effect
QDs	Quantum dots
pH	Power of Hydrogen
r.t.	Room Temperature
TA	Transverse Acoustic Phonon
TO	Transverse Optical Phonon
TGA	Thioglycolic Acid
HPLC	High Pressure Liquid Chromatography
UV	Ultra Violet
VB	Valence Band
ZnS	Zinc Sulfide

## **1. INTRODUCTION**

In recent years, nanometrology, engineering and nanotechnology have been subject to a growing tendency and enormous interest globally and funding from governments and businesses. Nanotechnology research and development require multidisciplinary studies such as physics, medicine, chemistry, genetics, biology and engineering. Nanoscale products are of enormous interest due to their unique link with size and tunable properties.

National Nanotechnology Initiative (NNI), nanotechnology investment began in 2001, inspired by a long-term vision, and with a budget of \$494 million. The US National Science Foundation provided budget for nanotechnology research and development \$1.5 billion in 2016 and we see that a similar budget in 2017 [1, 2].

In this study, the research is mostly focused on semiconductor nanocrystals which have great application potential in this R&D. The main studies started with the synthesis of the QD's with an analytical technique and growth of nanocrystals in solid matrices and growth stages identified following by nucleation, diffusion limited and Oswald ripening. I synthesized QD samples subjected to electric fields in order to observe their spectra and properties under extreme conditions.

### **1.1. OVERVIEW SEMICONDUCTOR QUANTUM DOTS AND QUANTUM CONFINEMENT IN SEMICONDUCTORS**

A quantum dot is a semiconductor nanocrystal which is a tiny particle corresponding to 10 to 50 atoms. In diameter it is approximately between 2 to 10 nanometers. Quantum dots (QD's) are often referred to as artificial atoms. Their electrons within them exist only in discrete energy states. They were first discovered in the 1980 by A. Ekimov in a glass matrix [3] and L.E. Brus in aqueous solutions [4, 5]. They have been extensively studied by multiple scientific disciplines in recent years due to their unique tunable optical and electronic properties. These nanometer-sized crystalline particles have a broad application area ranging from optical devices such as quantum dot lasers, IR photodetectors and display LEDs, photovoltaics, data storage devices, fluorescence labels, DNA nanosensors etc. Quantum dot

light-emitting devices with electroluminescence are tunable over the entire visible spectrum [6, 11].

## 1.2. QUANTUM DOT DIMENSIONS AND BOHR RADIUS

Semiconductor nanoparticles are tiny light-emitting particles which have dimensions approximately 1-100 nm varying from substance to substance. In this size scale the NPs are located at the transition region between molecular clusters and bulk materials, resulting in quantum confinement effects. An exciton is an electron hole pair attached via the electrostatic Coulomb force in a semiconductor. There is an average distance between electron and hole known as the exciton Bohr radius. When the radius of an NP is less than the Bohr radius of the exciton (the electron-hole pair is confined in all three spatial dimensions which is called quantum confinement) in the bulk material, the charge carriers become spatially confined and the continuous energy bands of the bulk semiconductor split into discrete energy levels, just like for molecules. [12] Excitons generated inside the quantum dot and confinement depend on the size of the dot.

Figure 1.1. shows the change in energy levels and band gap energies between bulk semiconductor and nanosized material (QDs). QD lies between atomic and molecular limit due to their small size, so their electronic energy levels are quantized, the energy levels for an electron in a quantum dot have only discrete values like a particle in a well, it is closer to atoms rather than a bulk material. It gives sharp absorption and emission spectra for QDs. The density of states,  $g(E)$ , might be a series of delta functions,  $\delta$ , at each of the allowed energy values [13].

$$g(E) = \delta(E - E_n) \quad n = 1, 2, \dots \quad (1.1)$$

Bulk semiconductors have extended crystalline limit and charge carriers can have a range of energies. In the bulk material, the energy levels are split into two, valence and conduction bands. There can be two electrons per energy level due to the Pauli Exclusion Principle. Separation between successive energy levels is very small, when the number of electrons



increases the energy levels get closer. These continuum energy bands are fixed and not changeable [14, 15].

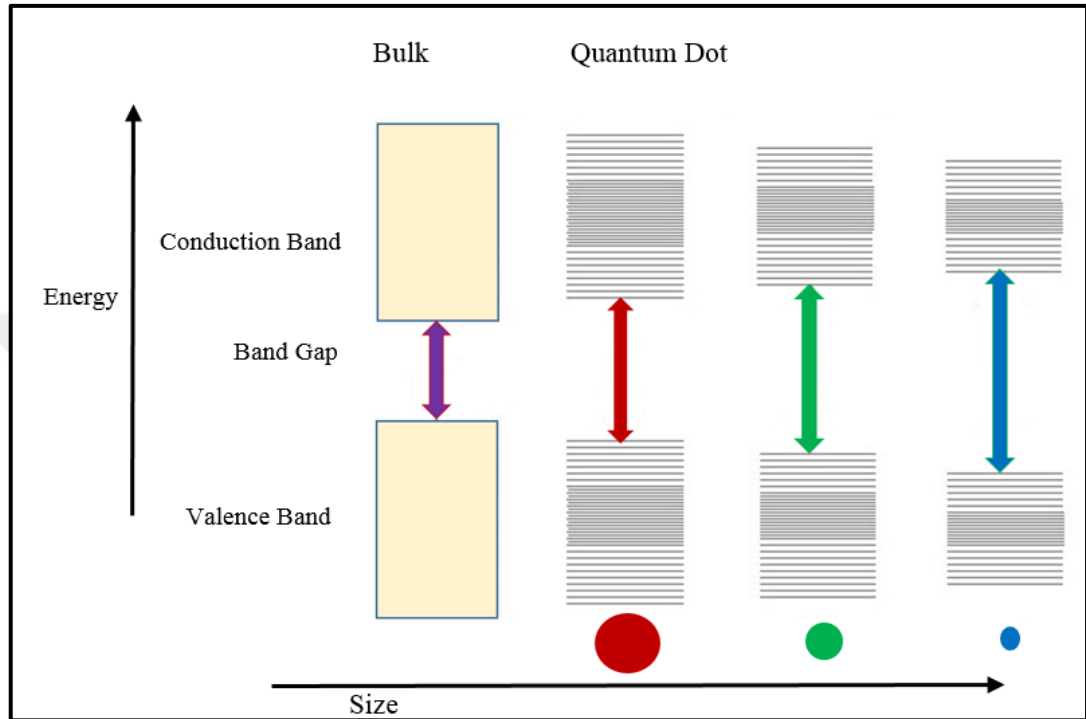


Figure 1.1. Energy levels and band gaps of a semiconductor from bulk crystals to nanosized crystals

The optical and electronic properties are also dependent on the size of the NPs or QDs. Strong quantum confinement can be observed when the QD's radius is smaller than the exciton Bohr Radius. As a consequence of this strong confinement the band gap energy of the QD's increases [16].

The distance between electron and hole defined as exciton Bohr radius,  $r_b$ , where  $m_e$  and  $m_h$  are effective masses of electrons and holes,  $\epsilon$  is the dielectric constant,  $\hbar$  and  $e$  are the Planck constant and charge of an electron respectively [17].

$$r_B = \frac{\hbar^2 \epsilon}{e^2} \left( \frac{1}{m_e} + \frac{1}{m_h} \right) \quad (1.2)$$

Among the various compositions of inorganic semiconductor nanocrystalites, are the ones made of groups III-V semiconductors (main groups III boron, aluminum, gallium, indium, main group V nitrogen, phosphorus, arsenic, antimony, bismuth) and II-VI semiconductors (subgroup II zinc, cadmium, main group VI oxygen, sulfur, selenium, tellurium) and silicon. The most interested and prominent II-VI group semiconductor quantum dots are cadmium selenide (CdSe) and cadmium telluride (CdTe). Table 1.1 lists some of the common semiconductors, including their band gap energies, exciton Bohr radius, periodic table classification.

Table 1.1. Parameters of the most common semiconductors

Semiconductor	Periodic Table Classification	Band Gap Energy $E_g$ (eV)	Exciton Bohr Radius $r_B$ (nm)	Dielectric Constant (F/m)
GaAs	III-V	1.518	12.5	12.9
CdTe	II-VI	1.600	7.5	10.2
CdS	II-VI	2.583	2.8	5.4
CdSe	II-VI	1.840	4.9	10.0
ZnSe	II-VI	2.820	3.8	9.1

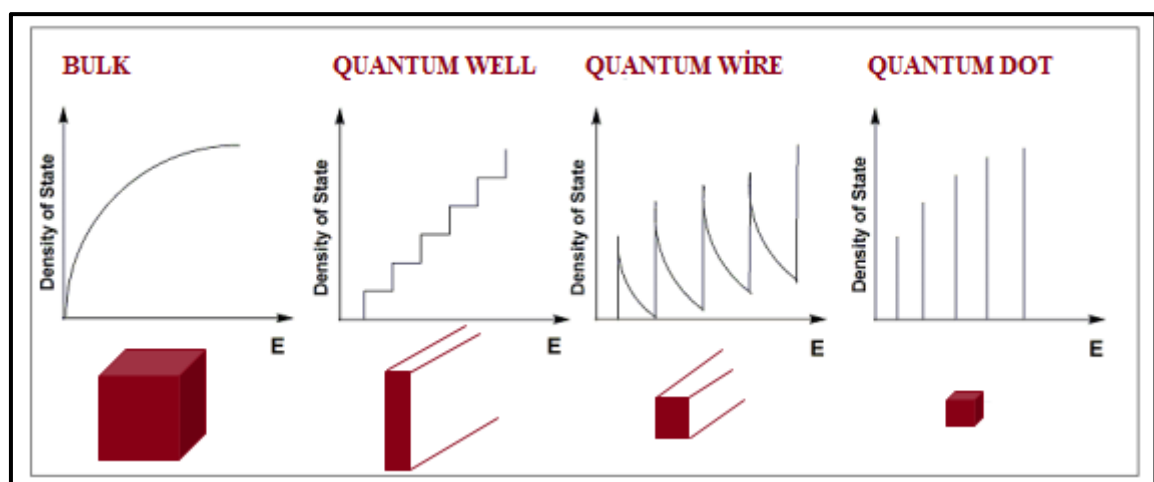


Figure 1.2. Density of states as a function of energy: bulk (3D), quantum well (2D), quantum wire (1D) and quantum dot (0D)

Transition in a semiconductor may be observed in two classifications: Intraband Transition and Interband Transition. An interband transition occurs from conduction band to the valence band (in exciton), an intraband transition occurs in conduction band or valence band. If the dimensions of the nanostructure increase, the energy of the confined states decreases so the inter-band transitions shift to longer wavelengths. The size of the particle is larger than the de Broglie wavelength, the inter-band transition energy goes to the bulk value [18].

### **1.3. METHODS OF SYNTHESIS FOR SEMICONDUCTOR NANOMATERIALS**

Semiconductor nanoparticle synthesis was first discovered in the early 80's by Alexei Ekimov in glass and by Louis Brus in aqueous form [19, 20]. Nearly in 40 years many improvements have been made to optimize the synthesis methods. These new approaches and modification increased the quality of the QDs, size distribution control is provided, explosive and toxic effects are reduced, for the more stable QD's and less aggregation appropriate precursors are found and used [21, 22, 23]. QDs can be synthesized using two methods which are top down method ion implantation, e-beam lithography, and X-ray lithography and bottom up method colloidal synthesis epitaxy [24, 25, 26].

Several different techniques can be used to fabricate QDs, such as gas, aqueous and solid phase processes. In this thesis, semiconductor nanocrystals were produced both in aqueous solution (colloidal synthesis) and solid phase.

### **1.4. STAGES DURING GROWTH OF QD IN SOLUTION**

The main and extensive studies in this thesis were carried out on CdTe nanoparticle which is a semiconductor potentially useful for a huge application area [27].

When synthesizing CdTe quantum dots in an aqueous medium, the particle growth process is an important parameter in the formation of nanoparticles QDs. Stability of these nanocrystals depends on the surfactant (generally called ligand/stabilizer). These surfactants are also used to control the size and shape of the nanocrystals. During the chemical reaction they bind to the surface of the nanoparticle and act as a spacer between the nanocrystals in the colloidal solution [28]. This method is aimed at growing nanoparticles of inorganic

materials with chemical reactions of their precursors. Precursor is used as a starting material and it is important to choose the appropriate starting material for synthesis [29, 30]

In this thesis, to control the size and shape of the nanocrystals, some experimental parameters (reaction heat, time and PH) were modified during the synthesis of semiconductor nanocrystals. In this synthesis method, three important growth stages were investigated for the CdTe semiconductor nanocrystals.

- i. Nucleation
- ii. Growth
- iii. Oswald Ripening

Nucleation is the first stage of the synthesis of semiconductor nanocrystal, defined as an irreversible formation of a nucleus of the new phase [31]. In the first stage of the synthesis, the nanoparticles' nuclei form rapidly and then more particles deposit onto the formed nucleus, called nucleation.

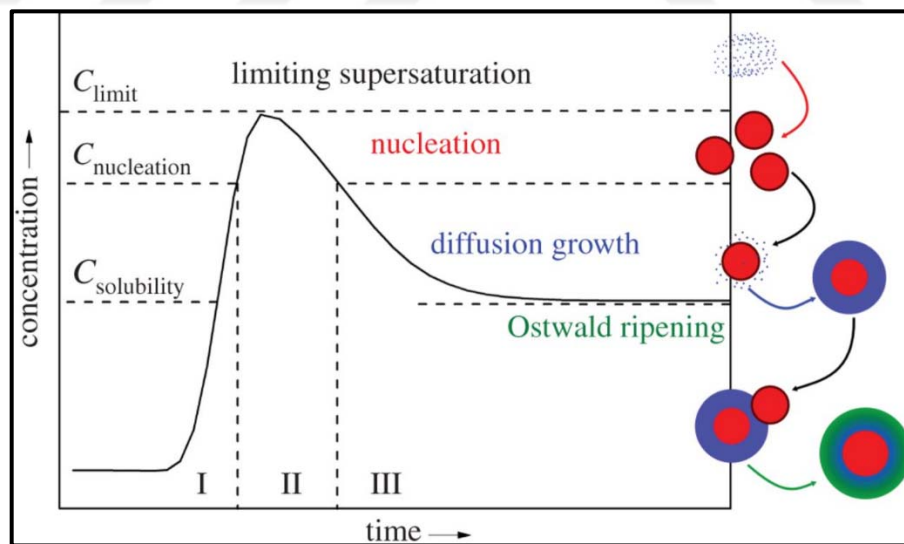


Figure 1.3. Schematic graph displaying the relationship between the precursor concentration and the reaction time for the solution phase synthesis process a- LaMer's Diagram (Concentration vs. Time) [32].

The formation of the nucleation stage was explained by Lamer diagram as shown below in Figure 1.3 [32]. When the precursor is added to the reaction vessel rapidly, atoms decompose with temperature and their concentration increases. The concentration of the atoms increases, to a saturation point for a brief period is reached where homogeneous nucleation occurs ( $C_{\text{nucleation}}$ ). These metal atoms start to aggregate and begin to cluster. The rate of nucleation must be high enough so that the concentration does not continue to climb. Instead, a burst of nuclei is created in a short period. The rate of growth of these nuclei must be fast enough to reduce the concentration below the nucleation concentration point. In this way, only a limited number of particles are created. The rate of growth must be slow enough; however, the growth period is long compared to the nucleation period.

In the next stage, the growth rate of nanoparticles is slower than that of the first stage and they reach the desired size over time. In this type of growth, the average nanocrystal radius increases with the square root of heat treatment time ( $R_{\text{ave}} \propto \sqrt{t}$ ). If the process is not quenched, this event is called Ostwald Ripening if the particles continue to grow where average particle radius is proportional to the cubic root of heat treatment time ( $R_{\text{ave}} \propto \sqrt[3]{t}$ ) [33].

In Section 2, the spectroscopic techniques; UV-Vis absorption and Raman Spectroscopy techniques used in this study to characterize the optical properties of the semiconductor nanoparticles is discussed. Section 3 is focused on the theory of the two electroabsorption mechanism: Quantum Confined Stark Effect and Franz Keldysh Effect. Also electroabsorption behaviour of the quantum structures is presented. Experimental part is discussed in Section 4 covers the preliminary experiment, material, synthesis of the samples, and experimental set-up. Section 5 is followed by the result analysis method and measurement uncertainty calculations, hysteresis analysis and equations used in calculations.

Experimental findings are analysed in Section 6 with graphs and tables. We show that absorption spectroscopy measurement result without field, determination of the dielectric permittivity, the particle size distribution calculation from absorption spectra, the band gap energies from Tauc Plot relation, the semiconductor nanoparticles radius with the aid of Brus Equation. All these measurements are performed with an without an external electric field. This is followed by the conclusion, references and appendix.

## 2. SPECTROSCOPIC CHARACTERIZATION TECHNIQUES FOR SEMICONDUCTOR NANOPARTICLES

### 2.1. UV-VIS ABSORPTION SPECTROSCOPY

The band gap is one of the fundamental properties of semiconductor nanocrystal QD. In the theory of the absorption spectra measurement, monochromatic light interacts with the sample and the difference between incoming and outgoing light intensity is collected and focused on the entrance slit of the monochromator shown in Figure 2.1. The result of the difference between incoming and transmitted light intensities is the amount of light absorbed at the given wavelength.

This absorption radiation is expressed by The Lambert Beer's Law [35].

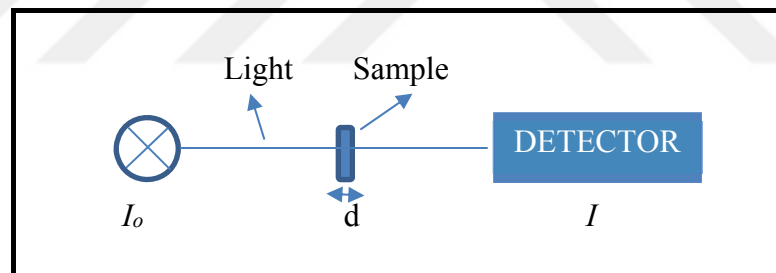


Figure 2.1. The basic principle of the absorption spectrum

where  $I_0$  represents the initial intensity emitted by the source,  $I$  is the radiation intensity after passing through the sample,  $d$  is the thickness of the sample,  $\alpha$  is the absorption coefficient of the sample and OD is the optical density.

$$OD = \alpha d = \ln\left(\frac{I_0}{I}\right) \quad (2.1)$$

The absorption spectra of measurement is one of the methods used to find the band gap energy separating the valence and the conduction band. This defines the feature of a semiconductor. Absorption spectroscopy measures the absorbance at a certain wavelength of a material and the absorbance data used to determine the band gap energy allows the Tauc plot to be realised.

Optical absorption is used to measure the absorption of interband transition energies in semiconductors. Quantum dots absorption spectra reveal the position and the energy associated with the first excitonic transition. Size-dependent properties can also be observed in UV-visible spectra, particularly in the nano and atomic scales. These include peak broadening and shift. The band gap of the material can be measured using this technique.

## **2.2. RAMAN SPECTROSCOPY**

Raman spectroscopy is a complementary vibrational spectroscopic technique to measure the vibrational modes of a molecule. Studying by Raman spectroscopy reveals the information about the chemical structure, molecular interaction and other useful information about the material. In the literature, Raman theory can be described as the inelastic scattering (Raman Scattering) of photons by atomic vibrations and phonons. In this technique, a laser light source is used to irradiate a sample, the frequency of photons in the laser (monochromatic light) changes upon interaction with a sample. Photons of the laser are absorbed by the molecule and the light re-emitted. The final frequency of the reemitted photons is shifted up or down in comparison with the initial original frequency, which is called the Raman effect. This frequency shift provides information about phonon modes; vibrational, rotational and other low frequency transitions in molecules. Raman spectroscopy generally can be used to work with solid, aqueous and gaseous samples.

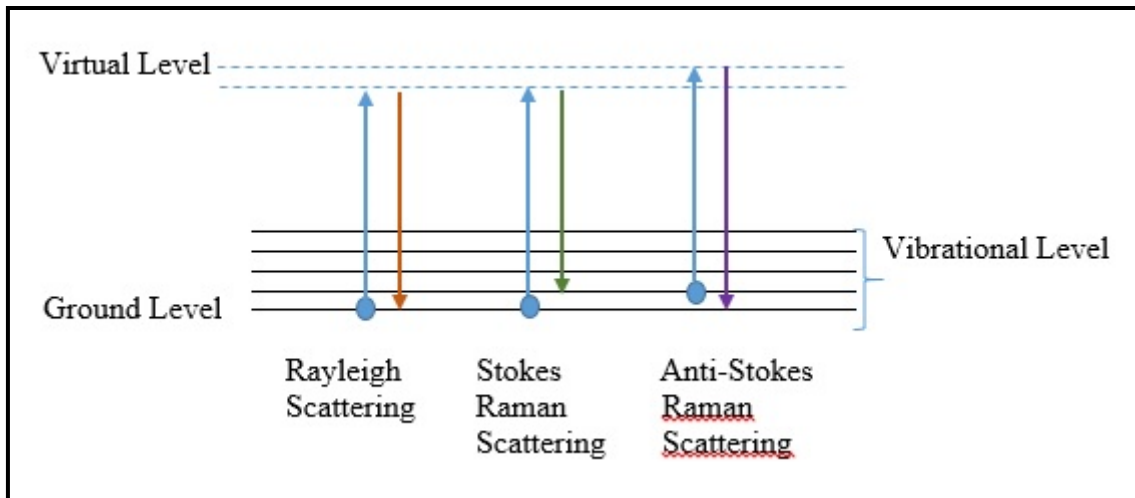


Figure 2.2. The Rayleigh and Raman Scattering Energy Diagram

The incident light interacts with the molecule, it induces electric dipole moment due to the electric field of incoming light which forces the electron cloud to vibrate and distorts to form a virtual state. This virtual state is not stable and the photon is immediately re-radiated as scattered light. Rayleigh scattering is a process in which an electron in the ground level is excited and goes back to the original ground level. In this type of scattering, the light interacts with the object and some of the light is scattered, the scattered light has the same frequency with the incoming light frequency. The energy does not change so Rayleigh scattered light has the same energy as the incident light. If the scattered light has different frequency than the incoming light it is called Raman Scattering. There are two types of Raman Scattering: Stokes Raman scattering and anti-Stokes Raman scattering shown in Figure 2.2. In Stokes Raman scattering an electron is excited from the ground level and falls to a vibrational level. It involves energy absorption by the molecule, thus Stokes Raman scattered light has lower frequency than incoming light. Anti-Stokes Raman scattering is a process in which an electron is excited from the vibrational level to the ground level [36]. It involves an energy transfer, thus anti-Stokes Raman scattered light has higher frequency than incoming light [37].

In this study, Raman Spectroscopy is used to investigate the phonon modes for examining the electronic structure of the nanostructure. The shift in the energy gives the information of these phonon modes in the nanosystem. If there is one type of atom in the structure, there will be only acoustic phonon present but if we are talking about two types of atoms, the



acoustic and the optical phonons will appear at the same time. The longitudinal and transverse components represent the direction of the motion [16]. Phonon mode types are given: LO: Longitudinal Optical, LA: Longitudinal Acoustic, TO: Transverse Optical, TA: Transverse Acoustic

Raman scattering is a technique that gives information about the size distribution of the nanoparticle. Phonon confinement and size distribution of the nanoparticles cause a shift and a broadening in the Raman peak. The size reduction of particles changes the vibrational properties by the agency of phonon confinement effect [39, 40]. In CdTe nanoparticles the crystalline Raman peak position is downshifted and broadened with respect to bulk materials.

There is a relation between frequency and wavevector known as a dispersion relation. In the diatomic lattice, the dispersion relations exhibit two types of phonons; the blue line represents optical mode, and the red line represents the acoustic mode. In the optical mode two neighbouring different atoms move against each other, but in the acoustic mode they can move together. In Figure 2.3, the x-axis represents the energy or frequency of the phonon and y-axis represents wavevector.

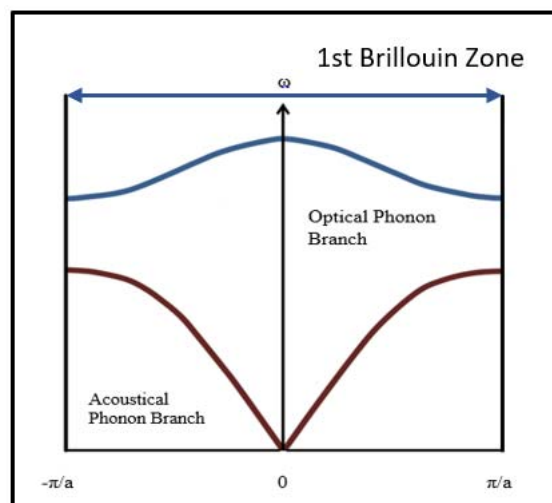


Figure 2.3. Optical and acoustical branches of the dispersion relation for a diatomic lattice

For the crystalline material the phonon dispersion has a maximum at the centre of the Brillouin zone (the boundaries of the first Brillouin zone are  $-\pi/a$  and  $\pi/a$ ), these maximum frequencies go down with the decreasing crystalline size. Brillouin zone is a particular choice of the unit cell of the reciprocal lattice (exists in reciprocal space or momentum space,  $k$ -space). The reciprocal lattice represents the Fourier transform of another lattice and this lattice is known as direct lattice, usually a periodic spatial function in real space. Optical phonons have a non zero frequency at the Brillouin zone and there will be no dispersion close to the long wavelength limit. Thus, these optical phonons interacting with the infrared radiation are in a mode of vibration where the positive and negative ions of adjacent lattice positions swing against each other creating a time varying electric dipole moment.

### 3. ELECTROABSORPTION IN SEMICONDUCTORS

#### 3.1. ELECTROABSORPTION IN SEMICONDUCTORS

When an external electric field is applied to semiconductors, their optical absorption spectra change, this is known as electroabsorption. There are two forms of electroabsorption: 1- the quantum confined Stark effect (QCSE), which is seen in quantum structures such as quantum dots, wires or wells and 2- Franz-Keldysh effect which is seen in bulk semiconductor materials. In this section these two main mechanisms have been discussed.

#### 3.2. THE QUANTUM CONFINED STARK EFFECT (QCSE)

The presence of the external field induces various changes in the optical properties of the nanomaterials due to the electronic states changing, known as Quantum Confined Stark Effect [41]. The QCSE effect especially has found application areas such as lasers, electro-absorption modulators and solar cells [42-44].

Recent research in applications of electric field has shown that controlling the size of the nanoparticles is important for the production of novel light sources. In 1993 Bawendi and co-workers produced monodisperse Cd chalcogenide semiconductor nanocrystals and investigated quantum-confined Stark effect in CdSe [45, 46]. M. Leroux and et al. have studied polarization effect on (Al,Ga)N/GaN quantum wells and relationship with QCSE [47]. Other work in the literature, using electric fields is time-resolved photoluminescence measurements. Electric field and temperature effects were studied in a GaAs-Al<sub>x</sub>Ga<sub>1-x</sub>As quantum-wells [48].

When an electric field is applied to the nanoparticles, the electron and hole are pulled in opposite directions and their wavefunctions overlap [49]. Figure 3.1 shows that the electron and hole wavefunctions for each state are distorted under these circumstances and their wavefunctions which are sinusoidal functions without electric field, change to Airy functions with an applied electric field [50]. Airy function is the solution to

$$y'' - xy = 0 \quad (3.1)$$

The following second order differential equation is called the Airy equation. Characterization of the solution changes from oscillatory to exponential in the Airy function.

The transition between these two states requires less energy and the absorption strength decreases, therefore light of a longer wavelength can be absorbed by the semiconductor nanoparticles.

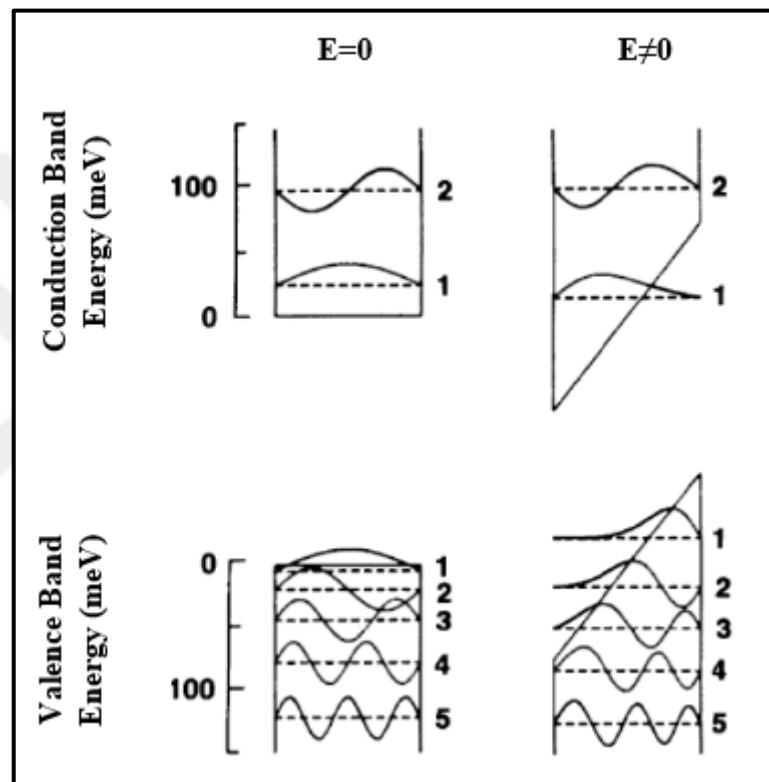


Figure 3.1. Electron and hole wavefunctions for the infinite potential well without field and with field [50].

### 3.3. FRANZ KELDYSH EFFECT

Franz-Keldysh effect is another electroabsorption mechanism observed in bulk semiconductors when an electric field is applied [51]. This effect is the result of the wavefunctions tunnelling into the band gap. When an external electric field is applied to a bulk semiconductor material, the electron and the hole move away from each other, their wavefunctions becoming Airy functions (shown below Figure 3.2.). When the overlap of the electron and hole wavefunctions decreases, the absorption also decreases according to the

Fermi's Golden Rule, which is also referred to as the rule of time-dependent perturbation theory. It is an equation to calculate the transition rate. The frequency dependence to the transition rate is proportional on an optical absorption spectrum. According to the Fermi's Golden Rule, the transition probability is constant in time, in many physical situations the transition probability is of the form;

$$\lambda = \frac{2\pi}{\hbar} |M|^2 \rho_f \quad (3.2)$$

where  $\lambda$  is the decay probability,  $M$  is the matrix element for the interaction and  $\rho_f$  is the density of final states.

The conduction and valence band edges tilt. By the agency of absorbed photon, an excess electron in the valence band can tunnel into the conduction band [52].

The Airy tail extends right into the classically forbidden band gap, allowing transitions below the bandgap. The application of an external electric field induces optical absorption below the band gap energy, this means that the absorption edge (the wavelength at which absorption starts), shifts to lower frequency with the external electric field application.

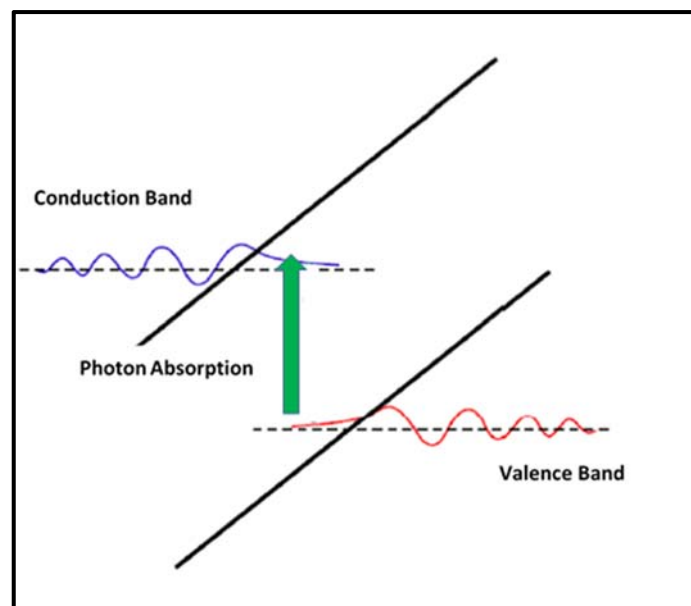


Figure 3.2. The Franz-Keldysh effect and the resulting change in absorption spectrum [51, 52]

If  $hf > E_g$ , oscillations in absorption at band gap, caused by the set-up of electron standing waves bouncing off the increasing potential.

If  $hf < E_g$ , absorption occurs due to the decaying wave function tails.

### 3.4. TIME-INDEPENDENT SCHRÖDINGER EQUATION

The main equation in the study of quantum systems is the Schrödinger equation, that answers most of the quantum mechanical questions; there is no known solution, except for simple problems. There are some methods to generate approximate solutions to the Schrödinger equation: 1- Variational Method 2- Perturbation Method. In this study perturbation theory is used to determine the energy and the wavefunction.

The energy of the system is written as;

$$H|\Psi\rangle = E|\Psi\rangle \quad (3.3)$$

where  $H$  is the Hamiltonian (energy) operator,  $\Psi$  is the wave function for the system, and  $E$  is the energy of the system. This is known as Dirac notation where a ket such as  $|\Psi\rangle$  represents the wavefunction  $\Psi$ .

### 3.5. PERTURBATIONAL METHOD

This is the most important method for solving problems in quantum mechanics, especially when we apply an external electric field to the nanostructure, the energy levels shift and wavefunctions become distorted due to the Stark effect.

The new energy levels and wavefunctions could be obtained by solving the Hamiltonian with the external field. In this study the theoretical part focused on solving this question: a weak electric field applied to a charged particle in the one-dimensional harmonic oscillator potential, the shift in the energy level caused by the electric field is found using the perturbation theory. [24] The perturbation is just a potential energy term ( $V=H' = -qEx$ ) of a particle of charge  $q$  in a constant electric field of magnitude,  $E$  oriented along the positive  $x$ -direction:

The lowest order unperturbed Schrödinger Equation is

$$H_n^0 \Psi_n^0 = E_n^0 \Psi_n^0 \quad (3.4)$$

In the nondegenerate perturbation theory  $\Psi_n^0$  are the eigenfunctions,  $E_n^0$  are the eigenvalues

$$\langle \Psi_n^0 | \Psi_m^0 \rangle = \delta_{nm} \quad (3.5)$$

Where  $\delta_{nm}$  is the Kronecker delta defined as

$$\delta_{m,n} = \begin{cases} 0, & \text{if } m \neq n \\ 1, & \text{if } m = n \end{cases} \quad (3.6)$$

When we perturb the system new eigenfunctions and eigenvalues are as shown below, new Hamiltonian as sum of two terms

$$H = H^0 + \lambda H' \quad (3.7)$$

We expand our solution as follows in terms of perturbation H,

$$E_n = E_n^0 + \lambda E_n^1 + \lambda^2 E_n^2 + \dots \quad (3.8)$$

$$\Psi_n = \Psi_n^0 + \lambda \Psi_n^1 + \lambda^2 \Psi_n^2 + \dots \quad (3.9)$$

Separating the equations for zeroth, first and second orders we get,

$$E_n^1 = \langle \Psi_n^0 | H' | \Psi_n^0 \rangle \quad (3.10)$$

$$\langle x \rangle = \int \Psi_n^* \hat{x} \Psi_n dx \quad (3.11)$$

The first order shift in energy is given simply by the expectation value of the perturbation taken with respect to the unperturbed eigenfunctions.

According to the perturbation theory, the first order correction to the eigenenergy is

$$E_n^1 = \langle \Psi_n^0 | -qEx | \Psi_n^0 \rangle \quad (3.12)$$

$$E_n^1 = -qE \langle \Psi_n^0 | x | \Psi_n^0 \rangle \quad (3.13)$$

$$E_n^1 = -qE \langle m | x | n \rangle \quad (3.14)$$

The easiest way to evaluate the bracket term is to use the harmonic oscillator ladder operators (raising and lowering operators). These operators increase or decrease the eigenvalue of another operator.  $\hat{a}_+$  is called the raising operator, it raises energy eigenstate  $\Psi$  up to the next highest energy eigenstate.  $\hat{a}_-$  is called lowering operator and it lowers energy eigenstate to the next lowest energy eigenstate.

$$\hat{x} = \sqrt{\frac{\hbar}{2m\omega}} (\hat{a}_+ + \hat{a}_-) \quad (3.15)$$

$$\langle m | \hat{x} | n \rangle = \sqrt{\frac{\hbar}{2m\omega}} \langle m | \hat{a}_+ + \hat{a}_- | n \rangle \quad (3.16)$$

$$\hat{a}_+ | n \rangle = \sqrt{n+1} | n+1 \rangle \quad (3.17)$$

$$\hat{a}_- | n \rangle = \sqrt{n} | n-1 \rangle \quad (3.18)$$

$$m = n \pm 1 \quad (3.19)$$

$$\langle m | \hat{x} | n \rangle = \sqrt{\frac{\hbar}{2m\omega}} [ (\sqrt{n+1}) \langle m | n+1 \rangle + \sqrt{n} \langle m | n-1 \rangle ] \quad (3.20)$$



$$\langle m|\hat{x}|n\rangle = \sqrt{\frac{\hbar}{2m\omega}} [(\sqrt{n+1})\delta_{m,n+1} + \sqrt{n}\delta_{m,n-1}] \quad (3.21)$$

Since all diagonal elements are zero, lowest order perturbation unchanged means there is no first order correction to the energy  $m \neq n$

$$\langle m_0|n_0\rangle = 0 \text{ so } E_n^1 = qE\langle m|\hat{x}|n\rangle = 0 \quad (3.22)$$

Therefore, the second-order energy is given by:

$$E_n^2 = \sum_{m \neq n} \frac{|\langle \Psi_m^0 | H' | \Psi_n^0 \rangle|^2}{E_n^0 - E_m^0} \quad (3.23)$$

and the equation becomes

$$E_n^2 = \sum_{m \neq n} (-qE)^2 \frac{|(m|\hat{x}|n)|^2}{E_n^0 - E_m^0} \quad (3.24)$$

and for a harmonic oscillator,

$$E_n^0 = \left(n + \frac{1}{2}\right) \hbar\omega \quad (3.25)$$

$$E_m^0 = \left(m + \frac{1}{2}\right) \hbar\omega \quad (3.26)$$

Using this in the above equations,

$$E_n^2 = (qE)^2 \left(\frac{\hbar}{2m\omega}\right) \sum_{m \neq n} \frac{|\sqrt{n+1} \delta_{m,n+1} + \sqrt{n} \delta_{m,n-1}|^2}{(n+1)\hbar\omega - (m+1)\hbar\omega} \quad (3.27)$$

$$(\delta_{m,n+1})^2 = 1 \quad (3.28)$$

and

$$E_n^2 = (qE)^2 \frac{1}{2m\omega^2} \left( \frac{n+1}{n-(n+1)} + \frac{n}{n-(n+1)} \right) \quad (3.29)$$

$$E_n^2 = (qE)^2 \frac{1}{2m\omega^2} \left( \frac{n+1}{-1} + \frac{n}{1} \right) \quad (3.30)$$

are the harmonic oscillator allowed energies. This is the second-order correction to the energy levels.

$$E_n^2 = \frac{-(qE)^2}{2m\omega^2} \quad (3.31)$$

$$E_n = \left( n + \frac{1}{2} \right) \hbar\omega - \frac{1}{2} \frac{(qE)^2}{m\omega^2} \quad (3.32)$$

We can actually find an exact solution for the perturbed potential in this case by a change of variables. The Schrödinger equation is written as

$$-\frac{\hbar}{2m} \frac{d^2\psi}{dx^2} + \left( \frac{1}{2} m\omega^2 x^2 - qEx \right) \psi = E\psi \quad (3.33)$$

after the change of variables,

$$x' = x - \left( \frac{qE}{m\omega^2} \right) \quad (3.34)$$

$$x = x' + \frac{(qE)}{m\omega^2} \quad (3.35)$$

$$x^2 = x'^2 + 2x' \frac{(qE)}{m\omega^2} + \frac{(qE)^2}{(m\omega^2)^2} \quad (3.36)$$

From (3.31):

$$-\frac{\hbar}{2m} \frac{d^2\Psi}{dx^2} + \left[ \left( \frac{1}{2} m\omega^2 \left( x'^2 + 2x' \frac{(qE)}{m\omega^2} + \frac{(qE)^2}{(m\omega^2)^2} \right) \right) - qE \left( x' + \frac{(qE)}{m\omega^2} \right) \right] \Psi = E\Psi \quad (3.37)$$

$$-\frac{\hbar}{2m} \frac{d^2\Psi}{dx^2} + \left( \frac{1}{2} m\omega^2 x'^2 + qEx' + \frac{(qE)^2}{2m\omega^2} - qEx' - \frac{(qE)^2}{m\omega^2} \right) \Psi = E\Psi \quad (3.38)$$

from (3.36)

$$-\frac{\hbar}{2m} \frac{d^2\Psi}{dx^2} + \left( \frac{1}{2} m\omega x'^2 - \frac{1}{2} \frac{(qE)^2}{m\omega^2} \right) \Psi = E\Psi \quad (3.39)$$

$$-\frac{\hbar}{2m} \frac{d^2\Psi}{dx^2} + \left( \frac{1}{2} m\omega^2 x'^2 \right) \Psi = E\Psi + \frac{1}{2} \frac{(qE)^2}{m\omega^2} \Psi \quad (3.40)$$

$$E_n = \left( n + \frac{1}{2} \right) \hbar\omega \quad (3.41)$$

the above equation becomes

$$E_n + \frac{1}{2} \frac{(qE)^2}{m\omega^2} = \left( n + \frac{1}{2} \right) \hbar\omega \quad (3.42)$$

$$E_n = \left( n + \frac{1}{2} \right) \hbar\omega - \frac{1}{2} \frac{(qE)^2}{m\omega^2} \quad (3.43)$$

## 4. EXPERIMENTAL SECTION

### 4.1. PRELIMINARY EXPERIMENTS

#### 4.1.1. Preparation of the Sample

In this study commercial CdSe/ZnS core shell type quantum dots in aqueous solution (Sigma Aldrich) were deposited on glass slides using a spin coating technique. All glass slides were cleaned in chromic acid solution for 24 hours, washed with distilled water and finally dried. The substrate was placed on the rotating disk of the spin-coater at 100 rpm and then CdSe/ZnS solution was dropped on the target substrate every 60 s. For each layer coating 2.5  $\mu\text{l}$  of solution was deposited on the substrate, one minute being allowed between consecutive layers so that the thin films could dry; this caused them to undergo a phase change to a solid. Finally, multilayered CdSe/ZnS films were obtained for measurements.

#### 4.1.2. Optical Measurements

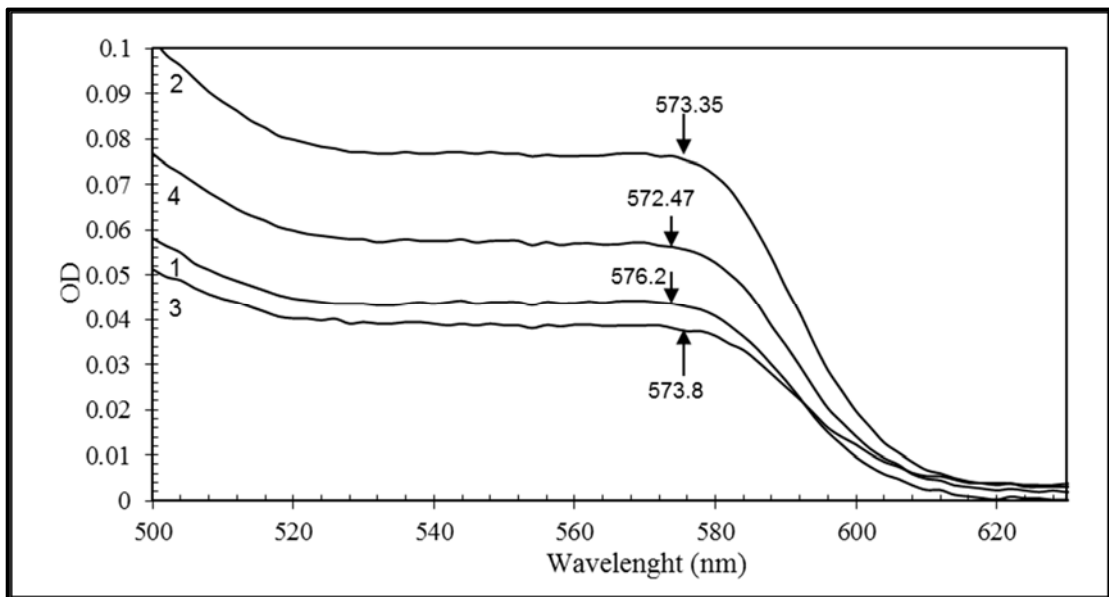


Figure 4.1. Optical absorption spectra for thin film CdSe/ZnS quantum dots before heat treatment.

In Figure 4.1 the absorption starts after 620 nm and each sample has its own absorption peak points. Each sample has different preparation conditions: Sample 1: 7 layers, 500 rpm, Sample 2: 7 layers, dry for 1 minute between layers, 500 rpm, Sample 3: 7 layers, dry for 1 minute between layers, 200 rpm.

The observed structure at around 570 nm is due to the production of excitons in the lowest bound state; the asymptotic absorption edge of bulk CdSe is 720 nm blue-shifted due to the quantum size effect. Optical absorption spectroscopy is an important tool to understand the behaviour of thin films. The average radius and radius distribution of quantum dots were estimated using the effective mass model in the strong confinement limit. Using this model, the following relationship between the energetic position of the first exciton peak and the average radius was used as an approximation.

$$E_R(eV) = E_g(eV) - \frac{0.14}{R(nm)} + \frac{0.356}{\mu[R(nm)]^2} \quad (4.1)$$

where  $E_R$  is the size dependent first exciton transition energy given by. The first term is the bulk band gap of the cadmium selenide crystal of  $E_g=1.727$  eV, the second term is the Coulomb potential energy between an electron and hole and the third term is the confinement energy for an electron and a hole. The symbol  $\mu$  is the reduced mass of an electron-hole pair and has a value of 0.106 in units of electron rest mass  $m_0$ . The average radius of quantum dots was estimated at 2.6 nm prior to the annealing process in Eq. 4.1.

Changing the spin speed of the spin coater (in rpm) controlled the distribution of the quantum dots and the thickness of the thin film layer. The low speed mode of the spin coater quantum dots inside the solution caused the quantum dots to be spun closer (clumped) together on the thin film. When the spin coater speed was increased the quantum dots tended to be more dispersed. This can be observed on the two photographs taken with the AFM at 100 rpm and 500 rpm, in Figure 4.2.

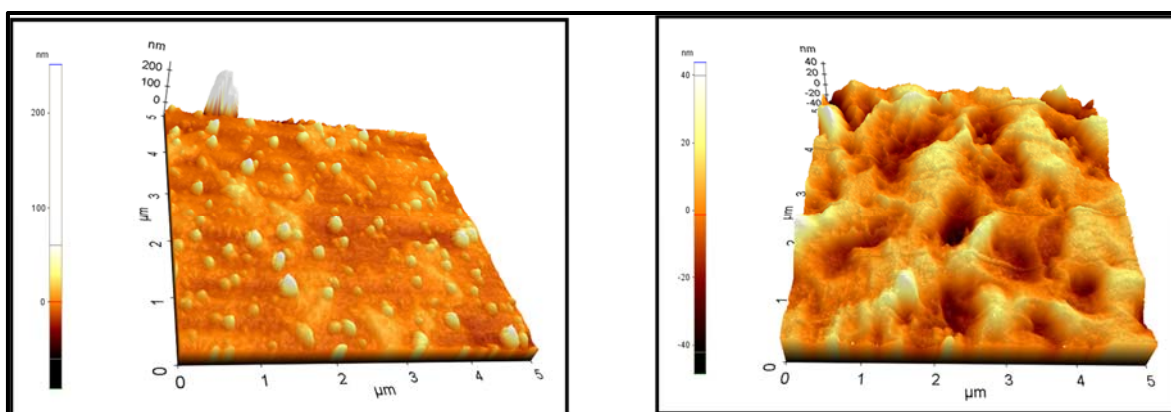


Figure 4.2. AFM surface topographical image of deposited CdSe/ZnS thin films with spin coater at 500 rpm and 100 rpm

The UV visible spectra of the thin films were recorded at a range between 573 nm to 576 nm. The peak absorption of their excitons in the first excited states is shown in Figure 4.3. The size of the CdSe/ZnS nanocrystals as calculated to have a radius range between 2.61 and 2.65 nm. In addition, the UV visible spectra of the quantum dot in solution; prior to spinning into a thin film samples were taken and are presented for two different percentage concentrations in Figure 4.3. The difference between the absorption peak of excitons in aqueous and as a solid thin film is 6.5 nm.

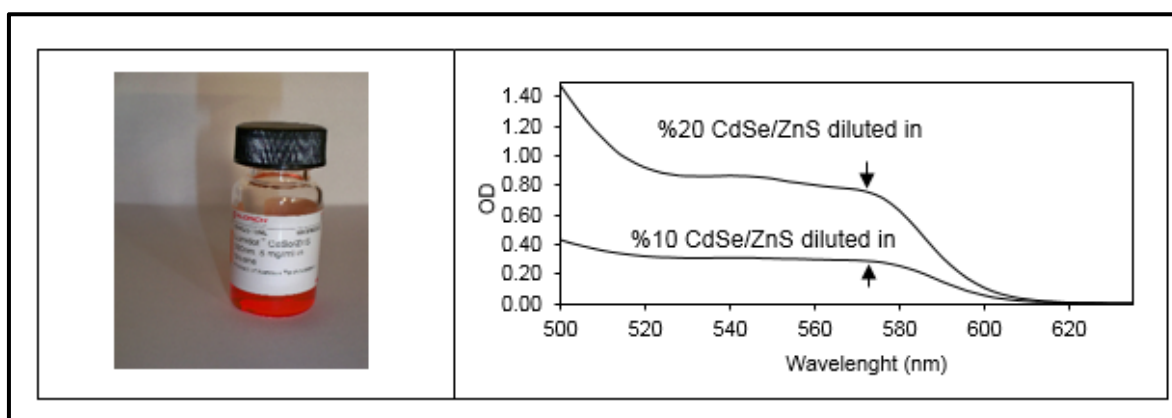


Figure 4.3. CdSe/ZnS core shell 590 nm quantum dots in solution with the different concentrations.

In the case of thin films annealed at 50 °C for a period of 1 hour in a water bath, the sizes of the quantum dots were calculated to range between 2.24 to 2.41 nm and the peak positions were shifted to 540 nm as shown in Figure 4.3. The dependence of the deposited and annealed (onto glass samples) CdSe/ZnS thin films energy shift and with respect to speed of the spin coater followed an increasing trend in Figure 4.4. This shows that the annealing process caused a decrease in the nanocrystals' size, an increase in emission wavelength and a decrease in exciton peak energy.

To see the variation of the CdSe/ZnS nanocrystals, the results of the optical densities as a function of the wavelength were calculated by using OD relationship in Eq. 4.2. Equation shows measured optical densities (OD) as a function of wavelength for four typical samples prepared at room temperature. The following equation was used to determine this information where  $d$  is the thickness of the investigated thin film, while  $I_o$  and  $I$  are the intensity of incident and transmitted light. correspondingly.

$$A = \ln\left(\frac{I_o}{I}\right) = \alpha d \quad (4.2)$$

To find the peak position of the graphs before and after annealing, second derivative methods were used in the Excel and peak fit programme. Results from the two programmes were compared with each other to check results; little difference was observed. In the peak fit analysis, the graphs indicated some trends which are shown below. The graphs of the CdSe/ZnS capped quantum dots cover three samples which were deposited at 100 rpm (Sample 3), 200 rpm (Sample 4) and 500 rpm (Sample 2). For each sample, the solution was dropped on the target substrate every 60 s with a one minute drying period, so that the solvent could evaporate between consecutive layers. The fourth sample was deposited at 500 rpm (Sample 1). In the third sample, the solution was dropped without waiting for solvent evaporation. This means that the two samples with the same spin rotation speed (500 rpm) had almost the same characteristics.

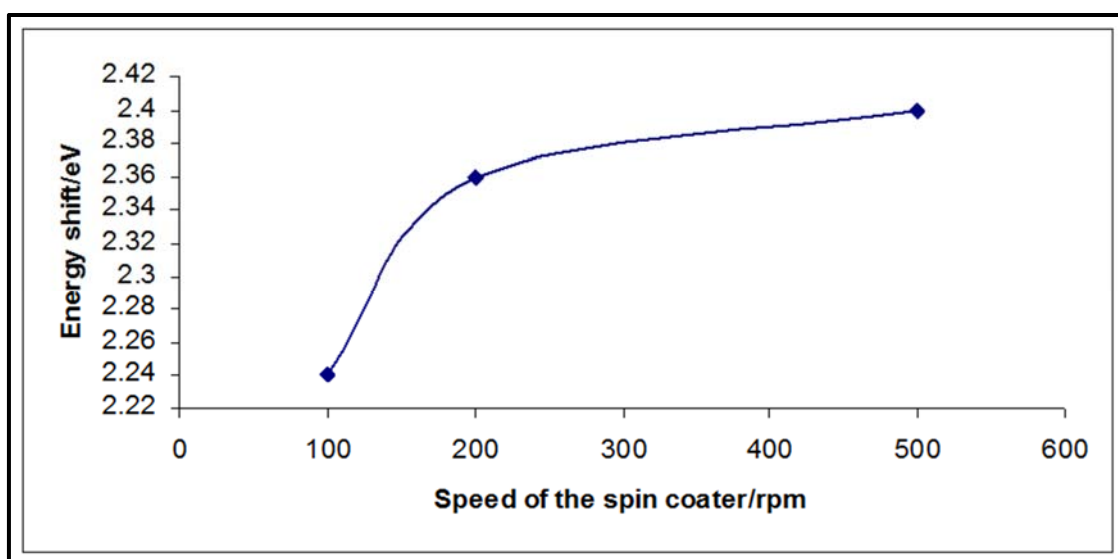


Figure 4.4. The change in energy shift and with respect to speed of the spin coater

#### 4.1.3. Optical Measurement Results

Table 4.1. Measurement result analysis of the various CdSe/ZnS nanoparticles

Sample	Certificate Emission Peak (nm)	Peak Position Before Heat Treatment (nm)	Peak Position After Heat Treatment (nm)	Radius distribution FWHM (before heat treatment) (nm)	Radius distribution FWHM (after heat treatment) (nm)	Radius size before heat treatment (nm)	Radius size after heat treatment (nm)	Speed of the spin coater (rpm)
1	589.00	569.37	516.75	39.16	28.44	2.58	2.14	500 rpm no wait
2	589.00	569.33	540.97	28.05	16.58	2.58	2.31	500 rpm
3	589.00	571.41	516.91	17.1	16.65	2.59	2.14	100 rpm
4	589.00	569.16	540.46	17.05	8.78	2.58	2.32	200 rpm

Table 4.1 represents the summary of the measurements for 4 samples. These information cover certificate absorption peak points, the absorption peak positions before and after heat treatment, size distribution before and after heat treatment.



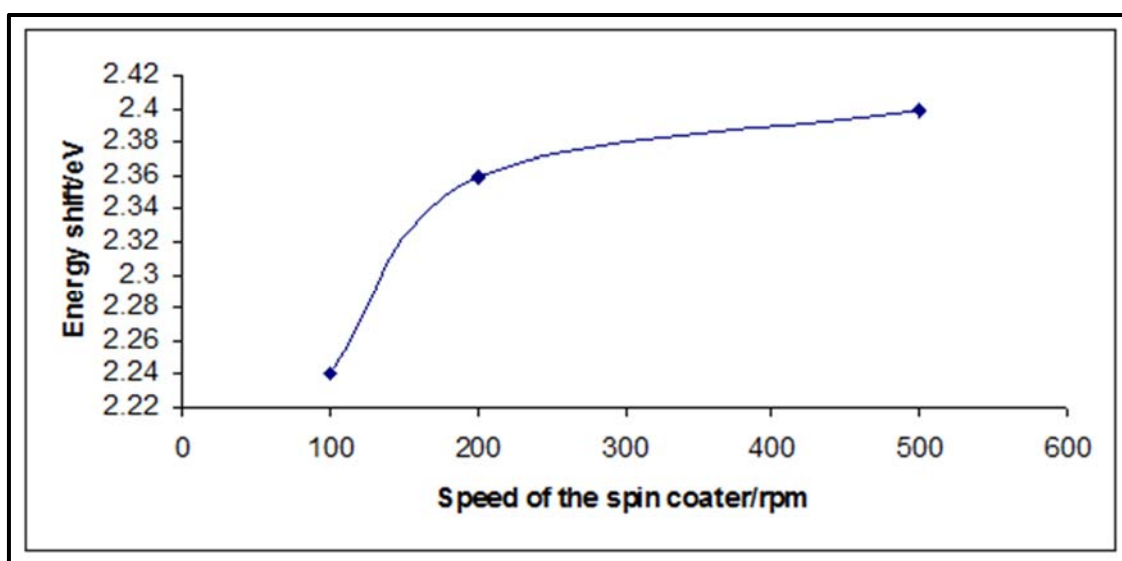


Figure 4.5. Optical absorption spectra for thin film CdSe/ZnS quantum dots after heat treatment.

Changing the spin coater speed affects the dispersion of quantum dots on the substrate leading to changes in its optical properties. This means that the cluster of quantum dots appears as larger particles in UV spectra, giving rise to shifts in the exciton spectra. No shift occurs in the exciton peak spectrum when the quantum dots are spun from a liquid to a solid thin film.

Annealing the quantum dots causes a blue shift in the exciton spectrum, due to migration of QD away from the clusters formed during spinning; this reduces the QD cluster sizes.

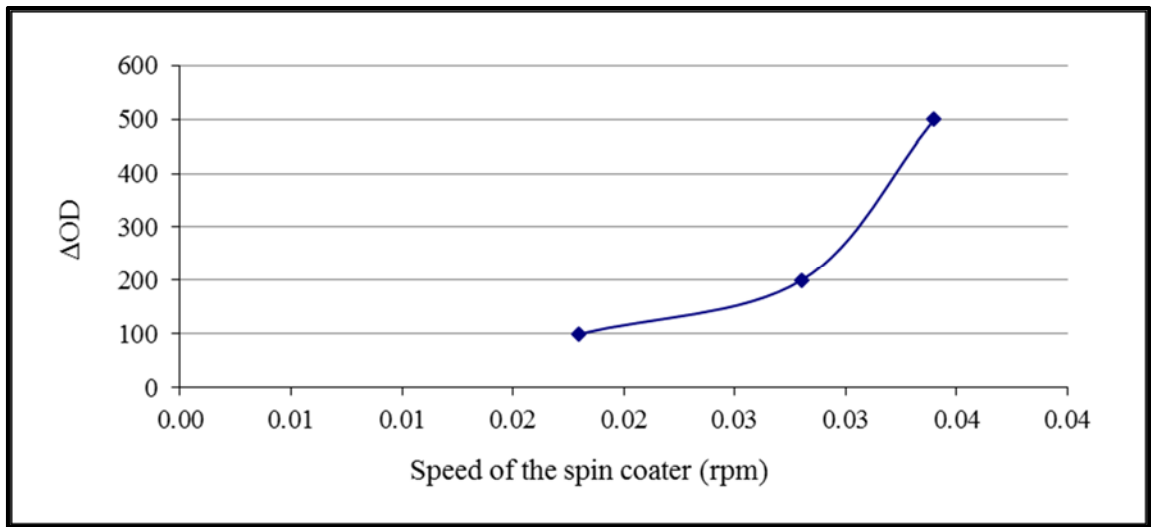
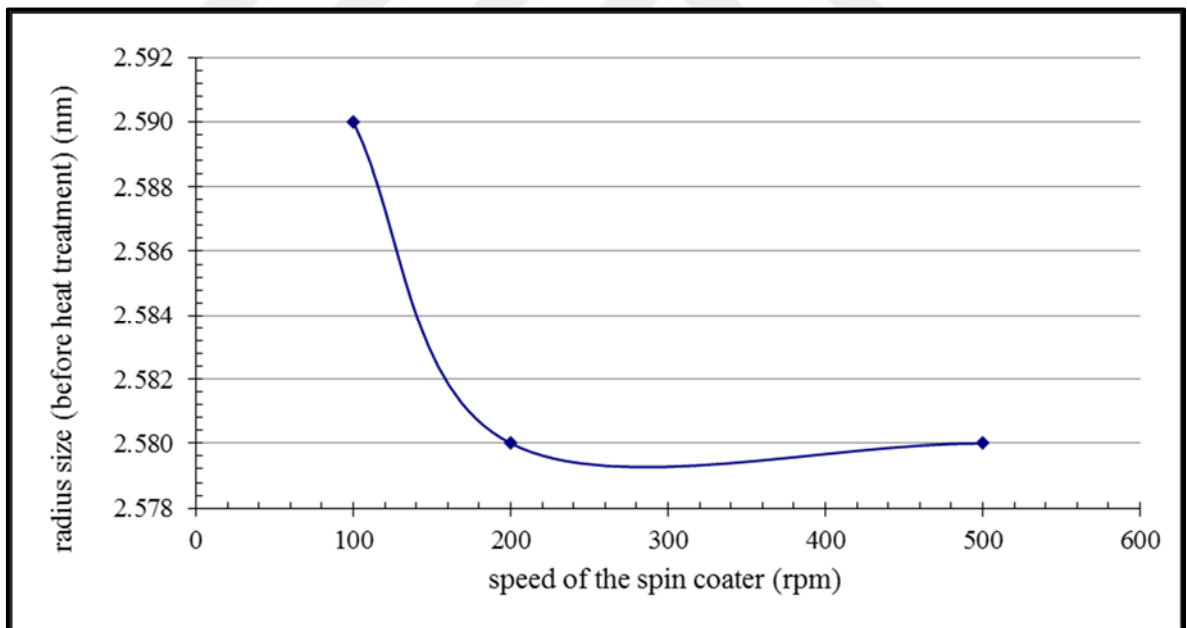


Figure 4.6. The optical density difference before annealing versus speed of the spin coater

(a)



(b)

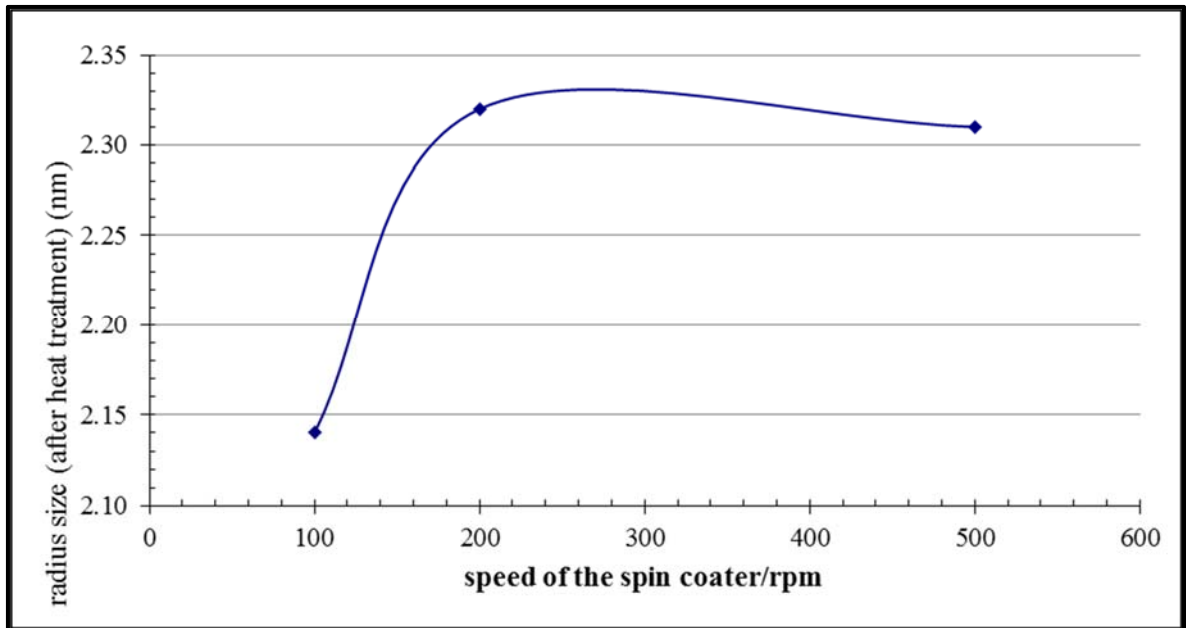


Figure 4.7. (a,b) Dependence of the deposited and annealed (onto glass samples) CdSe/ZnS quantum dots size with respect to speed of the spin coater

In Figure 4.8, no absorption between 650-700 nm. After 625 nm, absorption is beginning to take place approximately at 630 nm. Optical density decreases on annealing because the thickness of the thin films changes due to the migration.

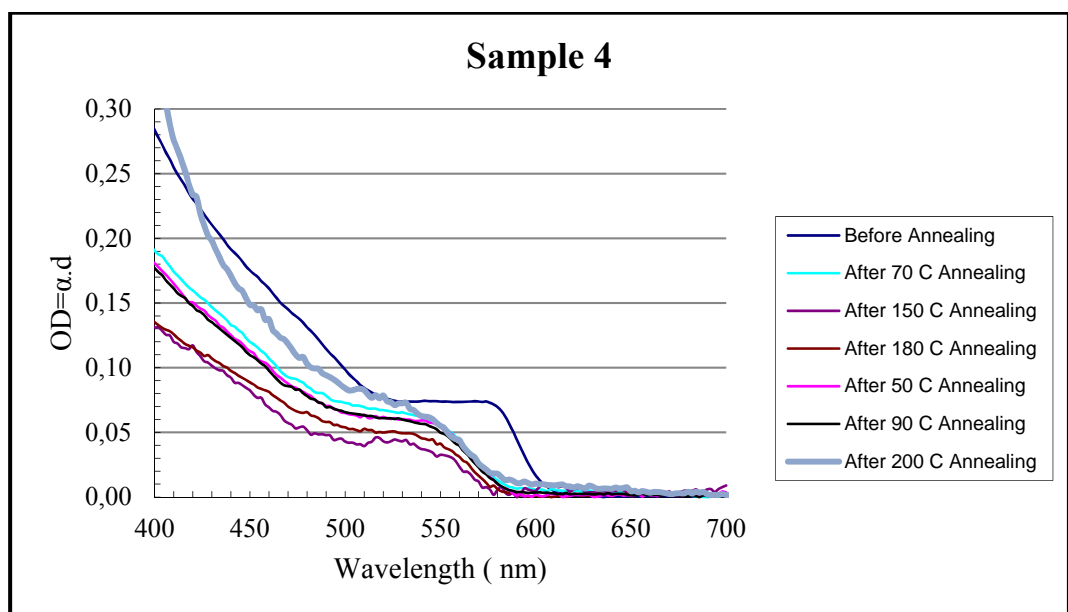


Figure 4.8. Optical absorption spectrum of Sample 4 at different temperatures

## 4.2. MAIN EXPERIMENTS

Main experiments cover both solid and the solution samples measurements. First experiments were started with the solid ones and continued with synthesis of the aqueous samples.

### 4.2.1. SOLID SAMPLE

#### 4.2.1.1. Preparation of the Solid Sample

For the solid samples, commercially available Schott colour glass filter RG830 doped with CdTe nanocrystals was used as starting material. This glass samples were manufactured by Schott AG in Germany. The Schott colour filter glass composition is 52% SiO<sub>2</sub>. 20% K<sub>2</sub>O. 20% ZnO and 5% B<sub>2</sub>O<sub>3</sub> [54].

In addition to that elementary analysis was done in ICP (Inductively coupled plasma mass spectrometry) Spectroscopy Measurement at TUBİTAK MAM. The results are shown below.

Table 4.2. Elementary analysis of RG830 glass sample

Elements	Results
Cd	0.20%
Te	0.16%
Zn	27.10%
Se	0.22%

Five different samples were prepared as-received, melted and heat treated (3 samples). Firstly, all five as-received colour filter glasses were sliced with a diamond saw, then they were melted at 1050 °C onto a platinum plate for 15 minutes to dissolve the particles and quench rapidly to room temperature. One of the samples was used directly as melted for optical and electro modulation measurements and the other one heat treated at a temperature below the glass transition temperature (RG850 glass transition temperature is at approximately 570 °C. At this temperature material goes from amorphous rigid state to a more flexible state) to initiate nucleation at 400 °C for 2 hours. Finally, three glass samples

were heat treated at a temperature higher than the glass transition temperature to grow the nanoparticles 660 °C for 3 hours, 8 hours and 12 hours, given in Table 4.3. After the heat treatment process, samples were polished with a special technique. Since the thickness and shape of the samples are important, shaping and sanding were done under water. Sandpaper and diamond paste were used to minimize the sample surface roughness.

Table 4.3. Heat Treatment Process of Solid Samples

Sample	Melting /RT quench stage		First Heat Treatment Process		Secondary Heat Treatment Process	
	Temperature (°C)	Time (min)	Temperature (°C)	Time (hours)	Temperature (°C)	Time (hours)
1	1050	15	400	2	660	3
2	1050	15	400	2	660	8
3	1050	15	400	2	660	12

The samples were annealed in a three zone horizontal furnace (Carbolite. GVA12/600) shown in Figure 4.8. For the control of the temperature distribution due to the large furnace dimensions, the furnace homogeneity study was carried out with two thermocouples. Homogeneity, stability and immersion depth analyses were carried out during the temperature fluctuation measurement in the furnace because it affects the uncertainty. To determine the temperature inside the furnace, S type reference temperature sensors (Hart Scientific. 5650) which were calibrated in TUBİTAK UME were used.



Figure 4.9. Picture of Carbolite 3 zone furnace for heat treatment process.

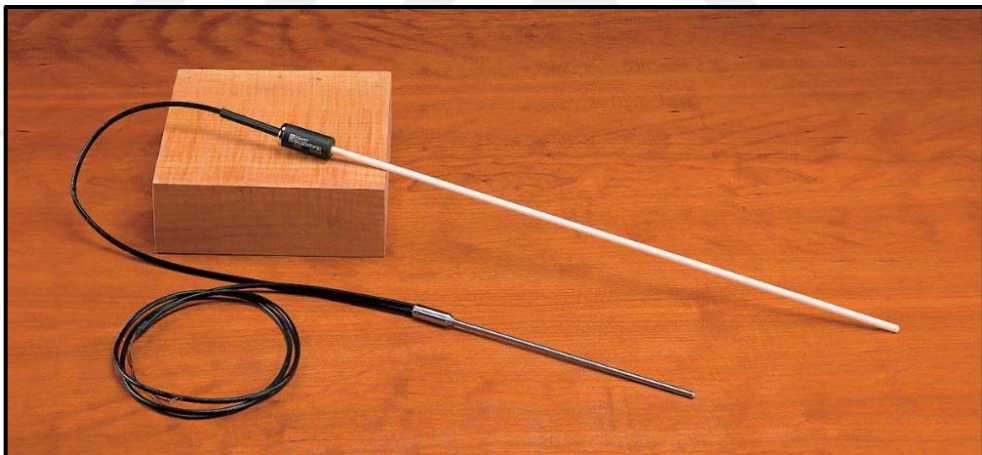


Figure 4.10. Picture of Hart Scientific S Type Thermocouple to Determine the Temperature of the Furnace.

#### **4.2.1.2. Sample Geometry**

Many methods have been tried to apply electric field to the sample, copper electrode coating, super glue ethyl cyenocylate but there was an electrical breakdown problem with these methods and the applications of the electric field could not be realized. One of the methods

to apply electric field to these samples was that ITO (indium-tin-oxide ) covered glass slides were used as a conductor. The sample was first sandwiched between two ITO covered glass slides. 64% nitric acid and 37% HCL solution was prepared for ITO patterning and slides were waited in it for 30 minutes for desolvation. The polished samples have a thickness of approximately 0.9 mm and were sandwiched between two ITO covered glass slides using transparent epoxy to prevent arching when an electric field is applied to the sample.

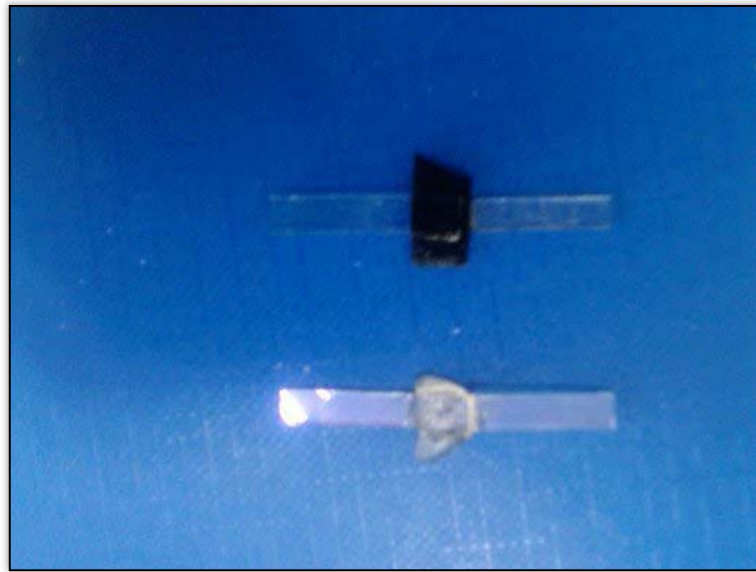


Figure 4.11. Picture of Solid Samples for high dc. voltage measurement.

Electrical connections to the DC power supply were made by two alligator clips which were clamped onto an exposed ITO portion of each slide. By applying d.c. voltages from 0 to 5.5 kV absorption spectra taken from the sample with the applied electric field either on or off, as shown in Figure 4.11.

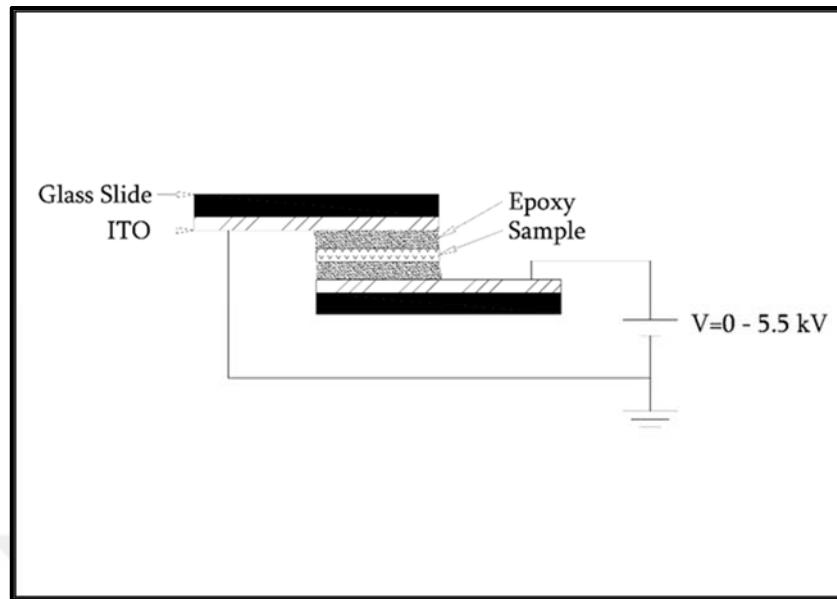


Figure 4.12. Sample preparations for Stark effect measurement.

#### 4.2.2. AQUEOUS SAMPLES

Production and testing of CdTe quantum dots require many resources. These were obtained from Physics, Genetics and Chemistry departments of the Yeditepe University and Yıldız Technical University Physics departments. There are two main chemical routes for the synthesis of high quality semiconductor colloids:

- Organometallic route
- Aqueous route

In this study, aqueous technique has been used for environmental and biological reasons. This method is more convenient because it is safe, easy and reproducible.

- Aqueous synthesis produces water soluble quantum dots
- Aqueous growth of quantum dots occurs at a lower temperature
- Aqueous methods are known to be cheap, easy and environmentally friendly



#### 4.2.2.1. Materials

Controlling the size of the QDs with a temperature controlled systems were imported and calibrated equipment were selected.

- Glass and plastic standard lab. Equipment (beaker, pipette, cuvettes, volumetric flask, tubes etc.)
- Platinum plate for annealing process
- Magnetic Stirrer and Condenser
- High temperature furnace (50, ..., 1200 °C)
- S type thermometer
- Centrifuge
- HPLC water machine



Figure 4.13. Preparative HPLC water analyzed in Sartorius Machine.

- PH meter
- Mass balance
- Absorption Spectrum System

- Uv-Vis Spectrum System
- High dc Voltage Source.



Figure 4.14. Picture of high dc voltage source.

#### 4.2.2.2. Chemicals and Reagents

To synthesize the QDs, the synthesis method was repeated many times in order to obtain high quality CdTe QDs. The chemicals utilised are given in the Table 4.4.

Table 4.4. Chemicals to synthesize water soluble CdTe QDs.

Chemical Symbol	Chemicals	Amount
Te	Tellurium powder	200 mg
NaBH <sub>4</sub>	Sodium Borohydride	200 mg
CdCl <sub>2</sub>	Cadmium Chloride	1 mmol
NaOH	Sodium Hydroxide	
-	Mercaptopropionic acid (or TGA or Cys)	0.2 ml
-	HPLC water	170 ml

### 4.2.3. Synthesis of Water Soluble CdTe Quantum Dots

In general, highly luminescent CdTe QDs were synthesized in an aqueous system by mixing tellurium and cadmium precursors in the presence of a thiolate capping agent.

Synthesis of CdTe quantum dots takes place in several steps over a two-day period [55-58]

- Synthesis of NaHTe
- Cadmium Ion Solution.

#### Synthesis of NaHTe (Precursor Solution)

- HPLC (Sartorius Water Purification Systems) water used to clean the glass vial (2-3 times cleaning process), glass vial dried at 60 °C in the furnace
- Te powder and NaBH<sub>4</sub> were combined in a dry glass vial with a 1:4 ratio (1.5312 g NaBH<sub>4</sub> and 0.3828 g Te)
- Te powder is metallic black and NaBH<sub>4</sub> is white
- This mixture dissolved in 5 ml HPLC water
- After 24 hours in the refrigerator, NaHTe solution was bright, clear and purple.



Figure 4.15. The NaHTe solution after a 24 hour waiting in refrigerator.

The steps utilised in this synthesis route follows:

Table 4.5. Preparation method of Cadmium Ion Solution

Step	Procedure
1	1 mmol cadmium chloride is dissolved in 150 ml HPLC water in a 250 ml three neck flask. The pH of this mixture should be adjusted to 7 or 8 by adding sodium hydroxide.
2	0.2 ml of mercaptopropionic acid (or TGA or cysteine) is added into the above mixture.
3	3 ml of the Te precursor solution (0.3 mmol) is swiftly injected into the reaction mixture
4	The reaction mixture will become reddish brown in colour indicating the formation of CdTe nuclei in the solution.
5	The mixture should then be aged (reflux) at 98°C until the desired CdTe QD size (emission colour) is achieved
6	The CdTe QDs can be purified using centrifugation to remove excess surfactants and unreactes precursors in 6000 rpm

The solution generally lightened to a golden-orange within the first 10 or 15 minutes of growth. The dots take time to grow. With the various buffer combinations, complete growth occurred between 2 and 12 hours. Seven samples were taken every hour and solutions in the vials contain various colour samples because each sample has different sized CdTe nanoparticles shown in Figure 4.18.

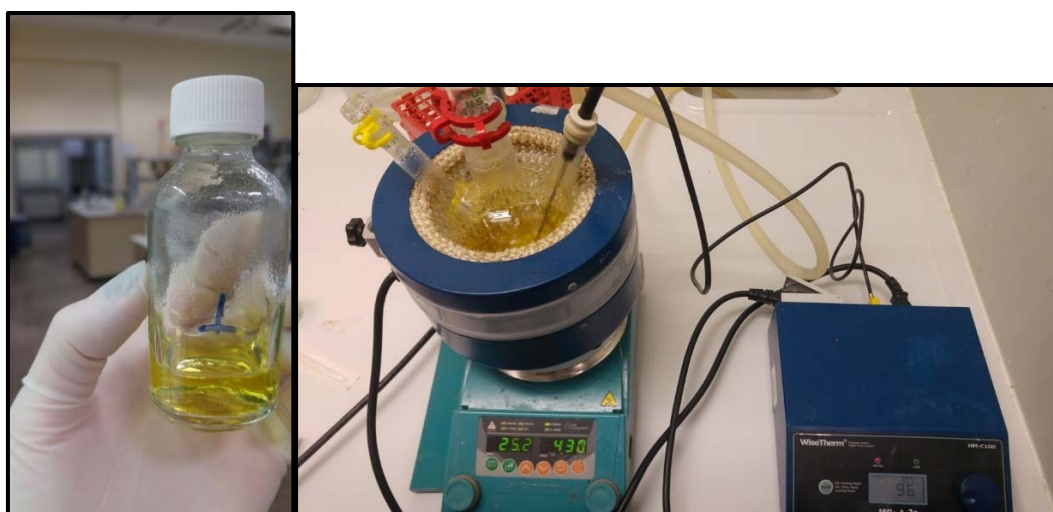


Figure 4.16. Yellow solution: After 15 minutes NaHTe has been added to Cd ion solution

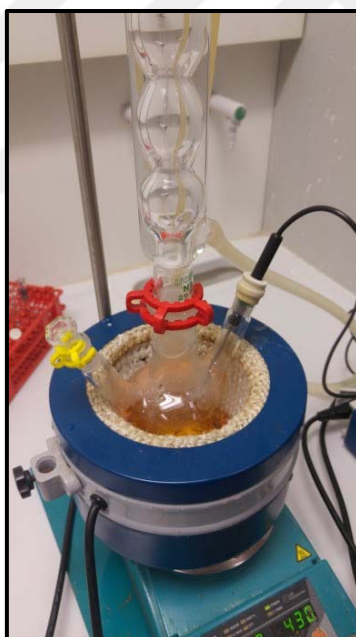


Figure 4.17. Orange solution: After 3 hours NaHTe has been added to Cd ion solution.

In the first minute of the synthesizing process, the sample is yellow as shown in Figure 4.16, and as time progresses, the colour turns red shown in Figure 4.17.

Table 4.6. Reaction Time of Samples

Sample No	Reaction Time
1	15 minutes
2	1 hour
3	2 hours
4	3 hours
5	4 hours
6	5 hours
7	5 hours 15 min.

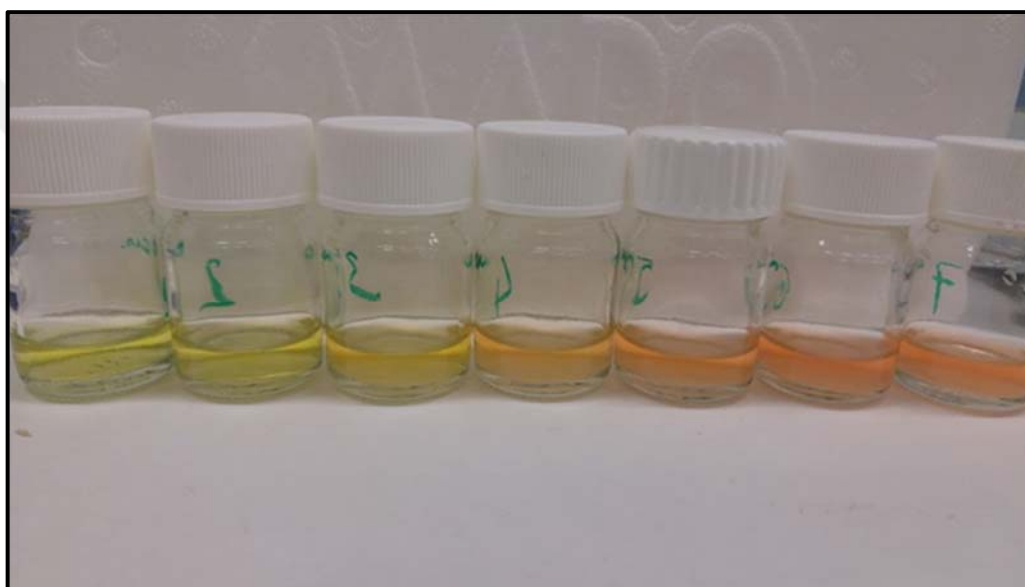


Figure 4.18. CdTe QDs in aqueous solution with different sizes.

## 5. METHOD

### 5.1. ABSORPTION SPECTRUM MEASUREMENT

All of the samples were characterized using UV-Vis absorption and linear optical absorption spectroscopy in order to determine the optical properties of the CdTe QDs. First measurements were recorded on Perkin Elmer Lambda 25 UV/Visible absorption spectrophotometer (closed system) at Yeditepe University (Genetics Department). The second set up (home made system) was performed at Yıldız Technical University (Physics Department Photonics Laboratory). The tungsten light source (50W power and constant current) was focused onto a 2 mm diameter spot of the sample. The transmitted light was collected and focused at the entrance slit of a 1/8-m Oriel Cornerstone 130 motorized monochromator having 1200 lines/mm grating shown in figure below. The optical measurements were performed with and without sample (as a reference) between 100-1050 nm. The results were used to determine the Lambert-Beer absorption coefficient ( $\alpha$ ).

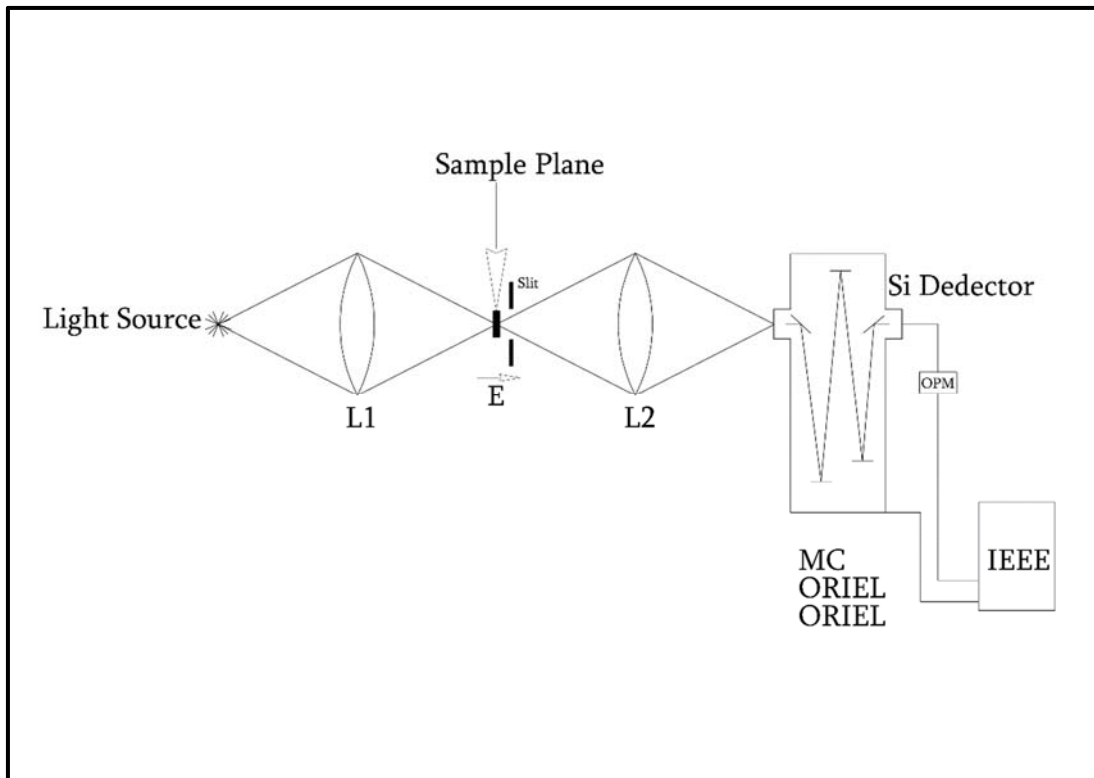


Figure 5.1. Optical spectrometer set-up for spectral measurements.

The Lambert Beer law is defined as;

$$A = \ln\left(\frac{I_0}{I}\right) = \alpha d \quad (5.1)$$

where  $A$  is the absorbance,  $\alpha$  the absorption coefficient and  $d$  is the thickness of the sample [59]

The absorption spectrum of each sample [Oriel 74000. Cornerstone 130 motorized monochromator 1/8 m. 1200 lines/mm grating] was characterized using linear optical absorption spectroscopy. The 50 W tungsten lamp powered by a constant current focused on the 2 mm diameter spot of the sample. The transmitted light was collected and focused at the entrance slit of the monochromator. As the source wavelength was scanned from 450 nm to 900 nm output signal was transferred to a computer through an optical power meter. First measurement taken as a reference ( $I_0$ ) without sample. The data had its light transmittance ( $I / I_0$ ) extracted and the absorption coefficient  $\alpha$  of each sample was determined from Lambert Beer Law where  $I$  is the light intensity after it passes through the sample,  $I_0$  is initial light intensity and  $d$  is the thickness of the sample.

The value of the direct band gap was evaluated from a Tauc plot which is a method for determination of the optical band gap in semiconductors from absorption spectra measurements [60-62]

$$\alpha(h\nu) = A(h\nu - E_g)^n \quad (5.2)$$

where  $\alpha$  is the extinction coefficient,  $h\nu$  photon energy and  $E_g$  optical band gap,  $n$  is the power factor of the transition mode and  $A$  is the absorption constant.

$n=1/2$  for allowed direct transition band gap semiconductor as CdTe

$$\alpha(h\nu) = A(h\nu - E_g)^{1/2} \quad (5.3)$$

The curve  $(\alpha h\nu)^2$  should have a section of a linear portion ( $y=mx+b$ ), the band gaps were determined by extrapolating this linear portion ( $\alpha=0$ ) of the plot of  $(\alpha h\nu)^2$  versus  $(h\nu)$ . The x-intercept of this line gives the optical band gap [63].



To determine the size of the particle the Brus equation (effective mass approximation) was used [64-66]. According to the effective mass model, first term is band gap energy of QD, second term is the band gap energy of bulk semiconductor, third term is equal to energy due to quantum confinement and last term is Coulombic interaction energy of exciton.  $E$  (eV) is approximated by:

$$E = \frac{c^*h}{\lambda_{onset}} = E_g^{bulk} + \frac{h^2}{8r^2} \left( \frac{1}{m_e^*} + \frac{1}{m_h^*} \right) - \frac{1.786e^2}{4\pi\epsilon\epsilon_0r} + polar.term \quad (5.4)$$

where  $r$  is the particle radius,  $m_0$  is the free electron mass,  $\epsilon$  is the relative permittivity,  $\epsilon_0$  is the permittivity of free space, and  $e$  is the charge of the electron. The polarization term is not included in this model, this small term is negligible in practice for spherical quantum dots.

In order to determine quantum dot radii from Equation 5.5 an experimental value for relative electrical permittivity,  $\epsilon$ , was calculated using a Hilbert transformation of the absorption spectrum. The Hilbert transform of a real valued function  $\omega$  is defined as;

$$\hat{H}(\omega) = \frac{1}{\pi} \int_{-\infty}^{\infty} \frac{\hat{H}(\omega')}{\omega - \omega'} d\omega' \quad (5.5)$$

Theoretically, the integral is evaluated as a Cauchy principal value.

Some physical parameters frequency has real and imaginary components cannot be specified independently from each other like complex dielectric permittivity [67]

$$\epsilon(\omega) = \epsilon_1(\omega) + i\epsilon_2(\omega) \quad (5.6)$$

$\epsilon$  is the electric permittivity of the glass matrix,  $\epsilon_1$  is the real part of electric permittivity which is related with energy stored and  $\epsilon_2$  is the imaginary part related with energy dissipation within the medium.  $\epsilon_1$  and  $\epsilon_2$  are provided to Hilbert Transformation relations

All Hilbert transformations were performed using the Matlab Programming environment, allowing the real values to be extracted for use.

By determining the bandgap  $E_g$  of the confined semiconductor nanoparticles from their absorption spectra their particle radii  $r$  can be estimated using this model.

The absorption edge is broader than bulk crystals due to variation in particle size (size distribution)  $n(r)$ . In the dilute concentration limit,  $n(r)$  can be obtained by assuming that the absorbance  $A$  at any wavelength is related to the total volume,  $V$ , of spherical particles  $V = \frac{4}{3}\pi r^3$  (with radius greater than or equal to the size corresponding to the absorption onset [68]).

$$A(r) \propto \int_r^{\infty} \frac{4}{3}\pi r^3 n(r) dr \quad (5.7)$$

Since  $n(r) = 0$  when  $r \rightarrow \infty$

$$n(r) \propto -\frac{dA/dr}{\frac{4}{3}\pi r^3} \quad (5.8)$$

Particle size distribution may be obtained from the absorption spectrum using Brus Equation. The derivative of the absorption curve can be obtained by converting the wavelength axis to energy and thus to radius via Equation 5.5. The gradients at each value of  $r$  can then be placed into Equation 5.9 and plotted. To determine the particle size distribution from this relation, absorption peak shapes closely follow Gaussian distributions, so full width half maximum (FWHM) of the were taken. This value was calculated from the Equation 5.10 given below in MATLAB curve fitting programme. In the Equation 5.11;  $a$  is the amplitude,  $b$  is the mean value (peak) and  $c$  is the FWHM.

$$f(x) = \frac{1}{\sqrt{2\pi}\sigma} \exp\left[-\frac{(x-\mu)^2}{2\sigma^2}\right] \quad (5.9)$$

$$f(x) = a \exp\left[-\frac{(x-b)^2}{c^2}\right] \quad (5.10)$$

$$FWHM = 2\sqrt{2\ln 2} \quad (5.11)$$

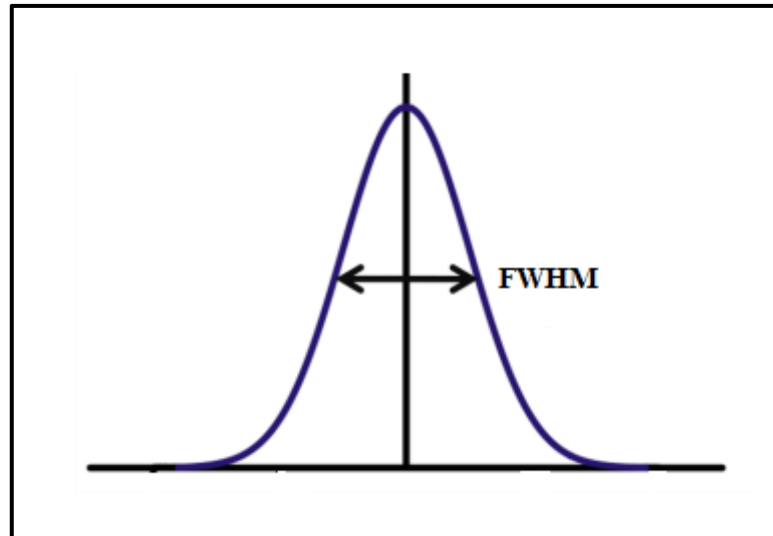


Figure 5.2. FWHM of a Gaussian Distribution.

## 5.2. RAMAN SPECTROSCOPY MEASUREMENT

Raman measurements were performed at room temperature using the 30 mW, 532 nm emission line of a Helium-Neon laser to excite the sample. Figure 5.3 represents the Raman peaks for three samples. Raman peaks were obtained by software from the “peak fit” programme analysis using a Lorentzian curve fitting, shown in Table 5.1

The comparison of the Raman spectra of the quantum dots which were prepared by different method shows that it has the same peak at around  $108 \text{ cm}^{-1}$ . This Raman peak is related disorder via activated acoustical phonons [69]. The second and third peaks at around  $138$  and  $168 \text{ cm}^{-1}$  in the spectrum are close to the CdTe TO and LO mode [70-72]. It is well known that strain produces a Raman shift of approximately  $\pm 3 \text{ cm}^{-1}$  [73] and that phonon confinement causes a red shift. The latter cannot explain the blue shift in the Raman frequency observed here [74].

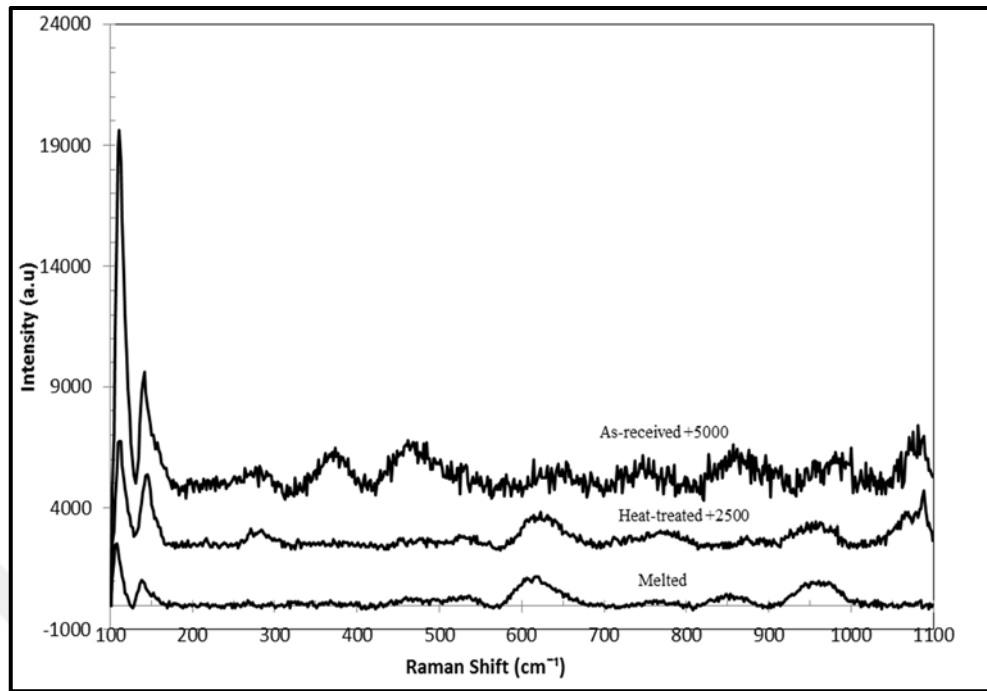


Figure 5.3. Raman spectra of RG 830 samples: as-received sample, melted sample, heat treated sample.

The Lyndanne-Sachs-Teller equation [75] gives the relationship between the frequencies of the TO and LO modes:

$$\omega_{TO} = \sqrt{\frac{\left(\frac{\epsilon_{\infty}}{\epsilon_0}\right)}{\omega_{LO}}} \quad (5.12)$$

Theoretically the ratio must be 1.48 for CdTe. For melted sample Raman spectroscopic data show that the LO mode at  $168 \text{ cm}^{-1}$  and the TO mode at around  $138 \text{ cm}^{-1}$ .

Table 5.1. Raman peak values of the samples.

Heat Treatment	Active Raman Lines ( $\text{cm}^{-1}$ )			
	Peak 1	Peak 2	Peak 3	Peak 4
As received	108	138	151	197
Heat Treated	108	141	-	-
Melted (RT)	108	138	168	216

The relative strain ( $\frac{\Delta a}{a}$ ) from Raman measurements was determined by Eq. 5.14

$$\Delta\omega_c(R) = \omega_L \left[ \left( 1 + 3 \frac{\Delta a}{a} (R) \right)^{-\gamma} - 1 \right] \approx -3\gamma\omega_L \frac{\Delta a}{a} \quad (5.13)$$

$\omega_L$  is LO phonon frequency of bulk specimen, and  $\gamma$  is the Grüneisen parameter of CdTe [76]. The experimental TO mode of the as received sample  $138 \text{ cm}^{-1}$  and the CdTe TO mode from the literature  $140 \text{ cm}^{-1}$ . The relative strain was determined to be  $-2.95 \times 10^{-3}$  for the as received sample. The other two samples (melted and heat treated) had strain values of  $-2.95 \times 10^{-3}$  and  $-1.47 \times 10^{-3}$ .

From the LO mode for the melted sample, the strain value was determined to be  $-3.88 \times 10^{-3}$

Table 5.2. Strain values from Raman Spectroscopy Measurement

<b>Raman</b>	<b>As received</b>	<b>Heat Treated</b>	<b>Melted</b>
Strain (TO)	-2.95E-03	-1.468E-03	-2.95E-03
Strain (LO)	-	-	-3.88E-03
Composition	%56 Zn		

The LO peak position at  $197 \text{ cm}^{-1}$  in Raman spectroscopy is related to the zinc corporation equation

$$\omega_{LO}(x) = -21.755x^2 + 57.706x + 170.05 \quad (5.14)$$

where  $\omega_{LO}$  is the LO phonon frequency of the bulk crystal.

Eq. 5.14 was obtained by digitizing the empirical phonon frequency against zinc content curves given in Reference. [24]

The peak position of LO vibrational mode indicates that the zinc content in ternary  $\text{Zn}_x\text{Cd}_{1-x}\text{Te}$  is 56%.

Raman spectra of aqueous CdTe QDs from 100 to 1000  $\text{cm}^{-1}$  are found under the same measurement conditions with solid samples. In the low Raman shift regime it was investigated and the peaks are 110, 140 and 160  $\text{cm}^{-1}$ . Raman peak is related to disorder via activated acoustical phonons, second peak 140  $\text{cm}^{-1}$  and 160  $\text{cm}^{-1}$  represent the TO and LO CdTe phonon modes respectively. The spectrum from the solid quantum dots differs from the solution quantum dots spectrum. In solution samples, acoustic and LO modes are shifted to the upper wavenumber by approximately 10  $\text{cm}^{-1}$ , this extra signal may come from the capping ligand molecule on the CdTe quantum dot.

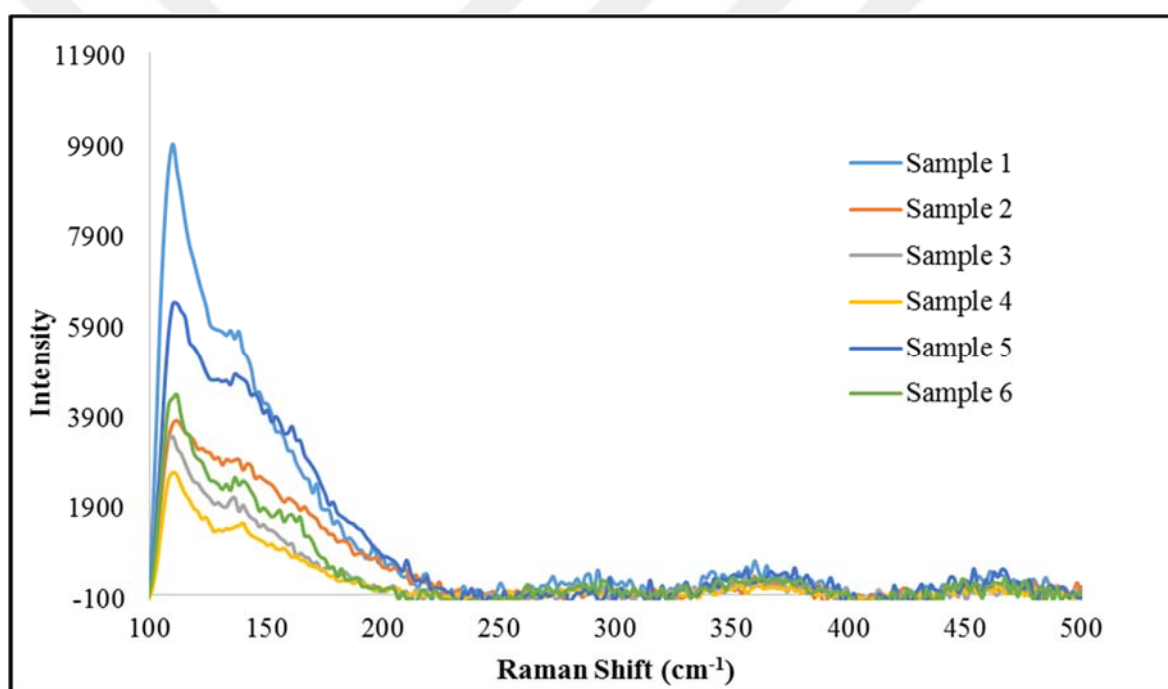


Figure 5.4. Raman spectra of CdTe QDs in aqueous solution

### 5.3. ELECTRO-ABSORPTION SPECTRUM MEASUREMENT

For the electroabsorption measurements systems several measurement setup were prepared and tested. Problems due to high voltage electrical breakdown, aggregation of the solution and fracture breaks due to very thin specimens were overcome. Suitable systems chosen to be performed at high dc. voltage measurements for solid and the aqueous sample are shown

below in Figure 5.4. and Figure 5.5. The process of preparing these systems is described in Sections 2.3 and 2.4. The absorption spectra of CdTe quantum dots under the influence of different electrical field strength measurements initiated from zero volt and gradually increased up to 5.5 kV. After the electric field measurements are completed the high dc. supply was adjusted to zero volt again to perform the repeatability and reproducibility of the measurements for both solid and aqueous samples.

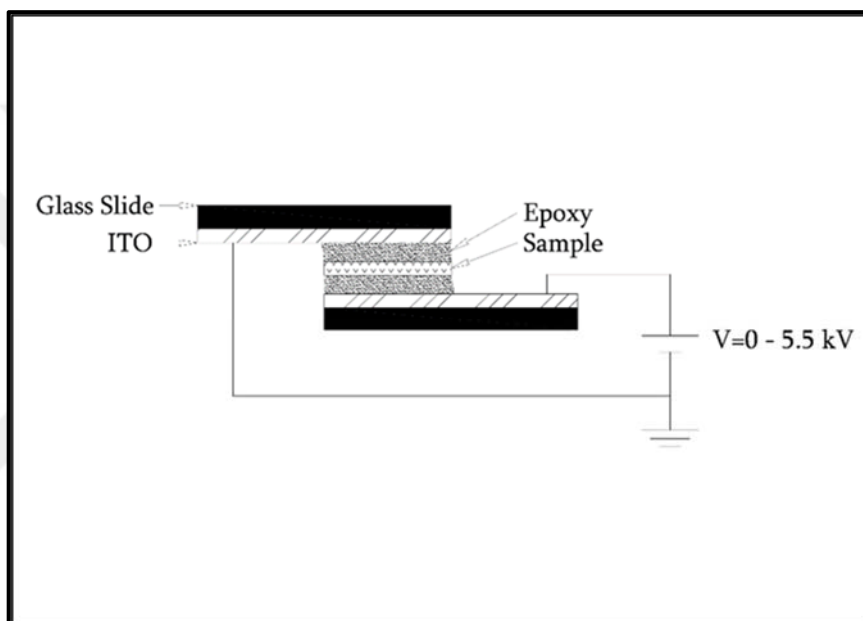


Figure 5.5. Diagram of Electro-Absorption Experimental Setup for Solid Samples.

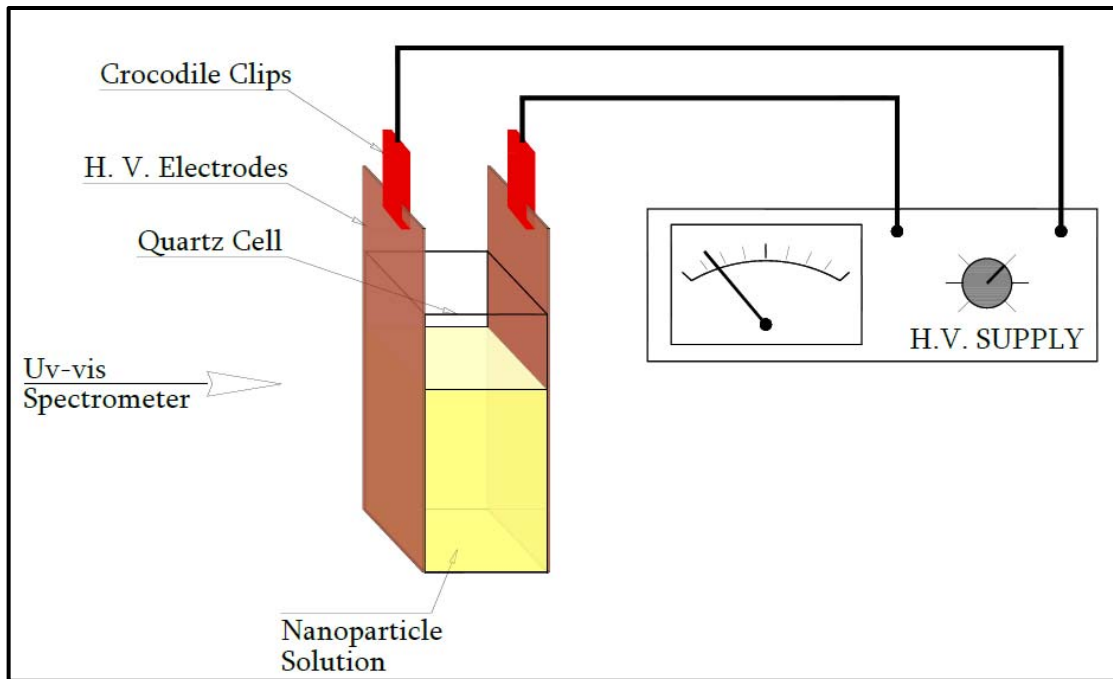


Figure 5.6. Diagram of Electro-Absorption Experimental Setup for Aqueous Solution

In this study, the shift in the energy level caused by the electric field was found using the perturbation theory and these results were compared with the experimental results. The problem is that, if the applied electric field reduces inside the nanostructure, theoretical calculations do not give us the exact solution. The field inside the cavity  $E_{in}$  is uniform and parallel to the initially applied field  $E_0$ ,  $\epsilon$  is the dielectric constant of the particle,  $\epsilon_0$  is the dielectric constant of the glass matrix where the QDs are embedded in and the magnitude of the inside electric field is [77]:

$$E_{in} = \frac{3\epsilon_0}{\epsilon + 2\epsilon_0} E_0 < E_0 \quad (5.15)$$

#### 5.4. REPEATABILITY OF THE MEASUREMENT (HYSTERESIS)

The absorption spectra measurements were repeated, considering the probability of the samples losing their properties with time and measurement system after the samples were synthesized. The repeatability measurement is important for the precision of the measurement, so the measurement was performed with same measurement procedure,



system, operator, environmental conditions on the same sample with the sequential measurement.

- Absorption measurement was carried out without field (0 V)
- High-voltage applications started at low voltage, field was applied to the sample up to the highest voltage that can be applied gradually (250 V, 500 V, 750 V etc.)
- DC. voltage source closed and at zero volt the measurement was repeated
- Then measurements were repeated from high to low voltage at the same measuring points (750 V, 500 V, 250 V) with the same process

Repeatability measurements were obtained with measurements taken first by increasing and then by decreasing the voltage.

## **5.5. CALCULATION OF THE MEASUREMENT UNCERTAINTY**

Uncertainty of the measurements depends on some components. So the measurement uncertainties need be well defined for reliable and realistic results. The calibrations of the measuring instruments used and the correct determination of the other uncertainty parameters will directly affect the quality of the measurements. For this reason, measuring instruments with high accuracy (calibrated) have been preferred throughout the thesis and efforts have been made to define measurement uncertainties.

Estimated measurement uncertainty was calculated for the absorption spectra measurement result evaluation. The optical band gaps were calculated via the absorption spectroscopy using Tauc Plot. Linear portion of the graph was extrapolated and intersected on x axis where the x intercept is zero was taken as band gap. The selected linear portion affects the results so this process was repeated 3 times by selecting different portions. There is an example for this calculation in Figure 5.6. Blue arrow represents the portion one which has 31 data points changing from 2.672 eV to 2.366 eV, and from these data points the band gap was calculated as 2.237 eV. From portion 2 (purple arrow), 24 data were selected from 2.616 eV to 2.385 eV, the band gap is 2.237 eV. The last portion (yellow arrow) includes 31 data between 2.661 eV and 2.357 eV, and the result was 2.234 eV. The difference between maximum and minimum band gap and taking the average provides the standard uncertainty. For each measurement (from 0V to maximum voltage), this calculation method was repeated and a

separate uncertainty value was found. The total uncertainty is the sum of each uncertainty value. This was calculated and divided by the square root of the number of measurements shown in Table 6.7.

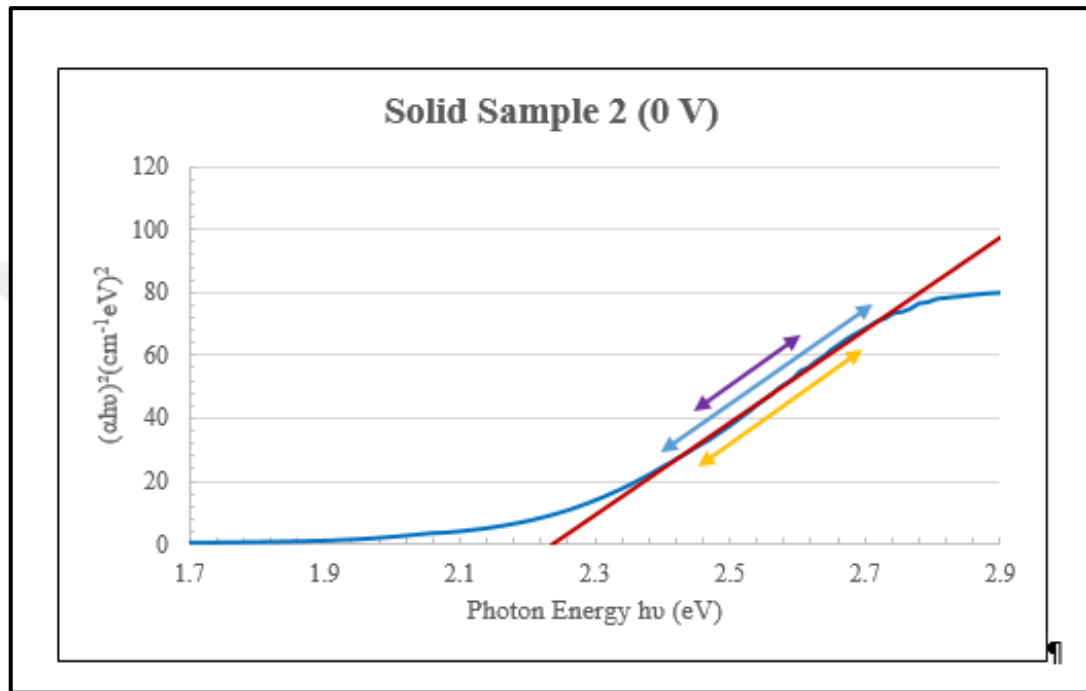


Figure 5.7. Optical spectrometer set-up for spectral measurements.

## 6. RESULTS

### 6.1. UV-VIS RESULTS FOR BOTH SOLID AND AQUEOUS SAMPLES

In this section, work was carried out to compare optical and electro-optical properties of the solid and aqueous solution semiconductor nanoparticles.

For both solid and the aqueous CdTe nanoparticles, suitable production methods for electric field measurements were sought and developed. Arrangement of the nanoparticles samples as synthesized in aqueous solutions many times to fabricate stable, repeatable and reproducible samples in terms of size and growth of the nanoparticle. The focus of this thesis was the fabrication of CdTe semiconductor nanocrystal, the application of high dc voltage measurements on these nanoparticles and to observe the behaviour they exhibit. During this investigation the process followed is shown in the following Table 6.1.

Table 6.1. Experimental Flow Table

<b>Process</b>	<b>Solid Sample</b>	<b>Solution Sample</b>
Absorption Spectra Measurement	✓	✓
UV-Vis Spectra Measurement	☒	✓
Raman Spectra Measurement	✓	✓
Band Gap Calculation From Tauc Plot	✓	✓
Dielectric Constant Calculation From Hilbert Transformation	✓	✓
Size Distribution Determination From Brus Equation	✓	✓
Size Distribution Calculation	✓	✓
Absorption Spectra Measurement Under High DC Voltage	✓	✓
Measurement Uncertainty Calculation	✓	✓

Initial experimental studies were started with commercially available RG830 Schott filter glass doped with CdTe semiconductor nanoparticles. Five samples were prepared under different conditions and they were characterized using linear optical absorption spectroscopy. In Figures 6.1, 6.2, 6.3 the absorption characteristic graphs indicate that first exciton peak moves to lower energies, cause red shift with the heat treatment time due to the quantum size effect. The band gap of these samples as determined by Tauc's plot which was explained in Section 5.1. Especially, the band gap results show that, when we increase the heat treatment time, the absorption wavelength increases but band gap energies are slightly red shifted.

Table 6.2. Band gaps of  $Zn_xCd_{1-x}Te$  semiconductor nanocrystals embedded in glass matrices.

<b>Sample</b>	<b>Band Gap (eV)</b>
As received	1.82
Melted	2.79
Solid Sample 1: Heat-treated 3 hours	2.56
Solid Sample 2: Heat-treated 8 hours	2.24
Solid Sample 3: Heat-treated 12 hours	2.11

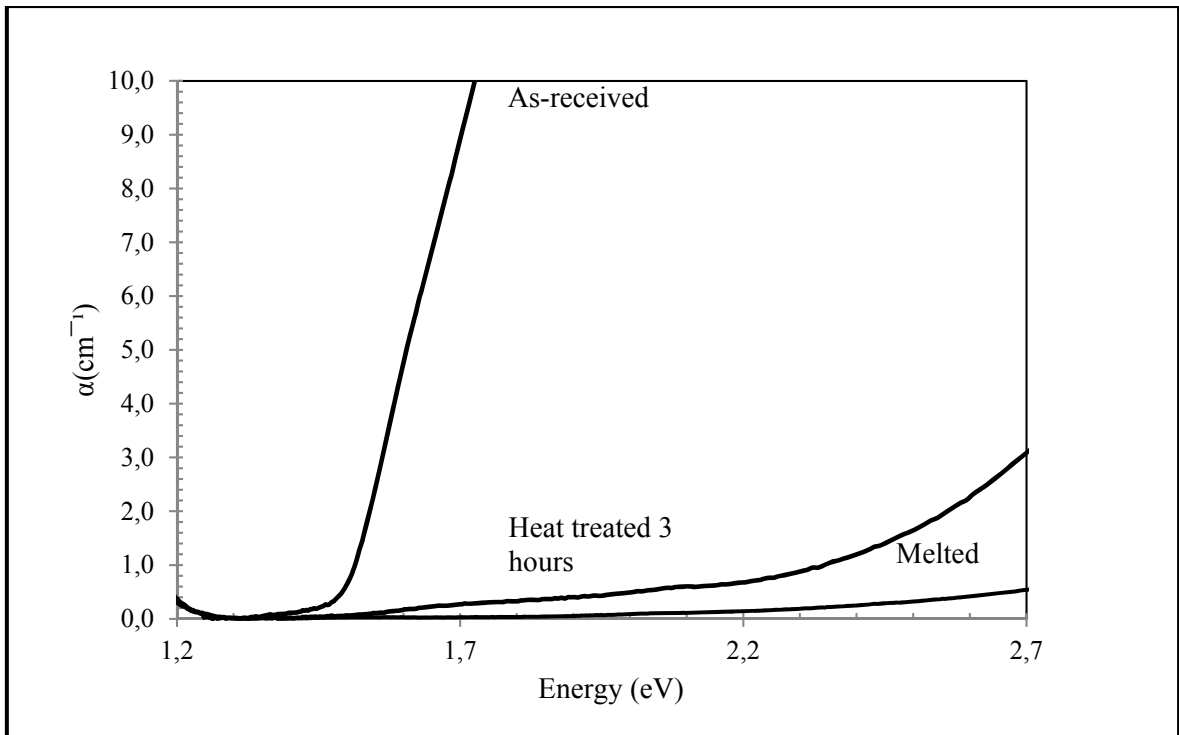


Figure 6.1. The absorption spectra of  $\text{Zn}_x\text{Cd}_{1-x}\text{Te}$  semiconductor nanocrystals embedded in glass matrices.

The three solid samples were characterized by the absorption spectra to find the optical properties in Figure 6.1. The other two solid samples which have different annealing process also analysed in the absorption spectroscopy shown below in Figure 6.2 and Figure 6.3. These graphs show that when we increase the heat treatment time, the band gap energies decrease.

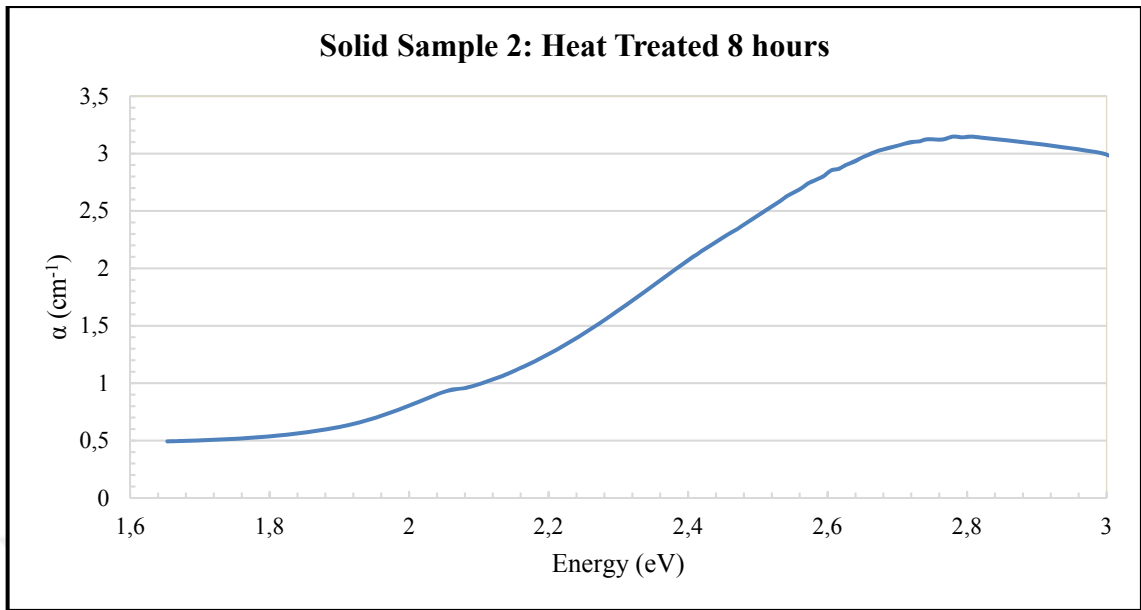


Figure 6.2. Graph of optical absorption spectra for the sample heat treated at 600 °C for 8 hours without field.

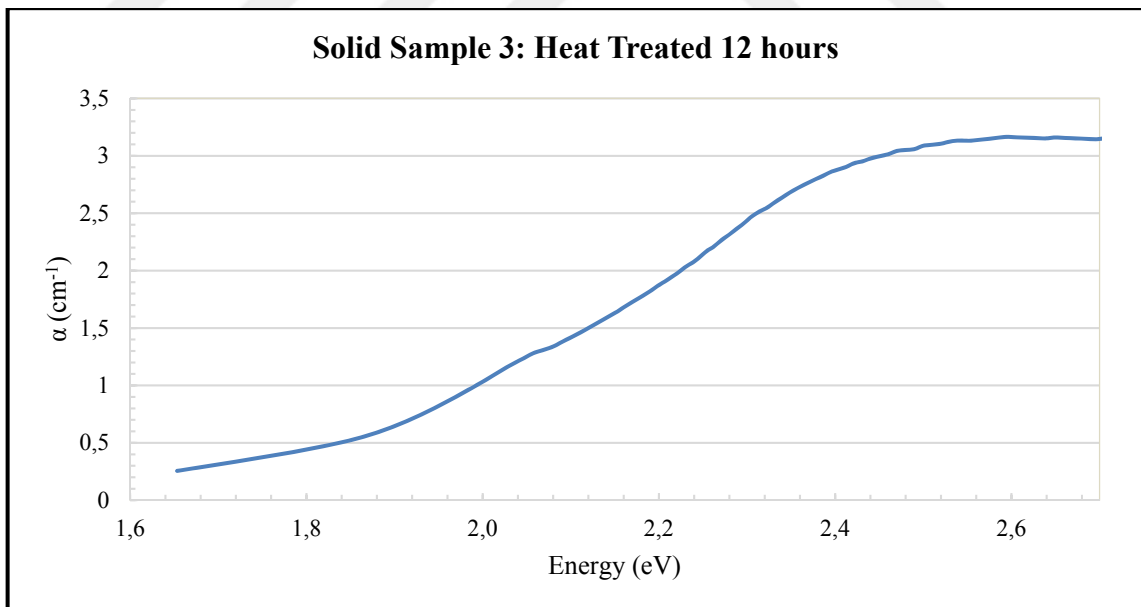


Figure 6.3. Graph of optical absorption spectra for the sample heat treated at 600 °C for 12 hours without field.

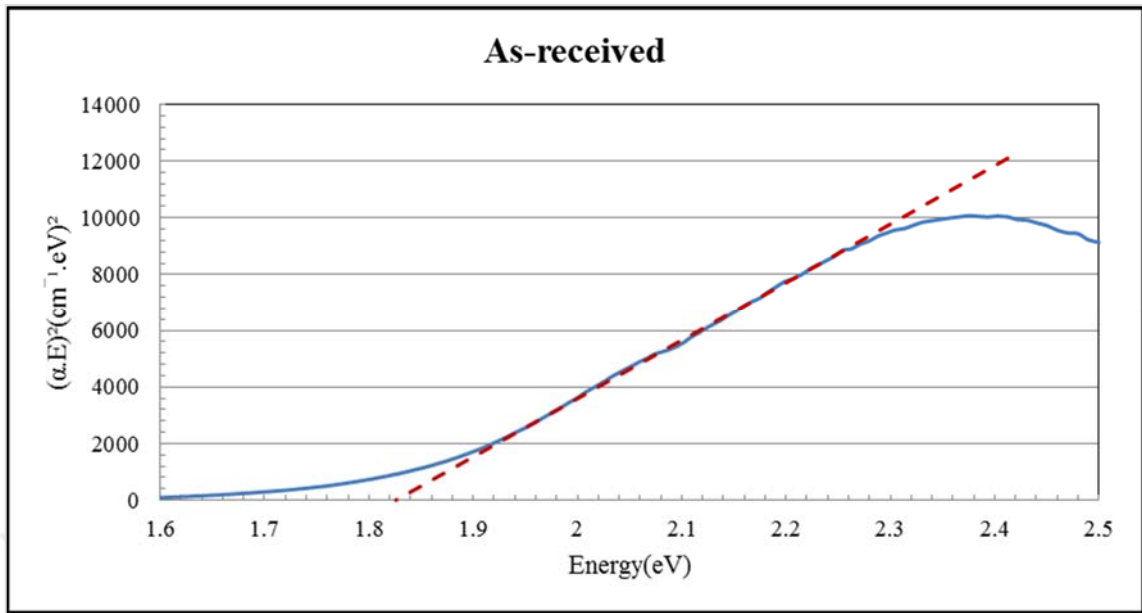


Figure 6.4. Tauc plot obtained from the optical absorption spectra of as-received sample without field.

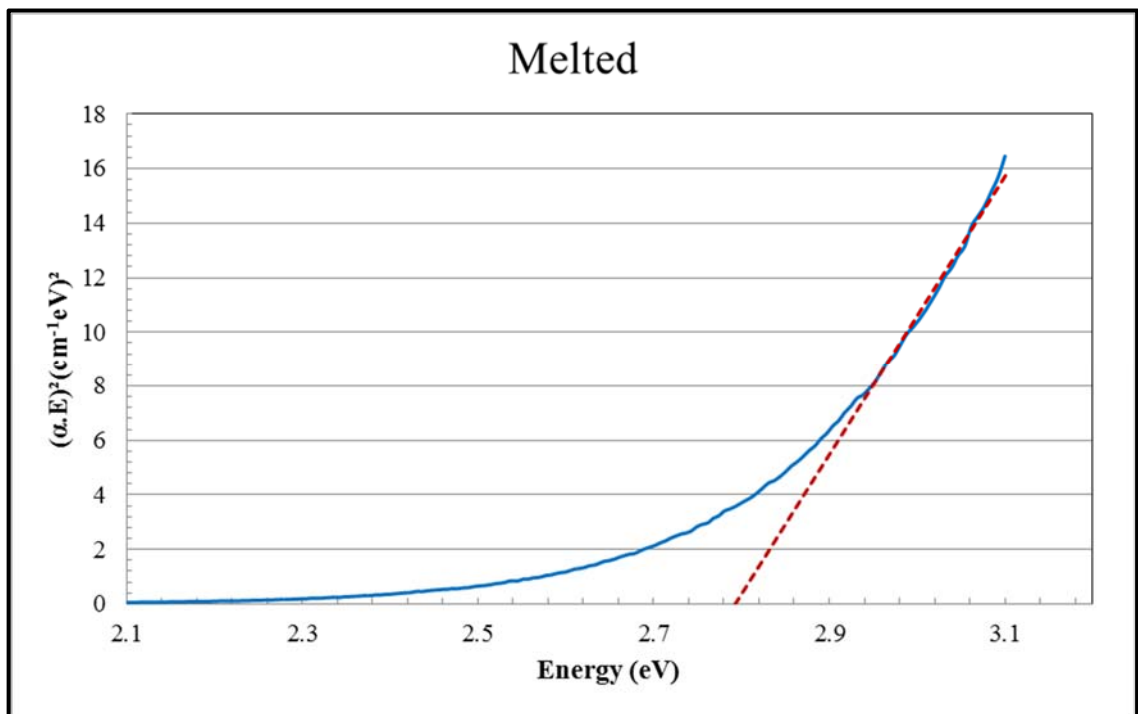


Figure 6.5. Tauc plot obtained from the optical absorption spectra of melted sample without field.

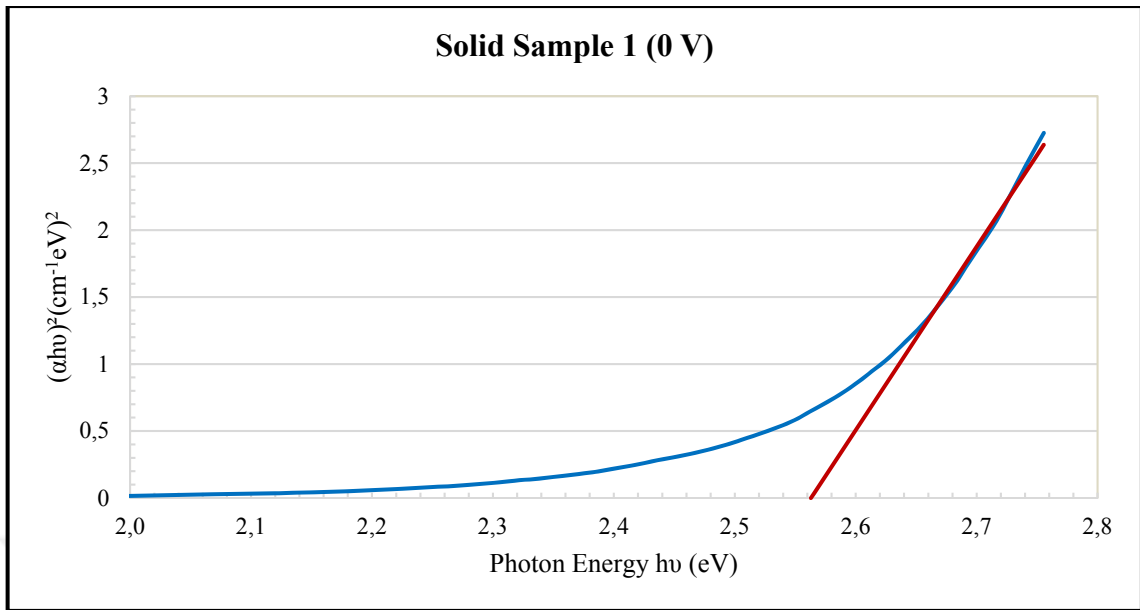


Figure 6.6. Tauc plot obtained from the optical absorption spectra of heat-treated sample without field.

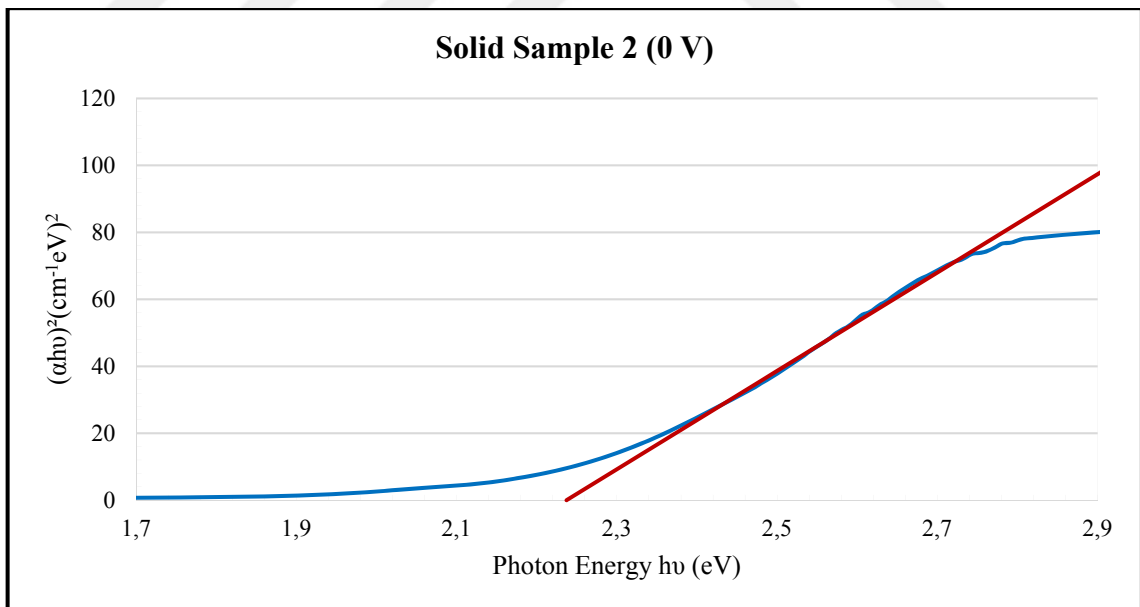


Figure 6.7. Tauc plot obtained from the optical absorption spectra of solid sample 2 without field.



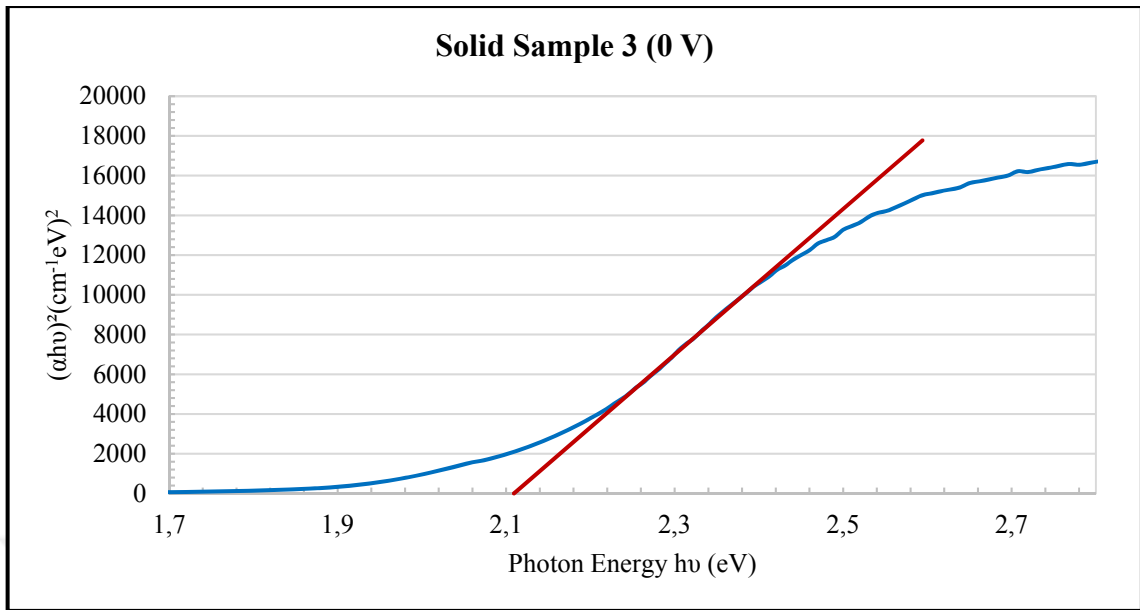


Figure 6.8. Tauc plot obtained from the optical absorption spectra of solid sample 3 without field.

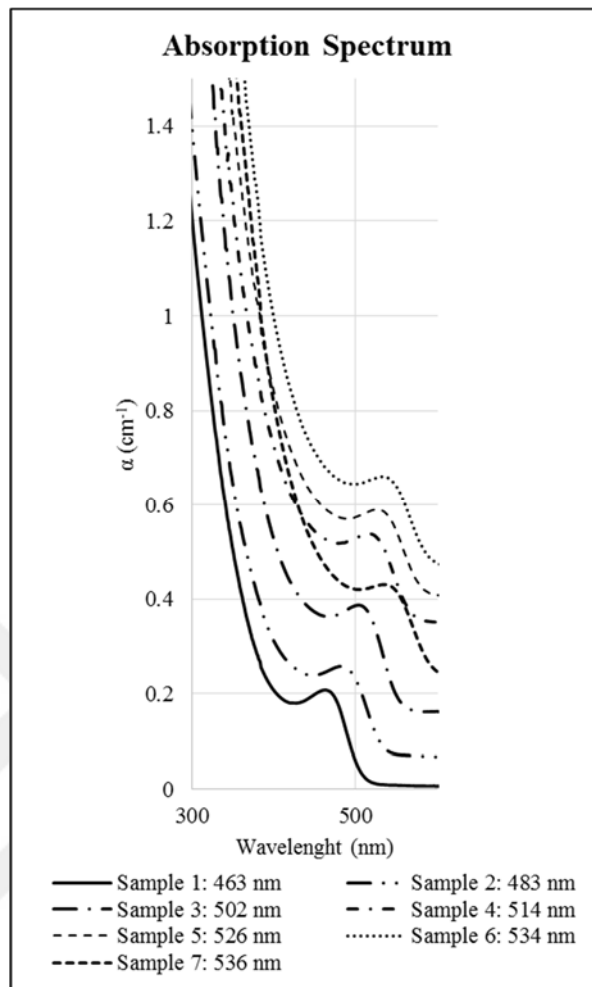


Figure 6.9. The absorption spectra of CdTe solution semiconductor nanocrystals without electric field (at Yeditepe uv-vis)

The optical absorption spectra of aqueous phase prepared CdTe QDs samples which were extracted at different heating time periods: Sample 1 (15 min), Sample 2 (60 min), Sample 3 (120 min), Sample 4 (180 min), Sample 5 (240 min), Sample 6 (300 min), Sample 7 (375 min) respectively. Figure 6.9. shows the absorption wavelength of each sample and these peak points are given in Table 6.3. From these data we can see that the exciton absorption peaks of the samples have red shifted with the heat treatment time.

Table 6.3. Table of solution samples absorption wavelength, band gap energies and heating time.

Solution Sample	Absorption Peak wavelength (nm)	Treatment Time	Band Gap (eV)
1	463	15 min	2.552
2	483	60 min	2.366
3	502	120 min	2.231
4	514	180 min	2.195
5	526	240 min	2.187
6	534	300 min	2.155
7	536	375 min	2.145

## 6.2. DIELECTRIC PERMITTIVITY RESULTS

In Figure 6.10 to Figure 6.19 below, the dielectric permittivity of the samples determined from the experimental optical absorption data are shown. Components of the real and imaginary part data were shown in Table 6.4 and the method was discussed in Chapter 5.1. To determine the particle radius from Brus equation, the electrical permittivity of the samples were determined from Hilbert Transformation shown below.

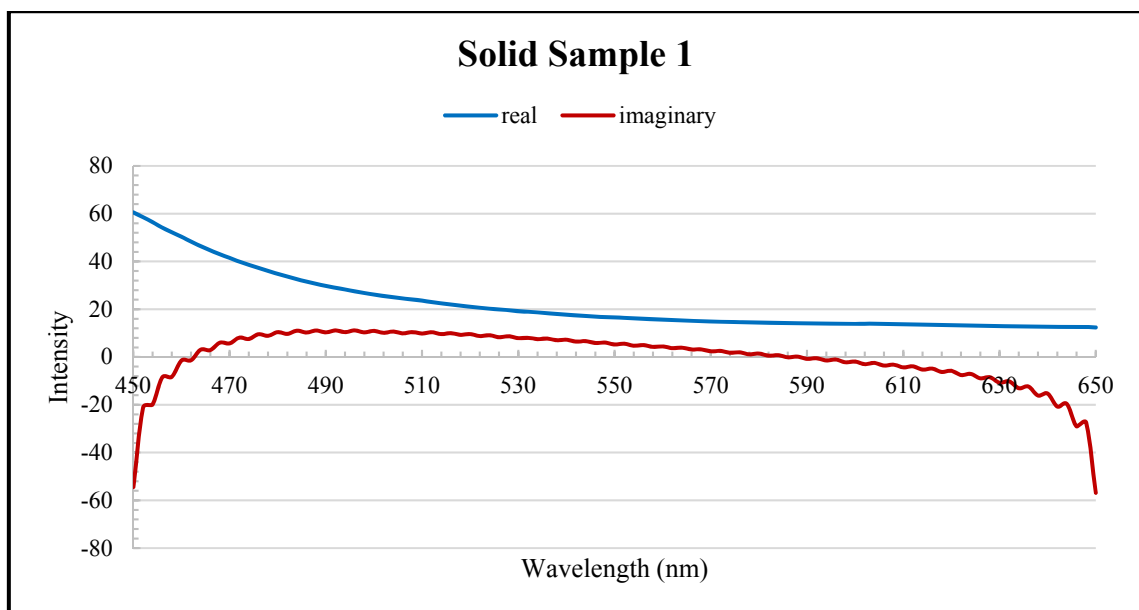


Figure 6.10. Components of the complex dielectric permittivity of solid sample 1.

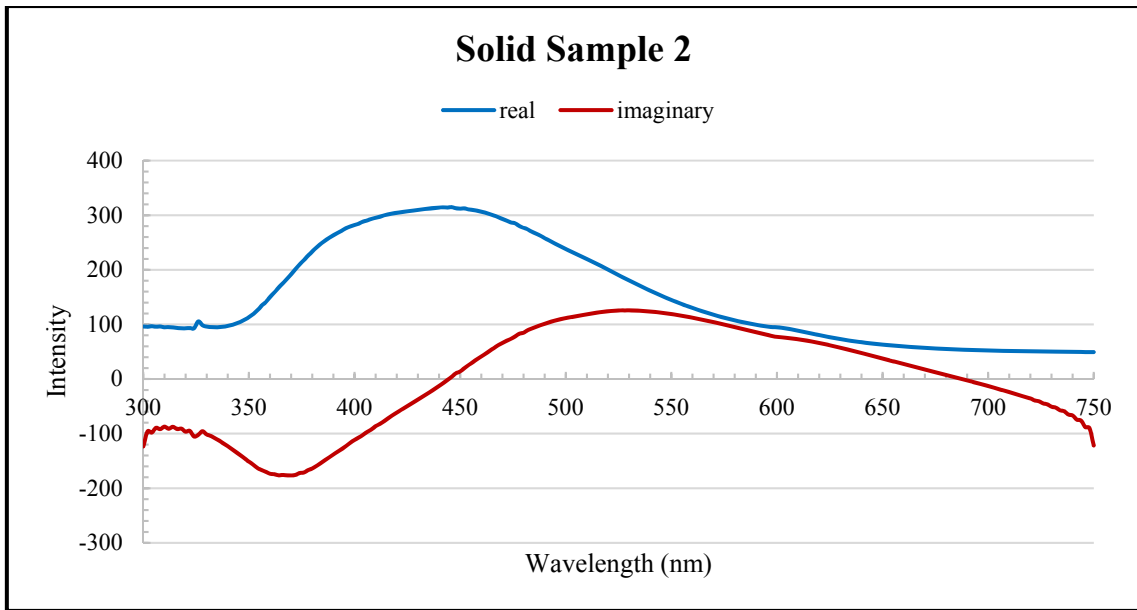


Figure 6.11. Components of the complex dielectric permittivity of solid sample 2

The real part of the dielectric permittivity used to determine the size of the particle from Brus equation. The dielectric permittivity value estimated from the graphs from Figure 6.11 to 6.19. Each sample has an absorption peak wavelength value, at this wavelength, the intensity of the figures gives us the real part of the dielectric permittivity.

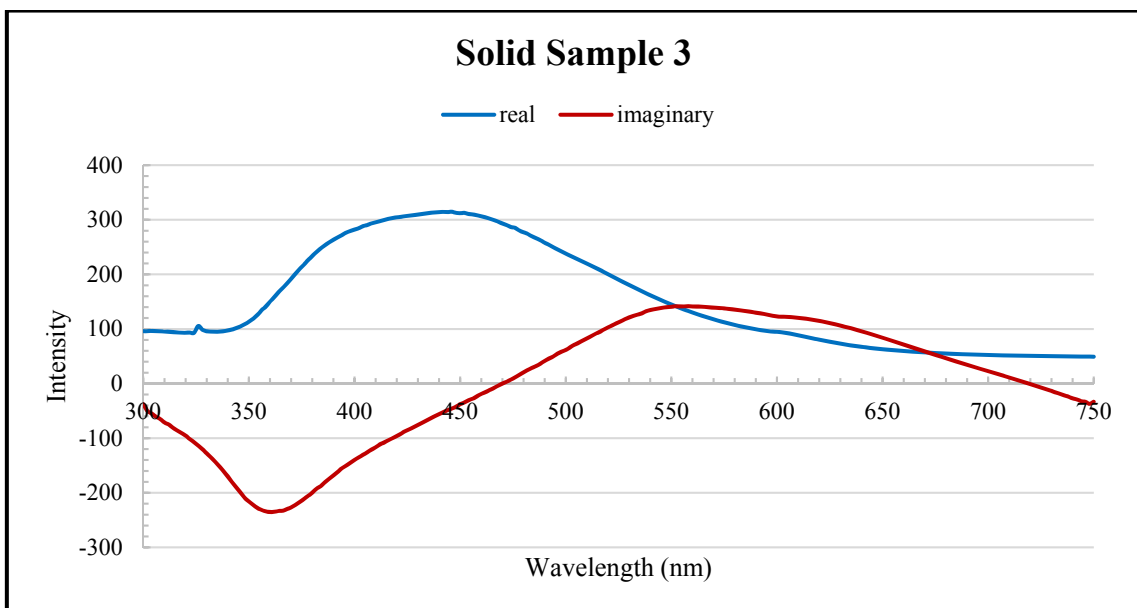


Figure 6.12. Components of the complex dielectric permittivity of solid sample 3.

Each figure shows the real and imaginary parts of the complex dielectric constant. The real part of the dielectric permittivity used in the calculation is an indication of the total amount of electric energy stored in the nanostructure in response to an external field.

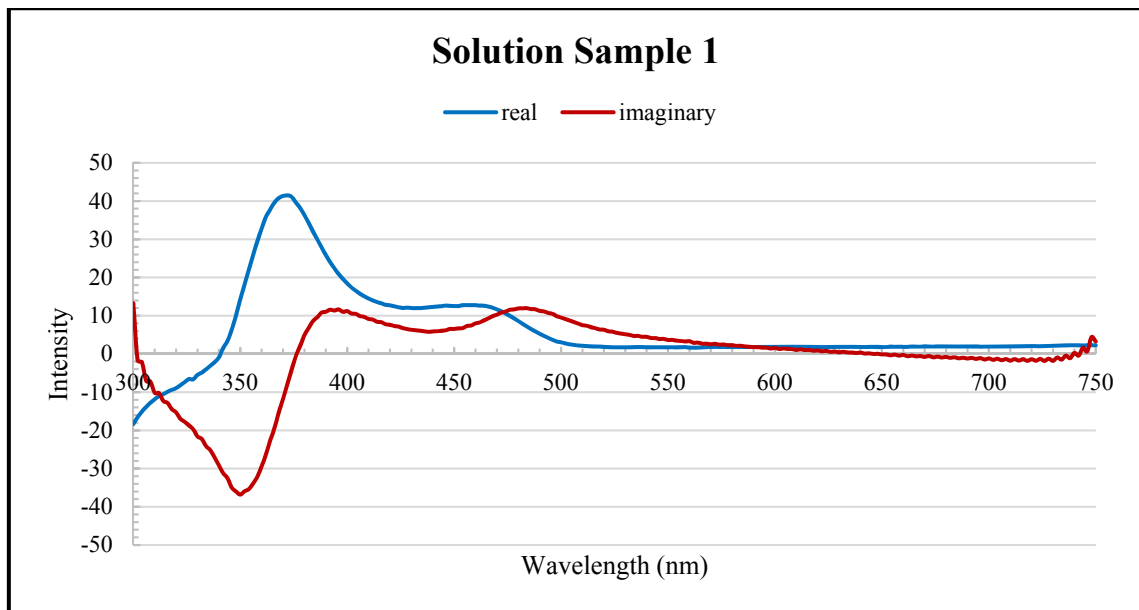


Figure 6.13. Components of the complex dielectric permittivity of aqueous sample 1.

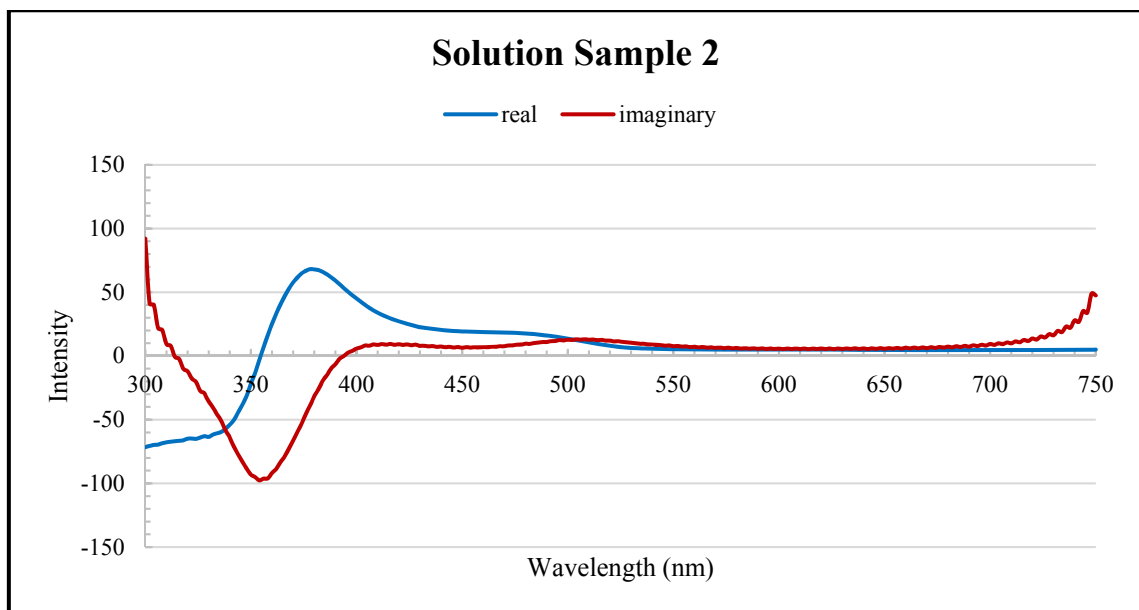


Figure 6.14. Components of the complex dielectric permittivity of aqueous sample 2.

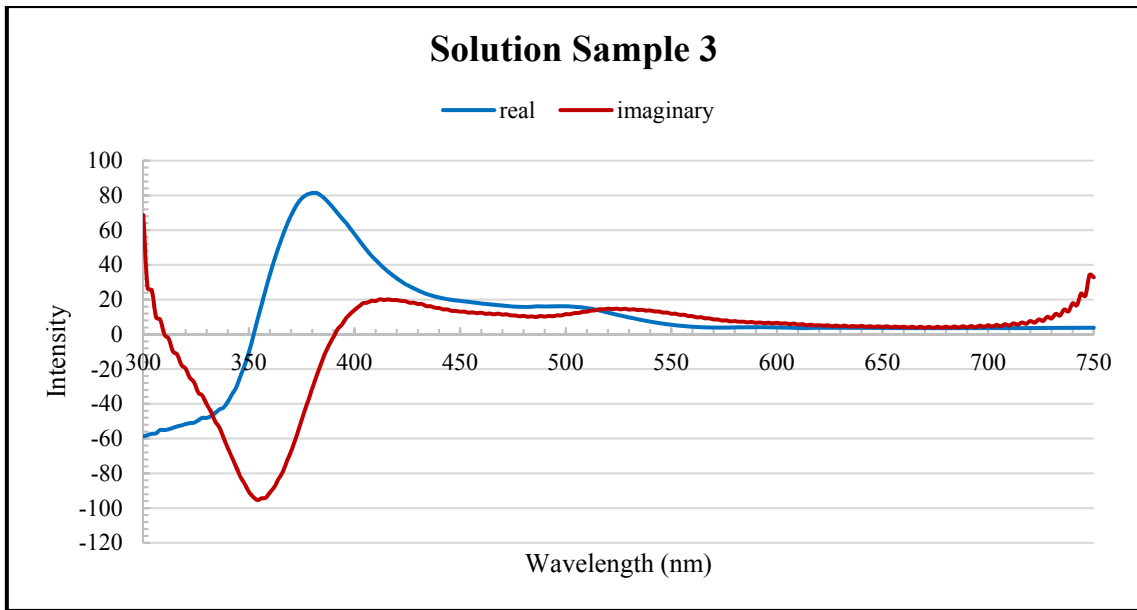


Figure 6.15. Components of the complex dielectric permittivity of aqueous sample 3.

This simulated graph clearly demonstrates the imaginary and real curvatures of the dielectric permittivity of the samples. For the solution samples, the real part values which is use to calculations are 17.9 F/m and 16.0 F/m for sample 2 and 3 respectively.

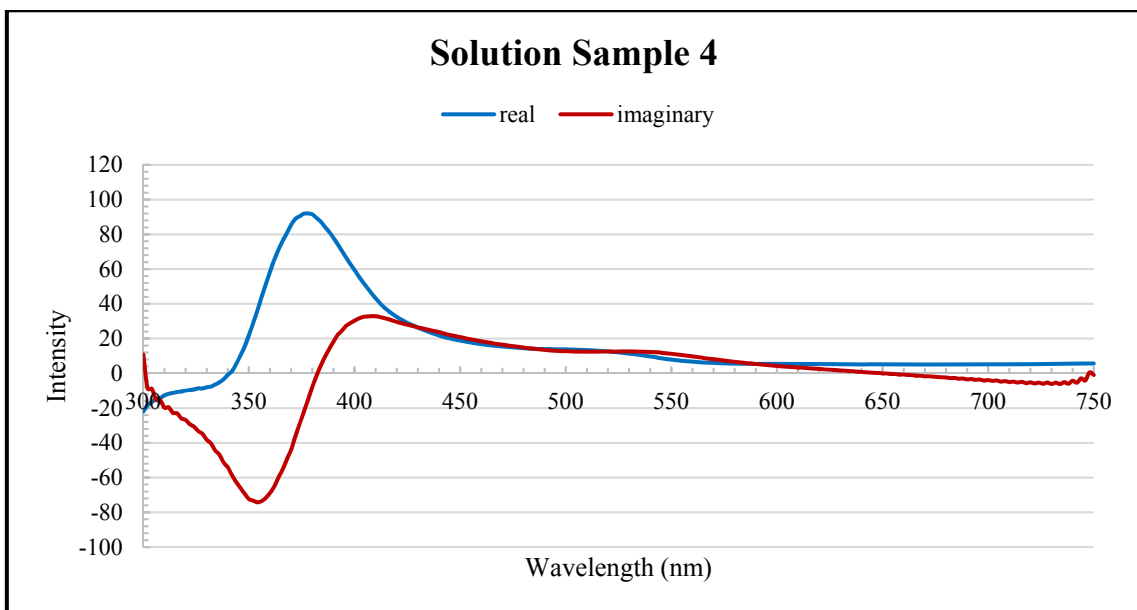


Figure 6.16. Components of the complex dielectric permittivity of aqueous sample 4.

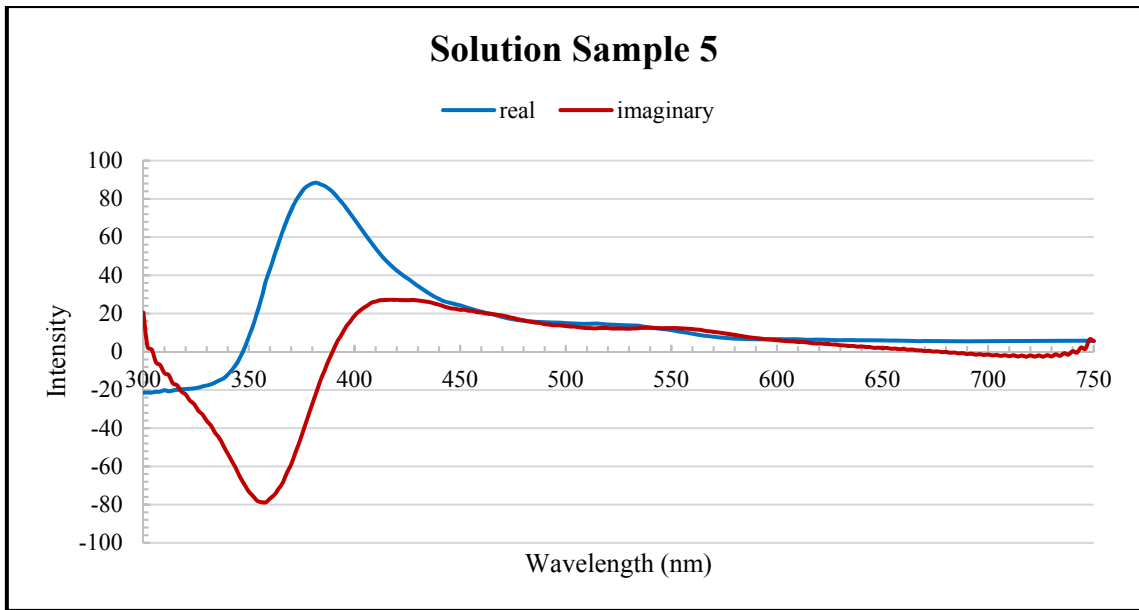


Figure 6.17. Components of the complex dielectric permittivity of aqueous sample 5

The real part of the data taken from the Hilbert Transformation graphs is 13.1 F/m for solution sample 4 and 14.0 F/m for solution sample 5.

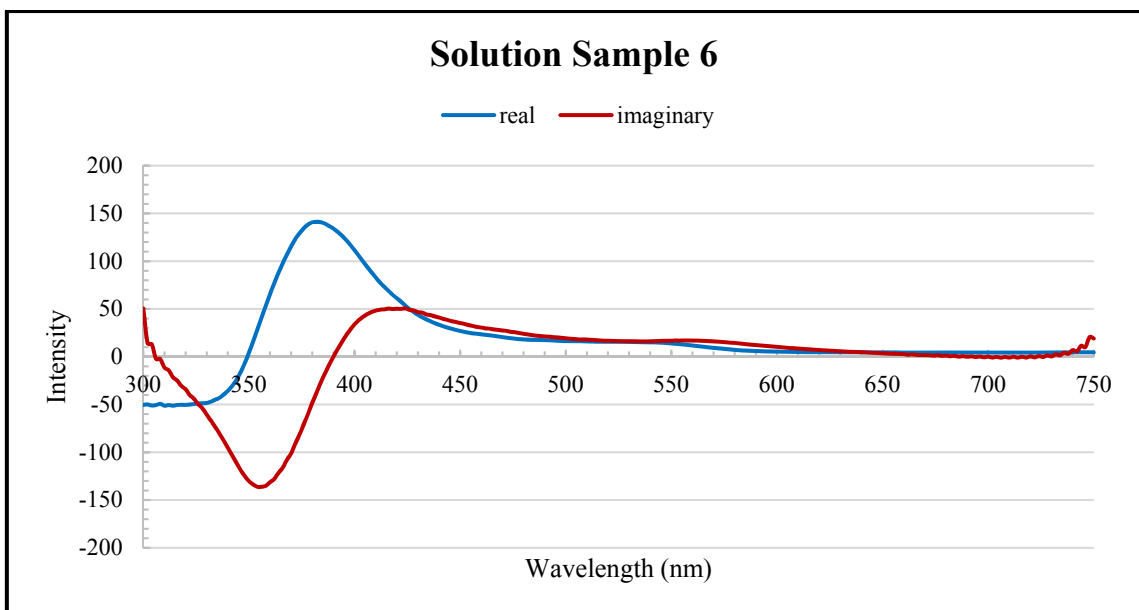


Figure 6.18. Components of the complex dielectric permittivity of aqueous sample 6.

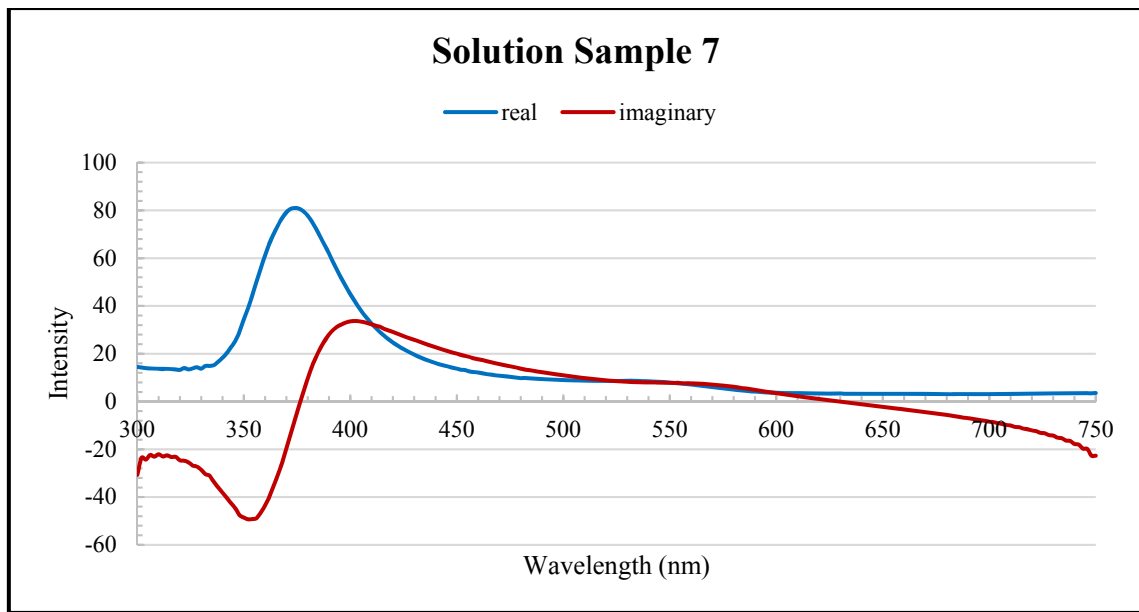


Figure 6.19. Components of the complex dielectric permittivity of aqueous sample 7

The real part of the samples is generally negative at low wavelengths and it increases from 350 to 450 nm. The imaginary part is in the negative region and is relatively small at high frequencies.

Table 6.4. Dielectric permittivity of the samples

Sample	$\epsilon_{\text{real}}$	$\epsilon_{\text{imaginary}}$
Solution 1	12.63	8.5
Solution 3	16.00	11.58
Solution 4	13.14	12.36
Solution 6	15.29	16.08
Solution 7	8.57	8.09
Solid 1	105.50	50.4
Solid 2	92.90	75.82
Solid 3	123.53	121.81

The minimum estimated value is 8.6 F/m while the highest value is 123.5 F/m. It was observed that the electric constants of the samples increased in proportion to the growth time during the synthesis. It is reported in the literature that the dielectric constants can change between 10-80 F/m according to the sample type. If the nanoparticle was embedded in the



glass sample, its dielectric permittivity is higher than that of the nanoparticles in solvent [78][79][80].

### 6.3. PARTICLE SIZE DISTRIBUTION ANALYSIS

Particle size distribution was obtained from the absorbance  $A$  at any wavelength related to the total volume of particles with radius discussed in Section 5.1. The derivative of the absorption curve was obtained by converting the wavelength axis to energy and thus to radius via Equation 5.5. The gradients at each value of  $r$  were then placed into Equation 5.9 and plotted. This procedure was carried out for each sample studied in this work. Figure 6.20 to Figure 6.42 show the particle size distribution obtained from the optical absorption spectrum with Gaussian curve.

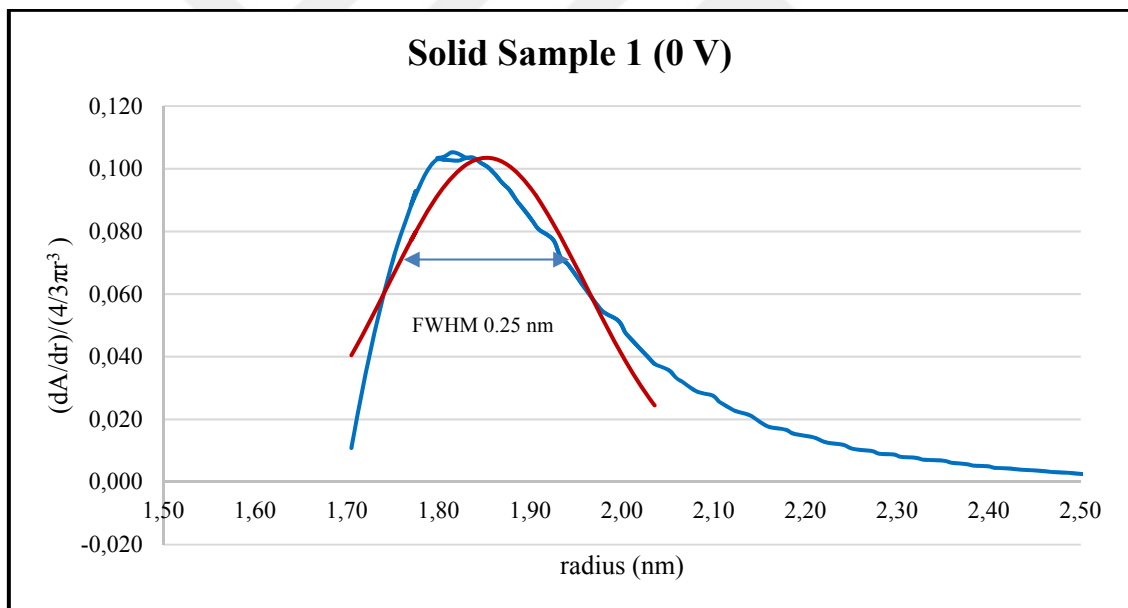


Figure 6.20. Particle size distribution curve of solid sample 1 at 0 V.

In the Figure, the blue line represents the original measurement value obtained from the particle size distribution relation. And the red one is the best Gaussian shape which was determined from the Matlab Programme. This allowed the extraction of reliable FWHM of peaks and more accurate comparison about particle size distribution without field and with field. Figure 6.20 shows the real and estimated Gaussian shape for solid sample 1 without field and the FWHM value was found to be 0.25 nm.

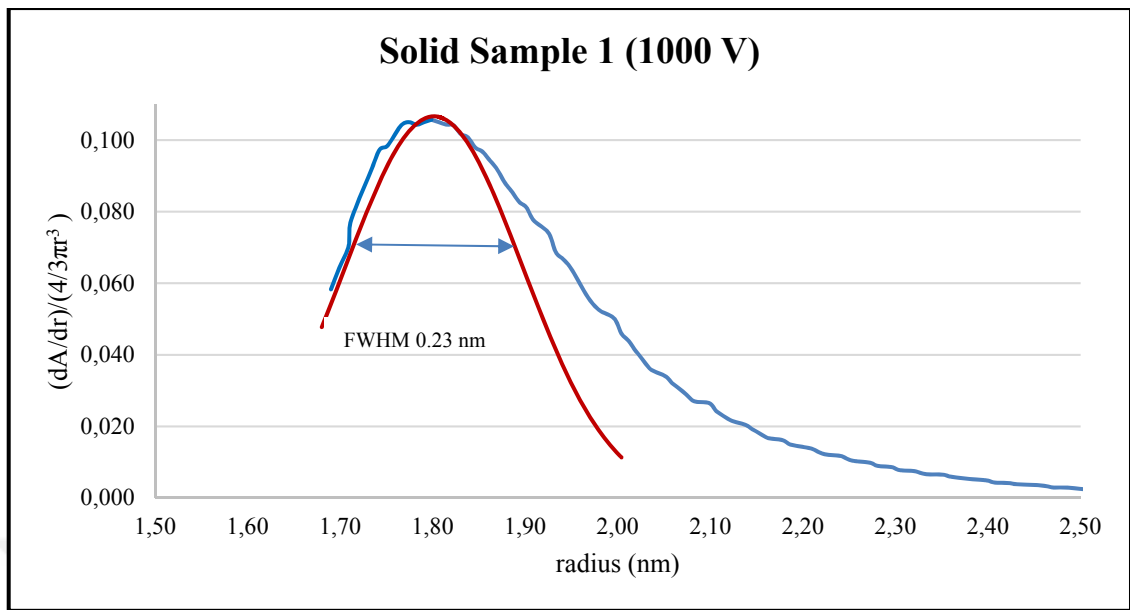


Figure 6.21. Particle size distribution curve of solid sample 1 at 1000 V.

Application of electric field causes reduction in particle size distribution approximately %8 for solid sample 1. It was clearly seen that the particle dispersion value drops to 0.23 nm after applying 1000 V to the sample.

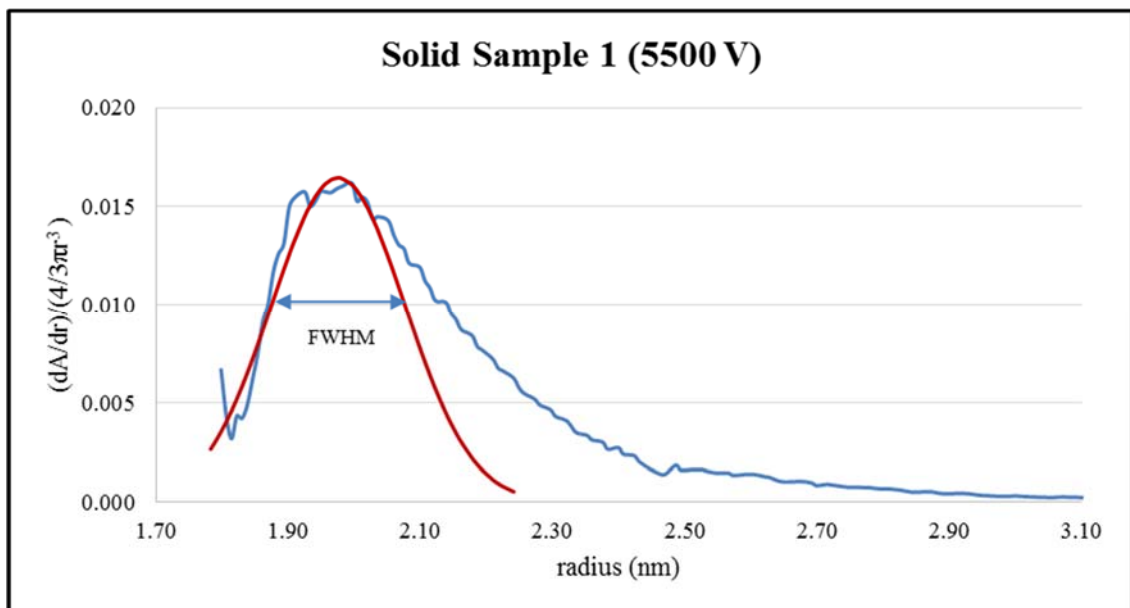


Figure 6.22. Particle size distribution curve of solid sample 1 at 5500 V.

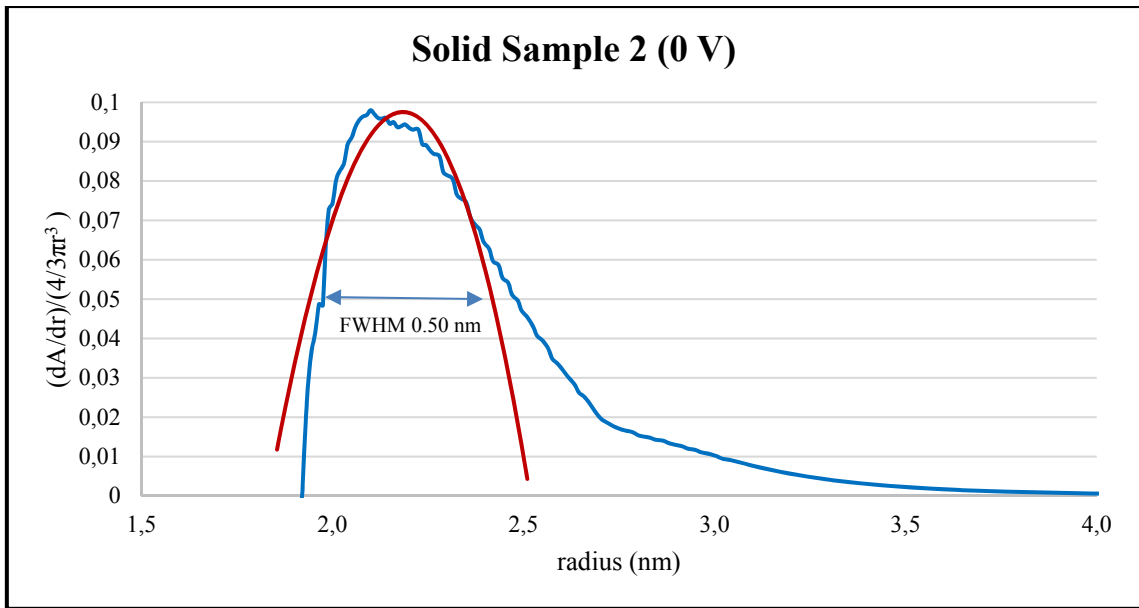


Figure 6.23. Particle size distribution curve of solid sample 2 at 0 V.

The size distribution of CdTe particles for solid sample 2 produced after application of 1000 V and 3000 V are narrower than the no field case shown in Figure 6.24.

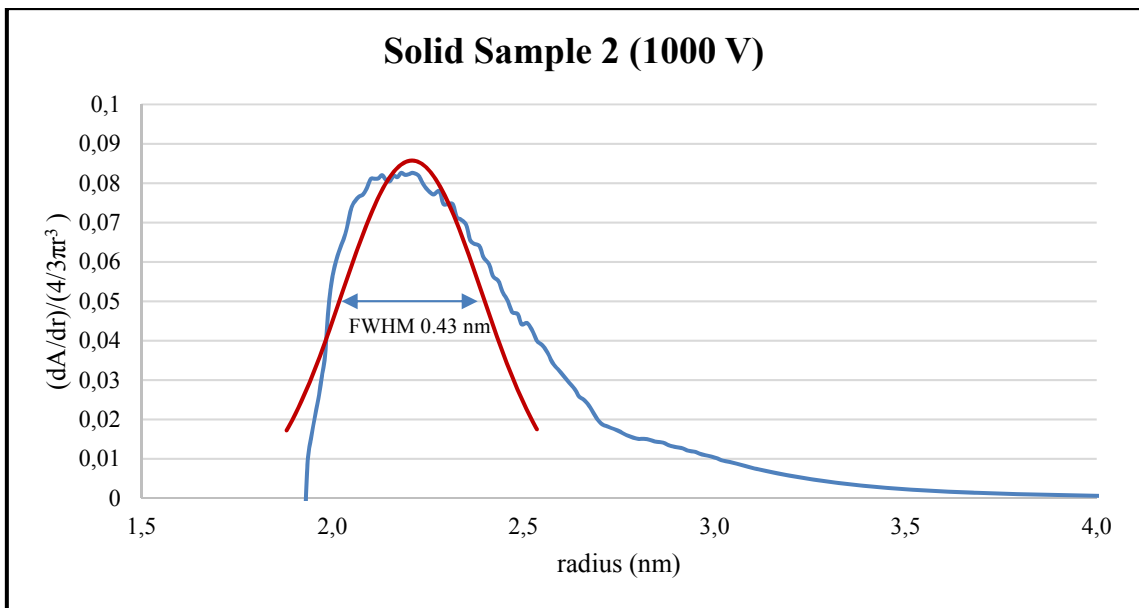


Figure 6.24. Particle size distribution curve of solid sample 2 at 1000 V.

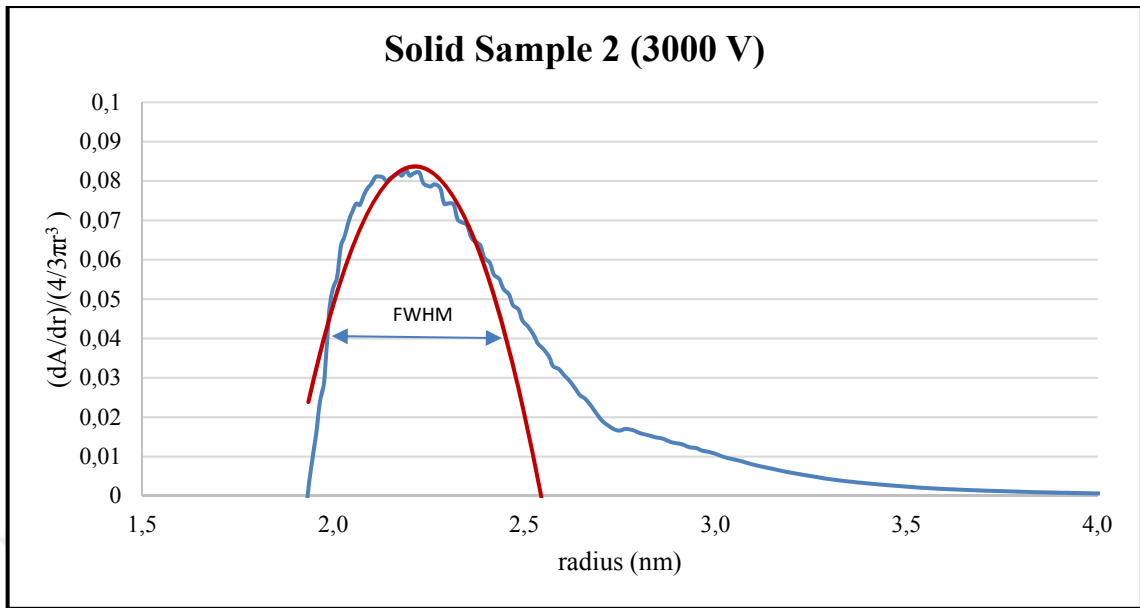


Figure 6.25. Particle size distribution curve of solid sample 2 at 3000 V.

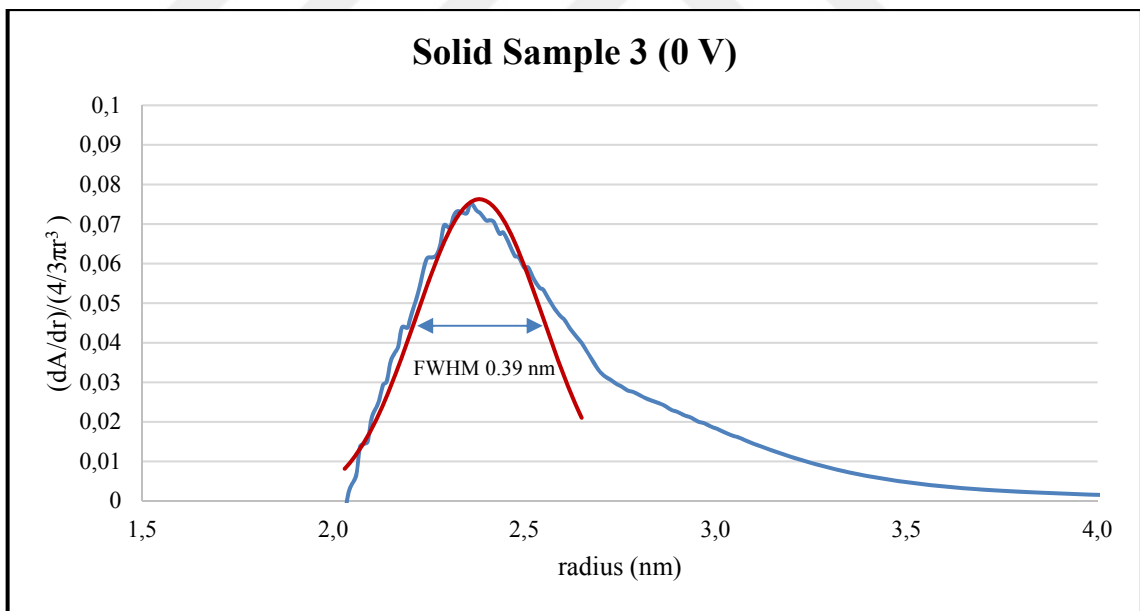


Figure 6.26. Particle size distribution curve of solid sample 3 at 0 V.

The results for the solid sample 3 at zero volt have a FWHM of 0.39 nm and this size distribution value begins to fall under the influence of high electric field.

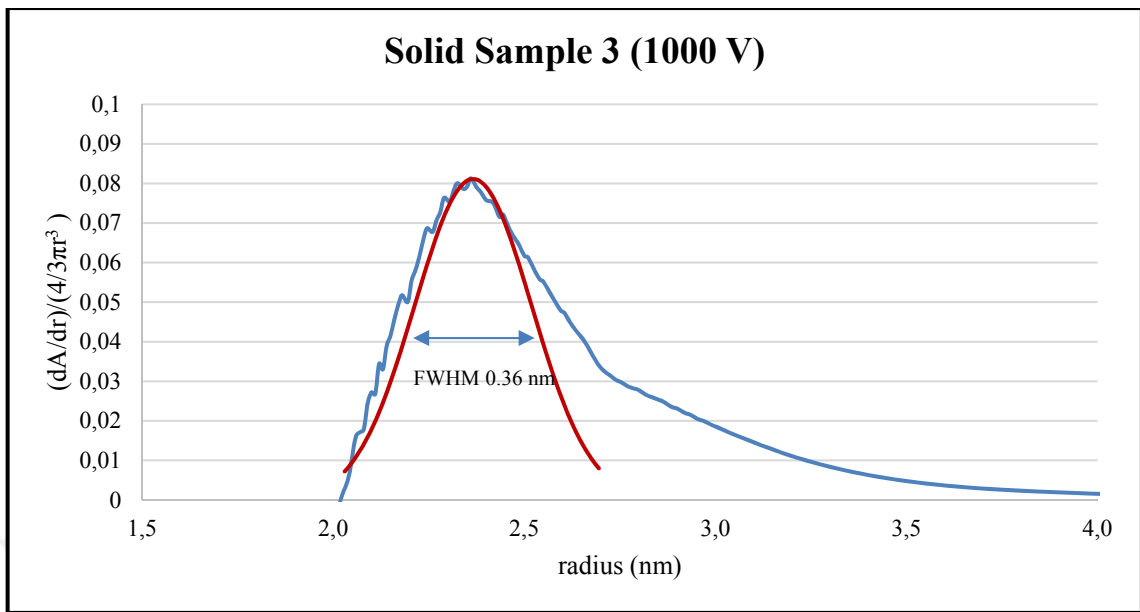


Figure 6.27. Particle size distribution curve of solid sample 3 at 1000 V

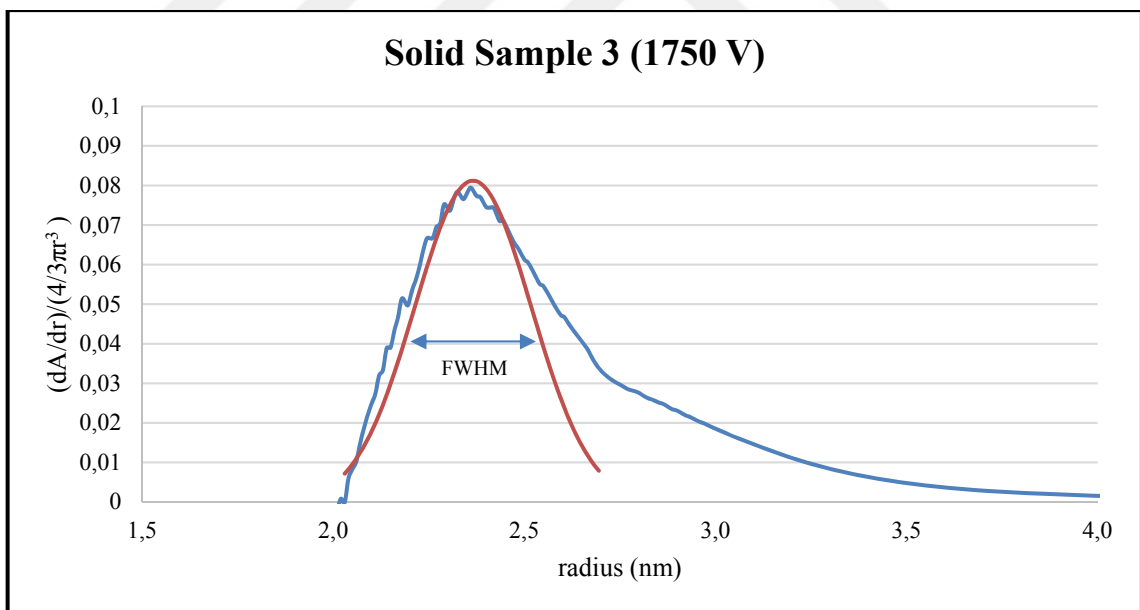


Figure 6.28. Particle size distribution curve of solid sample 3 at 1750 V

For the solid samples, we can easily say that according to the graphs above, the full width half maximum of the absorption peaks is considerably broadened and decreases with increasing particle size. When we apply electric field to the sample, these absorption peaks become narrower.

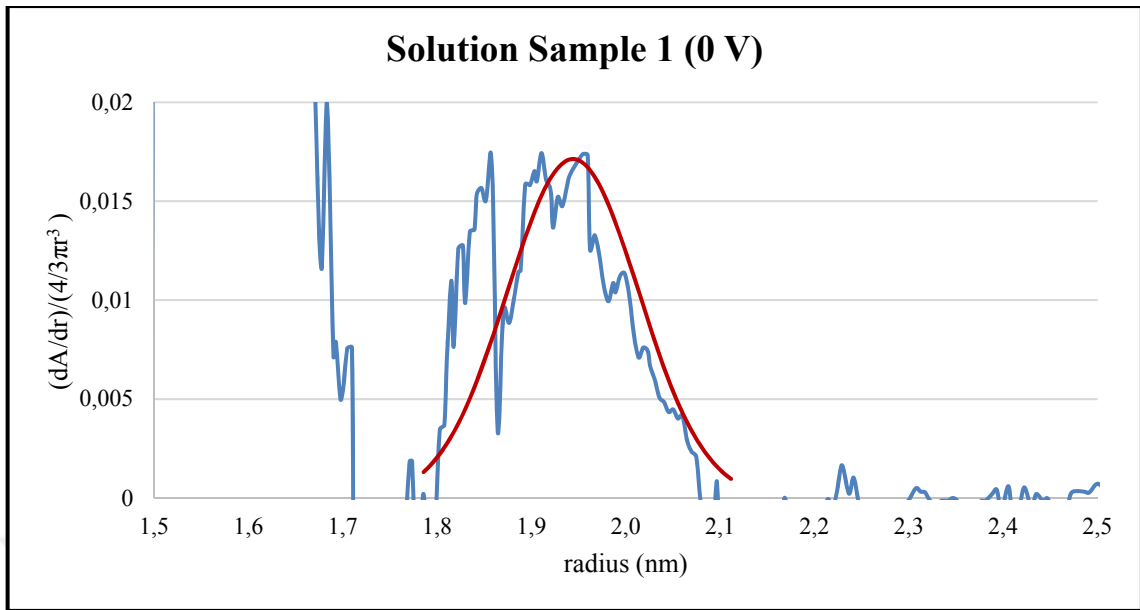


Figure 6.29. Particle size distribution curve of solution sample 1 at 0 V.

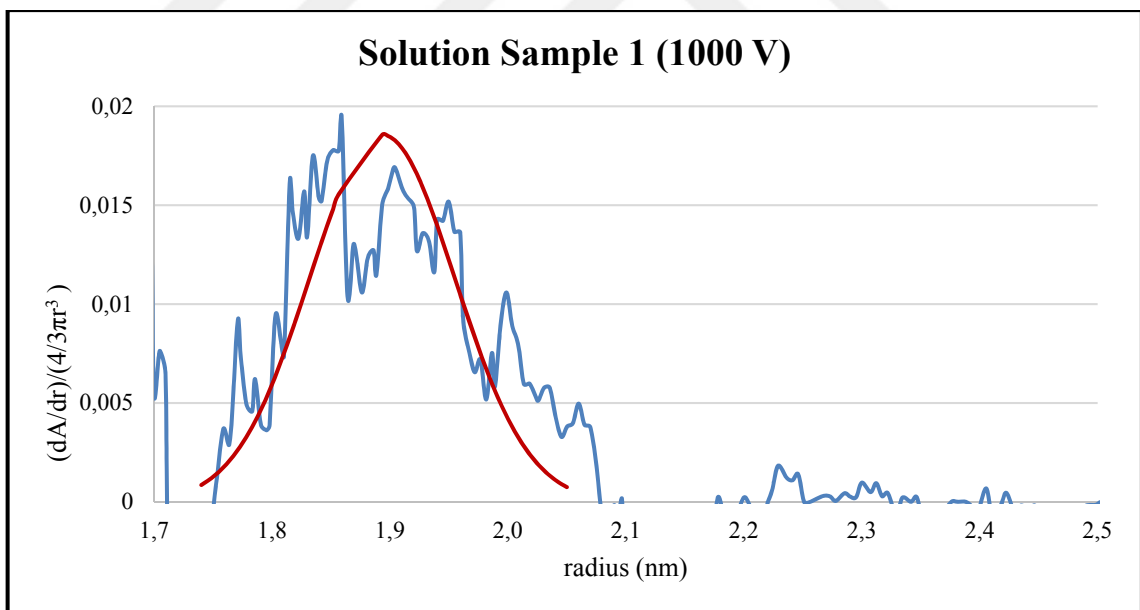


Figure 6.30. Particle size distribution curve of solution sample 1 at 1000 V.

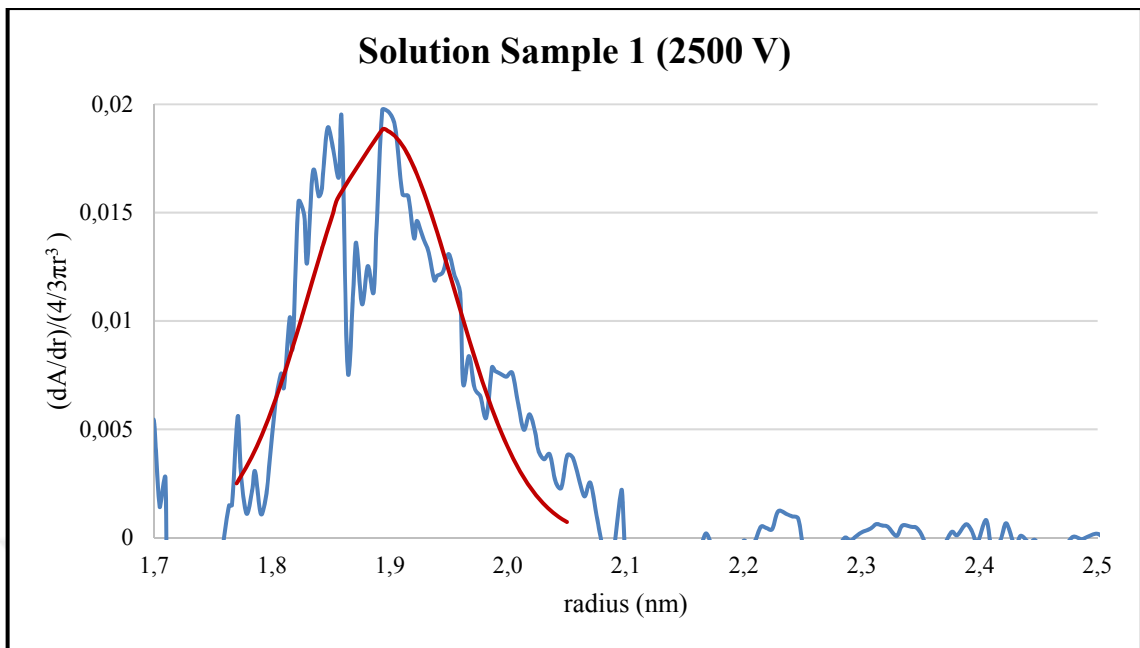


Figure 6.31. Particle size distribution curve of solution sample 1 at 2500 V.

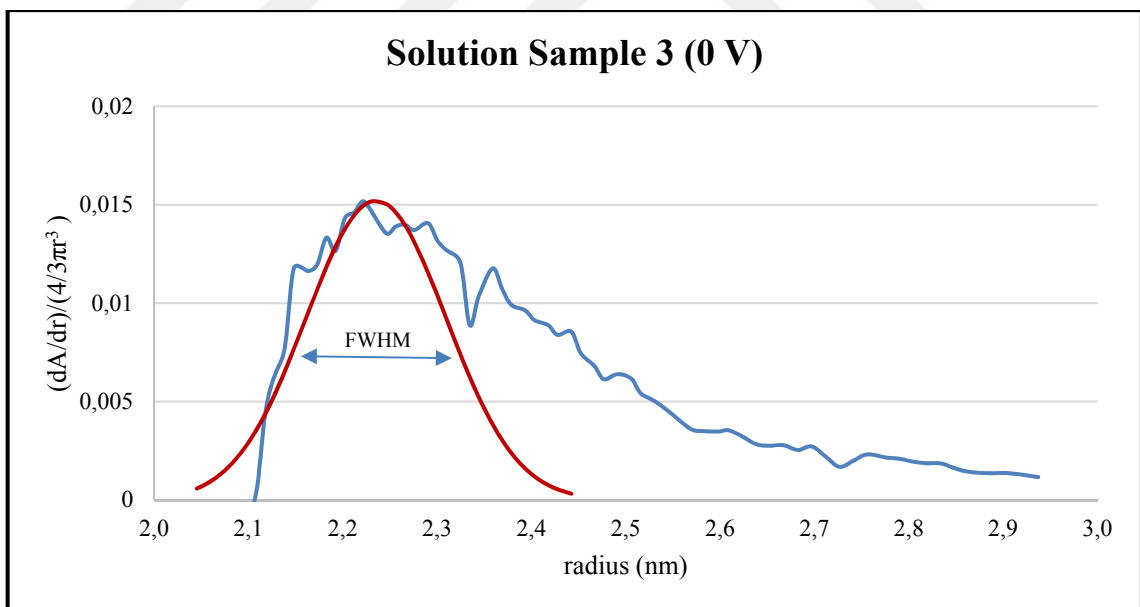


Figure 6.32. Particle size distribution curve of solution sample 3 at 0 V.

More noise was observed in optical absorption spectroscopic measurements of some samples than in the other samples. For this reason, in the Excel programme, exponential smoothing is used to get a more realistic picture.

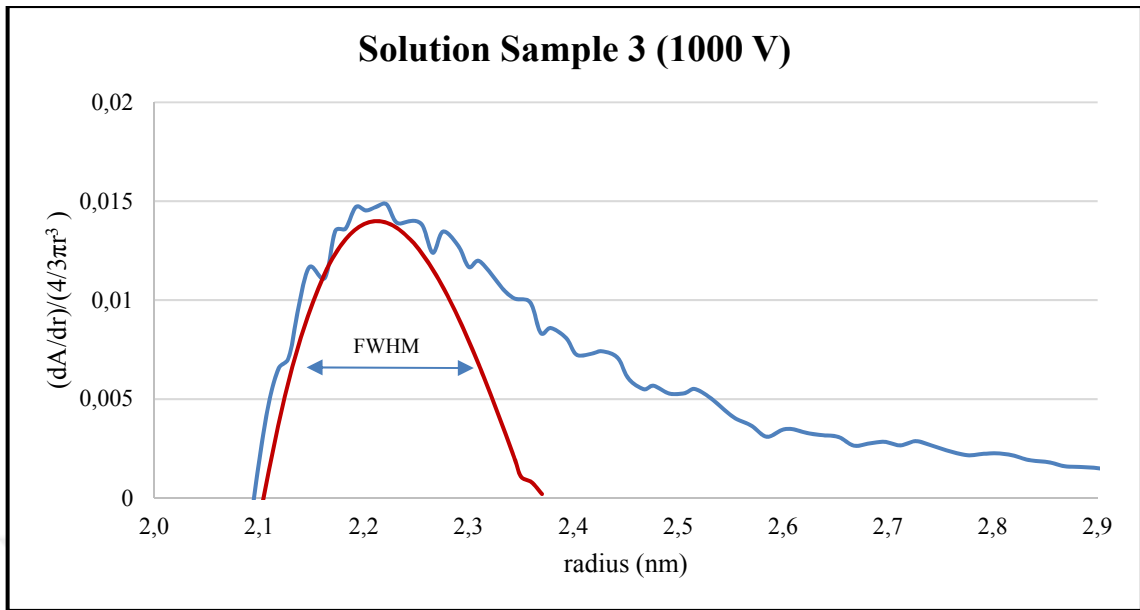


Figure 6.33. Particle size distribution curve of solid sample 3 at 1000 V.

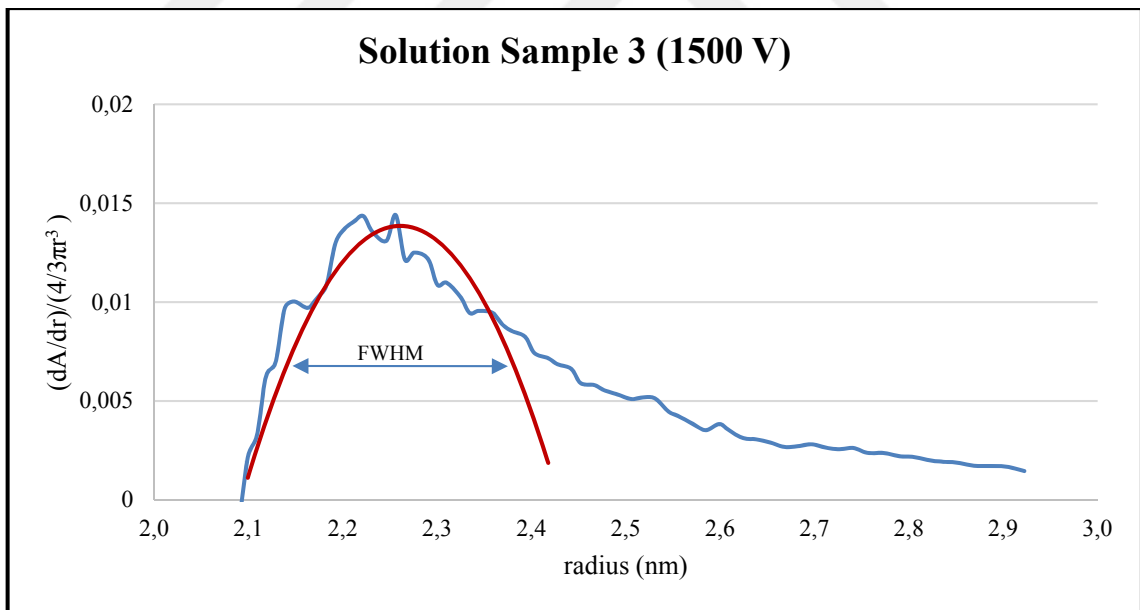


Figure 6.34. Particle size distribution curve of solution sample 3 at 1500 V.



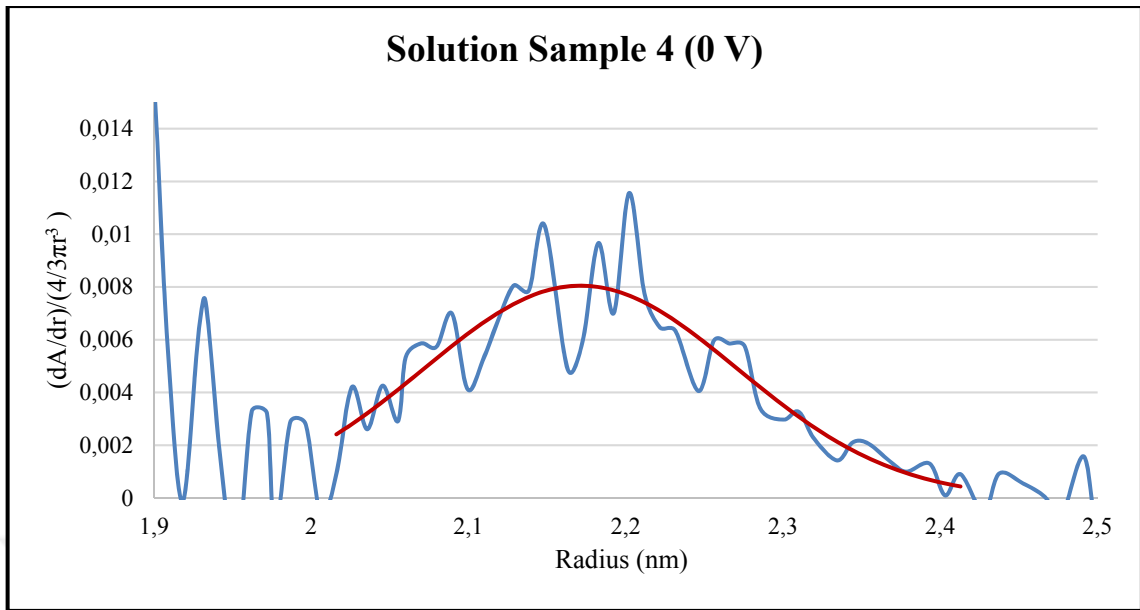


Figure 6.35. Particle size distribution curve of solution sample 4 at 0 V.

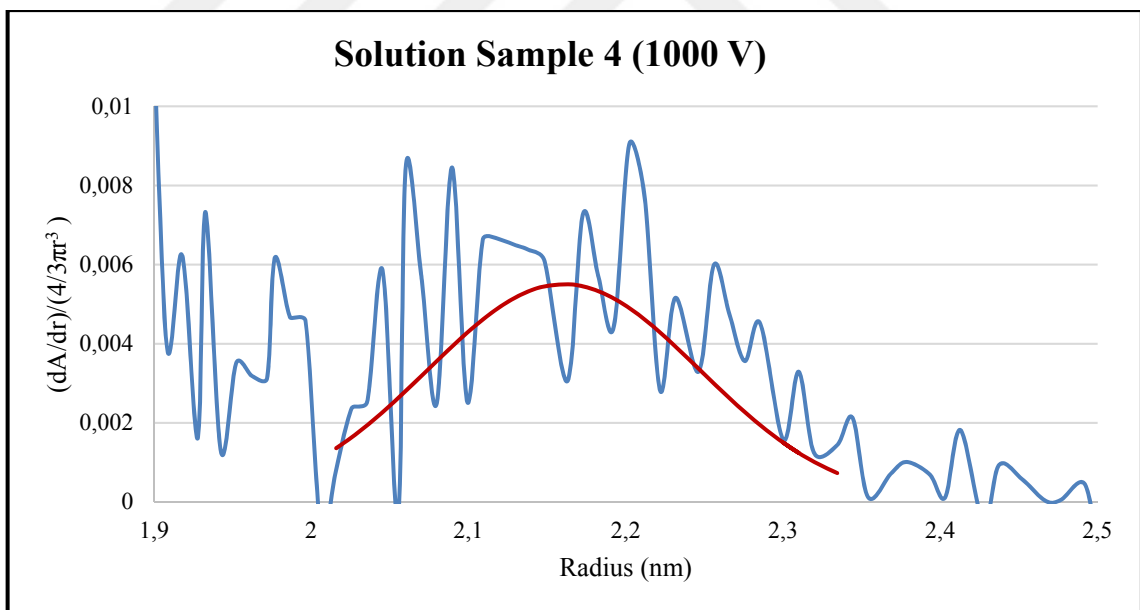


Figure 6.36. Particle size distribution curve of solution sample 4 at 1000 V.

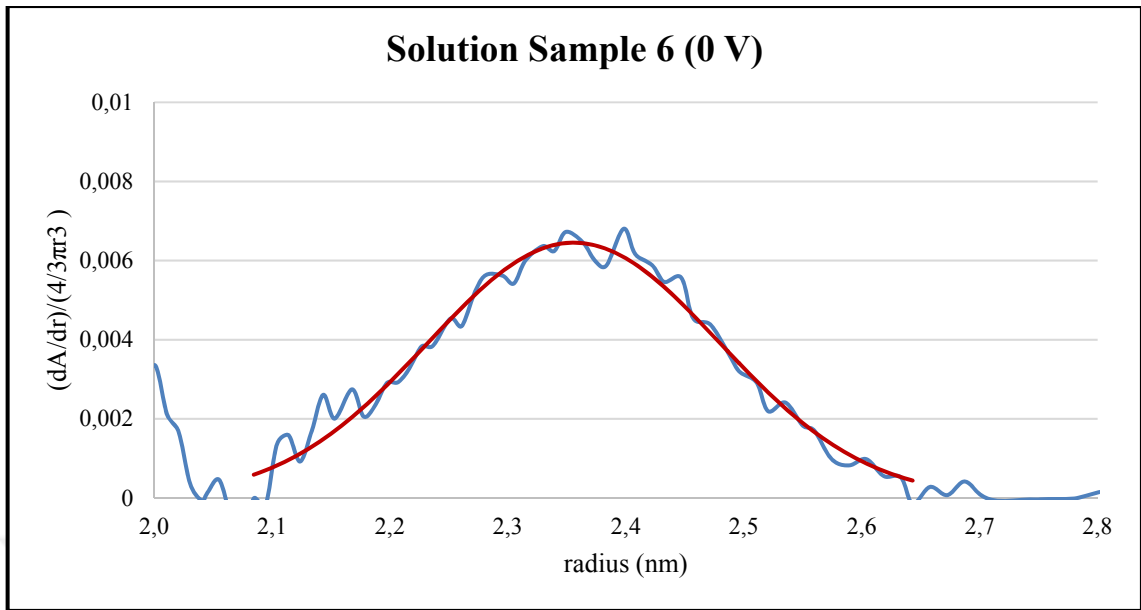


Figure 6.37. Particle size distribution curve of solution sample 6 at 0 V.

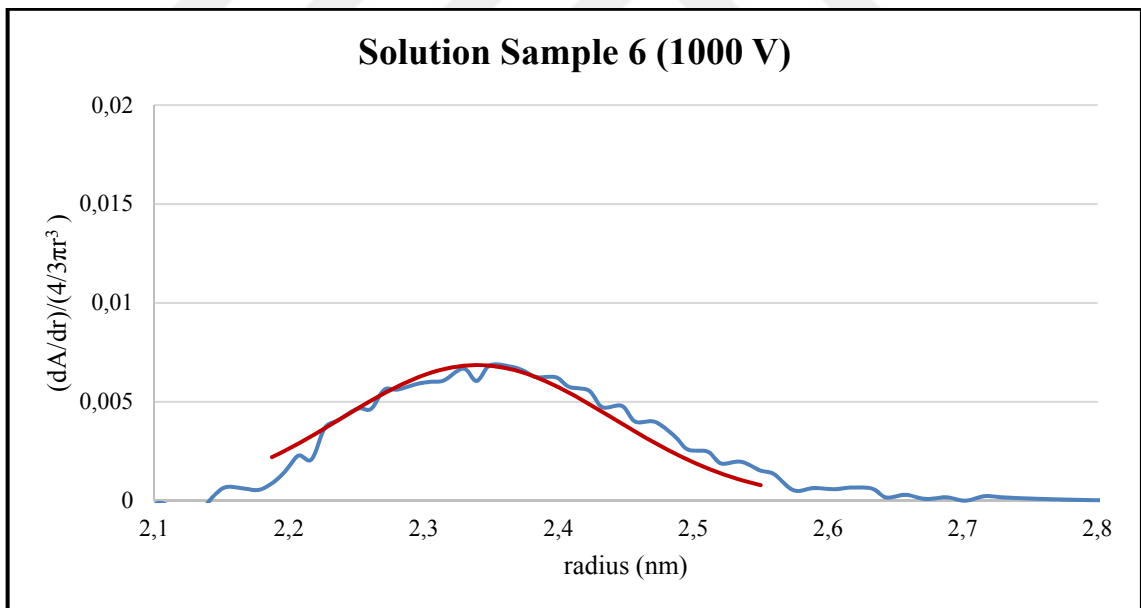


Figure 6.38. Particle size distribution curve of solution sample 6 at 1000 V.

Figure 6.35 to 6.38 show the simulated data taken from the Matlab programme for the particle size distribution results for samples with and without electric field.

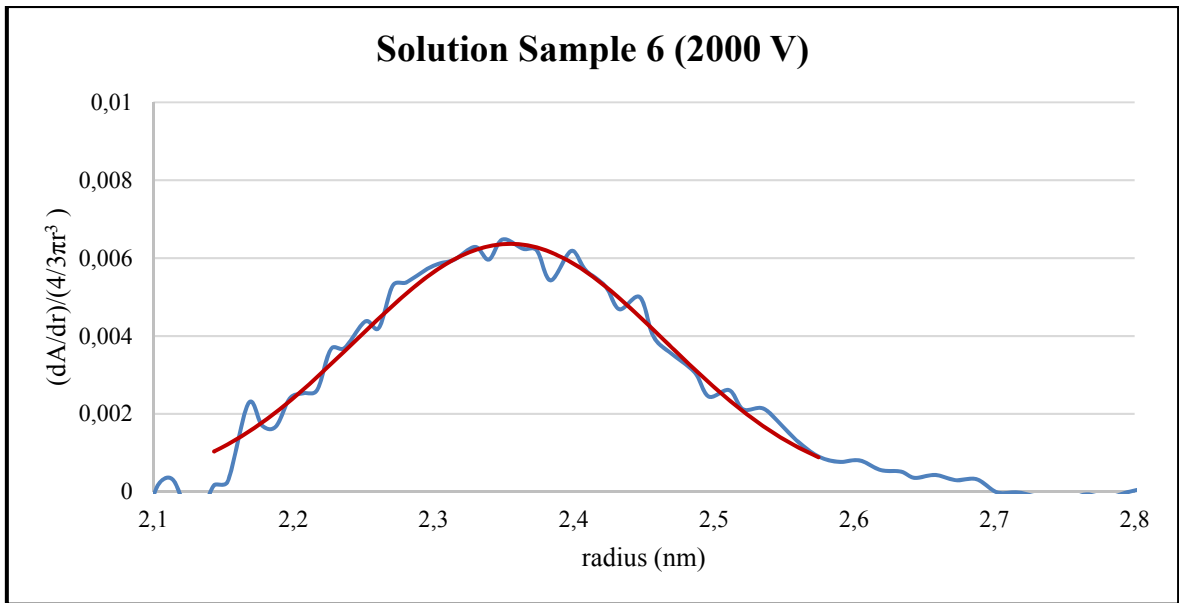


Figure 6.39. Particle size distribution curve of solution sample 6 at 2000 V.

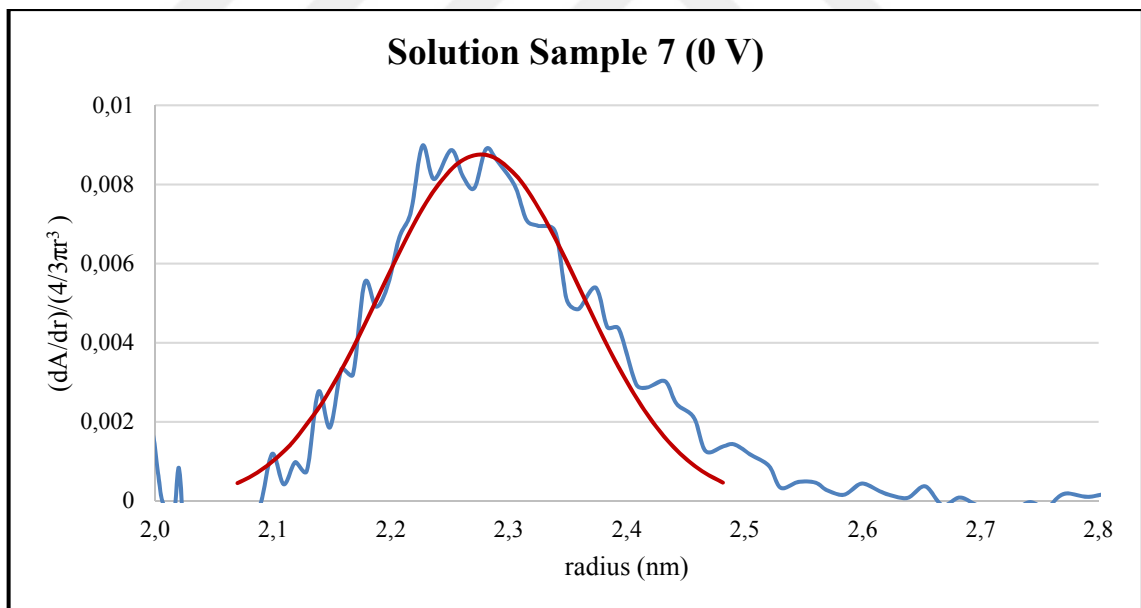


Figure 6.40. Particle size distribution curve of solution sample 7 at 0 V.

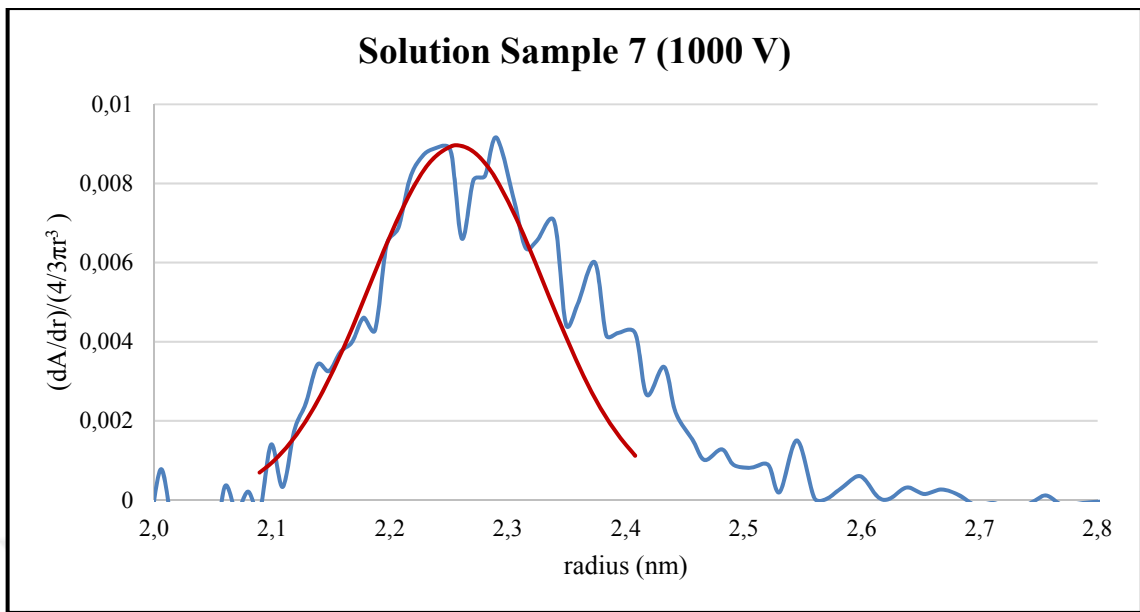


Figure 6.41. Particle size distribution curve of solution sample 7 at 1000 V.

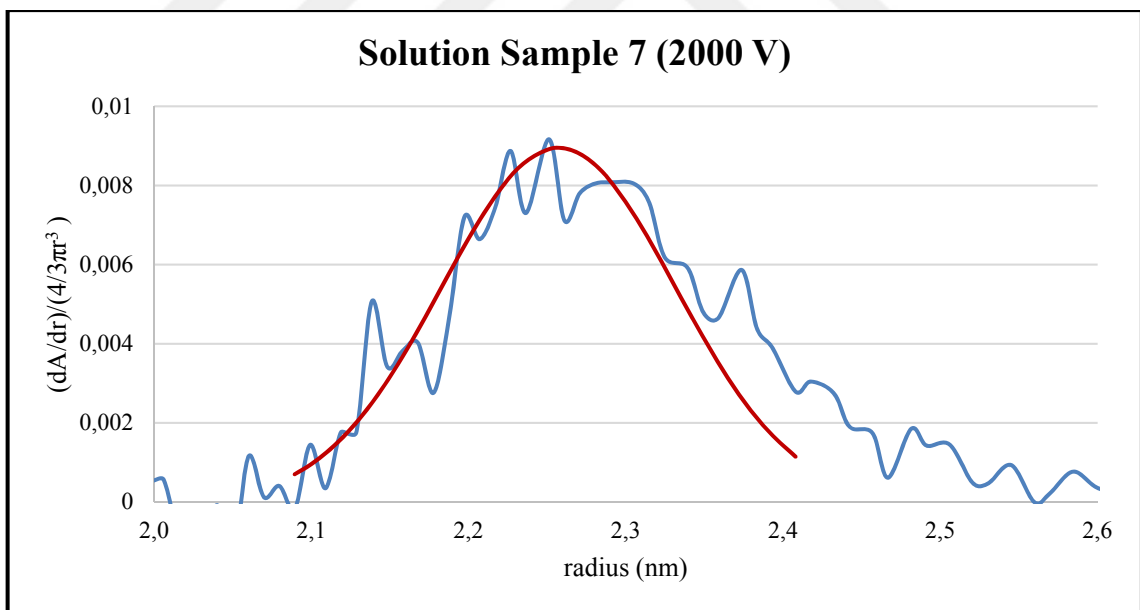


Figure 6.42. Particle size distribution curve of solution sample 7 at 2000 V.

Table 6.5 shows all estimated size distribution results of the samples with and without field. To compare the results, only at 1 kV measurements were analyzed. The average radius of the samples was calculated from Brus Equation which was discussed in Section 5.1.

Percentage change of the size distribution and radius were calculated all about comparing with field and without field values. The FWHM of the distribution curve of CdTe nanocrystals for solid samples is maximum at 0.50 nm, being considerably broader than the CdTe nanocrystals in solution samples which have a maximum FWHM 0.29 nm without field.

Table 6.5. Size distribution of the samples

Samples		Electric Field (kV)	Size Distribution FWHM (nm)	% change in size distribution due to applied field	Average radius computed from band gap (nm)	% change in radius due to applied field
Solid	1	No field	0.25	-8.0	1.920	+7.8
		With field(1.0)	0.23		2.070	
	2	No field	0.50( $\pm 0.006$ )	-14.0	2.360	+4.4
		With field(1.0)	0.43( $\pm 0.006$ )		2.465	
	3	No field	0.39( $\pm 0.04$ )	-7,7	2.580	+1.9
		With field(1.0)	0.36( $\pm 0.04$ )		2.630	
Solution	1	No field	0.16( $\pm 0.02$ )	-6,3	1.925	+1.0
		With field(1.0)	0.15( $\pm 0.02$ )		1.945	
	3	No field	0.18	-16.7	2.285	+2.4
		With field(1.0)	0.15		2.340	
	4	No field	0.23	-13.0	2.315	+2.2
		With field(1.0)	0.20		2.365	
	6	No field	0.29( $\pm 0.001$ )	-17.2	2.395	+0.6
		With field(1.0)	0.24( $\pm 0.001$ )		2.410	
	7	No field	0.20( $\pm 0.06$ )	-15.0	2.325	+0.6
		With field(1.0)	0.17( $\pm 0.06$ )		2.340	

Clearly nanoparticles synthesized in solution have a narrower size distribution compared to those in glass, which get narrow (6% to 17%) on the application of an electric field for nanoparticles  $>2$  nm in solution. This is also true for the solid samples, but occurs for nanoparticles  $<2$  nm. All nanoparticles suffer a red shift, decreasing their band gap and leading to a higher calculated radius on application of an electric field.

To determine the uncertainty of the particle size distribution measurement, best Gauss curve fits were formed and FWHM values found for at 0 V (Curve 1) and after high dc. voltage measurements again 0 V (Curve 2). The standard uncertainty was calculated from the difference between Curve 1 FWHM and Curve 2 FWHM value which is a rectangular distribution converted to the normal distribution (divided by  $\sqrt{3}$ ).

Table 6.6. Measurement uncertainty of calculation of the particle size distribution.

Sample	FWHM Curve 1 (nm)	FWHM Curve 2 (nm)	Uncertainty (nm)
Solid Sample 2	0.49	0.48	0.006
Solid Sample 3	0.46	0.39	0.039
Solution 1	0.20	0.16	0.021
Solution 6	0.29	0.29	0.000
Solution 7	0.32	0.20	0.060

As can be seen in Figure 6.44, the FWHM tends to be narrower with field. The centre of the Gauss peak means average particle radius shift upper average particle radius. In addition to that, when we go back zero volt after finishing all electrical field application, it almost seems to return to its first zero reading.

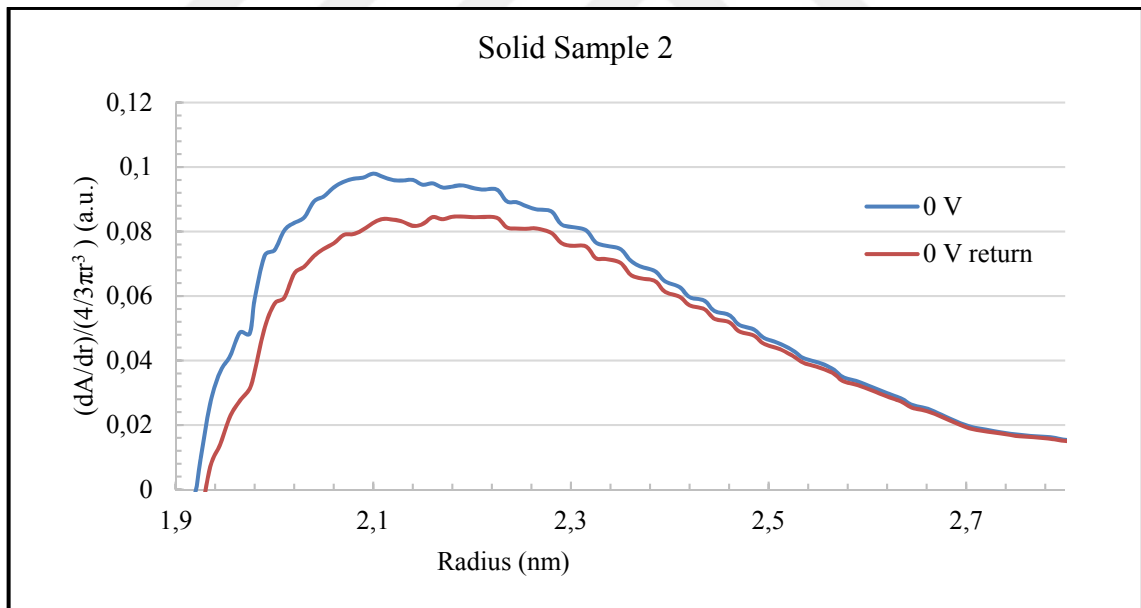


Figure 6.43. Particle size distribution for CdTe quantum dots at 0 V before and after application of electric field.

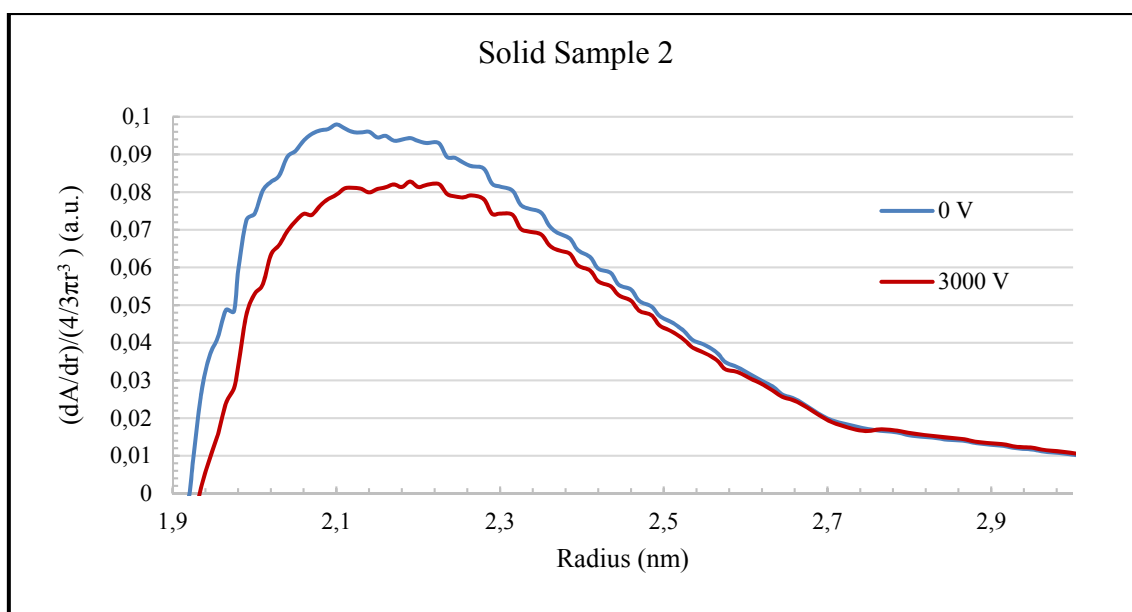


Figure 6.44. Particle size distribution for CdTe quantum dots at 0 V and 3000 V.

#### 6.4. ELECTRO-ABSORPTION SPECTRUM MEASUREMENT RESULTS

The electro-optical measurements were operated for the solid sample and the aqueous solutions as shown in Figures 6.45 and 6.46.

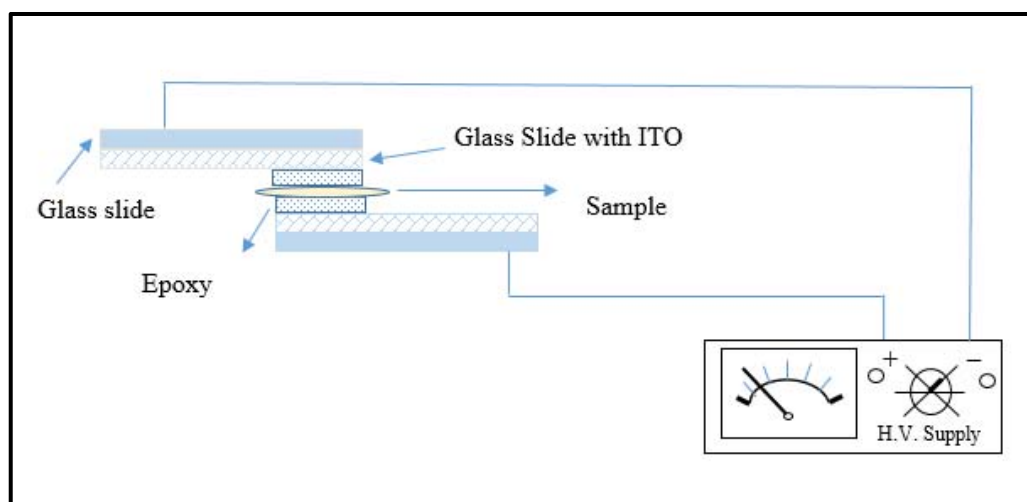


Figure 6.45. Diagram of the electro-optical absorption measurement set-up for solid samples.

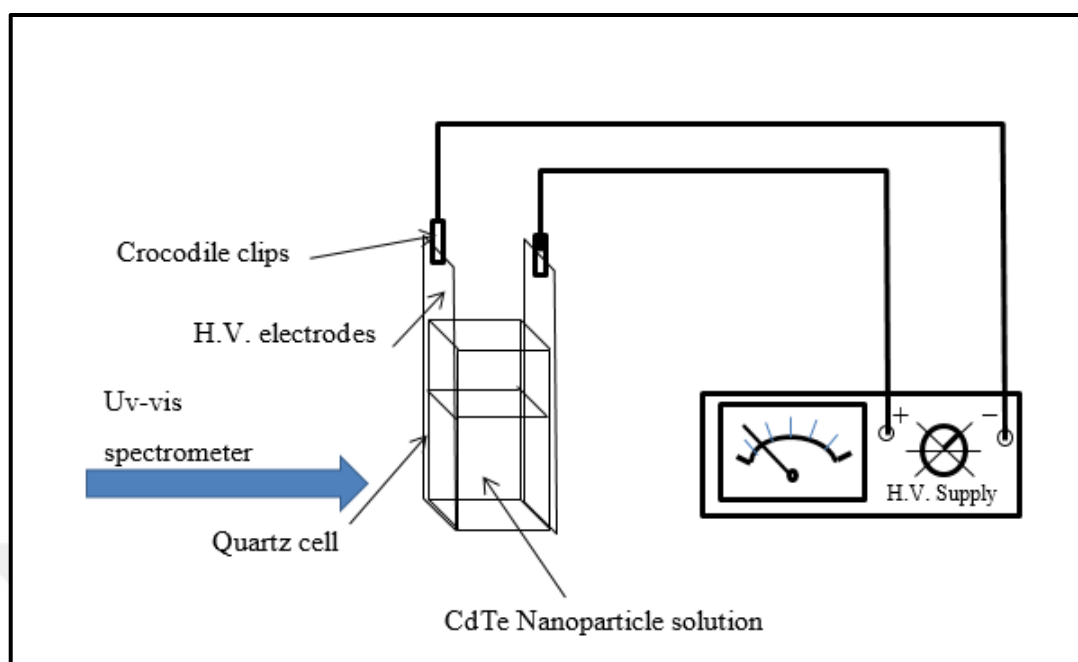


Figure 6.46. Illustration of electrical connections to the aqueous solution samples.

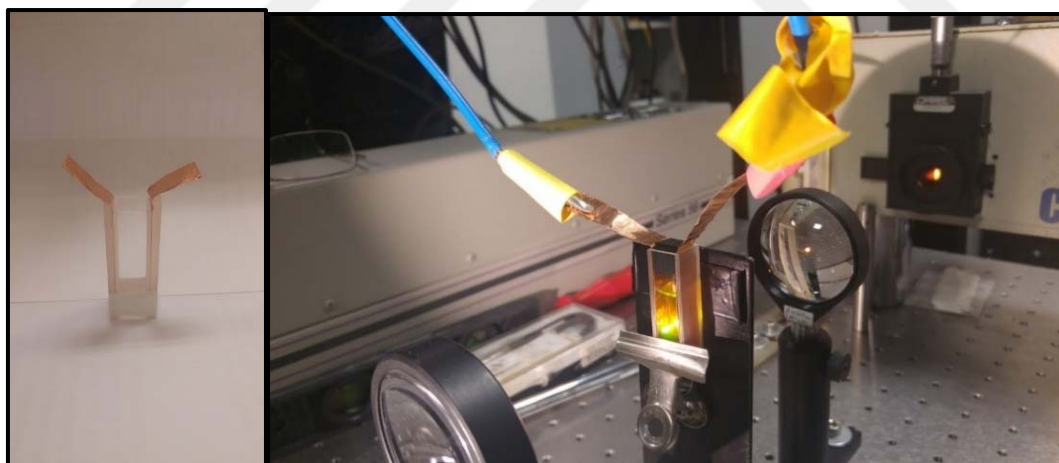


Figure 6.47. Picture of quartz tube and electro-absorption measurement set up for solution samples.

From the absorption spectra the bandgaps ( $E_g$ ) of all samples were determined with and without field. Table 6.7 shows the annealing time, band gap energies, radius and measurement uncertainties.



Table 6.7. Band gap energies and radius of different samples

Quantum dot Sample	Annealing Time	Colour	Band Gap (eV)	Radius (nm)
Solution Sample 1	15 min	yellow	2.552( $\pm$ 0.005)	1.925( $\pm$ 0.002)
Solution Sample 3	2 hours	orange-yellow	2.231( $\pm$ 0.007)	2.285( $\pm$ 0.010)
Solution Sample 4	3 hours	orange	2.195( $\pm$ 0.009)	2.315( $\pm$ 0.010)
Solution Sample 6	5 hours	orange-red	2.155( $\pm$ 0.006)	2.395( $\pm$ 0.010)
Solution Sample 7	5 hours 15 minutes	red	2.145( $\pm$ 0.005)	2.325( $\pm$ 0.007)
Solid Sample 1	3 hours	orange	2.563( $\pm$ 0.009)	1.920( $\pm$ 0.007)
Solid Sample 2	8 hours	brown	2.237( $\pm$ 0.006)	2.360( $\pm$ 0.007)
Solid Sample 3	12 hours	yellow	2.109( $\pm$ 0.006)	2.580( $\pm$ 0.012)

As a result of quantum confinement, the band gap of the CdTe semiconductor nanocrystal QDs became smaller with increasing size. This shows that, the band gap of the semiconductor nanocrystal QDs can be tuned by changing the size of the particle.

#### 6.4.1. Solid Sample 1: 3 Hours Annealed

Increasing measurements were taken from 0V to 5500 V, decreasing measurements were taken from 5500 V to 0 V respectively. Band gap energies,  $E_g$ , were calculated from the direct extrapolation of the absorbance from Tauc Plot discussed in Section 5.1. The real and the imaginary part of the electric permittivity of the samples were calculated from Hilbert transform properties of the Kramers-Krönig relations and given in Table 6.8. The real part of the permittivity was used to calculate the particle size. Radius calculations were determined from Brus equation also described in the same section. Tables 6.8 and 6.9 represent band gap energies produced from Figures 6.48 to 6.71 and radius under electric field variation with dielectric permittivity values.

Table 6.8. Band gap energies and size of solid sample under different electric fields.

<b>SOLID SAMPLE 1: 3 HOURS ANNEALED</b>				
<b>Electric Field (V)</b>	<b>Band Gap/increasing (eV)</b>	<b>Radius/increasing (nm)</b>	<b><math>\epsilon_{real}</math></b>	<b><math>\epsilon_{imaginary}</math></b>
0	2.563	1.990	105.5	50.4
1000	2.547	2.000		
2000	2.481	2.060		
2500	2.474	2.070		
2750	2.430	2.120		
3500	2.421	2.130		
5500	2.394	2.160		

The repeatability measurements were obtained with the same method using the same experimental set-up within short time interval. It was generally observed from repeatability measurements that all samples returned to their initial values after the application of the electric field. From Figures 6.48 to 6.59 it can be seen that band gap energies were decreasing with field and the radius of the QD particles were increasing linearly. Summary of these calculations were reported below in Table 6.9.

Table 6.9. Repeatability measurement band gap energies and size of solid sample 1 under different electric field.

<b>SOLID SAMPLE 1 : 3 HOURS ANNEALED (REPEATABILITY MEASUREMENT)</b>				
<b>Electric Field (V)</b>	<b>Band Gap /increasing (eV)</b>	<b>Radius /increasing (nm)</b>	<b>Band Gap /decreasing (eV)</b>	<b>Radius /decreasing (nm)</b>
0	2.563	1.920	2.558	1.920
500	2.550	1.930	2.544	1.930
1000	2.534	1.940	2.526	1.950
1500	2.514	1.960	2.511	1.960
2000	2.492	1.980	2.489	1.980
2500	2.465	2.000	2.470	2.000
3000	2.463	2.010	2.459	2.010
3500	2.445	2.020	2.448	2.020
4000	2.432	2.040	2.428	2.040
4500	2.423	2.050	2.421	2.050
5000	2.410	2.060	2.413	2.060
5500	2.399	2.070	2.399	2.070

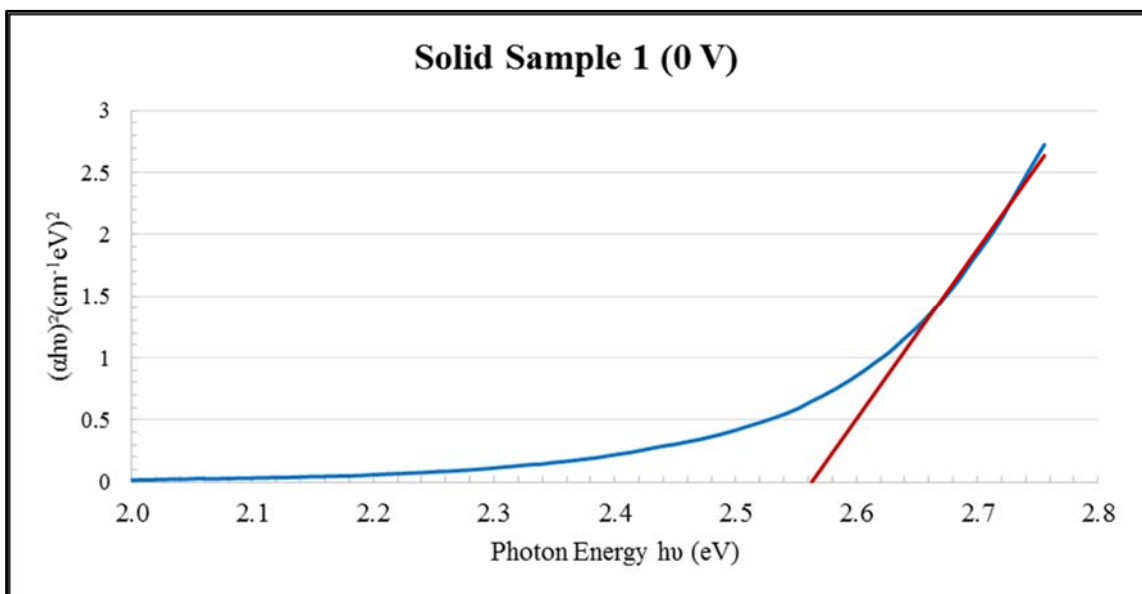


Figure 6.48. Plots of  $(\alpha h\nu)^2$  versus  $h\nu$  for Solid Sample 1 without field.

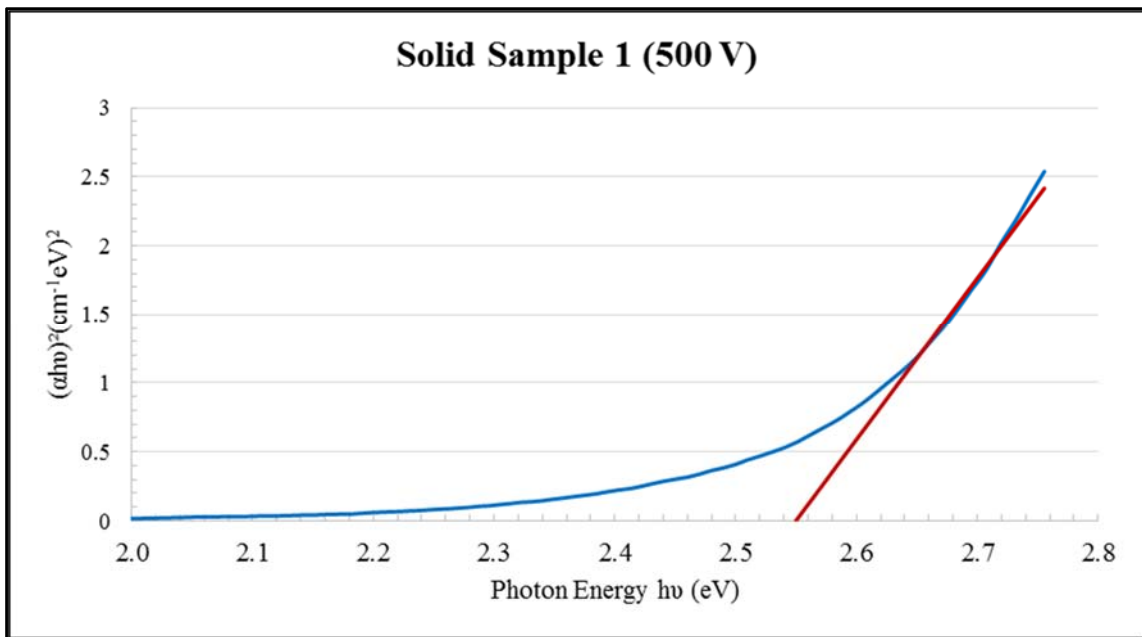


Figure 6.49. Plots of  $(\alpha h\nu)^2$  versus  $h\nu$  Solid Sample 1 at 500 V.

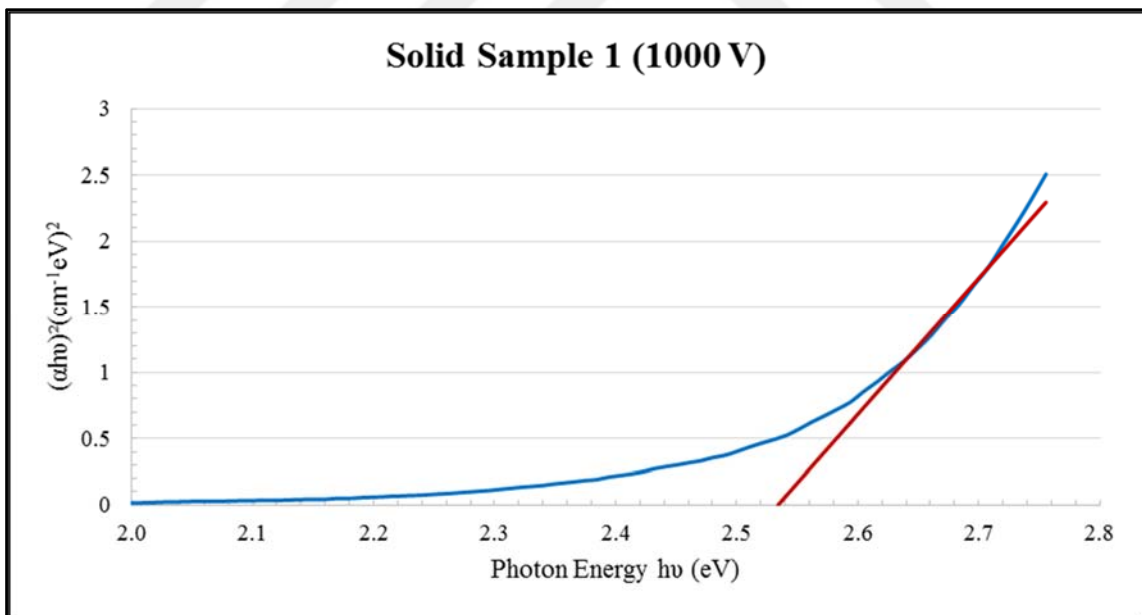


Figure 6.50. Plots of  $(\alpha h\nu)^2$  versus  $h\nu$  for Solid Sample 1 at 1000 V.

These three graphs demonstrate the band gap energy changes with application of electric field. When there is no electric field the band gap energy is 2.563 eV and when the electric field is gradually increased from 500 V to 1000 V, the band gap energies are 2.550 eV and 2.534 eV respectively.

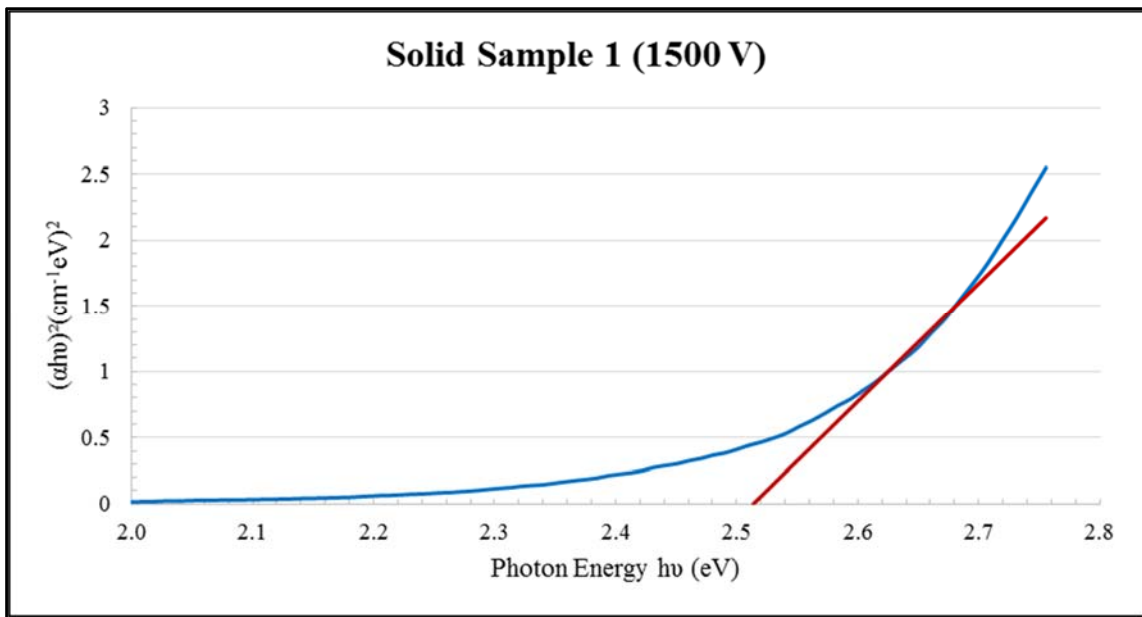


Figure 6.51. Plots of  $(\alpha h\nu)^2$  versus  $h\nu$  Solid Sample 1 at 1500 V.

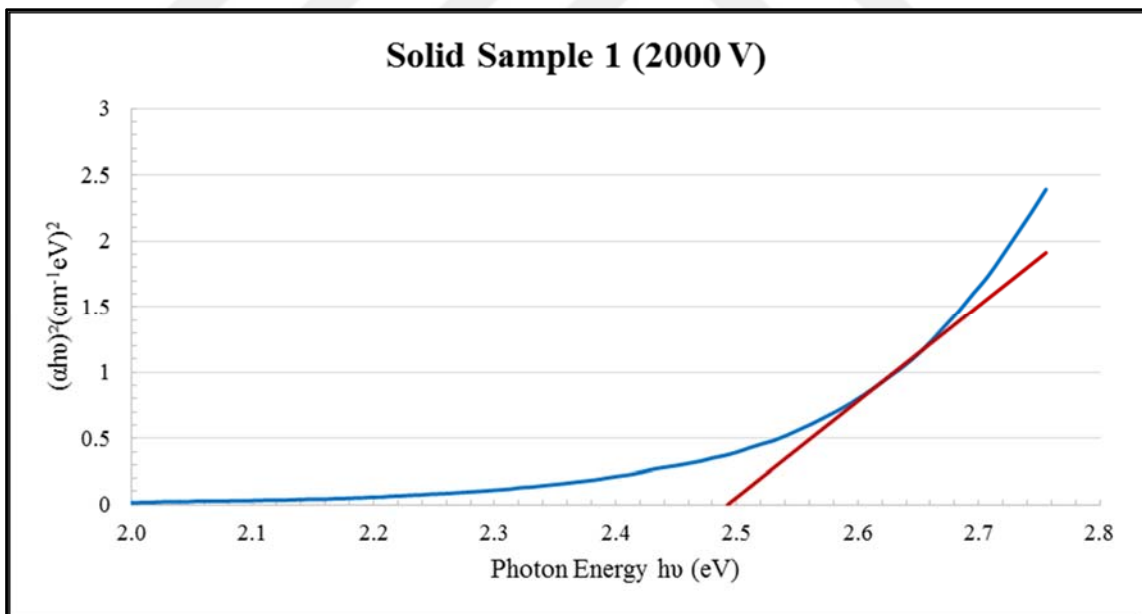


Figure 6.52. Plots of  $(\alpha h\nu)^2$  versus  $h\nu$  for Solid Sample 1 at 2000 V.

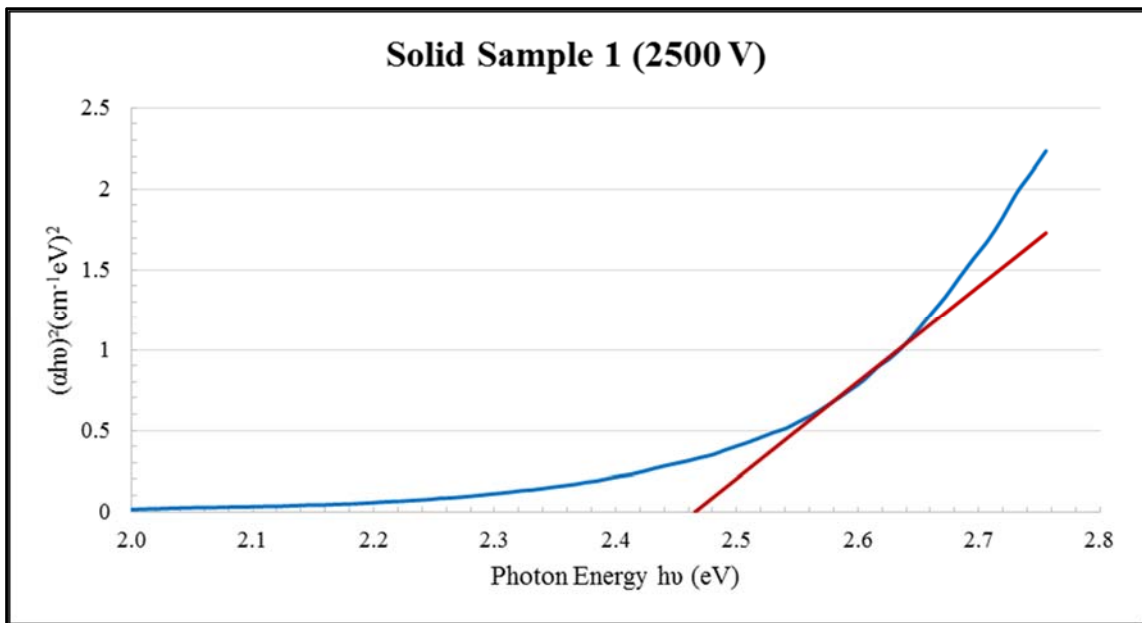


Figure 6.53. Plots of  $(\alpha h\nu)^2$  versus  $h\nu$  for Solid Sample 1 at 2500 V.

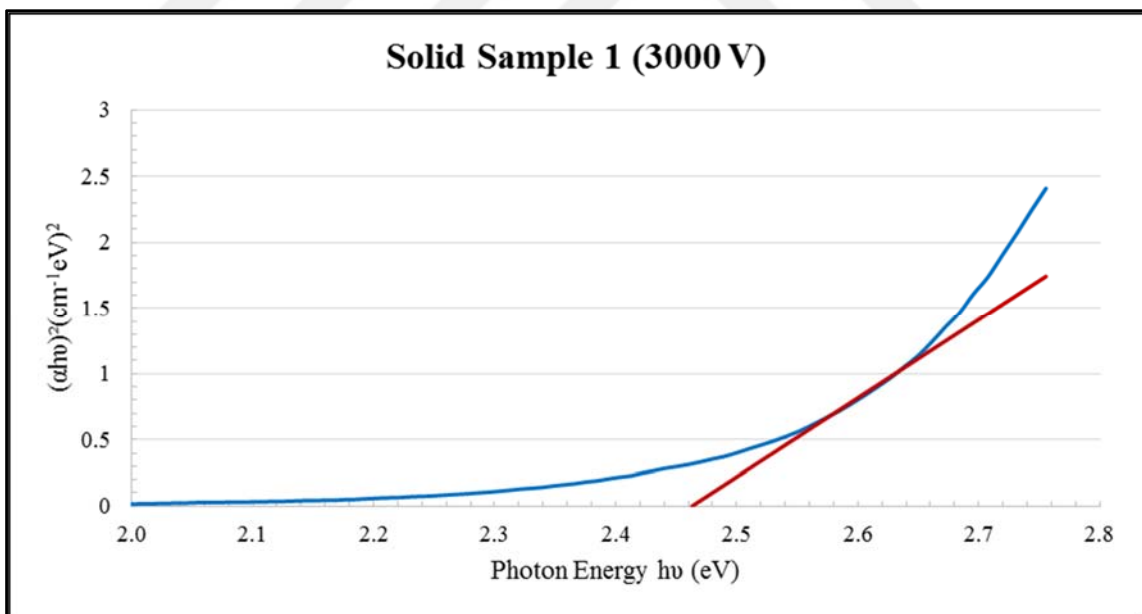


Figure 6.54. Plots of  $(\alpha h\nu)^2$  versus  $h\nu$  for Solid Sample 1 at 3000 V.

The above graphs for the solid sample 1 show the band gap energies under various electric fields. Band gap energies decrease from 2.465 eV to 2.463 eV.

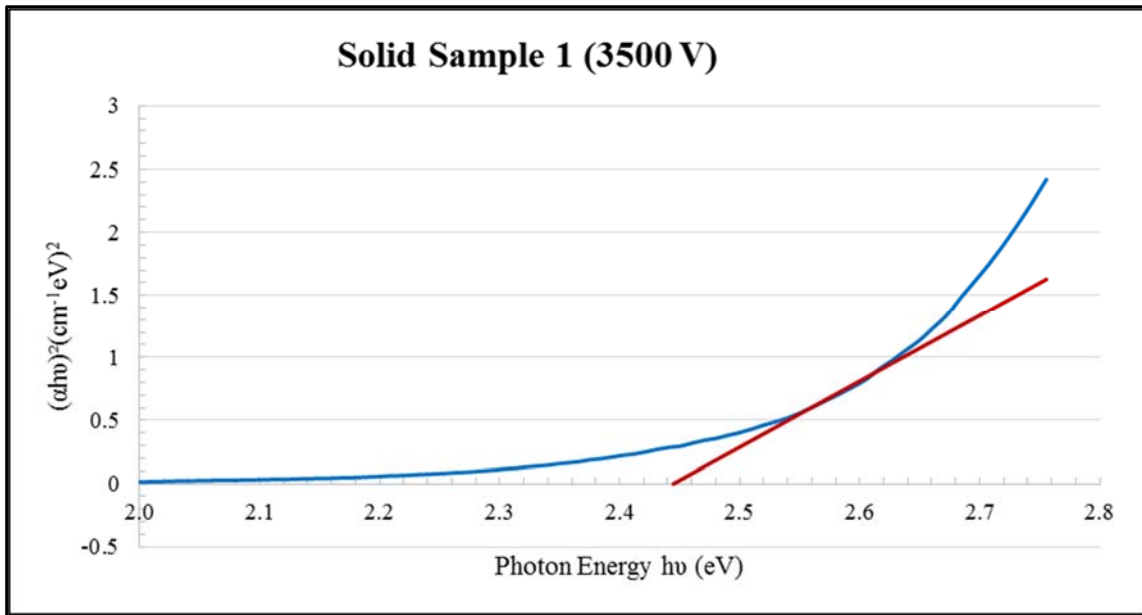


Figure 6.55. Plots of  $(\alpha h\nu)^2$  versus  $h\nu$  for Solid Sample 1 at 3500 V.

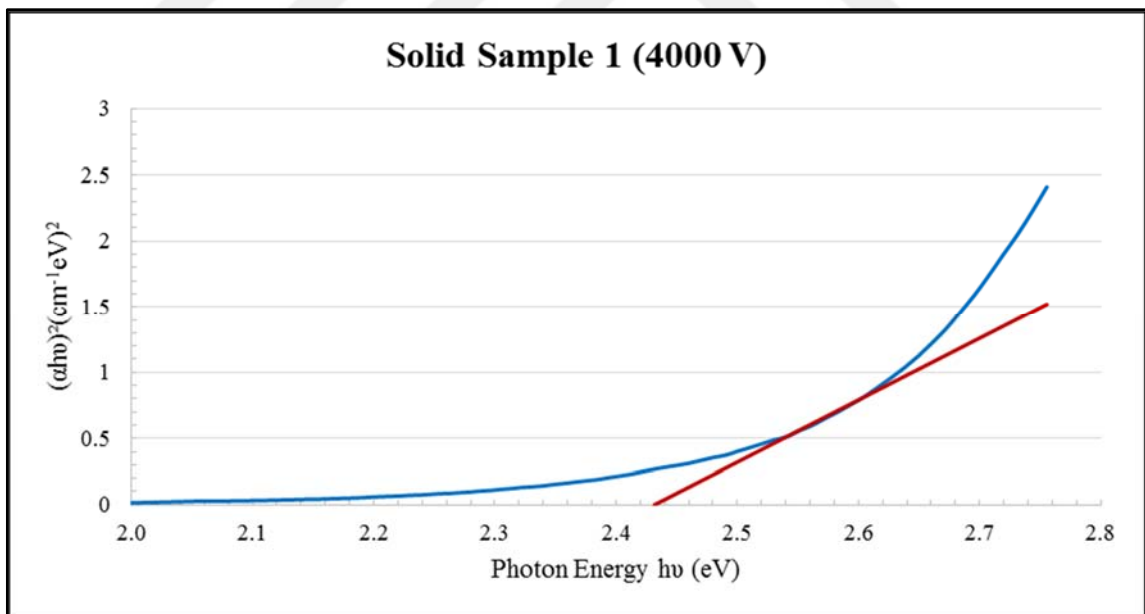


Figure 6.56. Plots of  $(\alpha h\nu)^2$  versus  $h\nu$  for Solid Sample 1 at 4000 V.

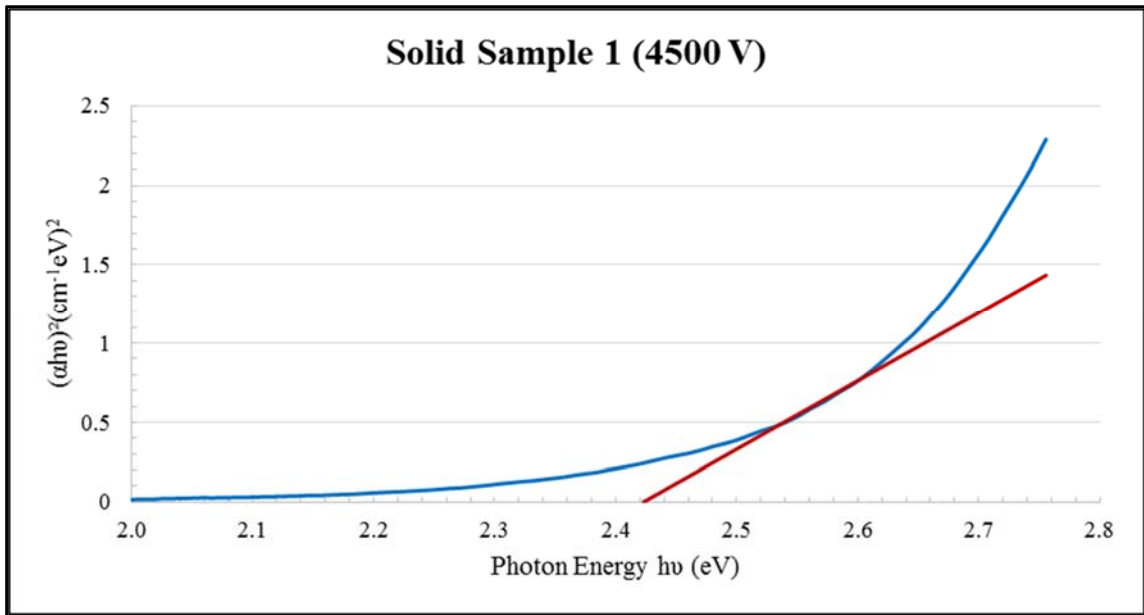


Figure 6.57. Plots of  $(\alpha h\nu)^2$  versus  $h\nu$  for Solid Sample 1 at 4500 V.

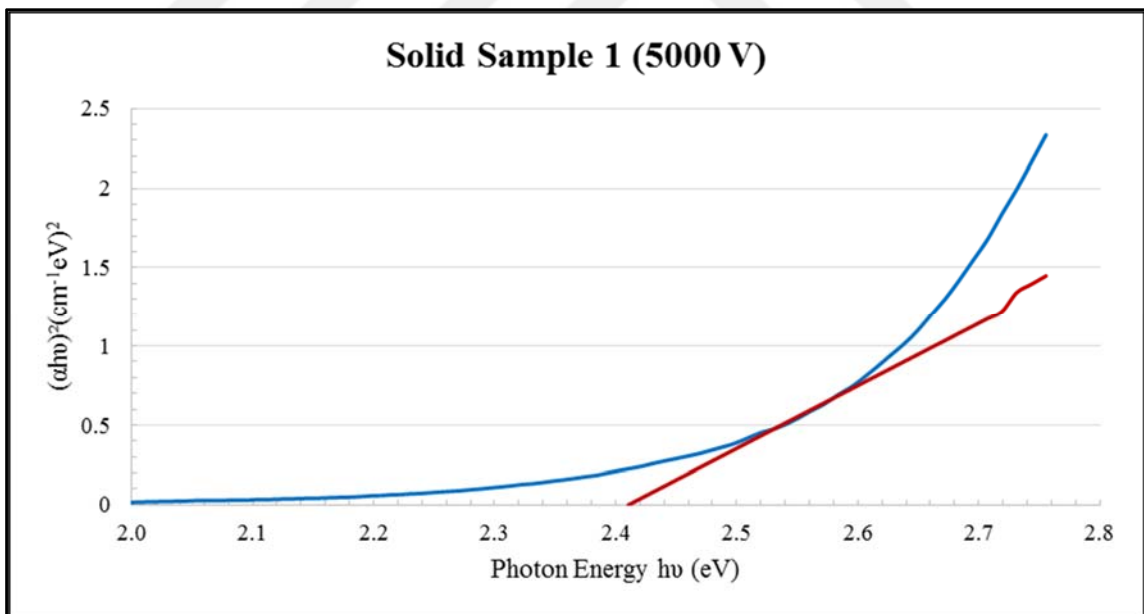


Figure 6.58. Plots of  $(\alpha h\nu)^2$  versus  $h\nu$  Solid Sample 1 at 5000 V.



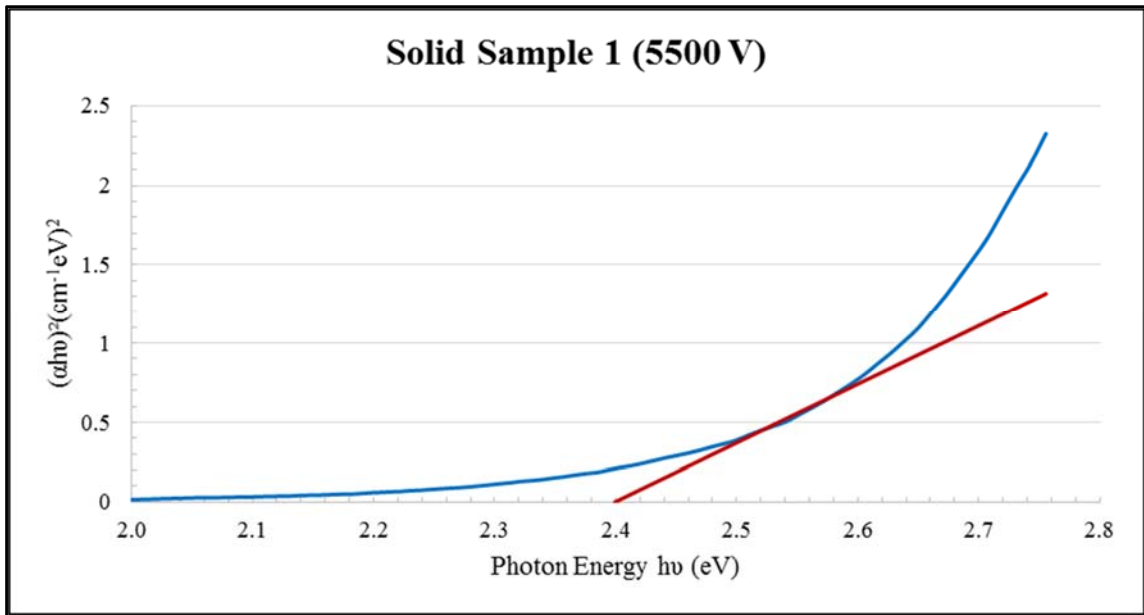


Figure 6.59. Plots of  $(\alpha h\nu)^2$  versus  $h\nu$  for Solid Sample 1 at 5500 V.

All measurements were repeated under the same conditions for repeatability of the measurement. But this time measurements were performed in decreasing order at each measurement point. Derived band gaps from Tauc Plots were shown in the graphs below.

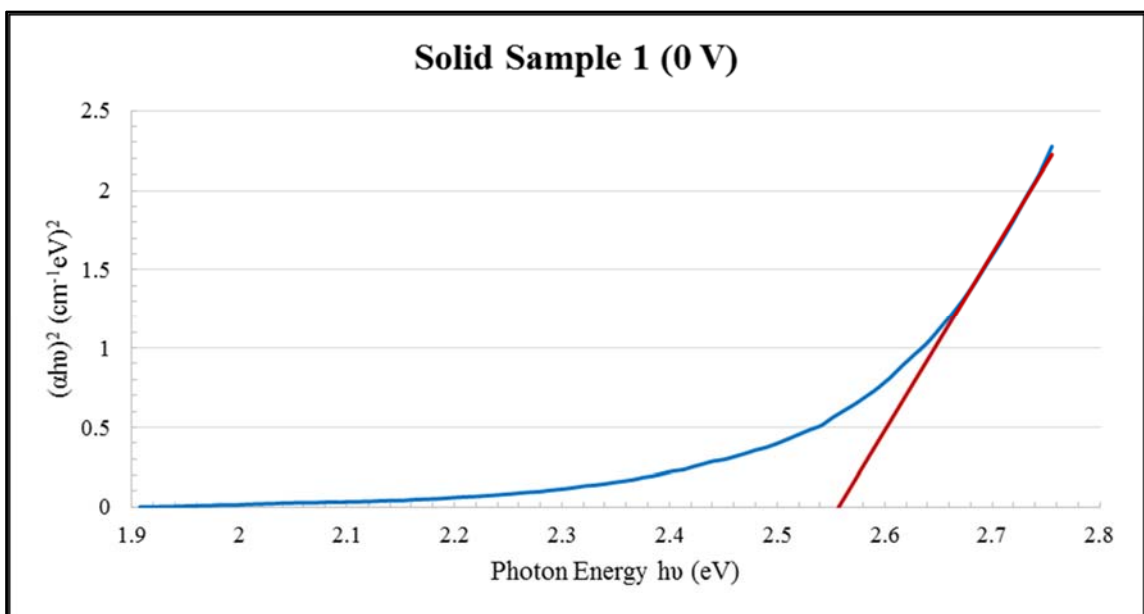


Figure 6.60. Plots of  $(\alpha h\nu)^2$  versus  $h\nu$  for Solid Sample 1 at 0 V.

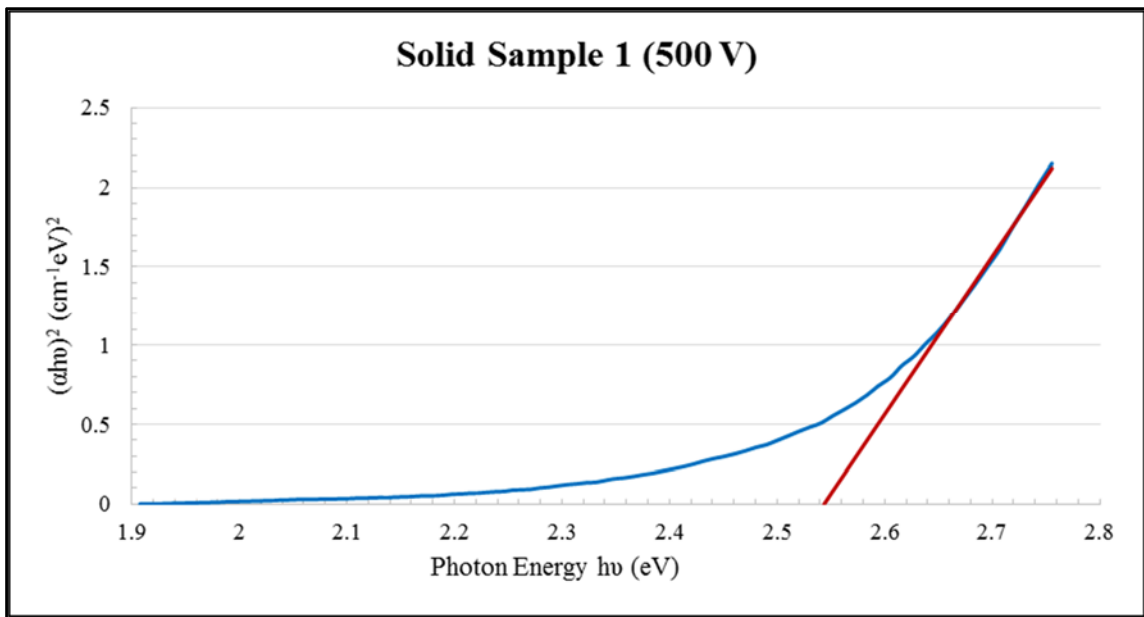


Figure 6.61. Plots of  $(\alpha h\nu)^2$  versus  $h\nu$  for Solid Sample 1 at 500 V.

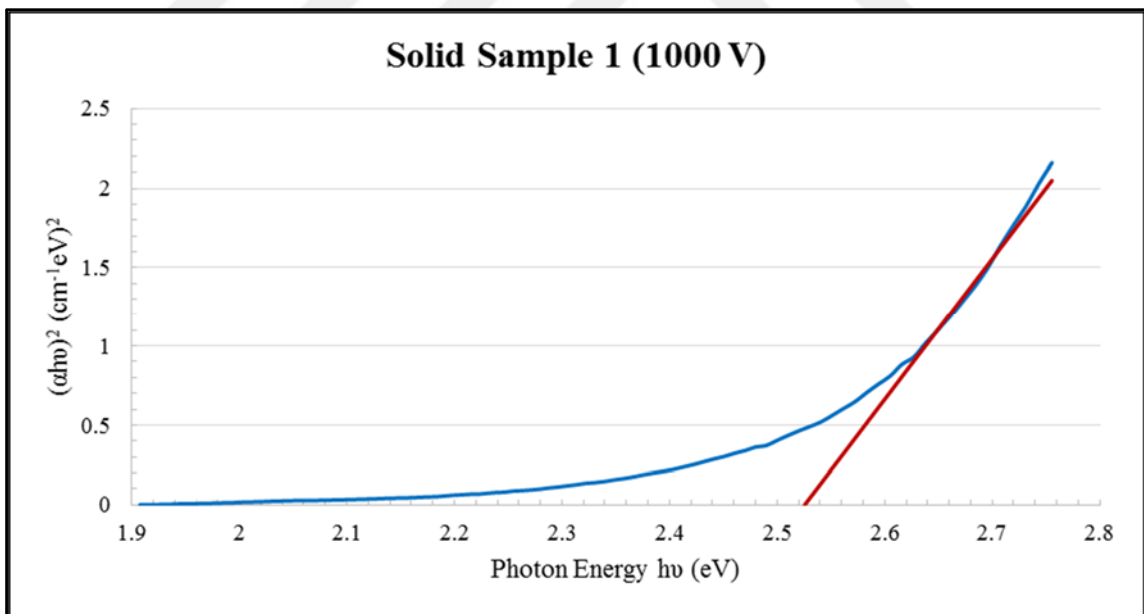


Figure 6.62. Plots of  $(\alpha h\nu)^2$  versus  $h\nu$  for Solid Sample 1 at 1000 V.

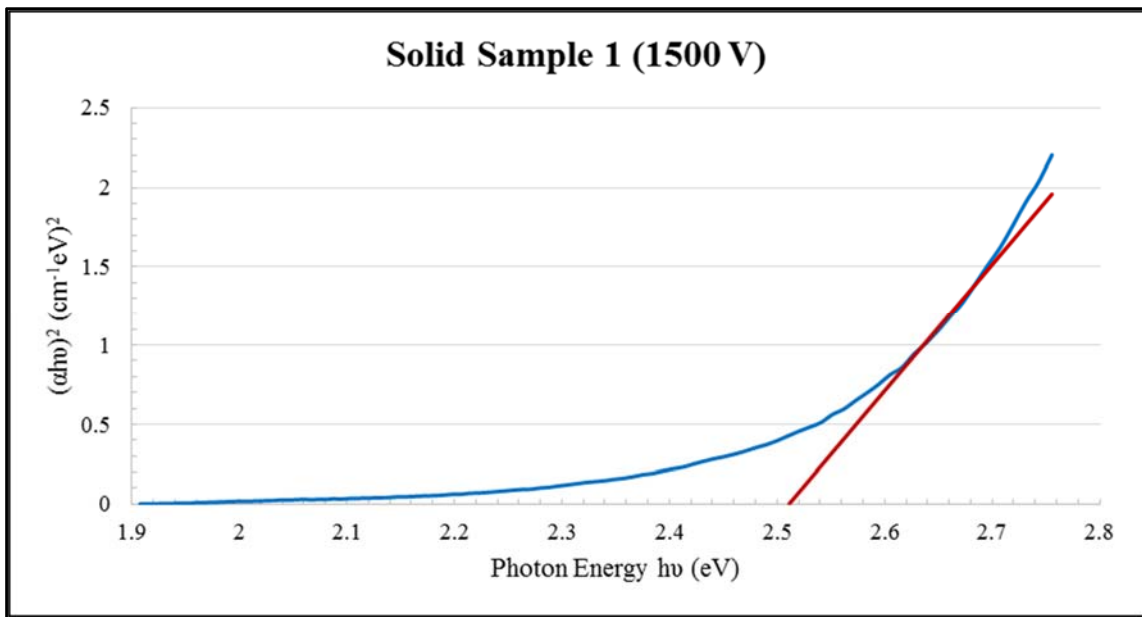


Figure 6.63. Plots of  $(\alpha h\nu)^2$  versus  $h\nu$  for Solid Sample 1 at 1500 V.

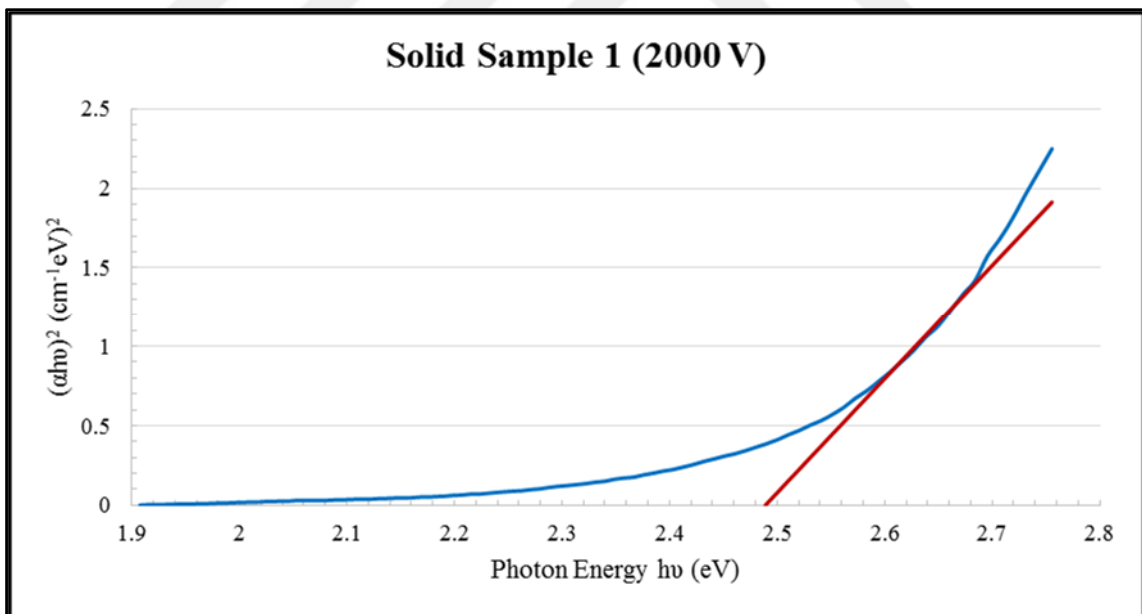


Figure 6.64. Plots of  $(\alpha h\nu)^2$  versus  $h\nu$  for Solid Sample 1 at 2000 V.

Graphs 6.60 to 6.64 are examples of data taken for solid sample 1 for repeatability measurements. Each raw data having a straight portion were extended to the x-axis to find the band gap energies. Band gap energies were estimated from 2.558 eV to 2.489 eV.

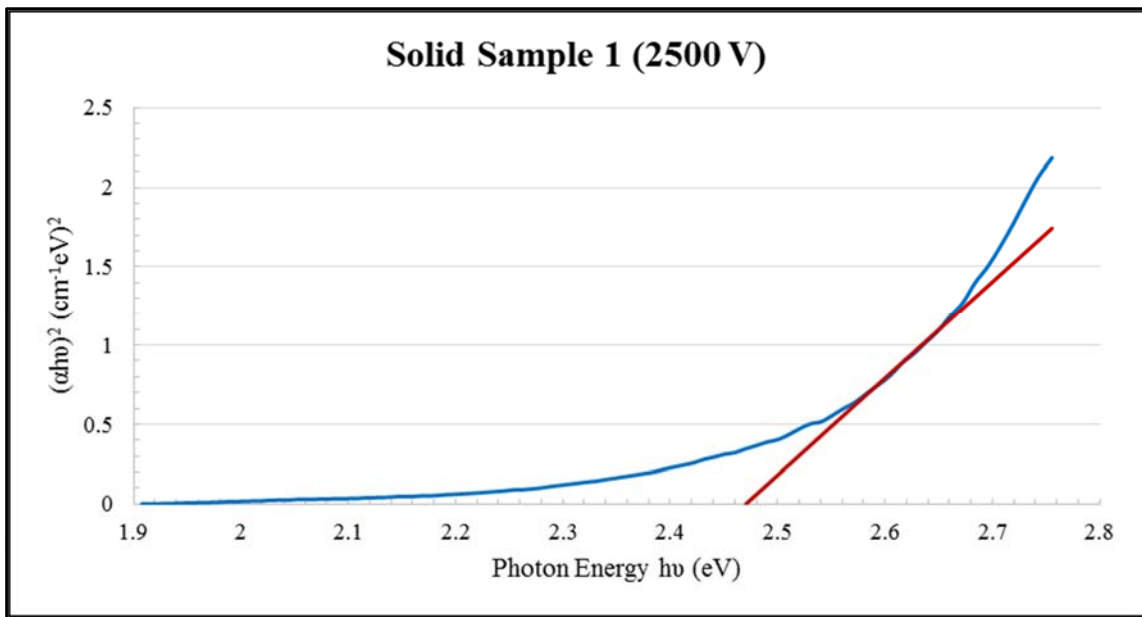


Figure 6.65. Plots of  $(\alpha h\nu)^2$  versus  $h\nu$  for Solid Sample 1 at 2500 V.

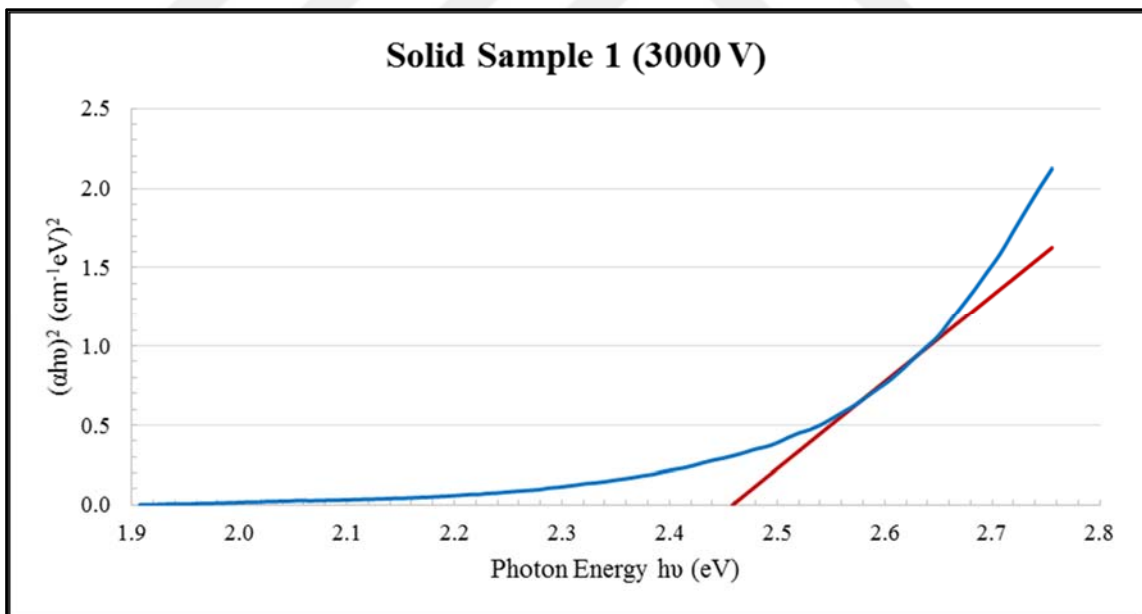


Figure 6.66. Plots of  $(\alpha h\nu)^2$  versus  $h\nu$  for Solid Sample 1 at 3000 V.

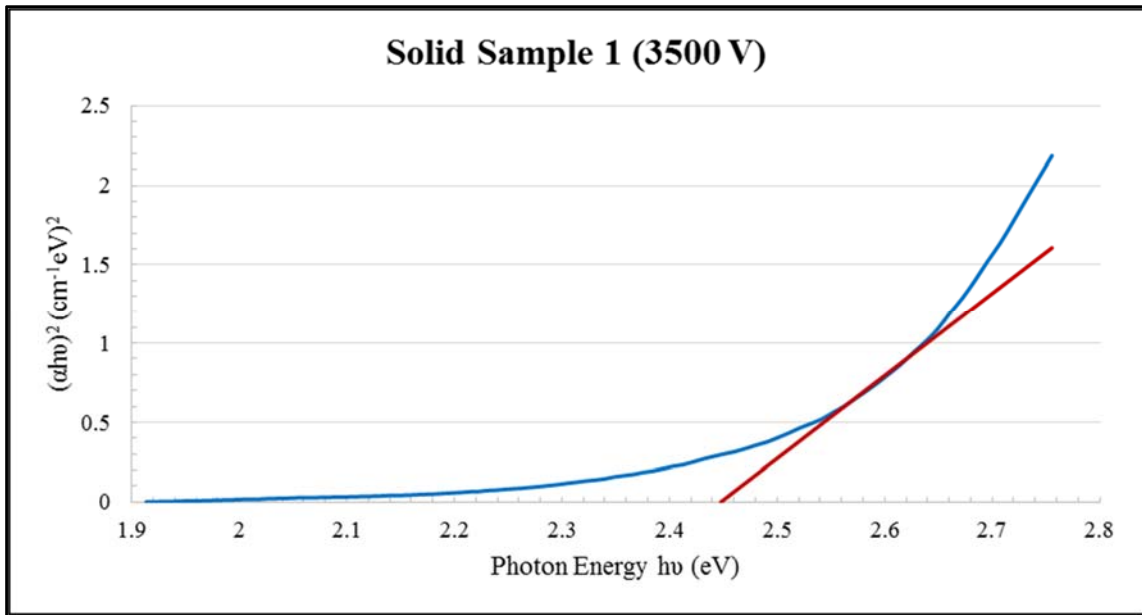


Figure 6.67. Plots of  $(\alpha h\nu)^2$  versus  $h\nu$  for Solid Sample 1 at 3500 V.

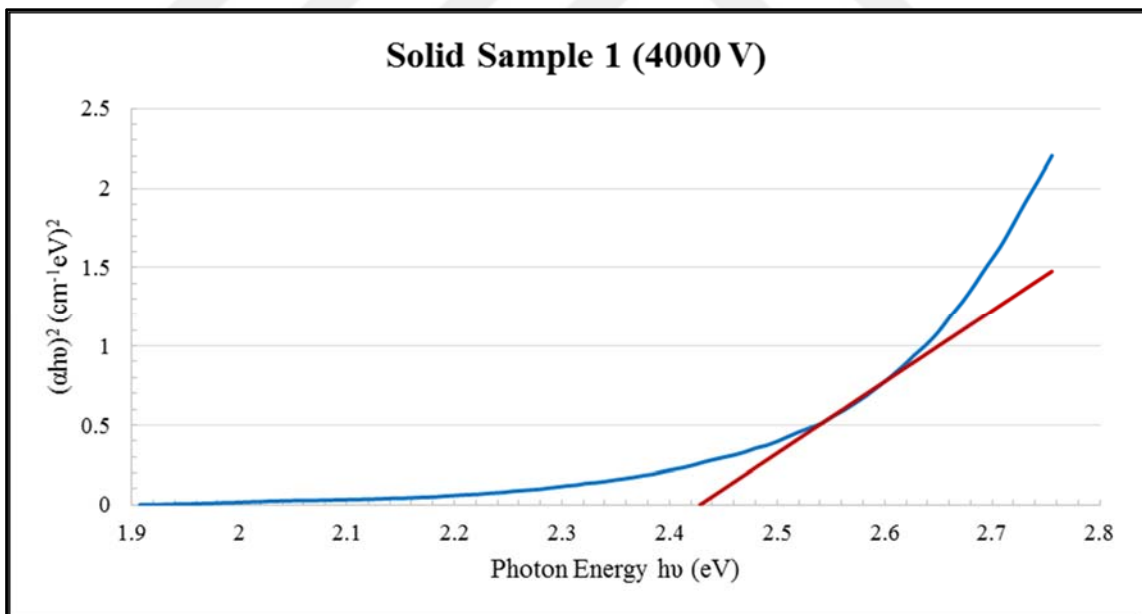


Figure 6.68. Plots of  $(\alpha h\nu)^2$  versus  $h\nu$  for Solid Sample 1 at 4000 V.

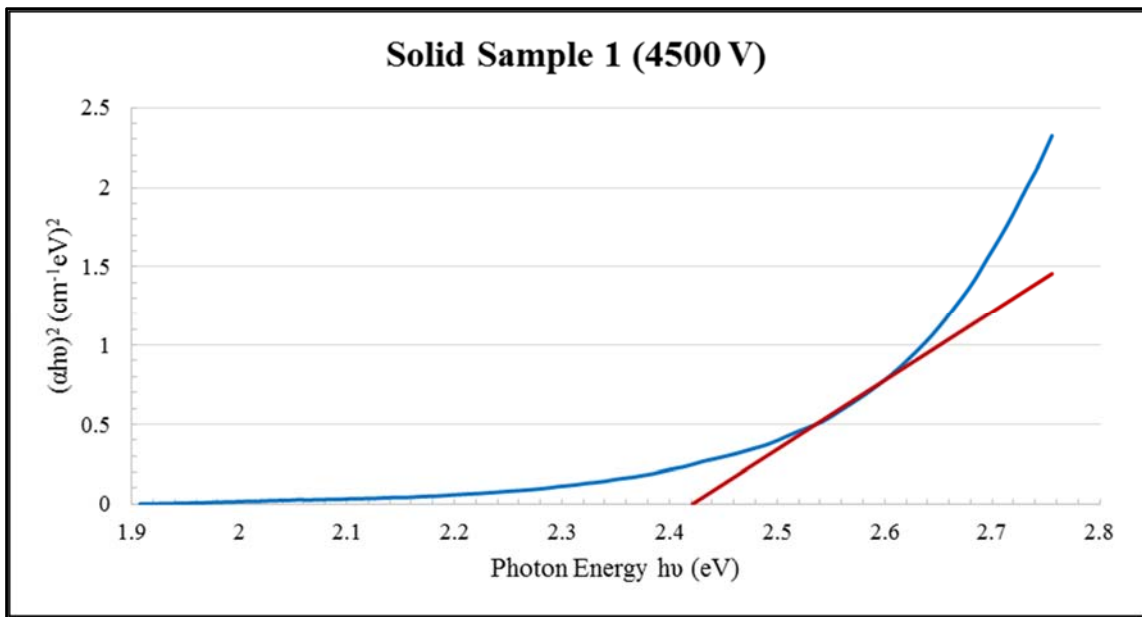


Figure 6.69. Plots of  $(\alpha h\nu)^2$  versus  $h\nu$  for Solid Sample 1 at 4500 V.

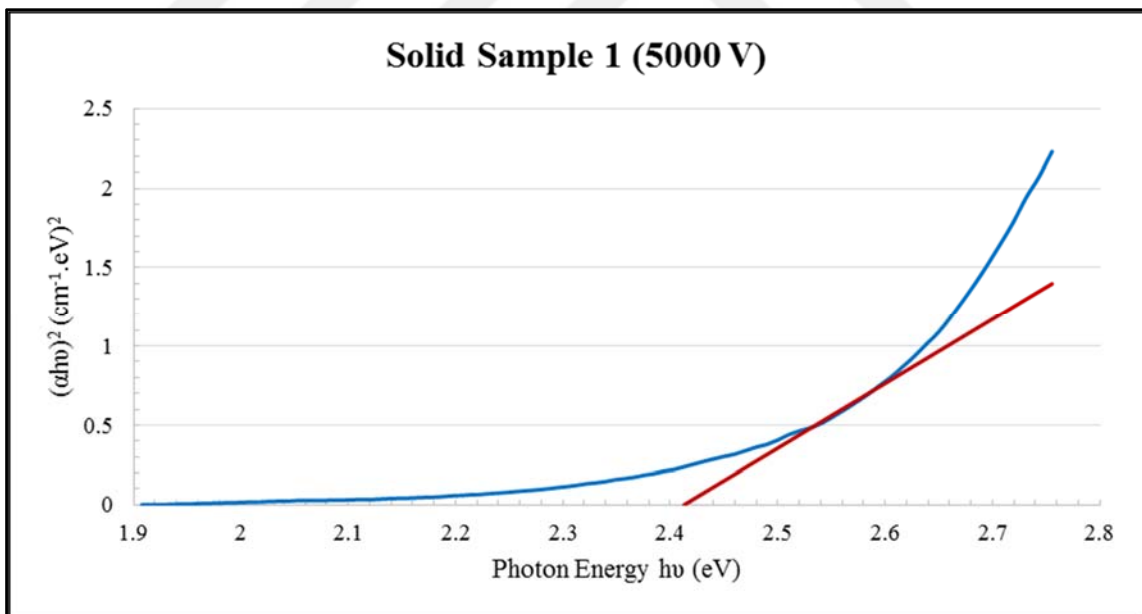


Figure 6.70. Plots of  $(\alpha h\nu)^2$  versus  $h\nu$  for Solid Sample 1 at 5000 V.

Repeatability measurements results show that, the difference between reproducible measurements is within the measurement uncertainty.

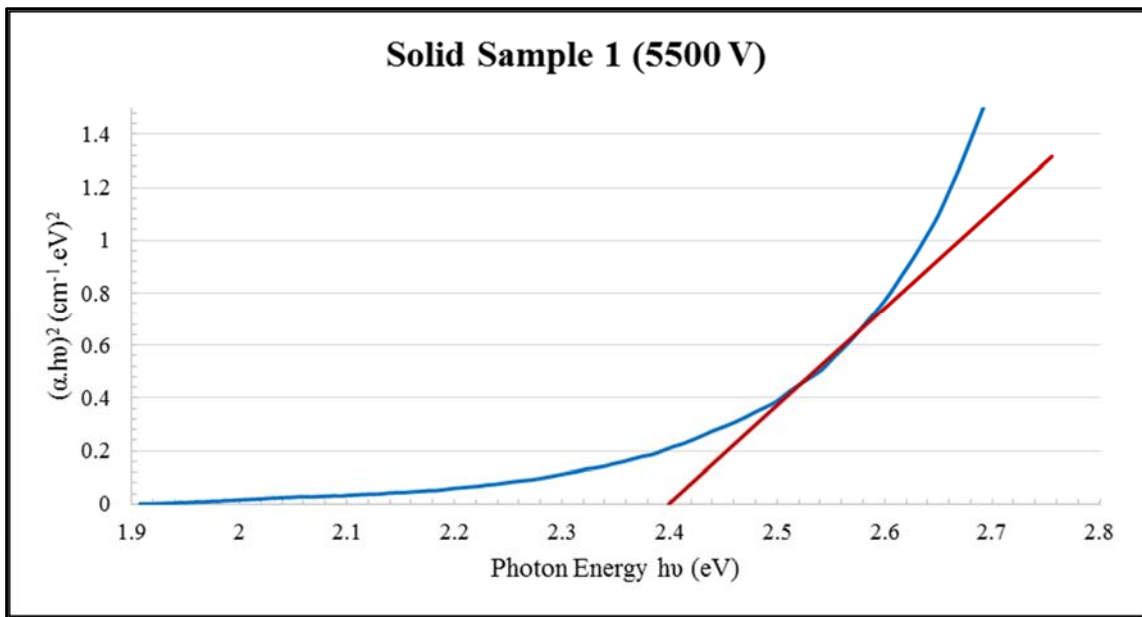


Figure 6.71. Plots of  $(\alpha h\nu)^2$  versus  $h\nu$  for Solid Sample 1 at 5500 V.

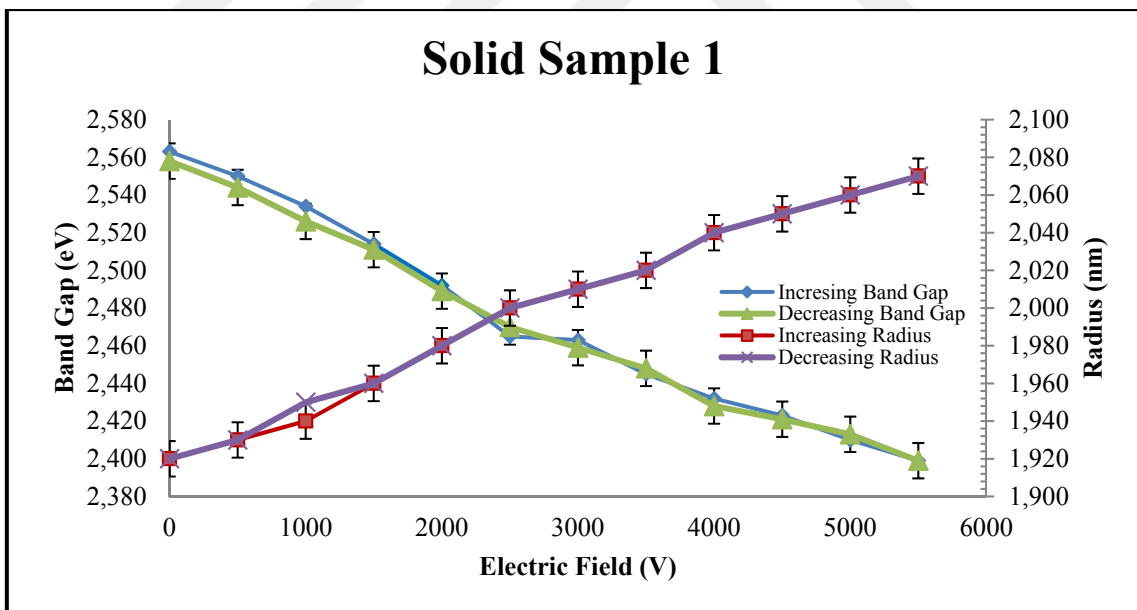


Figure 6.72. Band gap energies versus electric field of increasing and decreasing measurement with measurement uncertainty bar.

To understand the repeatability of the measurement, two sets of measurements were carried out at least twice. Firstly, the electric field was gradually increased and then the same measurement points were measured from high to low. Figure 6.73 shows the first measurements where an electric field was applied going from low to high and Figure 6.74 represents just the opposite where an electric field was applied from high to low. As can be observed from Figure 6.72, the hysteresis effect was within the measurement uncertainty which was calculated as described in Sections 5.3 and 5.4.

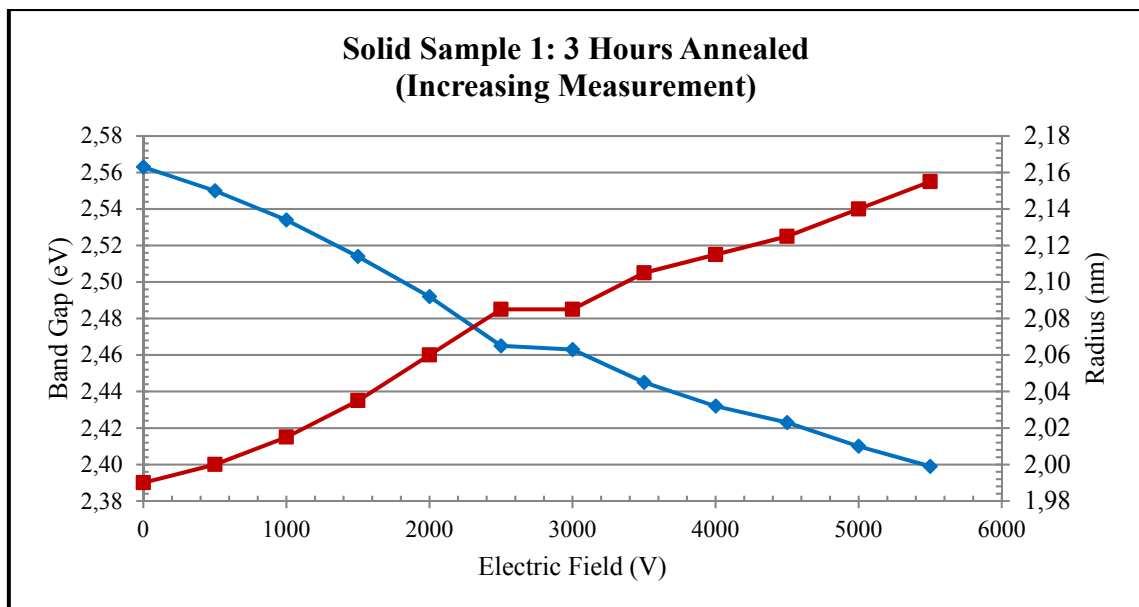


Figure 6.73. Graph of band gap and radius versus electric field.



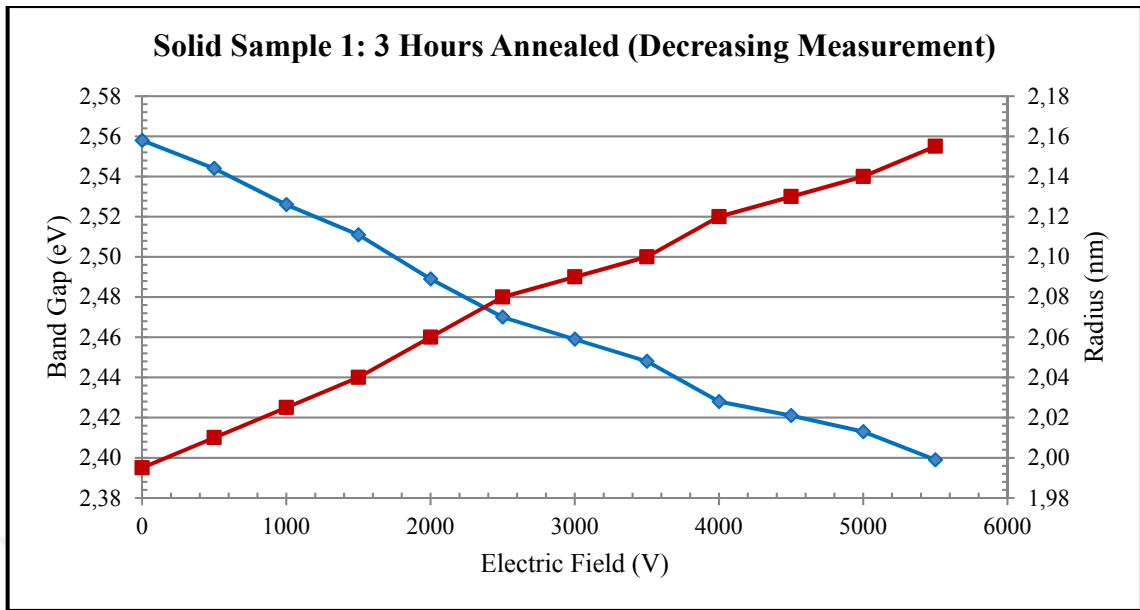


Figure 6.74. Graph of band gap and radius versus electric field after decreasing order measurement.

#### 6.4.2. Solid Sample 2: 8 Hours Annealed

For the solid sample 2 which has an 8 hours annealing process, the optical absorption spectra measurements were performed with the same method as in the previous sample. The results represented in the graph from 6.75 to 6.81 show the band gap energies decrease with the field. The particle size increases depending on the band gap energy.

Table 6.10. Band gap energies and size of solid sample under different electric field.

SOLID SAMPLE 2: 8 HOURS ANNEALED				
Electric Field (V)	Band Gap (eV)	Radius (nm)	$\epsilon_{real}$	$\epsilon_{imaginary}$
0	2.237	2.360	92.90	75.82
500	2.207	2.405		
1000	2.188	2.435		
1500	2.180	2.445		
2000	2.178	2.450		
2500	2.173	2.460		
3000	2.169	2.465		

Table 6.11. Repeatability measurement band gap energies and size of solid sample under different electric field.

Electric Field (V)	Band Gap /increasing (eV)	Radius /increasing (nm)	Band Gap /decreasing (eV)	Radius /decreasing (nm)
0	2.237	2.360	2.238	2.355
500	2.207	2.405	2.205	2.410
1000	2.188	2.435	2.191	2.430
1500	2.180	2.445	2.183	2.440
2000	2.178	2.450	2.180	2.445
2500	2.173	2.460	2.174	2.460
3000	2.169	2.465	2.169	2.465

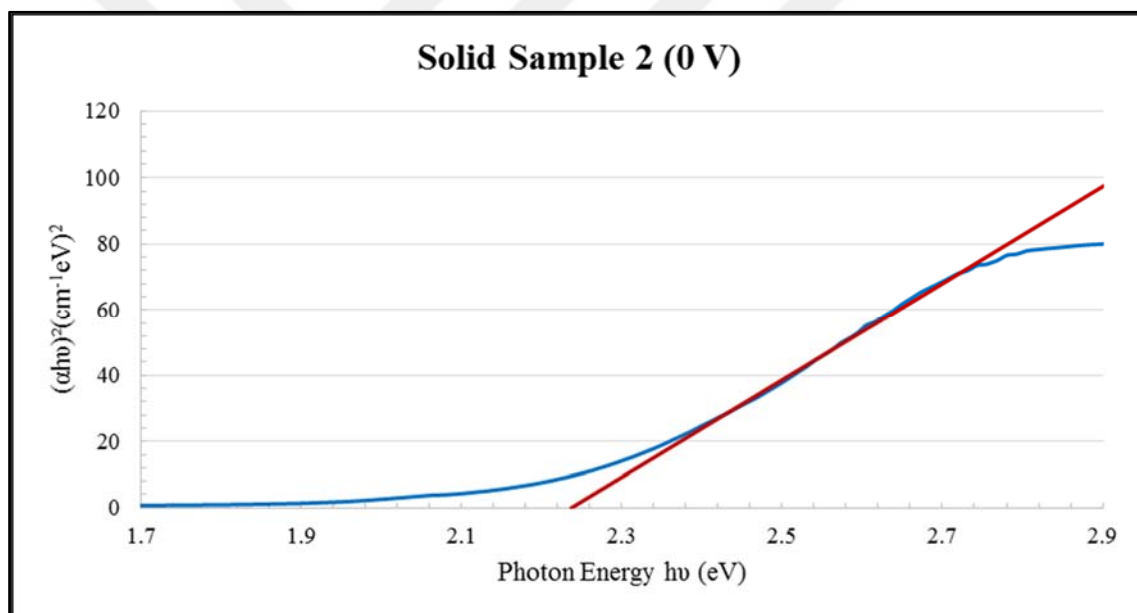


Figure 6.75. Plots of  $(\alpha h\nu)^2$  versus  $h\nu$  for Solid Sample 2 at 0 V.

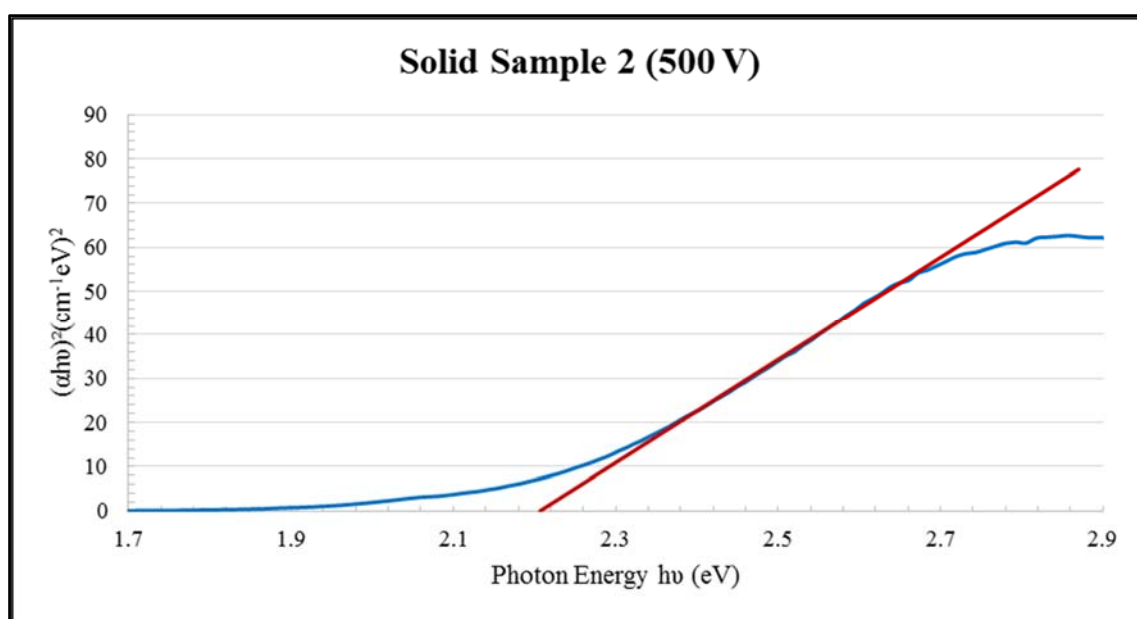


Figure 6.76. Plots of  $(\alpha h\nu)^2$  versus  $h\nu$  for Solid Sample 2 at 500 V.

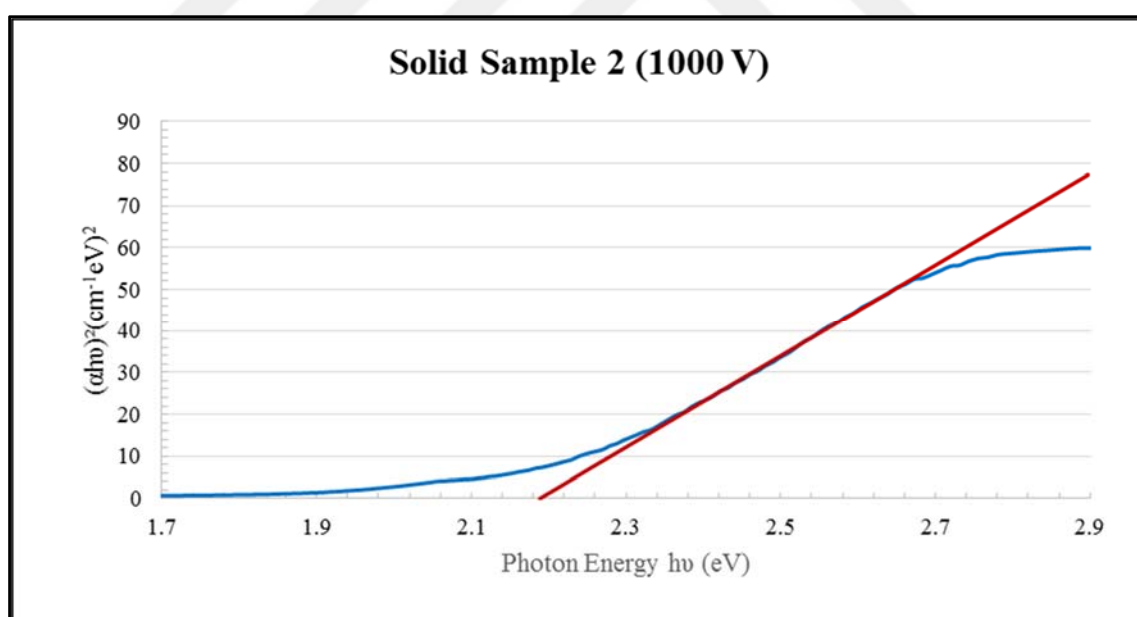


Figure 6.77. Plots of  $(\alpha h\nu)^2$  versus  $h\nu$  for Solid Sample 2 at 1000 V.

Figures 6.75, 6.76 and 6.77 show the variation of band gaps under different electric field applications. The estimated values from Tauc Plot relation were 2.237 eV for 0 V, 2.207 eV for 500 V and 2.188 eV for 1000 V.

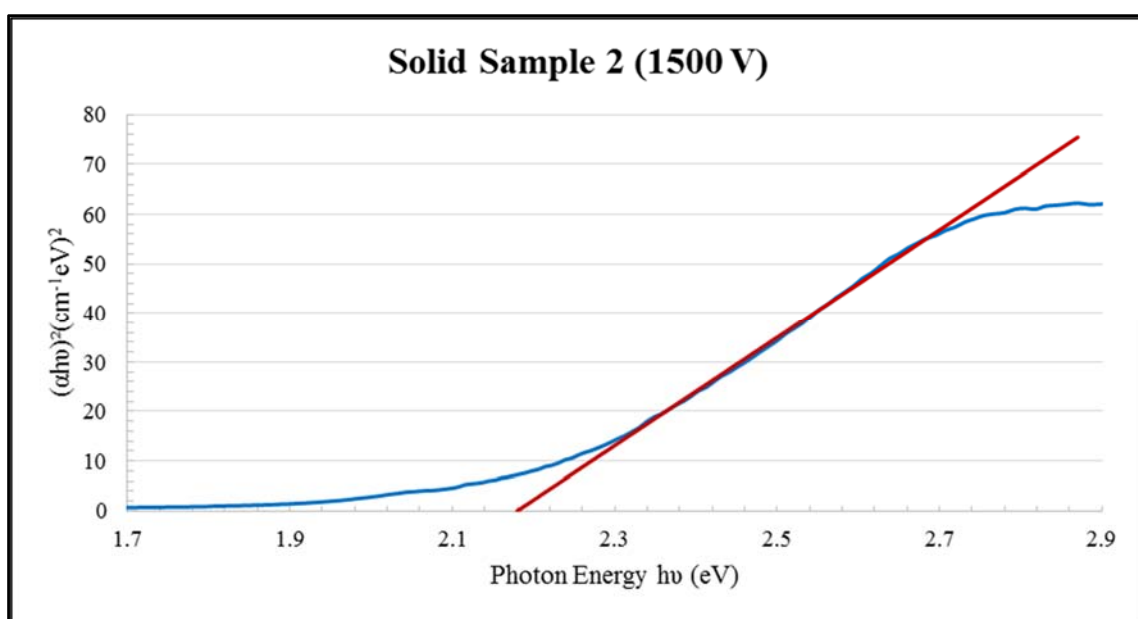


Figure 6.78. Plots of  $(\alpha h\nu)^2$  versus  $h\nu$  for Solid Sample 2 at 1500 V.

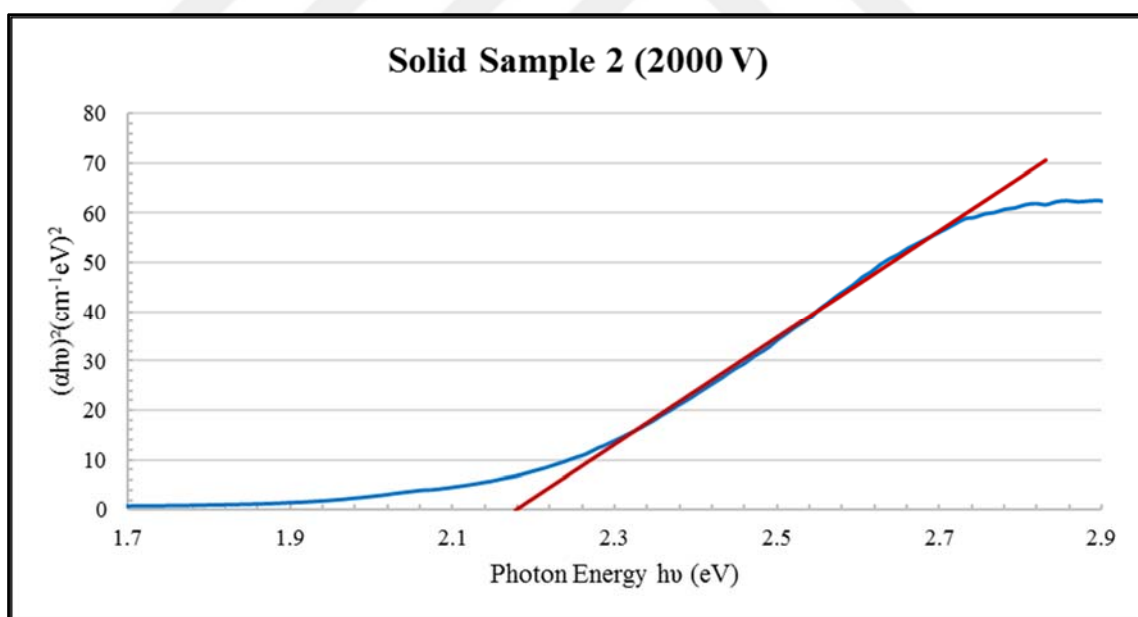


Figure 6.79. Plots of  $(\alpha h\nu)^2$  versus  $h\nu$  for a Solid Sample 2 at 2000 V.

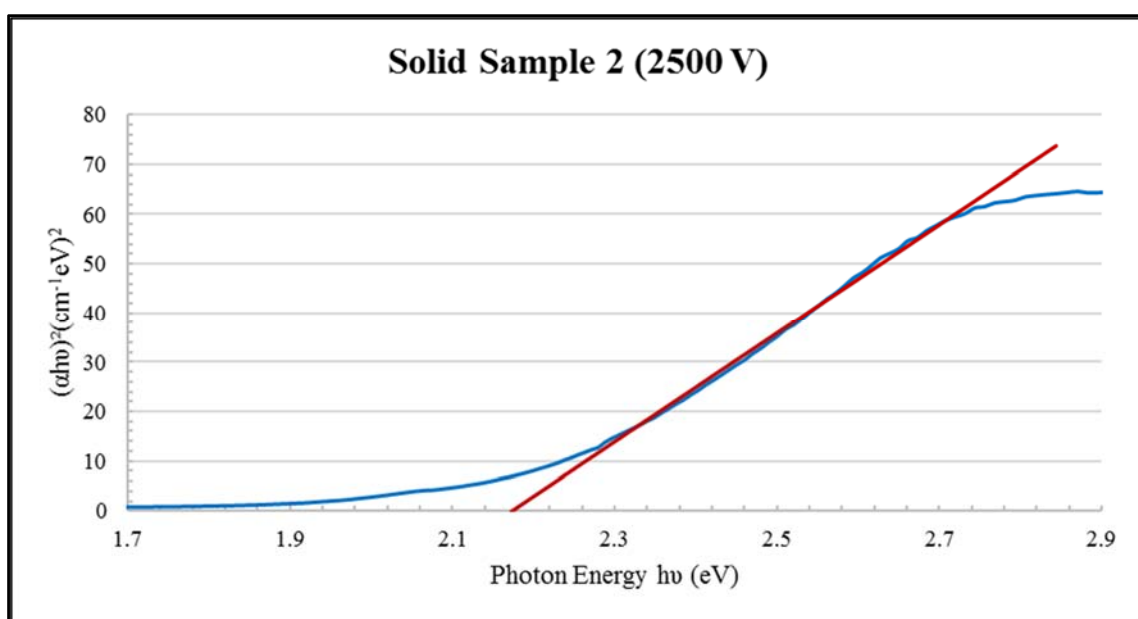


Figure 6.80. Plots of  $(\alpha h\nu)^2$  versus  $h\nu$  for Solid Sample at 2500 V.

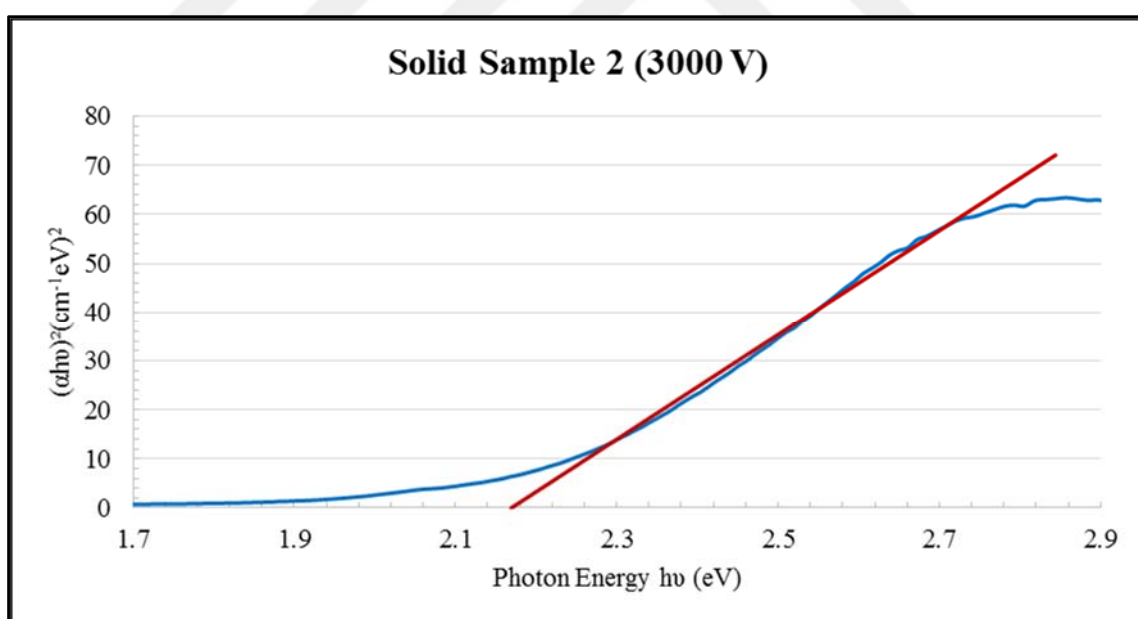


Figure 6.81. Plots of  $(\alpha h\nu)^2$  versus  $h\nu$  for Solid Sample 2 at 3000 V.

The repeatability measurements were progressively made from high to low electric field. To identify the combined uncertainty and evaluate the repeatability of the measurements, the difference between the same measurement points were calculated. For example at 1000 V, the band gap energy was found to be 2.188 eV and in the second round of the measurements the band gap energy was 2.191 eV at 1000 V. Difference between these two results is 3.0 meV. Uncertainty of the measurements were calculated according to Section 5.4 and values shown in Table 6.7 were compared with this value.

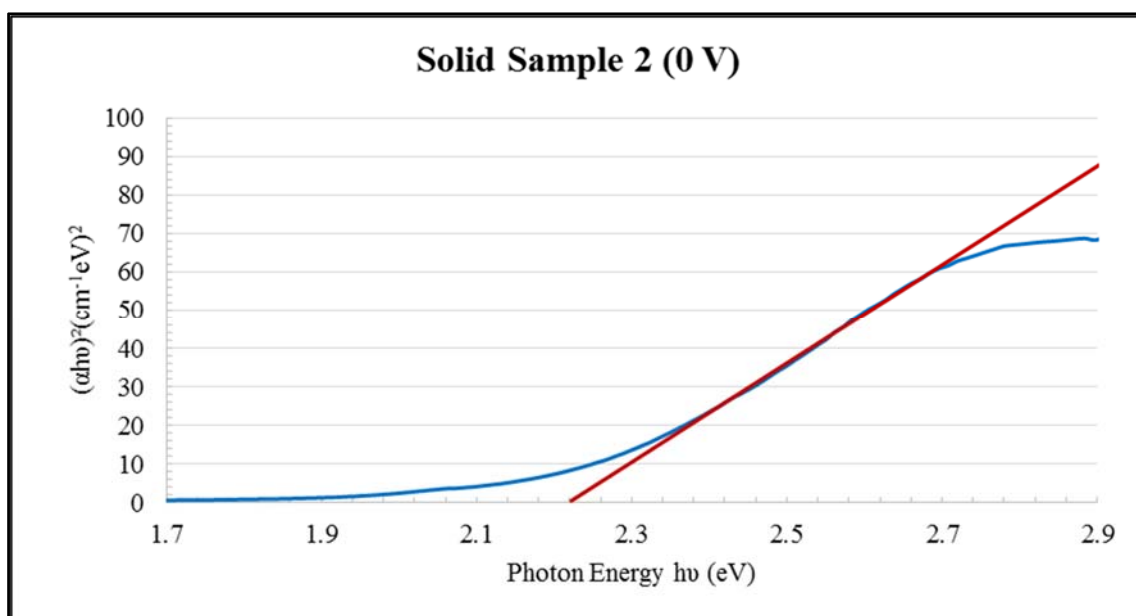


Figure 6.82. Plots of  $(\alpha h\nu)^2$  versus  $h\nu$  for Solid Sample 2 at 0 V.

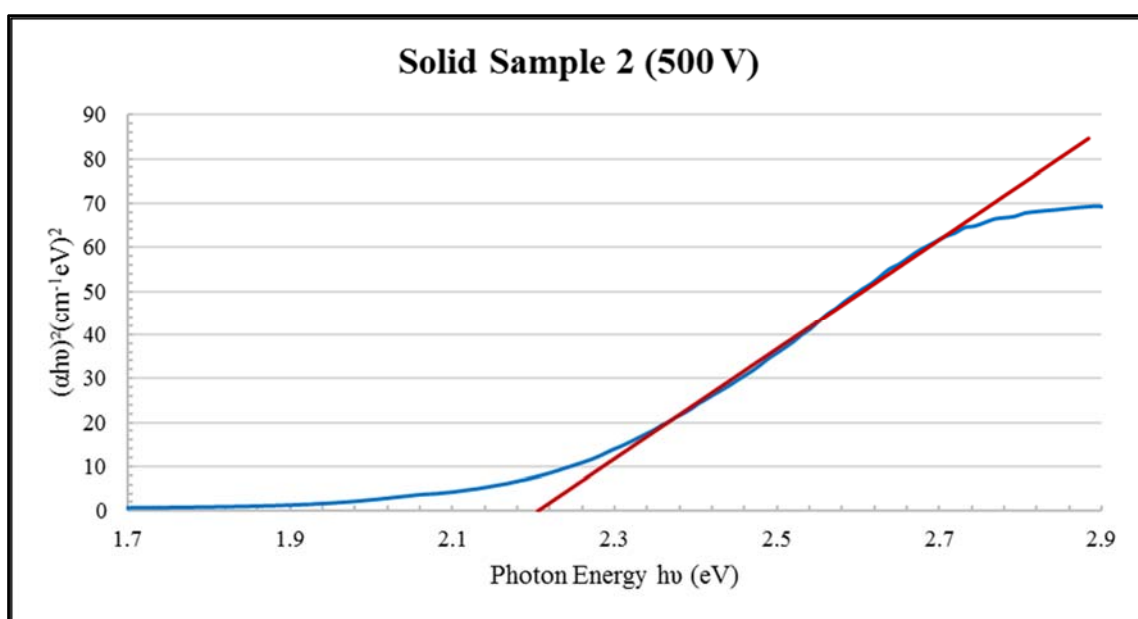


Figure 6.83. Plots of  $(\alpha h\nu)^2$  versus  $h\nu$  for Solid Sample 2 at 500 V.

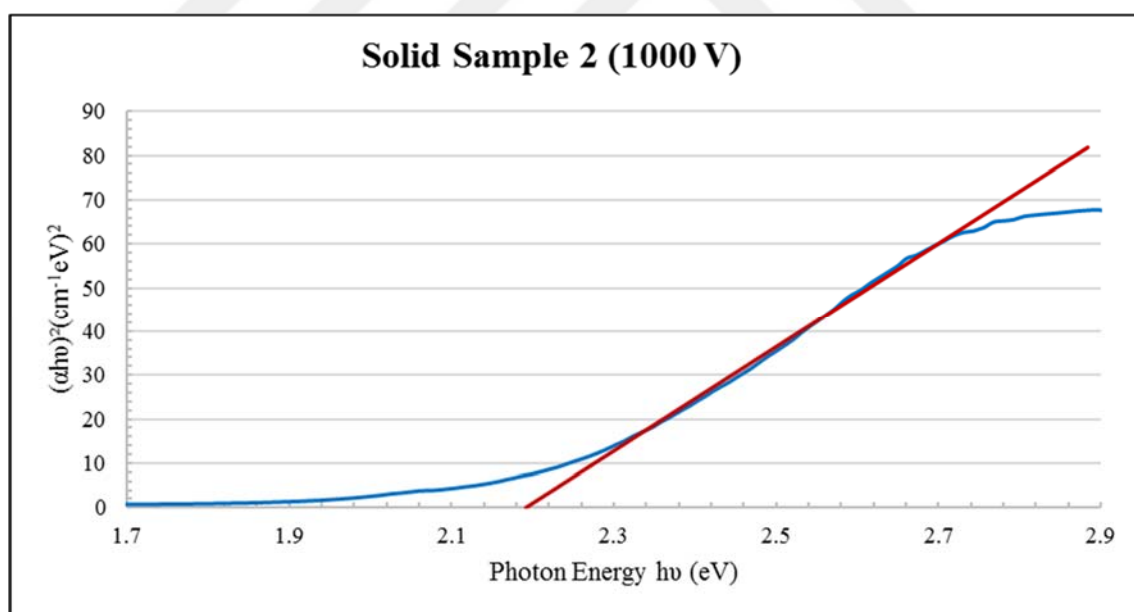


Figure 6.84. Plots of  $(\alpha h\nu)^2$  versus  $h\nu$  for Solid Sample 2 at 1000 V.

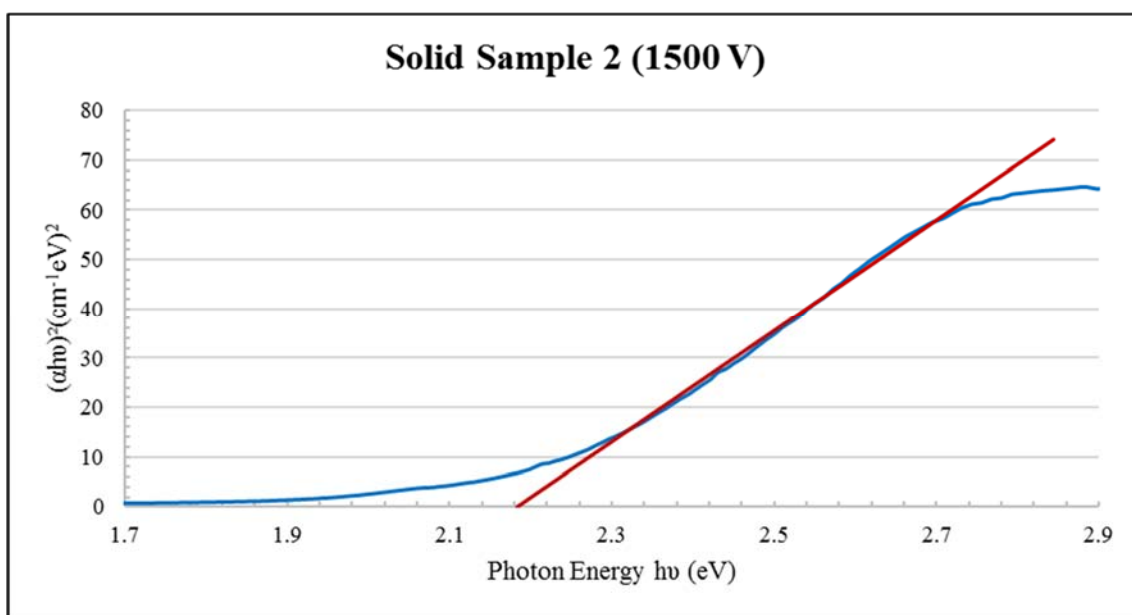


Figure 6.85. Plots of  $(\alpha h\nu)^2$  versus  $h\nu$  for Solid Sample 2 at 1500 V.

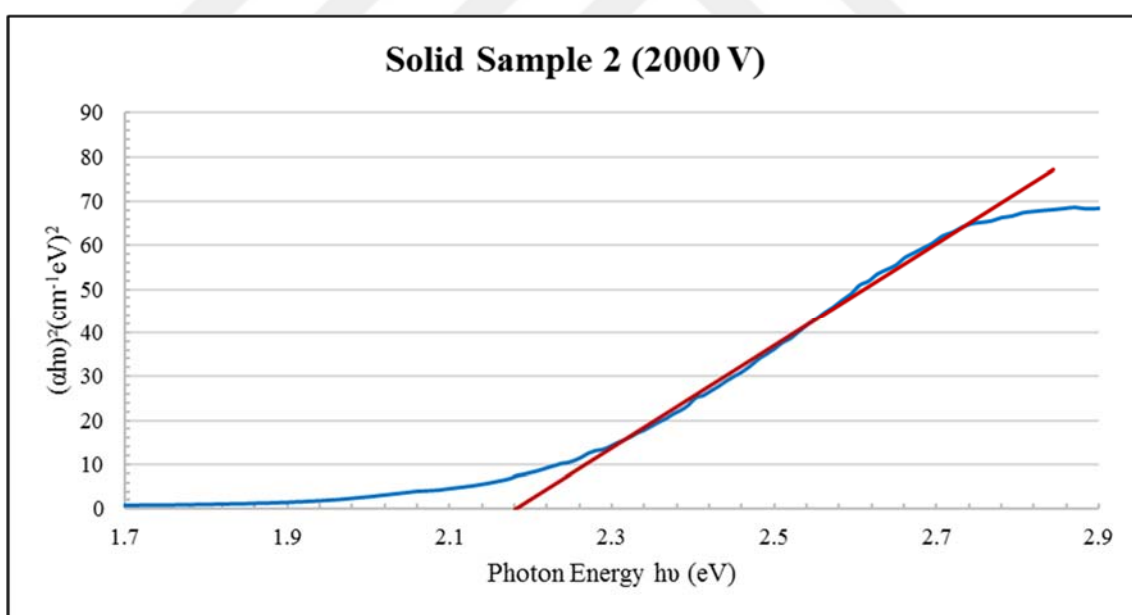


Figure 6.86. Plots of  $(\alpha h\nu)^2$  versus  $h\nu$  for Solid Sample 2 at 2000 V.

For solid sample 2, the repeatability and reproducibility measurements were performed under the same measurement conditions, and measurement uncertainty was calculated and evaluated.



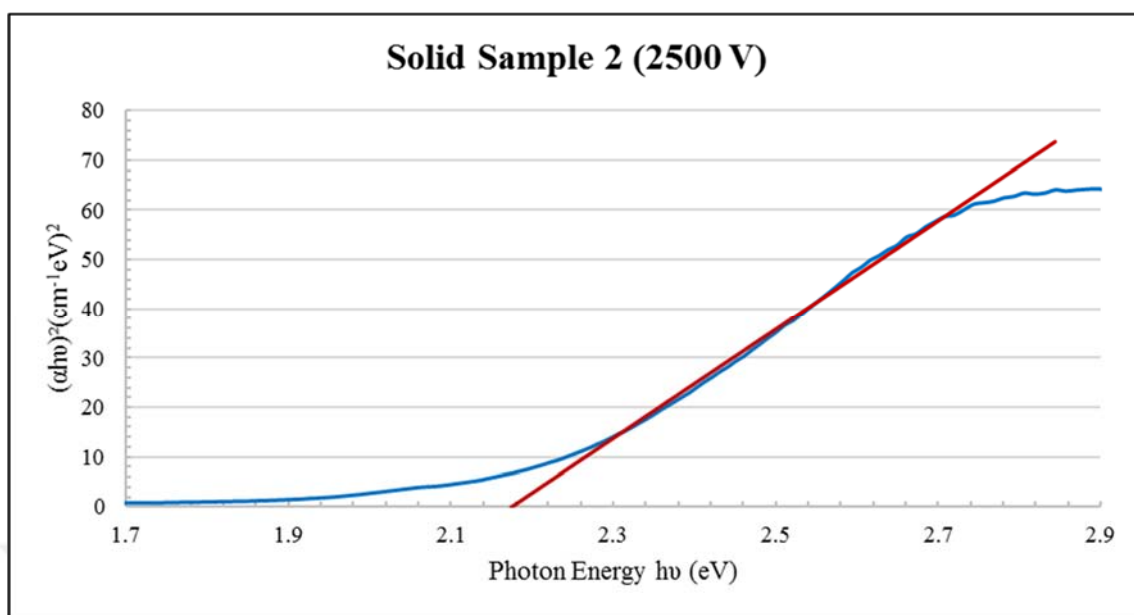


Figure 6.87. Plots of  $(\alpha h\nu)^2$  versus  $h\nu$  for Solid Sample 2 at 2500 V.

Figures 6.88 and 6.89 show the band gap energies and radius of the solid sample 2 under various electric fields.

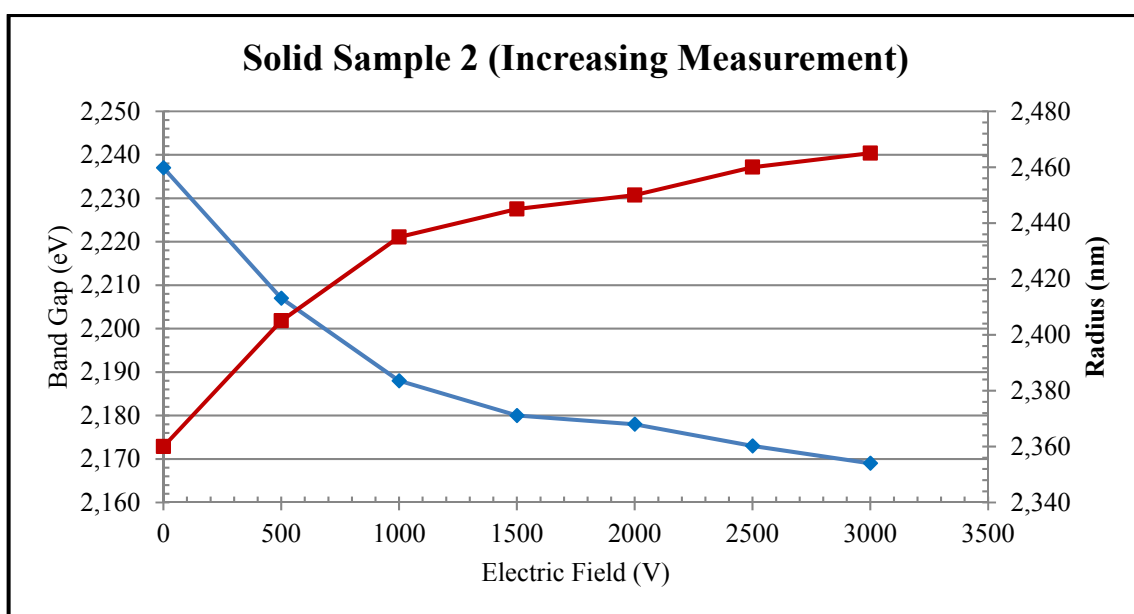


Figure 6.88. Band gap energies and radius versus electric field of increasing measurement.

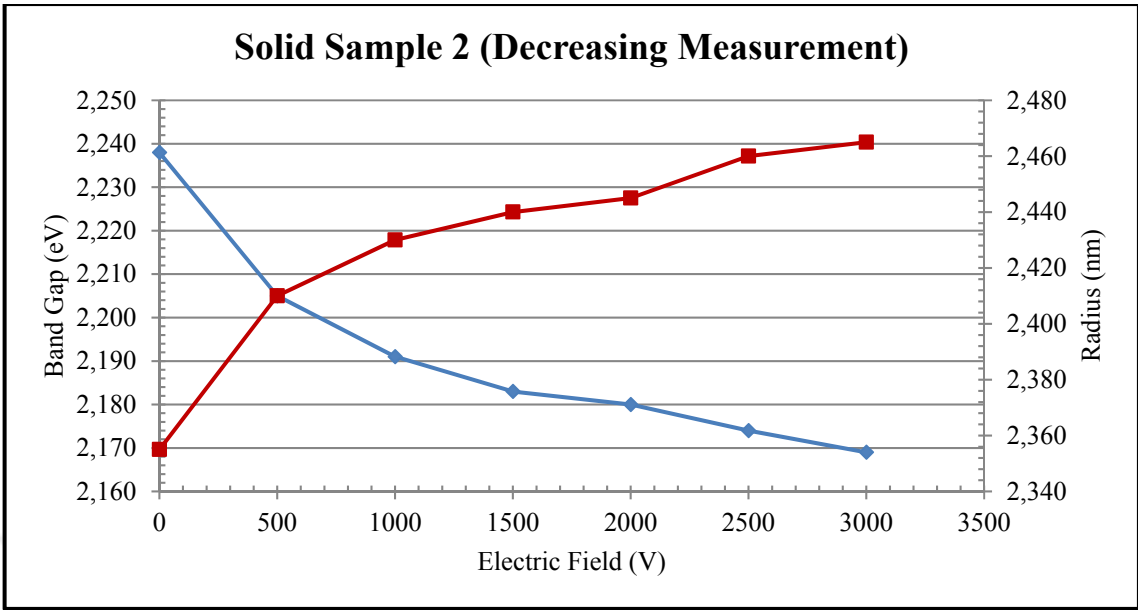


Figure 6.89. Band gap energies and radius versus electric field of decreasing measurement.

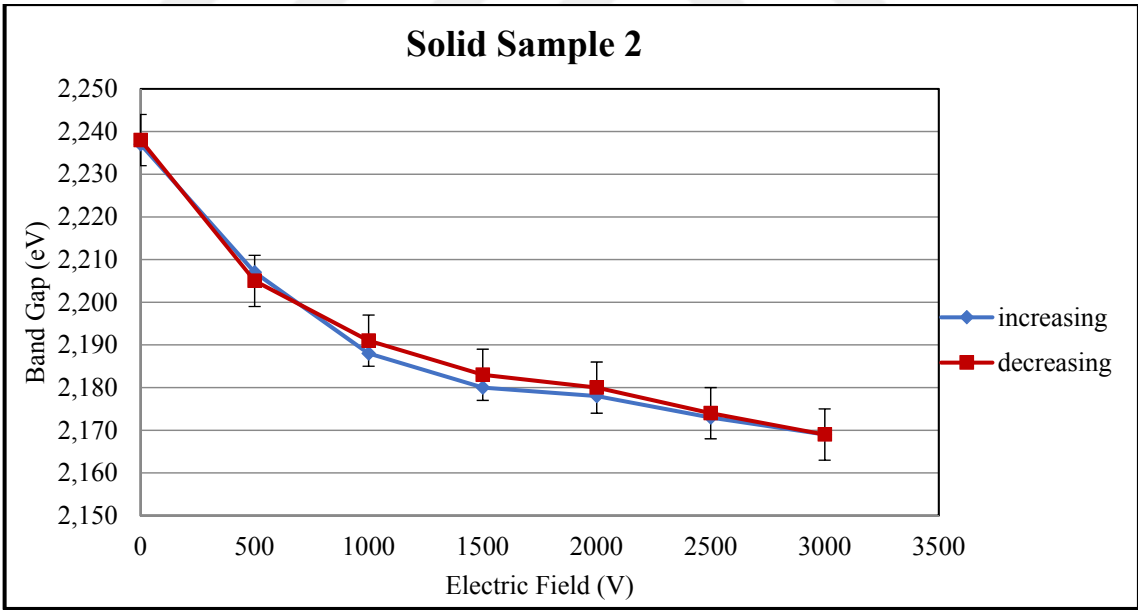


Figure 6.90. Band gap energies versus electric field of increasing and decreasing measurement with measurement uncertainty bar.

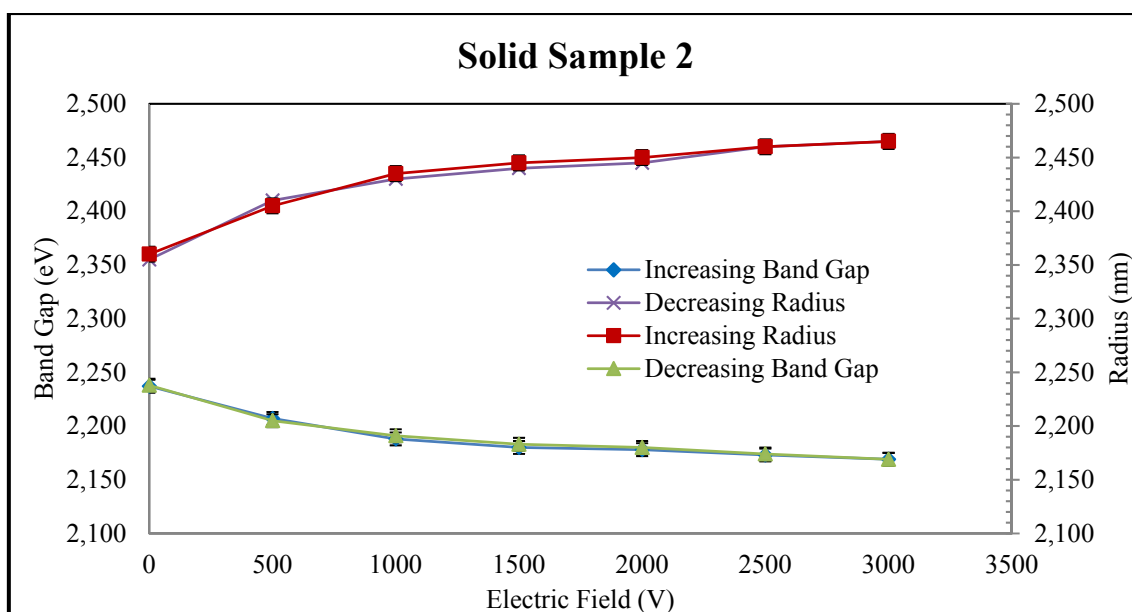


Figure 6.91. Band gap energies, radius vs. electric field with uncertainty bar.

#### 6.4.3. Solid Sample 3: 12 Hours Annealed

The last solid sample which has a longer annealing time than the others, has the lowest band gap energy. It is exposed to seven different electric fields and the band gap energies, dielectric permittivity and radius value were calculated for each measurement point. As can be seen in Table 6.12, the values of band gap energies decrease with the electric field and the CdTe QD nanoparticles increase linearly.

Table 6.12. Band gap energies and size of solid sample under different electric fields

SOLID SAMPLE 3: 12 HOURS ANNEALED				
Electric Field (V)	Band Gap (eV)	Radius (nm)	$\epsilon_{real}$	$\epsilon_{imaginary}$
0	2.109	2.580	123.53	121.81
250	2.102	2.590		
500	2.094	2.605		
1000	2.092	2.610		
1500	2.091	2.615		
1750	2.081	2.630		
0	2.108	2.580		

It is demonstrated that the use of graphic representations to estimate the band gap energies is an appropriate and eligible technique from Tauc plot, shown below from Figure 6.92 to Figure 6.99.

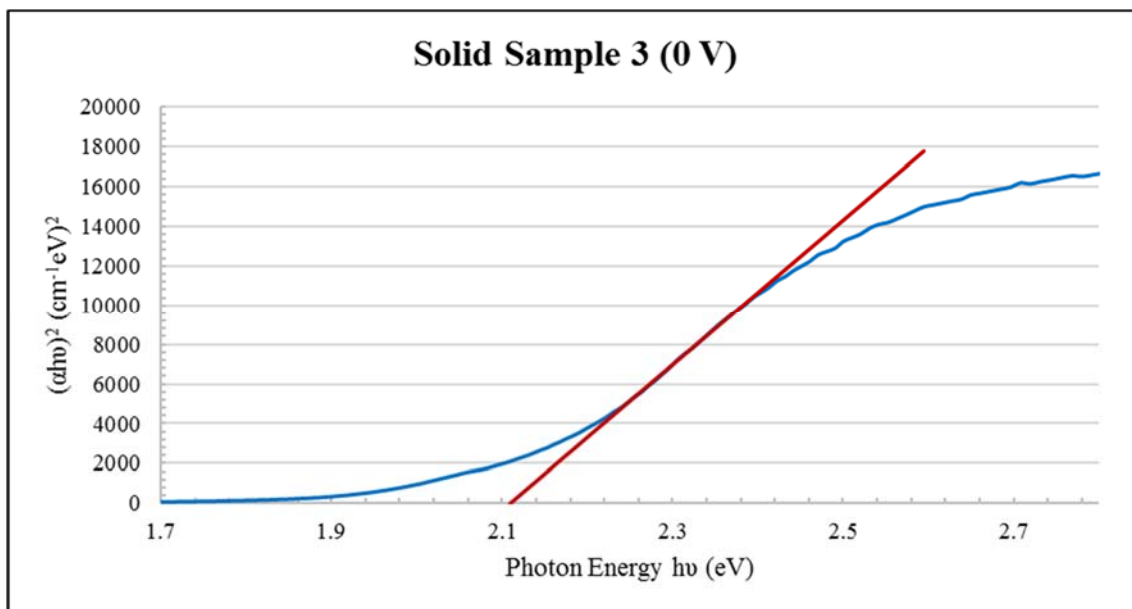


Figure 6.92. Plots of  $(\alpha h\nu)^2$  versus  $h\nu$  for Solid Sample 3 at 0 V.

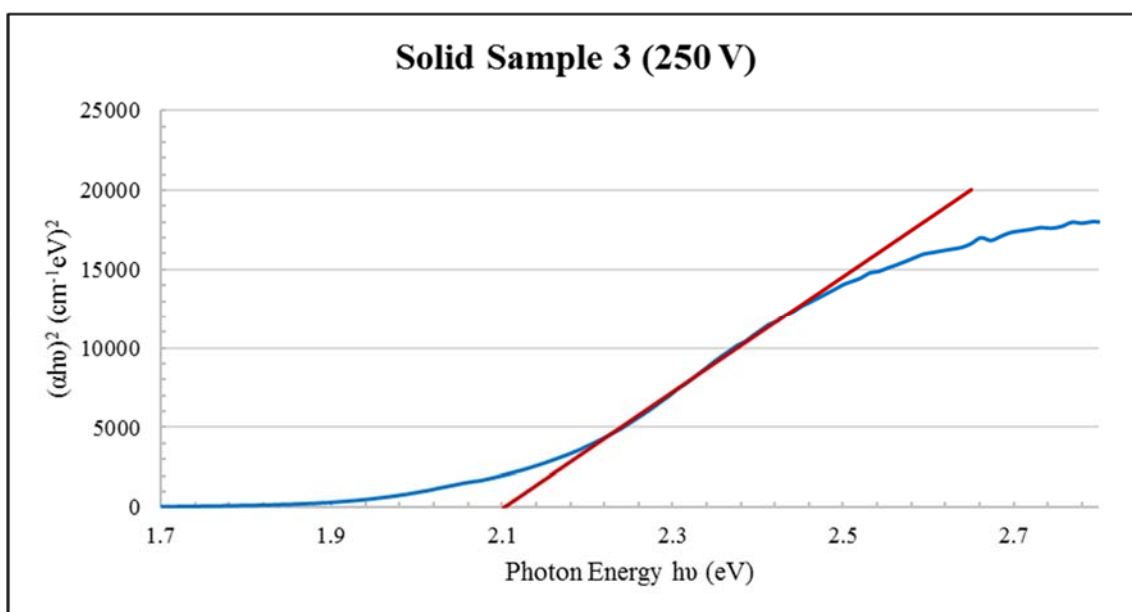


Figure 6.93. Plots of  $(\alpha h\nu)^2$  versus  $h\nu$  for Solid Sample 3 at 250 V.

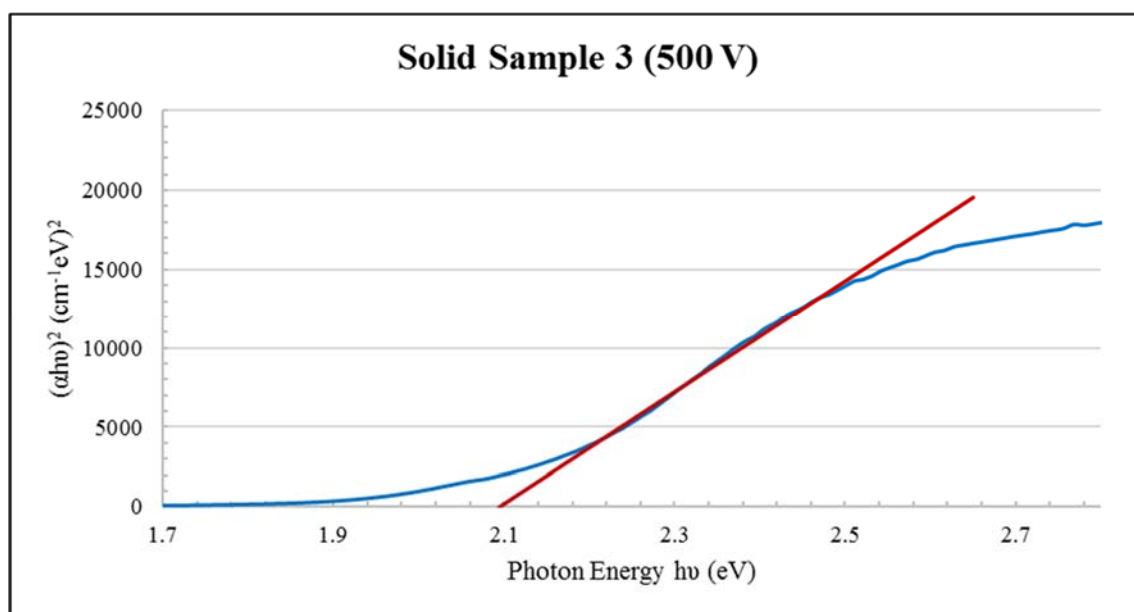


Figure 6.94. Plots of  $(\alpha h\nu)^2$  versus  $h\nu$  for Solid Sample 3 at 500 V.

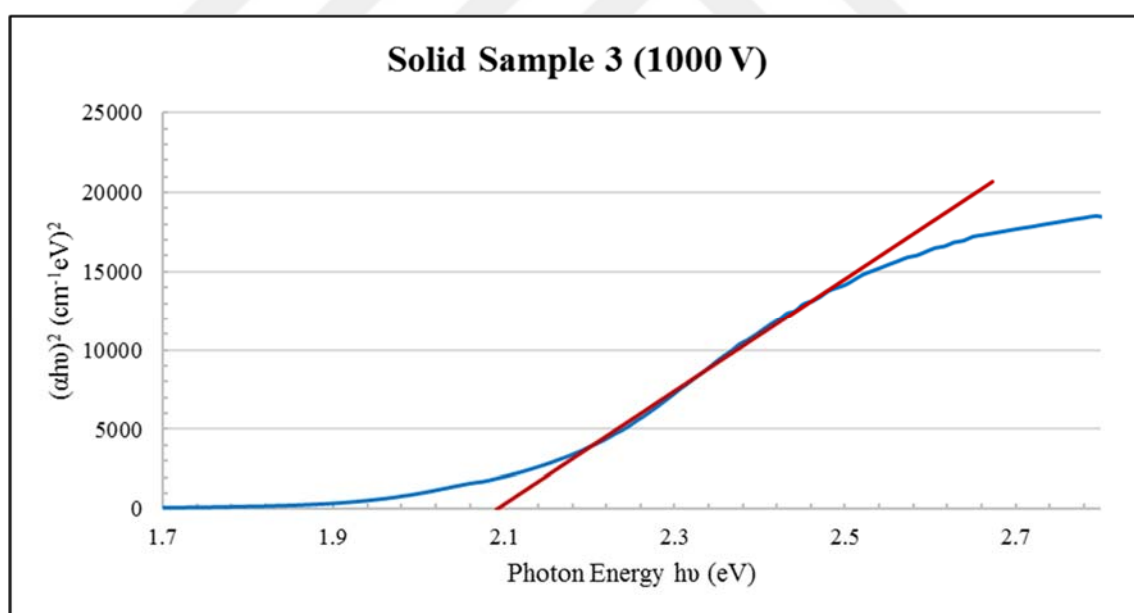


Figure 6.95. Plots of  $(\alpha h\nu)^2$  versus  $h\nu$  for Solid Sample 3 at 1000 V.

Solid sample 3 has the minimum band gap energies for all the solid samples because of the high heat treatment time. The band gap results from the absorption spectroscopy were reported in Figure 6.92, Figure 6.93, Figure 6.94 and Figure 6.95.

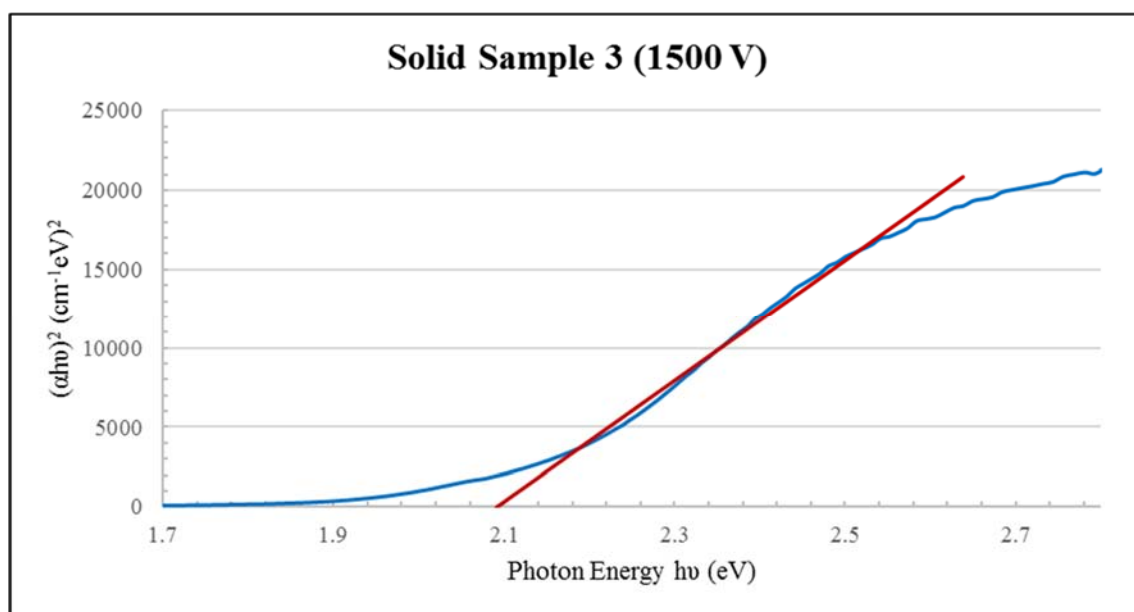


Figure 6.96. Plots of  $(\alpha h\nu)^2$  versus  $h\nu$  for Solid Sample 3 at 1500 V.

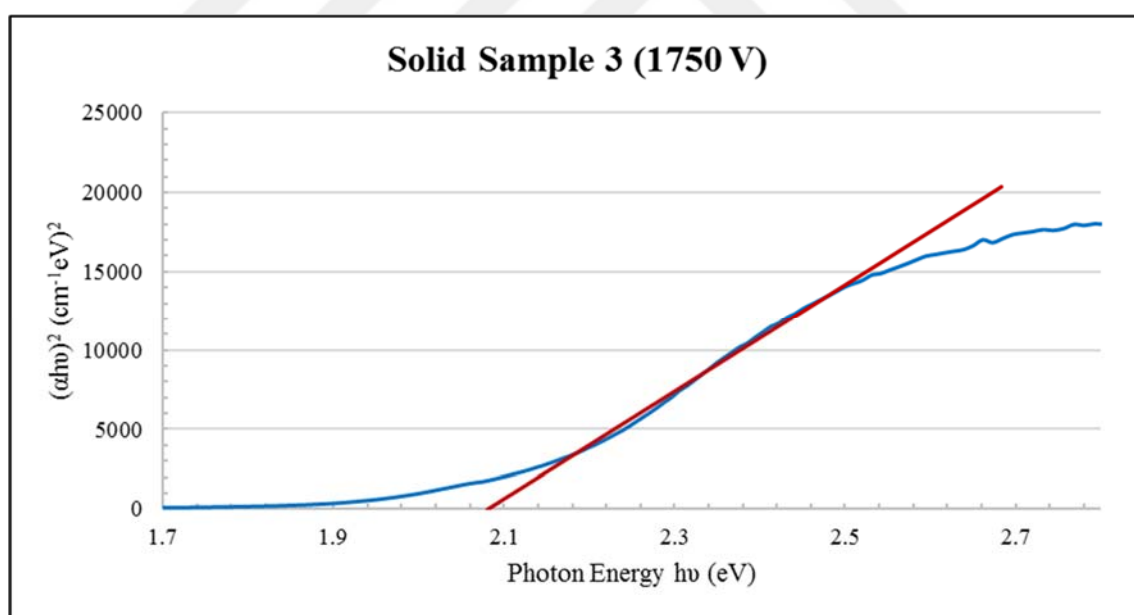


Figure 6.97. Plots of  $(\alpha h\nu)^2$  versus  $h\nu$  for Solid Sample 3 at 1750 V.

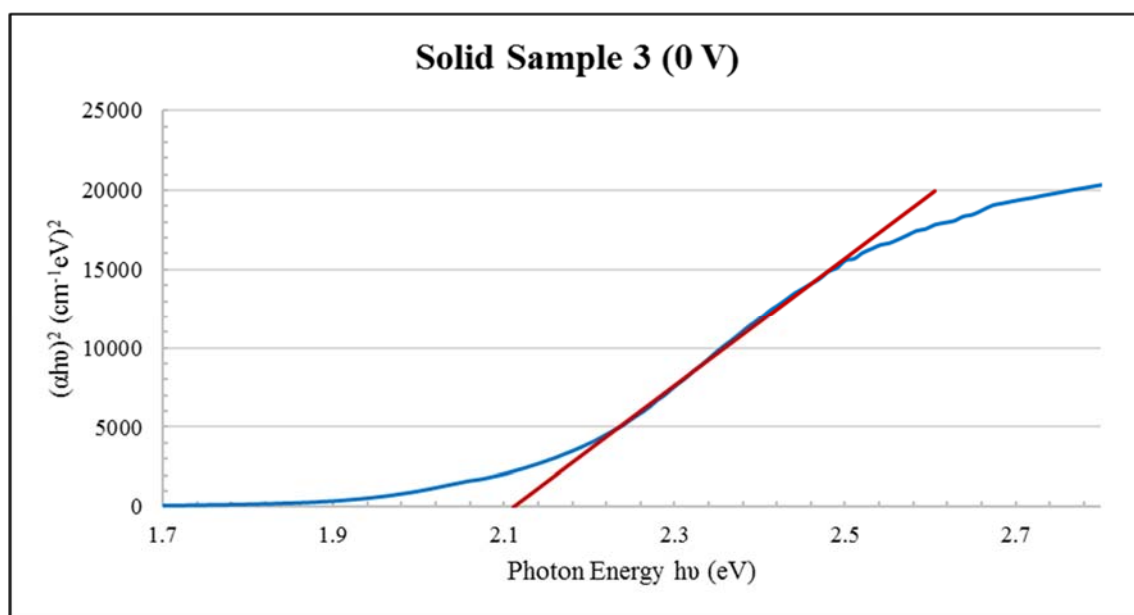


Figure 6.98. Plots of  $(\alpha h\nu)^2$  versus  $h\nu$  for Solid Sample 3 at 0 V.

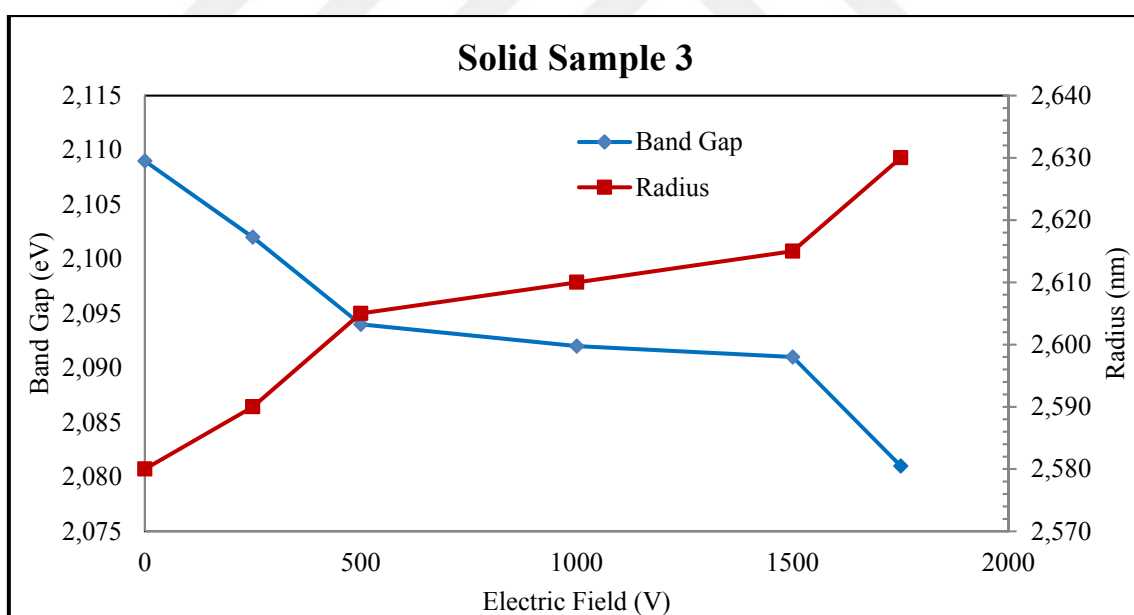


Figure 6.99. Graph of band gap and radius versus electric field.

The band gap energy and radius versus electric field graph gives the information about solid sample 3. As we can see there is an increasing trend for radius up to highest electric field value.

#### 6.4.4. Solution Sample 1: 15 minutes Heat-Treated

Solid sample measurements were completed and in this section the aqueous solution samples were characterized using the same linear optical absorption spectroscopy system but the set-up was made suitable for aqueous samples. The applied electric field in aqueous samples did not reach as high values as the applied electric field in solid samples. This sample is the first aqueous sample taken during the synthesis of quantum dots which has the smallest nanoparticle size. We see that the particle sizes are getting bigger depending on the heat-treatment temperature in the samples taken after that. The characterization process in the solution samples was the same with solid samples, first the band gap energies were found and then the electric permittivity and finally the particle radius were calculated.

All these results which were written in Tables 6.13, 6.14, 6.15, 6.16 and 6.17 show the band gap energies, radius and electric permittivities of the aqueous samples.

Table 6.13. Band gap energies and size of solution sample 1 under different electric field.

<b>SOLUTION SAMPLE 1</b>				
<b>Electric Field (V)</b>	<b>Band Gap/ (eV)</b>	<b>Radius/ (nm)</b>	<b><math>\epsilon_{\text{real}}</math></b>	<b><math>\epsilon_{\text{imaginary}}</math></b>
0	2.552	1.925	12.63	8.50
500	2.543	1.930		
750	2.540	1.935		
1000	2.538	1.935		
1250	2.537	1.935		
1500	2.530	1.940		
2500	2.522	1.945		
0	2.556	1.920		



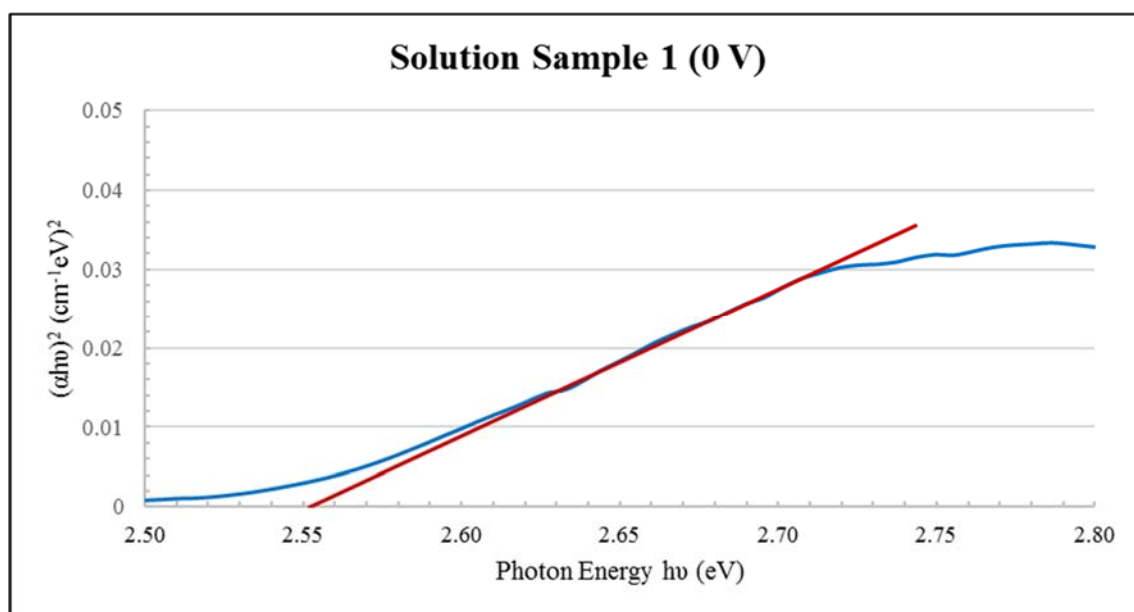


Figure 6.100. Plots of  $(\alpha h\nu)^2$  versus  $h\nu$  for Solution Sample 1 at 0 V.

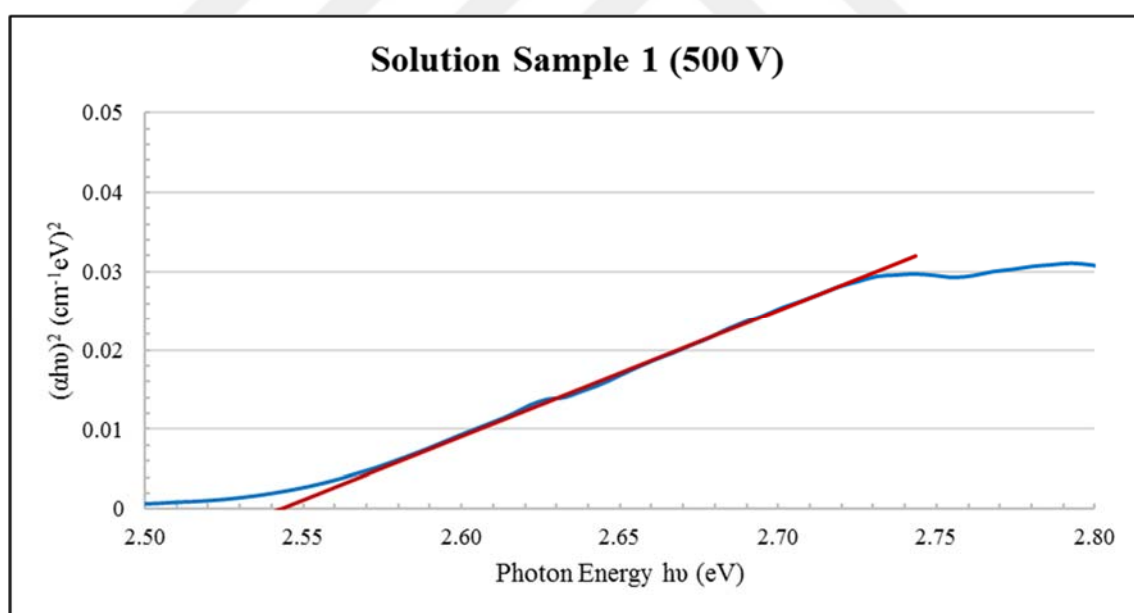


Figure 6.101. Plots of  $(\alpha h\nu)^2$  versus  $h\nu$  for Solution Sample 1 at 500 V.

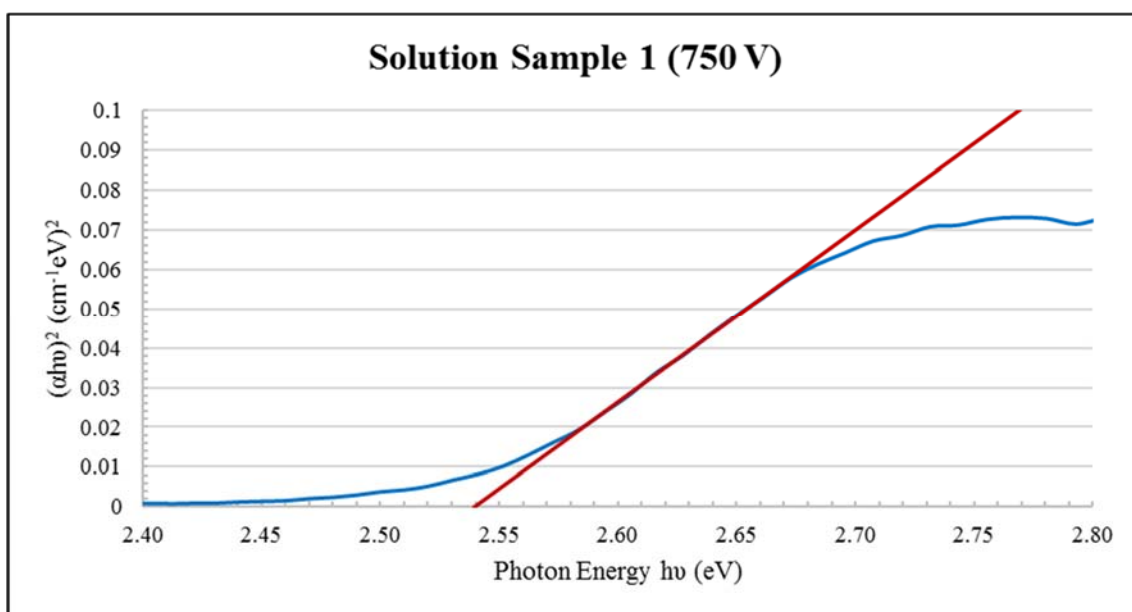


Figure 6.102. Plots of  $(\alpha h\nu)^2$  versus  $h\nu$  for Solution Sample 1 at 750 V.

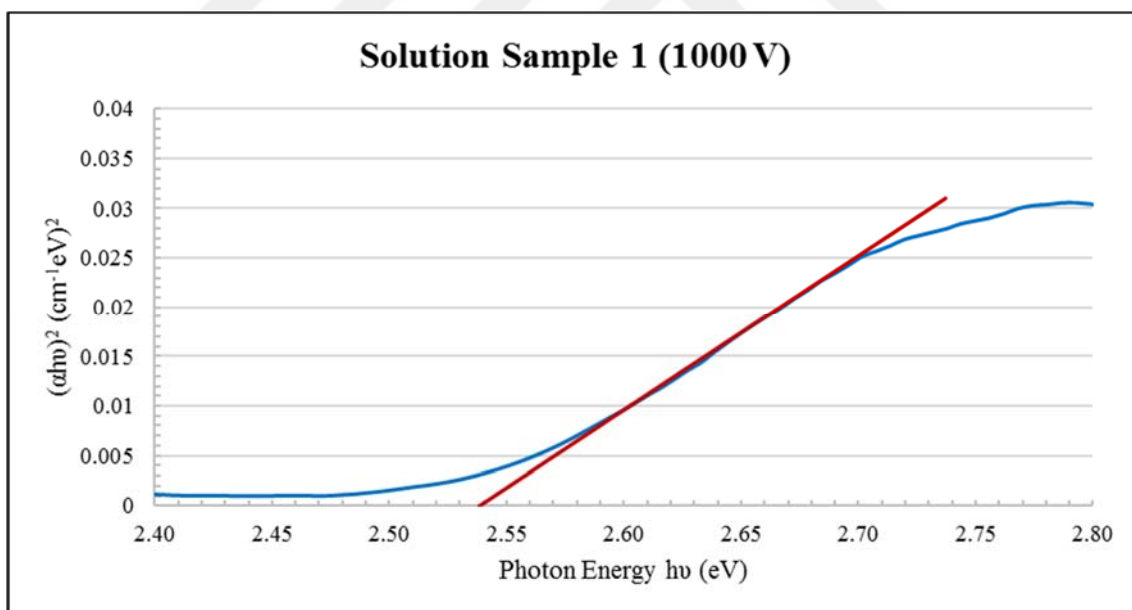


Figure 6.103. Plots of  $(\alpha h\nu)^2$  versus  $h\nu$  for Solution Sample 1 at 1000 V.

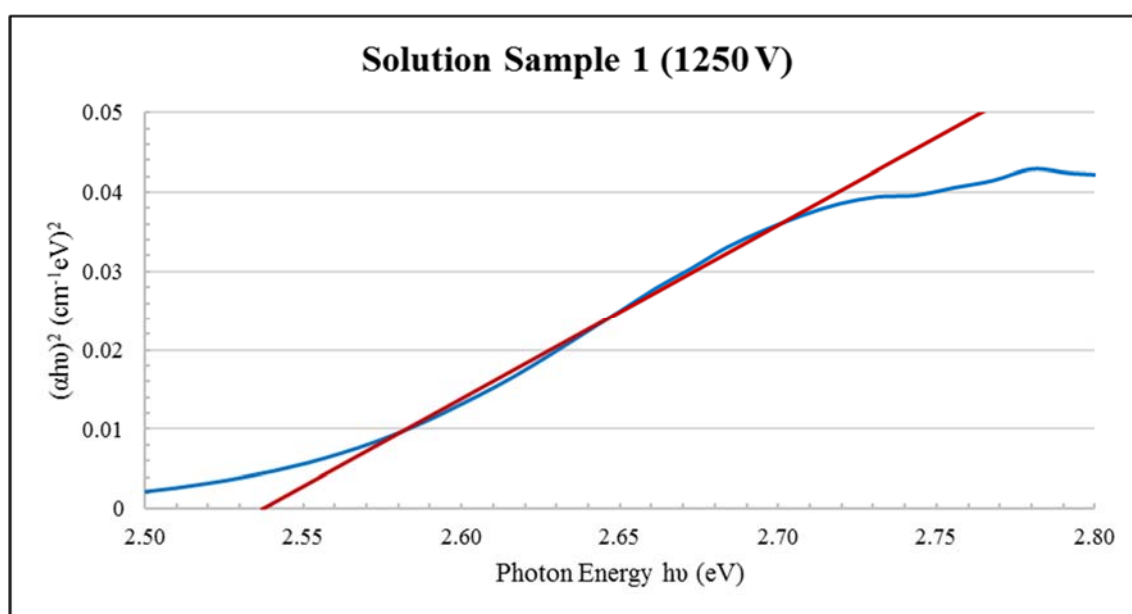


Figure 6.104. Plots of  $(\alpha h\nu)^2$  versus  $h\nu$  for Solution Sample 1 at 1250 V.

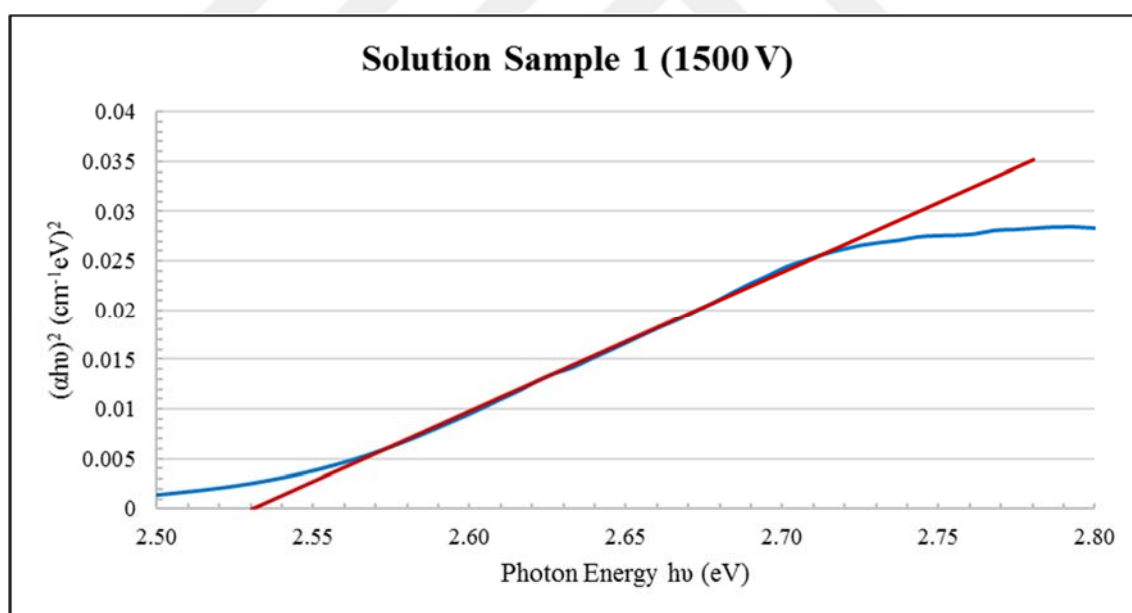


Figure 6.105. Plots of  $(\alpha h\nu)^2$  versus  $h\nu$  for Solution Sample 1 at 1500 V.

Figures 6.100 to 6.105 show the optical absorption spectroscopy data taken for the first solution sample to find the band gap energies.

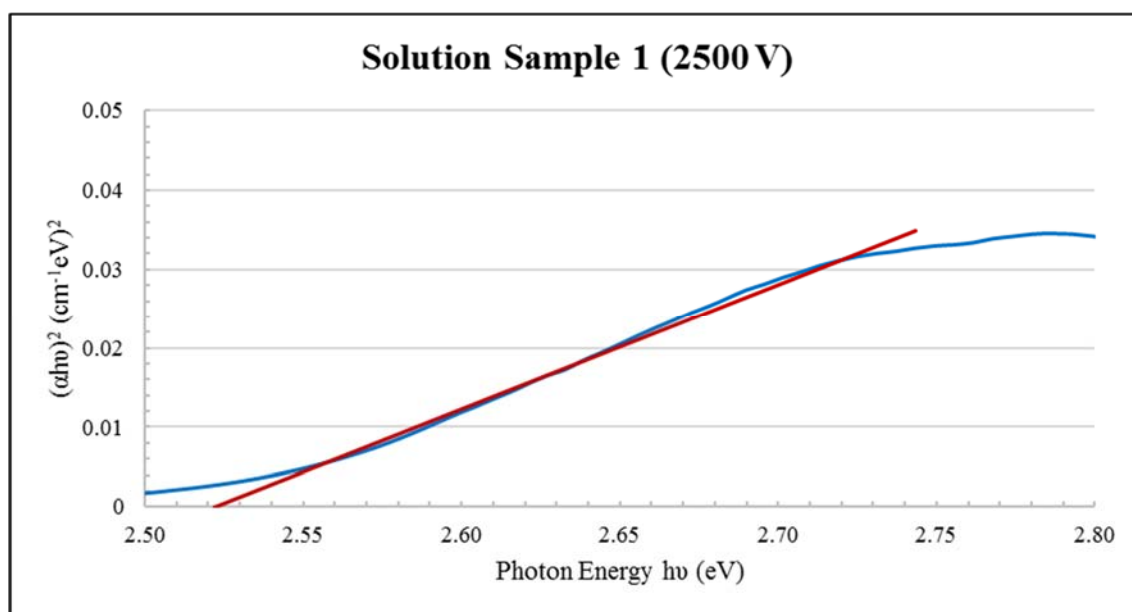


Figure 6.106. Plots of  $(\alpha h\nu)^2$  versus  $h\nu$  for Solution Sample 1 at 2500 V.

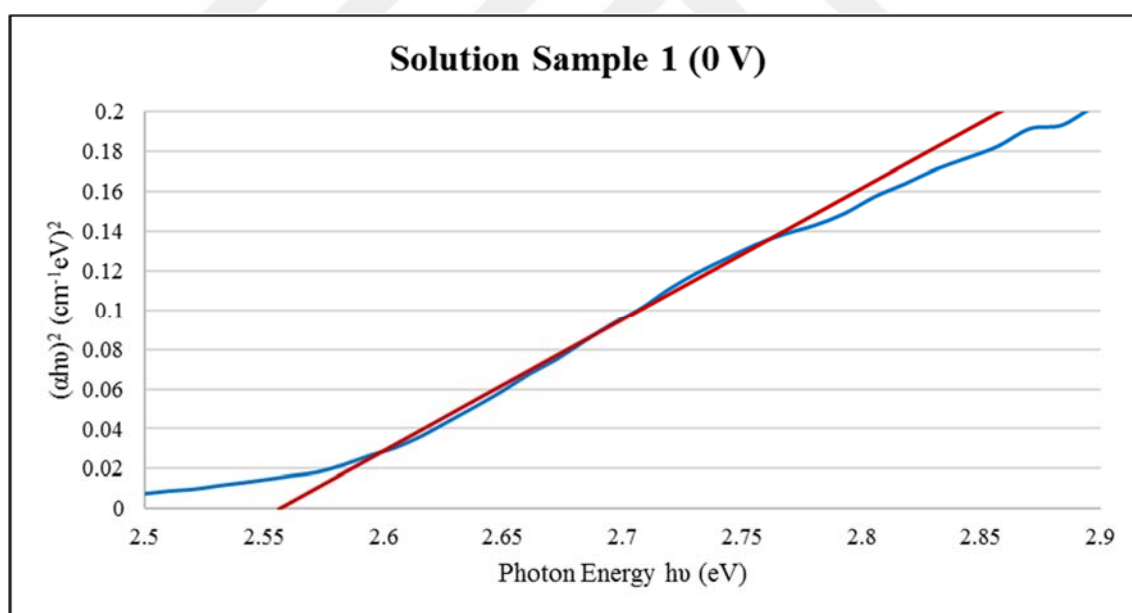


Figure 6.107. Plots of  $(\alpha h\nu)^2$  versus  $h\nu$  for Solution Sample 1 at 0 V.

Band gap energies change from 2.552 eV to 2.522 eV when the electric field increased. To perform more reliable and accurate measurements, the repeatability and hysteresis measurements were done.

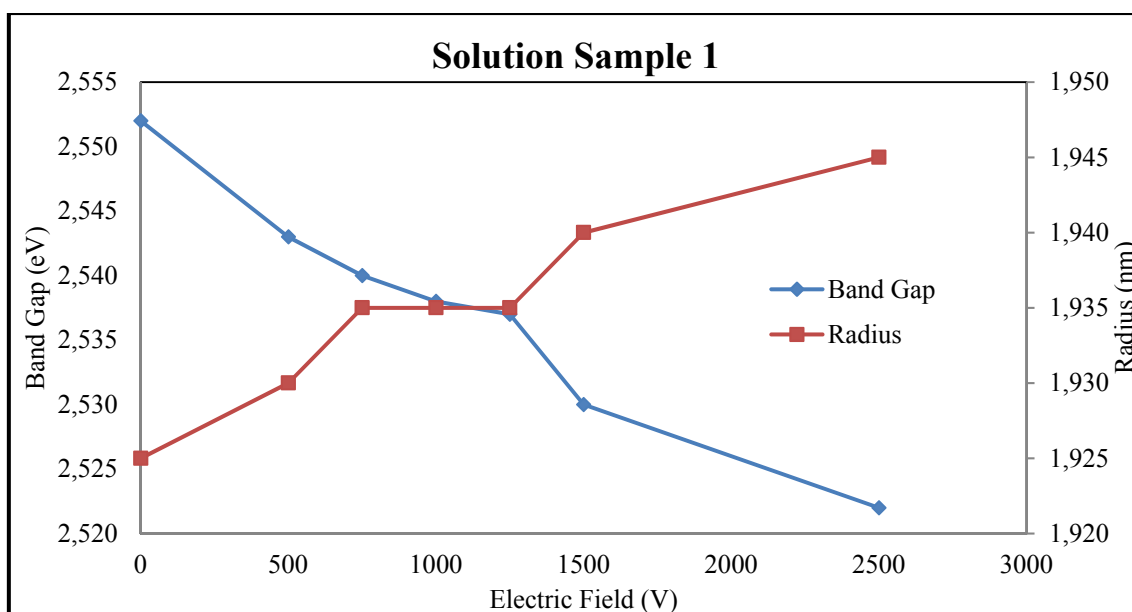


Figure 6.108. Plot of bandgap, radius versus applied electric field for aqueous solution sample 1, from the table above.

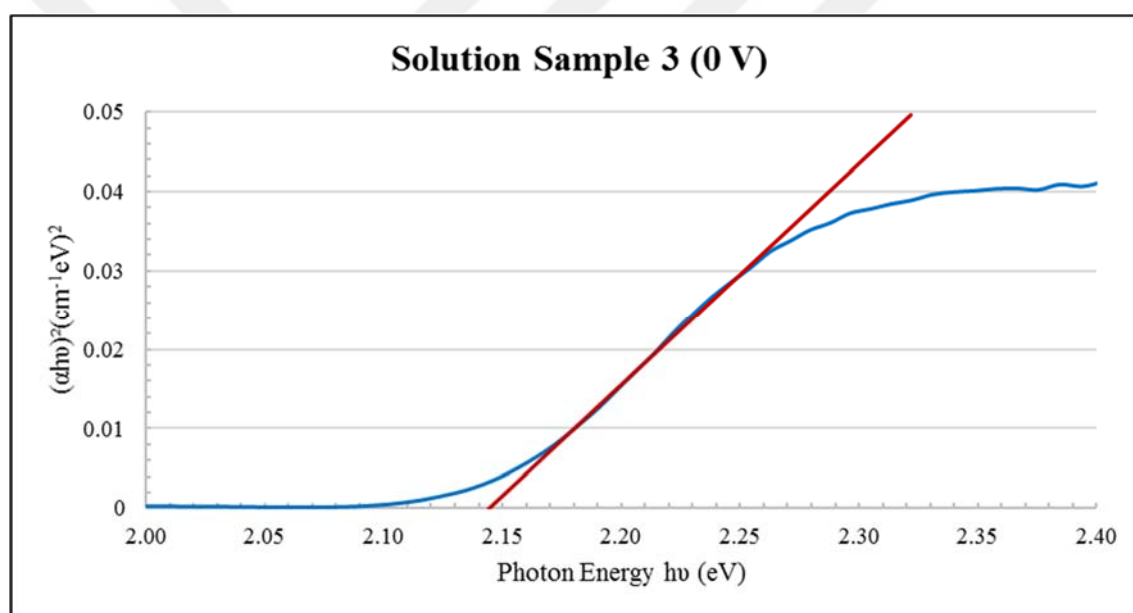
It can be seen that the greatest decrease in the band gap was achieved at 2500 V shown above in Figure 6.108. However, the highest electric field value applicable to solid samples was not reached in aqueous samples.

#### 6.4.5. Solution Sample 3: 2 Hours Heat-Treated

This sample taken two hours after the start of the synthesis process has a larger radius than the first sample due to the heat treatment time. The results for the band gap and radius under various electric field were given in Table 6.14. The measurements made at approximately 5 different measurement points were terminated with measurements taken at zero point (without field) again. The band gap values were determined from the Tauc plot relation shown below from Figure 6.109 to Figure 6.116. It is seen that decreasing the band gap energies of the CdTe QDs increased the size of the particles with the applied electric field.

Table 6.14. Band gap energies and size of solution sample 3 under different electric field.

SOLUTION SAMPLE 3 (2 Hours)				
Electric Field (V)	Band Gap/ (eV)	Radius/ (nm)	$\epsilon_{\text{real}}$	$\epsilon_{\text{imaginary}}$
0	2.231	2.285	16.00	11.58
250	2.230	2.290		
500	2.224	2.300		
750	2.214	2.310		
1000	2.208	2.320		
1500	2.195	2.340		
0	2.229	2.290		

Figure 6.109. Plots of  $(\alpha h\nu)^2$  versus  $h\nu$  for Solution Sample 3 at 0 V.

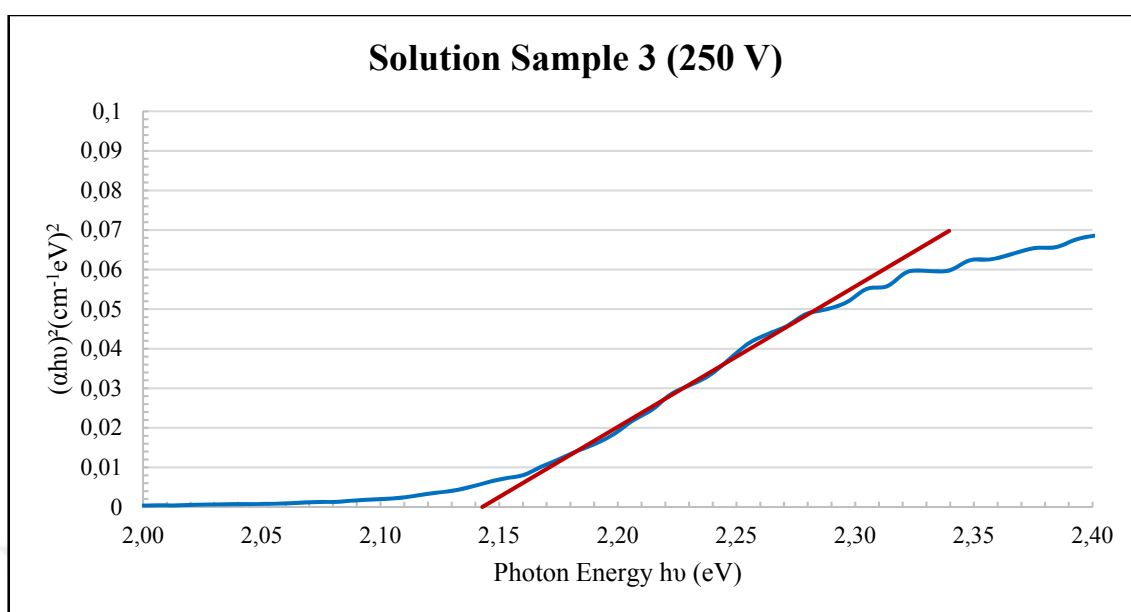


Figure 6.110. Plots of  $(\alpha h\nu)^2$  versus  $h\nu$  for Solution Sample 3 at 250 V.

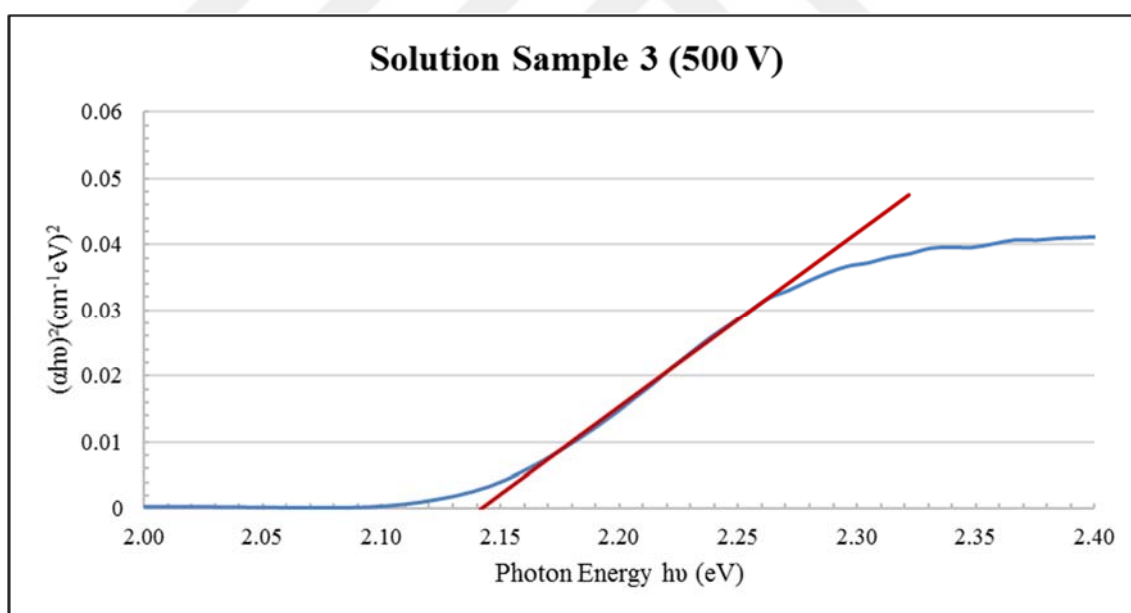


Figure 6.111. Plots of  $(\alpha h\nu)^2$  versus  $h\nu$  for Solution Sample 3 at 500 V.

Figures 6.109, 6.110 and 6.111 show a comparison of the zero and non-zero electric field measurements for solution sample 3.

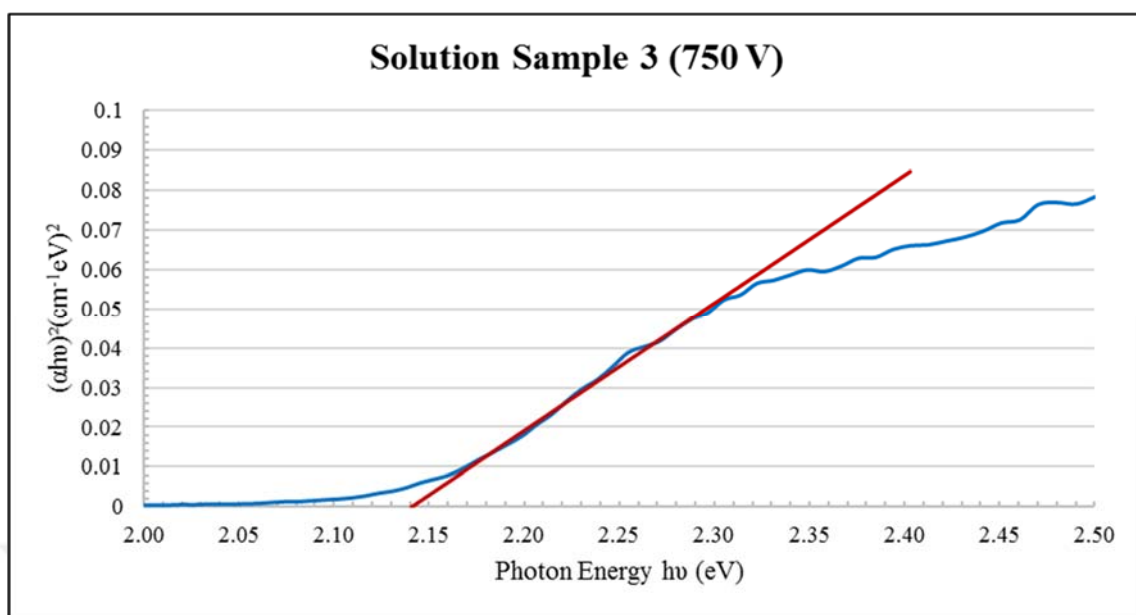


Figure 6.112. Plots of  $(\alpha h\nu)^2$  versus  $h\nu$  for Solution Sample 3 at 750 V.

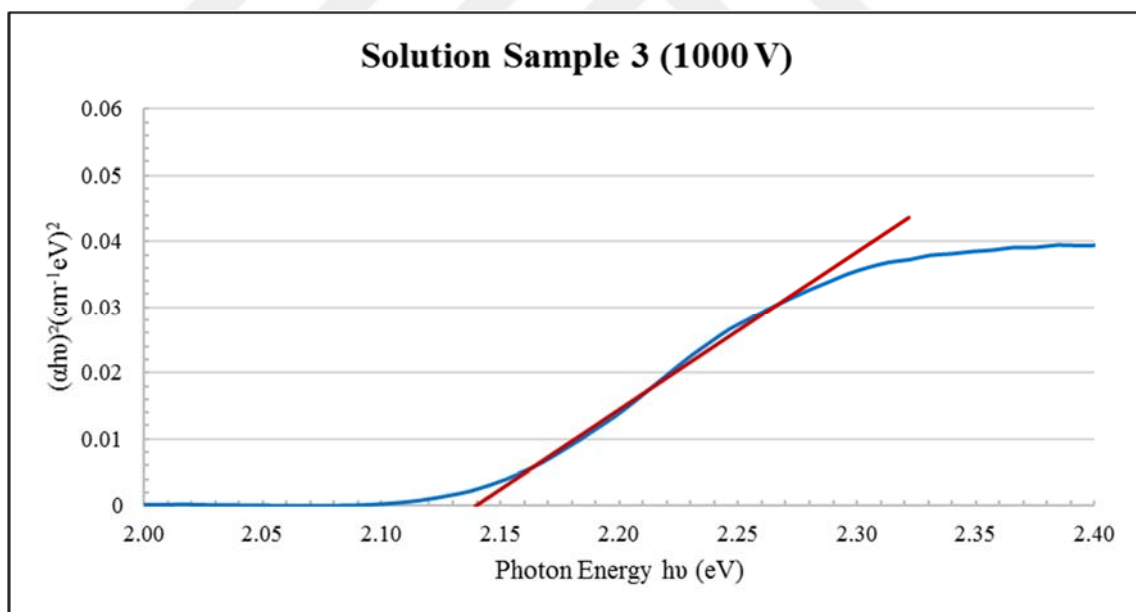


Figure 6.113. Plots of  $(\alpha h\nu)^2$  versus  $h\nu$  for Solution Sample 3 at 1000 V.



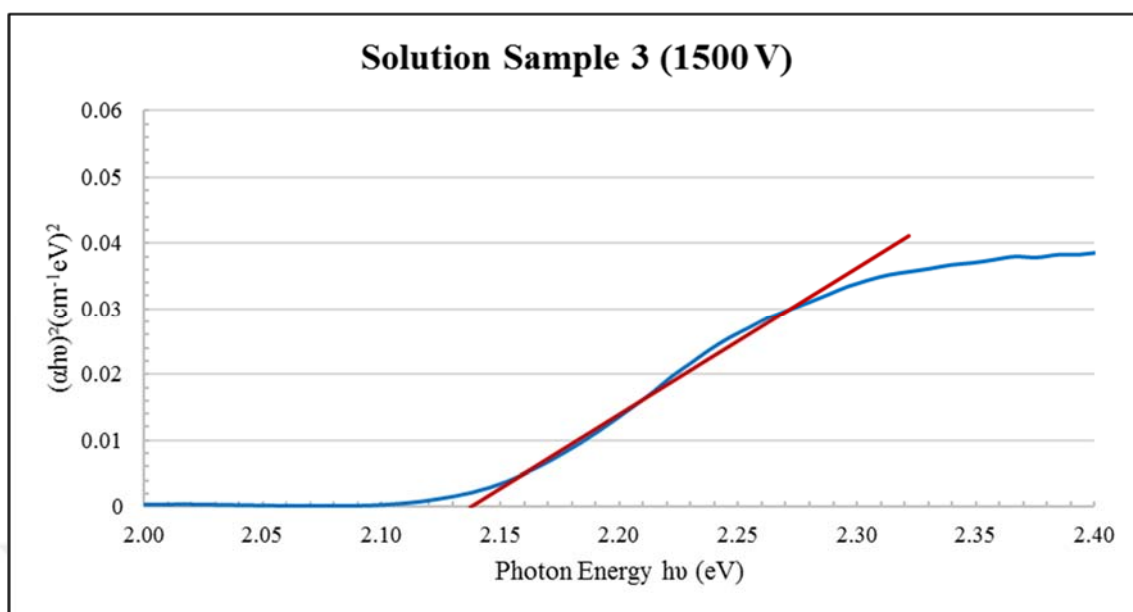


Figure 6.114. Plots of  $(\alpha h\nu)^2$  versus  $h\nu$  for Solution Sample 3 at 1500 V.

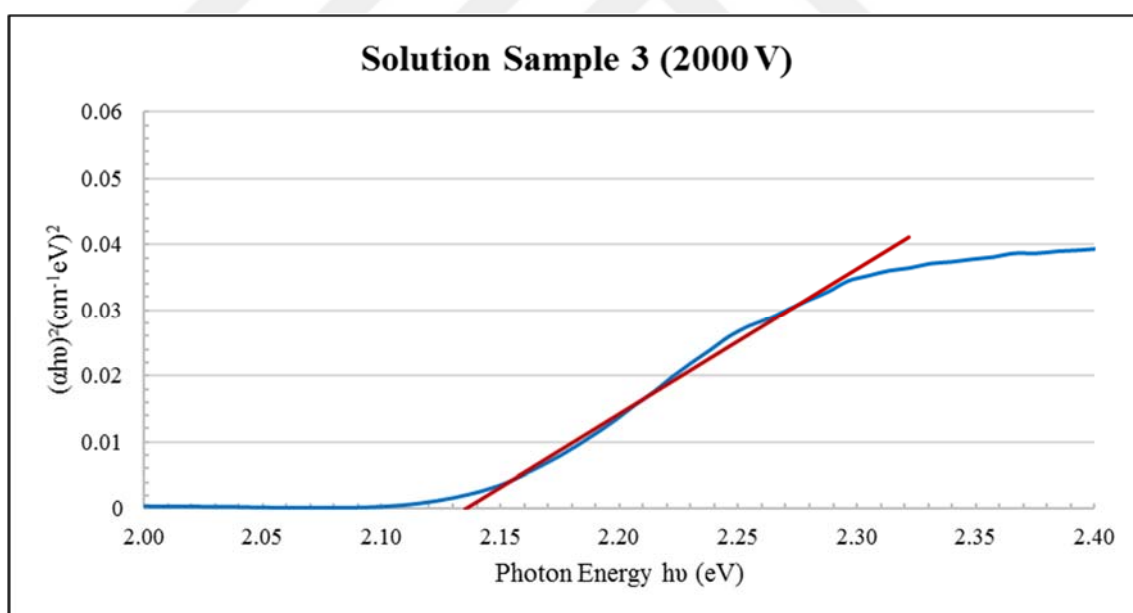


Figure 6.115. Plots of  $(\alpha h\nu)^2$  versus  $h\nu$  for Solution Sample 3 at 2000 V.

The above graphs for the solution sample 3 show the same trend as demonstrated for the other solution sample optical absorption spectroscopy measurements which were performed to estimate the band gap energies.

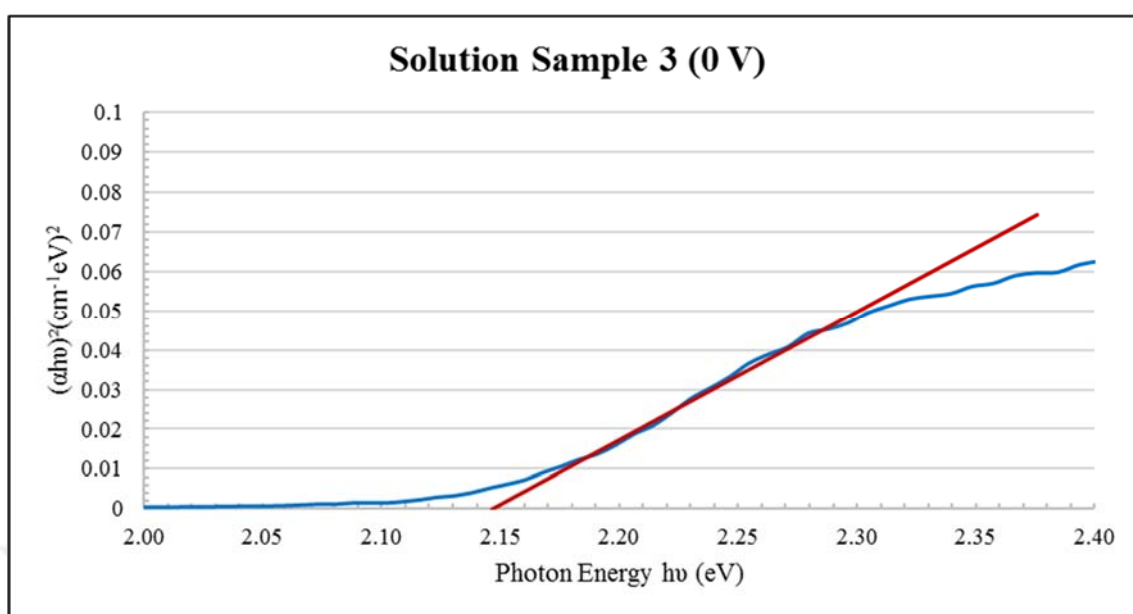


Figure 6.116. Plots of  $(\alpha h\nu)^2$  versus  $h\nu$  for Solution Sample 3 at 0 V.

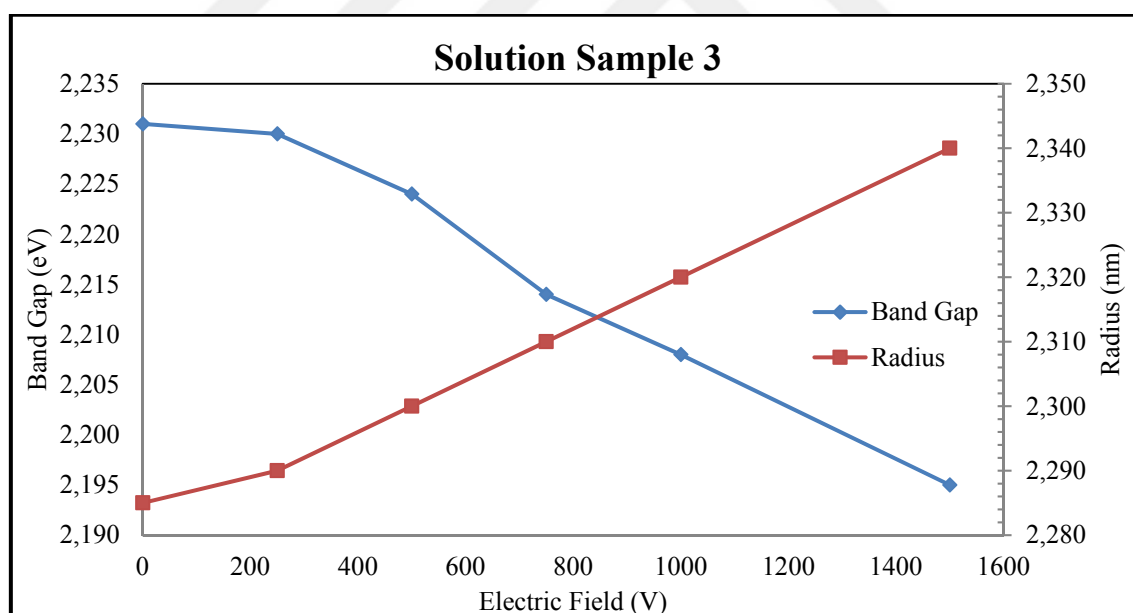


Figure 6.117. Plot of bandgap, radius versus applied electric field for solution sample 3, from table above.

The change in band gap of solution sample 3 as the applied voltage was decreased is shown above together with the nanoparticles in the samples increased with applied voltage computed from these values using Brus equation.

#### 6.4.6. Solution Sample 4: 3 Hours Heat-Treated

The two graphs in Figures 6.118 and 6.119 are the band gap energies which were determined by extrapolating the linear portion of the absorption spectra of the solution sample 4. Table 6.15 shows both band gap energies and radius at different electric field.

Table 6.15. Band gap energies and size of solution sample 4 under different electric fields.

SOLUTION SAMPLE 4: 3 HOURS				
Electric Field (V)	Band Gap/ (eV)	Radius/ (nm)	$\epsilon_{real}$	$\epsilon_{imaginary}$
0	2.195	2.315	13.14	12.36
1000	2.165	2.360		
1000	2.164	2.365		
0	2.190	2.325		

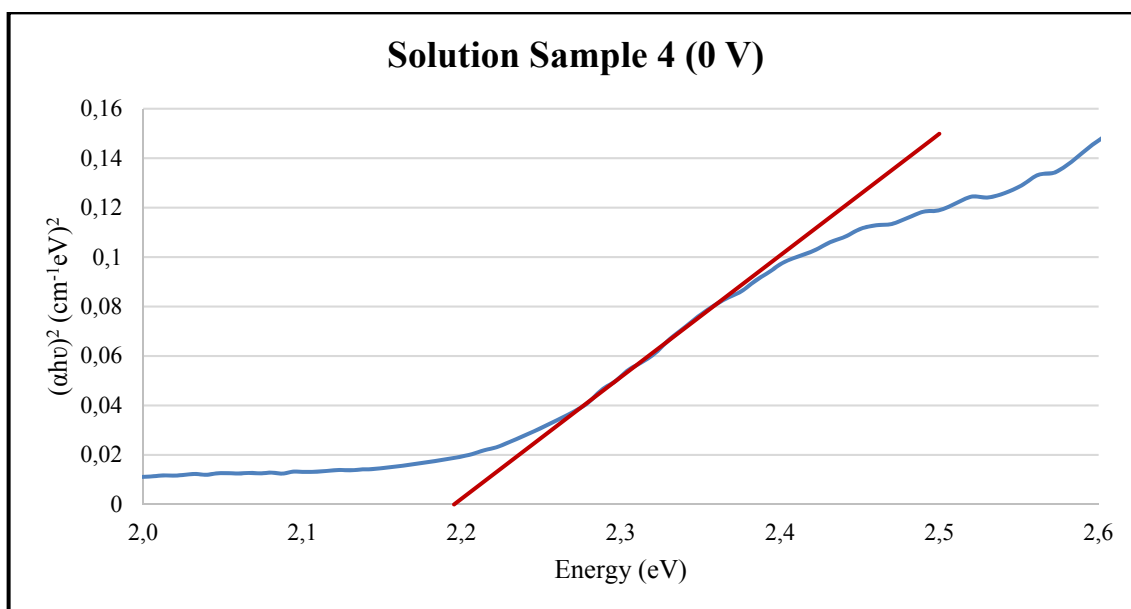


Figure 6.118. Plots of  $(\alpha h\nu)^2$  versus  $h\nu$  for Solution Sample 4 at 0 V.

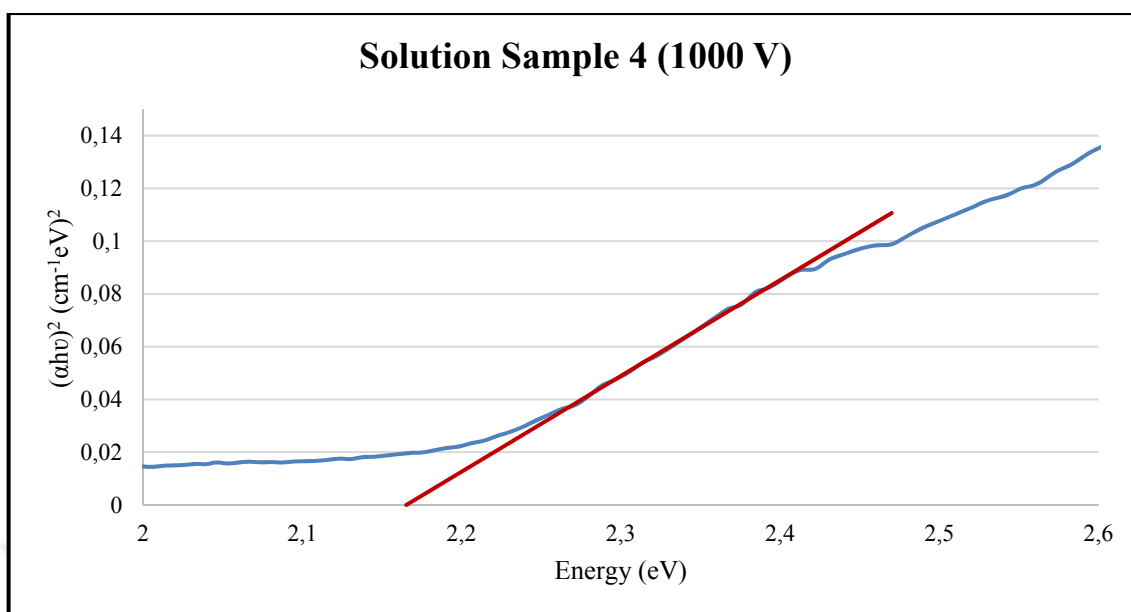


Figure 6.119. Plots of  $(\alpha h\nu)^2$  versus  $h\nu$  for Solution Sample 4 at 1000 V.

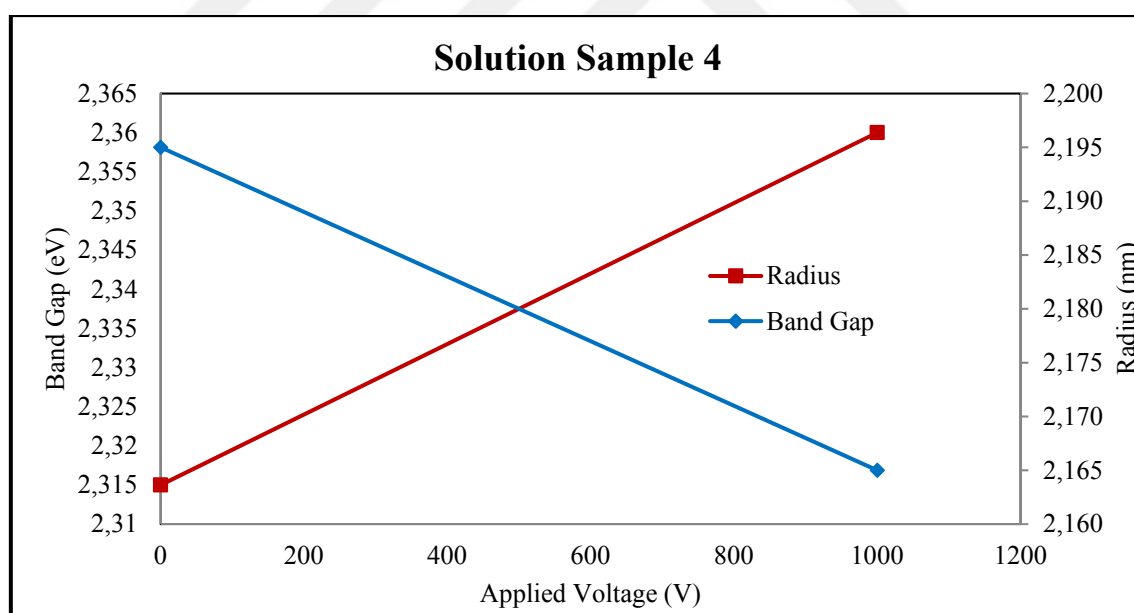


Figure 6.120. Plot of band gap, radius versus applied electric field for solution sample 4.

Above in Figure 6.120 we can see the band gap energies and radius changing with field for solution sample 4.

### 6.4.7. Solution Sample 6: 5 Hours Heat-Treated

Table 6.16. Band gap energies and size of solution sample 6 under different electric fields.

SOLUTION SAMPLE 6: 5 HOURS				
Electric Field (V)	Band Gap/ (eV)	Radius/ (nm)	$\epsilon_{real}$	$\epsilon_{imaginary}$
0	2.155	2.395	15.29	16.08
500	2.154	2.395		
1000	2.150	2.400		
1500	2.148	2.405		
2000	2.146	2.410		

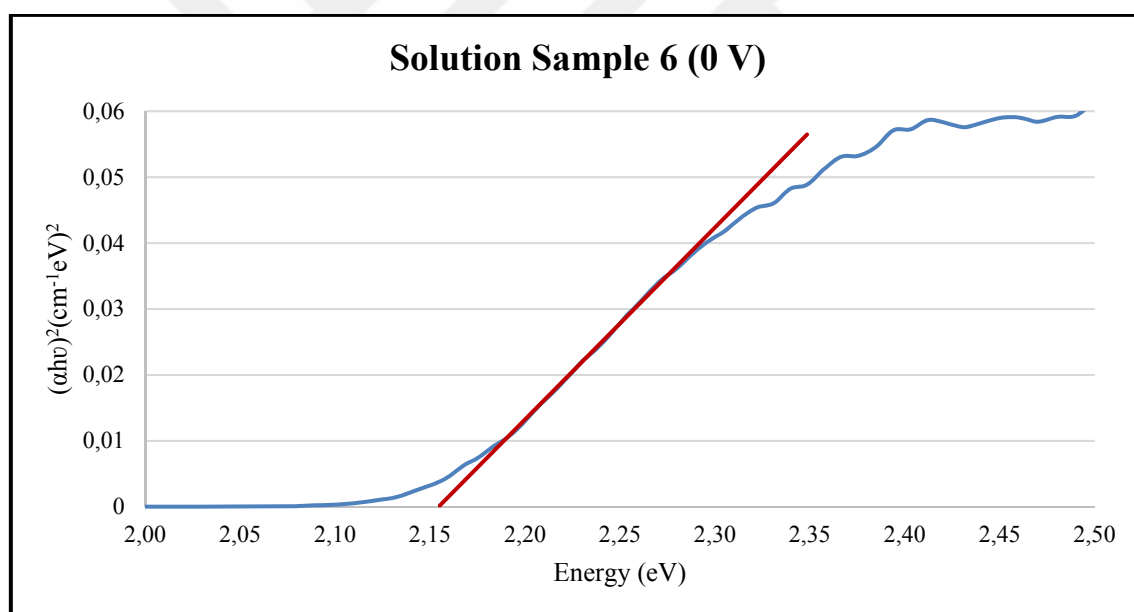


Figure 6.121. Plots of  $(\alpha h\nu)^2$  versus  $h\nu$  for Solution Sample 6 at 0 V.

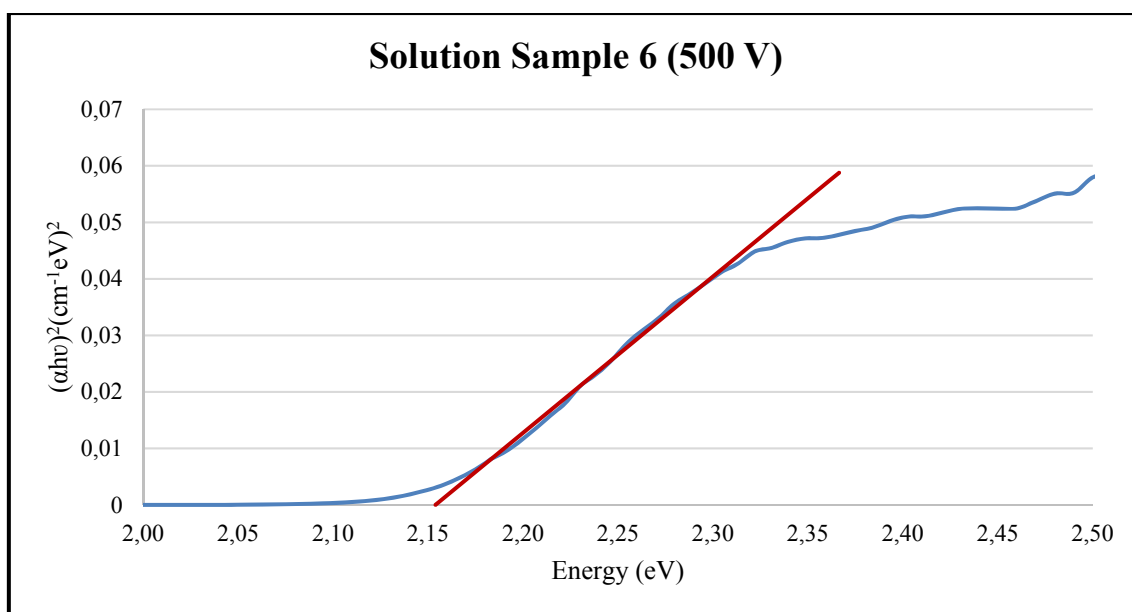


Figure 6.122. Plots of  $(\alpha h\nu)^2$  versus  $h\nu$  for Solution Sample 6 at 500 V.

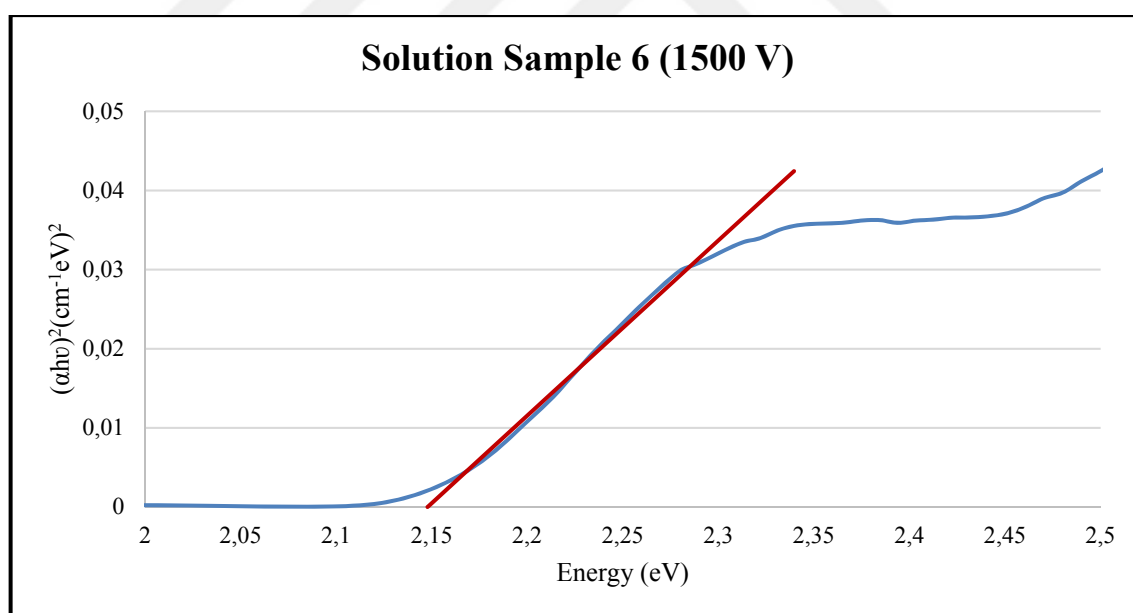


Figure 6.123. Plots of  $(\alpha h\nu)^2$  versus  $h\nu$  for Solution Sample 6 at 1500 V.

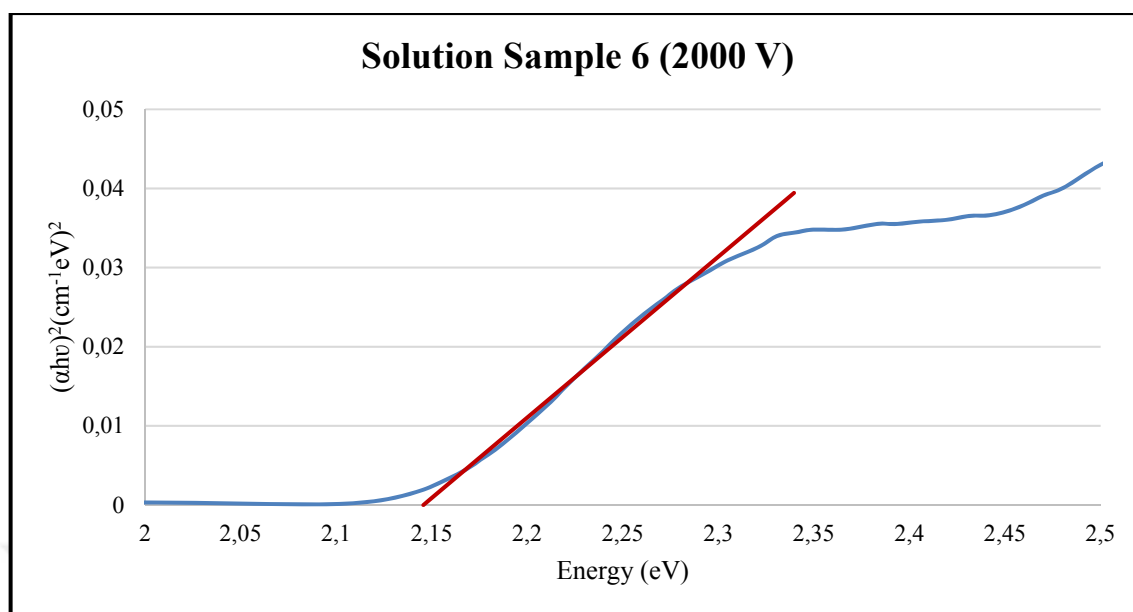


Figure 6.124. Plots of  $(\alpha h\nu)^2$  versus  $h\nu$  for Solution Sample 6 at 2000 V.

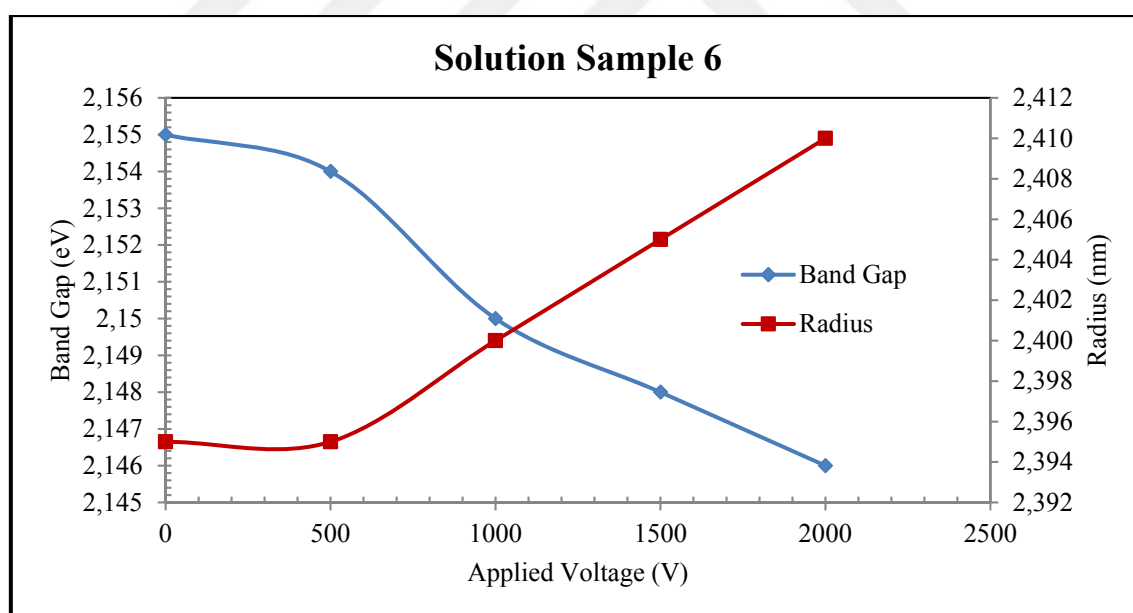


Figure 6.125. Plot of band gap, radius versus applied electric field for solution sample 6.

As a result of these calculations shown in Table 6.16, the band gap and radius variation with field was given in Figure 6.125. The trend demonstrated that nanoparticles suffer a red shift,

decreasing their band gap and leading to a higher calculated radius on application of an electric field.

#### 6.4.8. Solution Sample 7: 5 Hours 15 Minutes Heat-Treated

Band gap energies were determined from Tauc plot shown below Figures 6.126-6.133 and in the direction of this information, the radii were derived from the Brus equation given in Table 6.17. For the solution sample 7, the applied voltage was increased in steps and reading taken at 0 V again after all measurements finished to assess whether the band-gap returned to its original value. The results of this sample show that the band gap returned to its original energy with 0.05% hysteresis.

Table 6.17. Band gap energies and size of solution sample 7 under different electric fields.

<b>SOLUTION SAMPLE 7: 5 HOURS 15 MINUTES</b>				
<b>Electric Field (V)</b>	<b>Band Gap/ (eV)</b>	<b>Radius/ (nm)</b>	<b><math>\epsilon_{\text{real}}</math></b>	<b><math>\epsilon_{\text{imaginary}}</math></b>
0	2.145	2.325	8.57	8.09
250	2.143	2.330		
500	2.142	2.330		
750	2.140	2.335		
1000	2.138	2.335		
1500	2.137	2.340		
2000	2.135	2.340		
0	2.146	2.325		



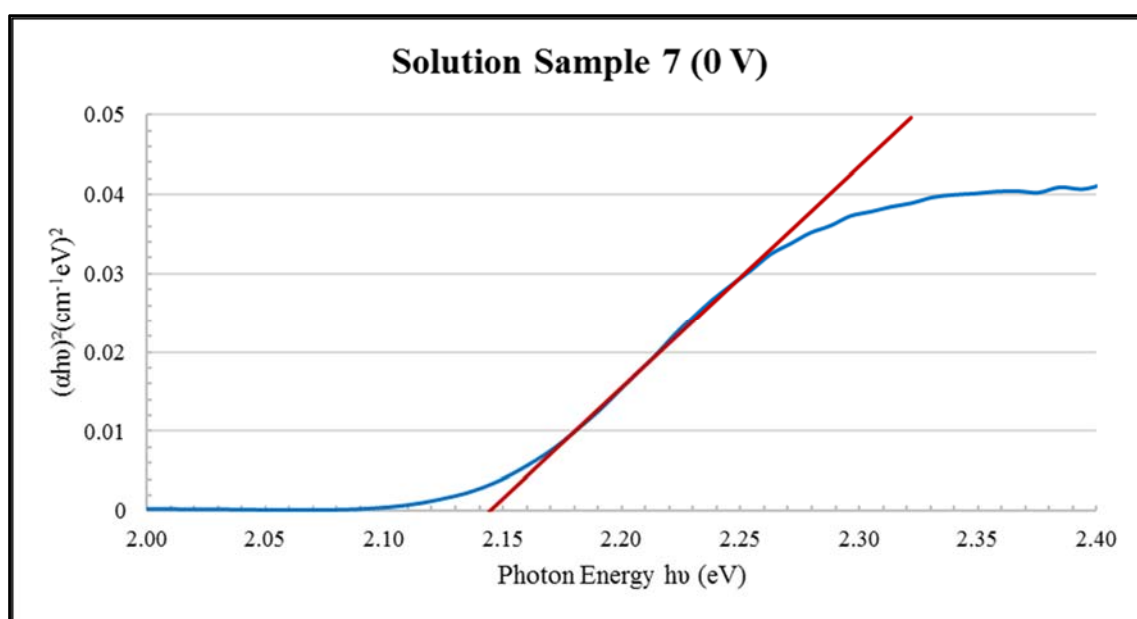


Figure 6.126. Plots of  $(\alpha h\nu)^2$  versus  $h\nu$  for Solution Sample 7 at 0 V.

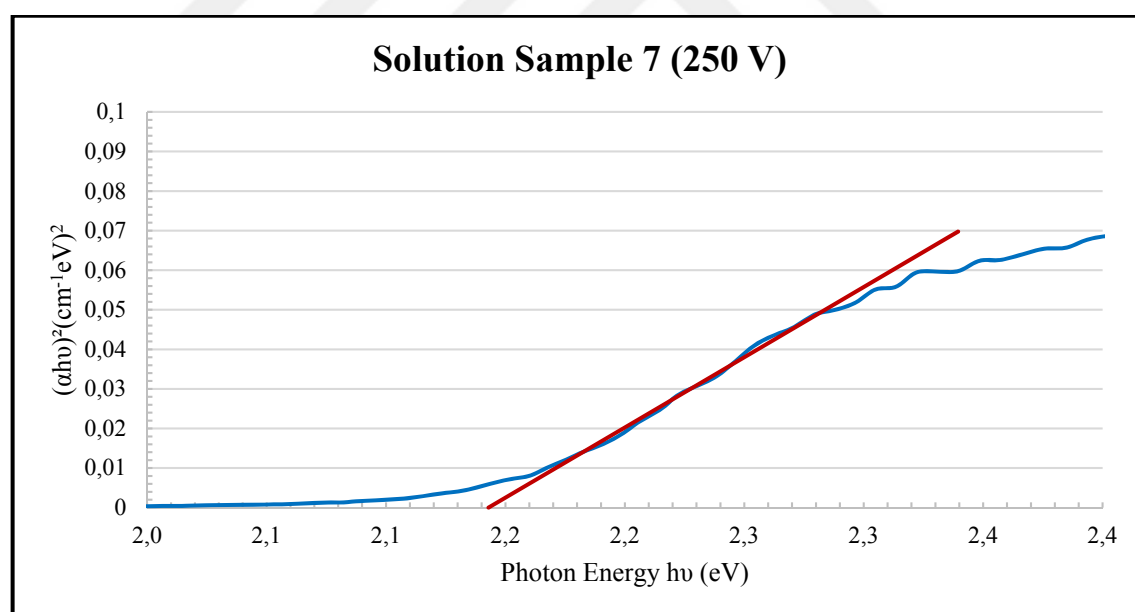


Figure 6.127. Plots of  $(\alpha h\nu)^2$  versus  $h\nu$  for Solution Sample 7 at 250 V.

The last solution sample was also analysed under different electric fields and the bandgap energies were decreased with increasing electric field.

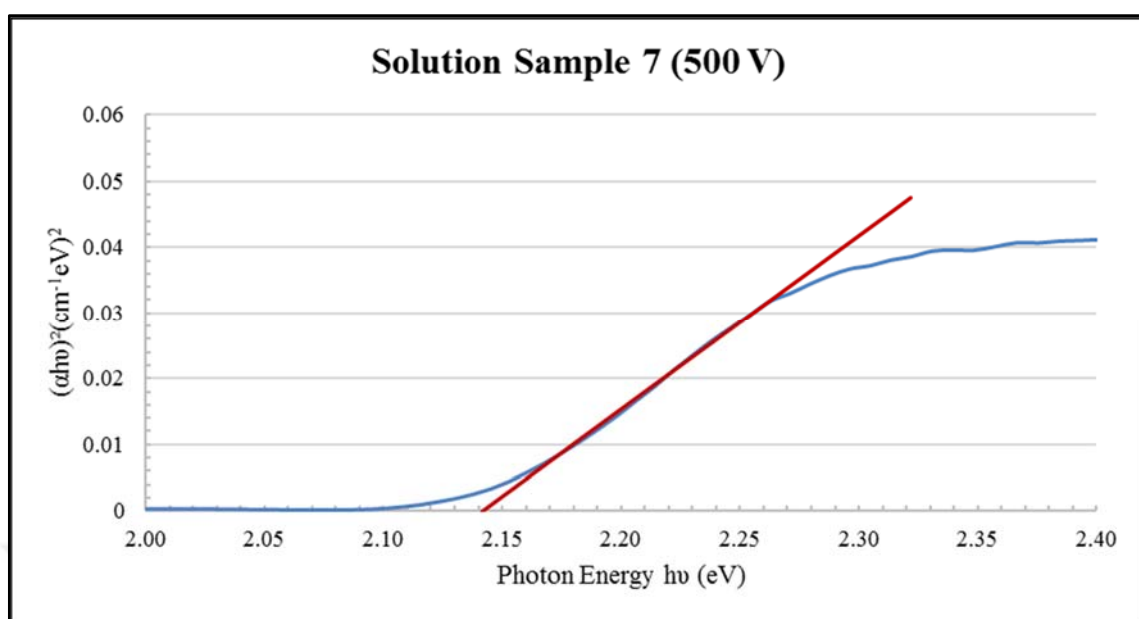


Figure 6.128. Plots of  $(\alpha h\nu)^2$  versus  $h\nu$  for Solution Sample 7 at 500 V.

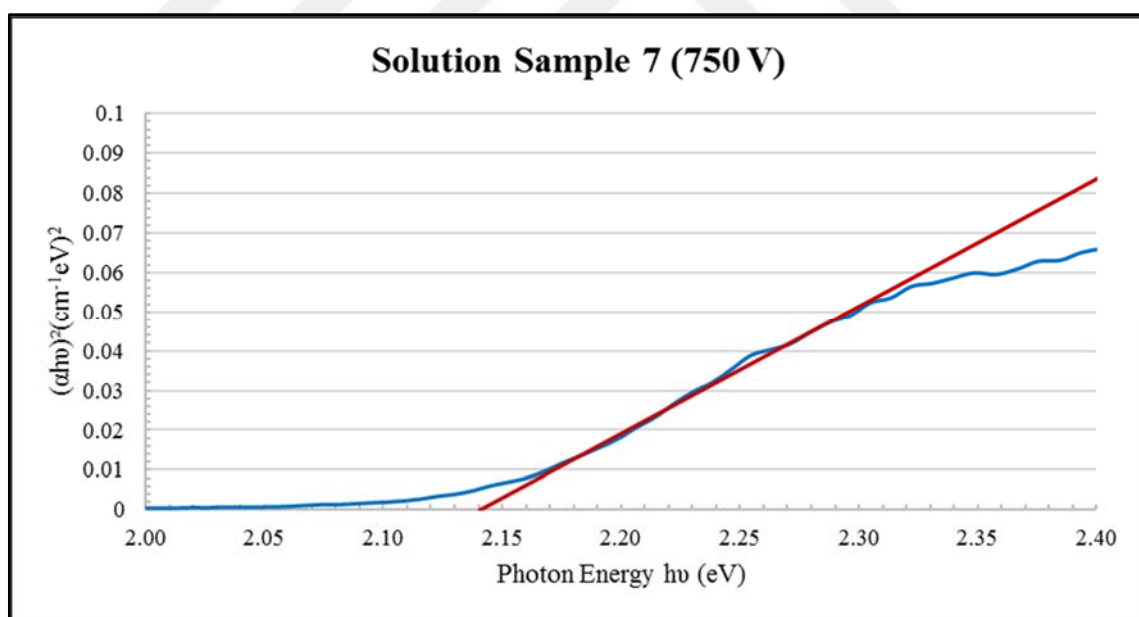


Figure 6.129. Plots of  $(\alpha h\nu)^2$  versus  $h\nu$  for Solution Sample 7 at 750 V.

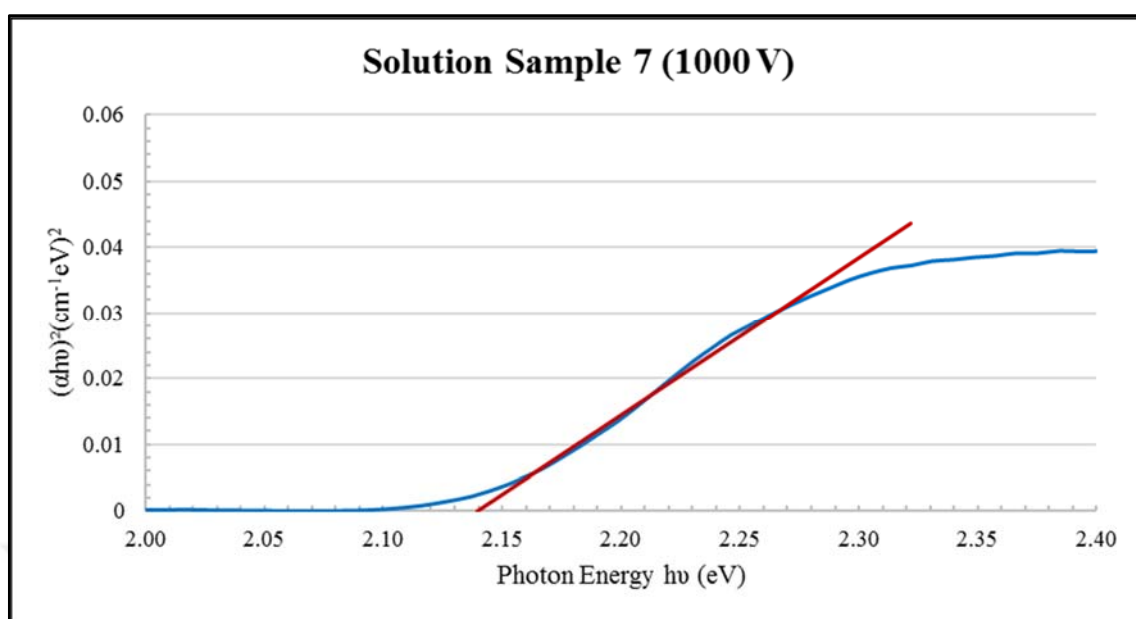


Figure 6.130. Plots of  $(\alpha h\nu)^2$  versus  $h\nu$  for Solution Sample 7 at 1000 V.

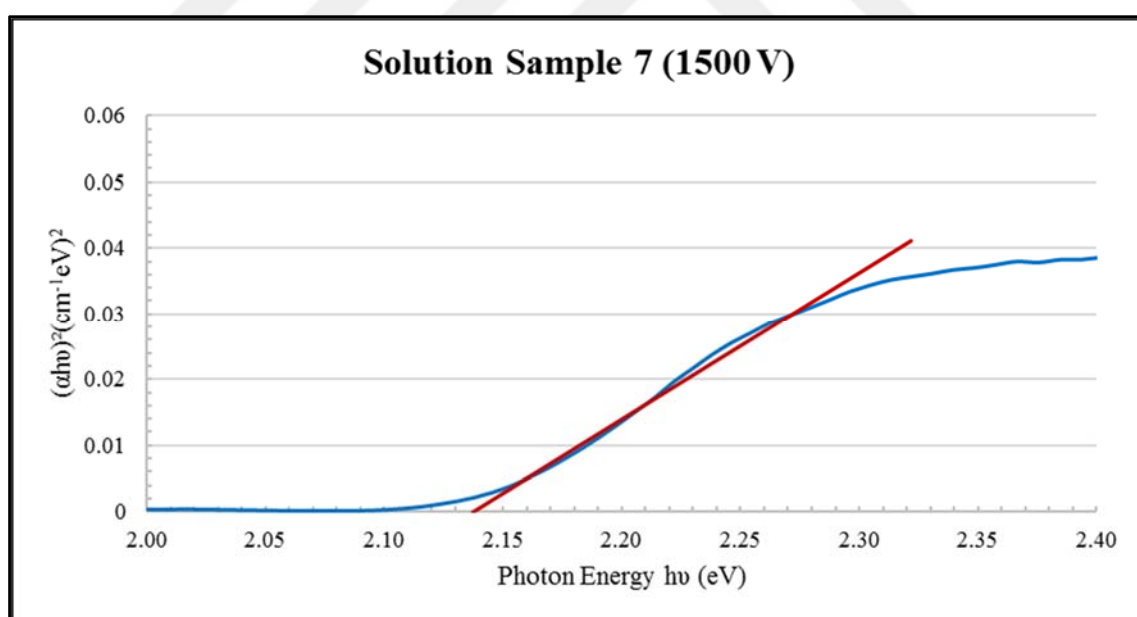


Figure 6.131. Plots of  $(\alpha h\nu)^2$  versus  $h\nu$  for Solution Sample 7 at 1500 V.

The Figures 6.130 and 6.131 above show the band gap energies for solution sample 7 at 1000 V and 1500 V, respectively.

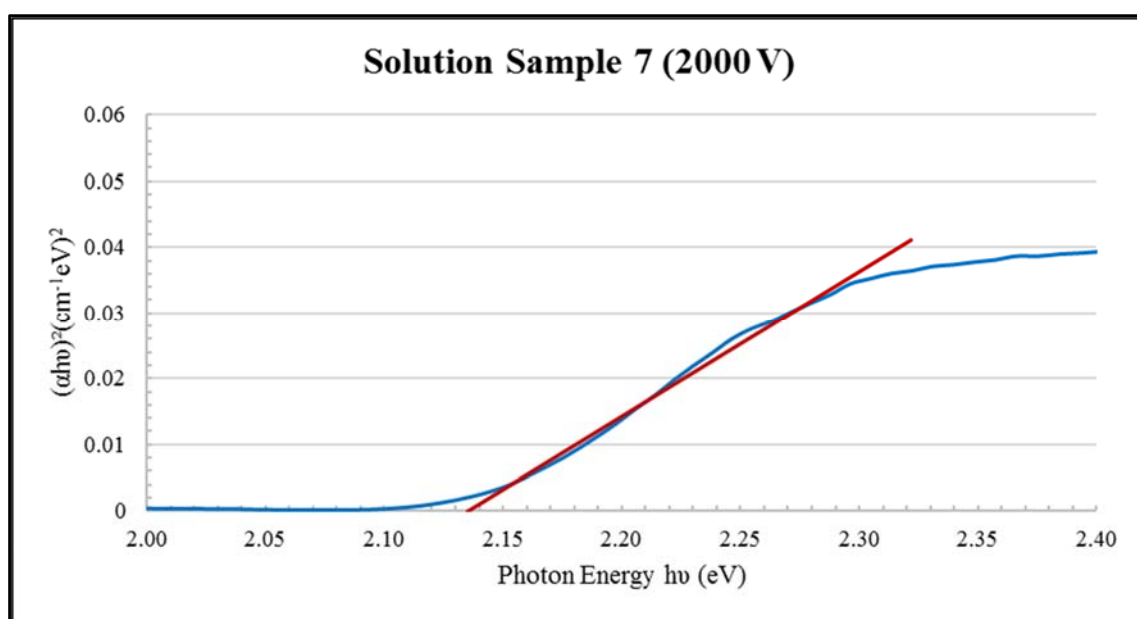


Figure 6.132. Plots of  $(\alpha h\nu)^2$  versus  $h\nu$  for Solution Sample 7 at 2000 V.

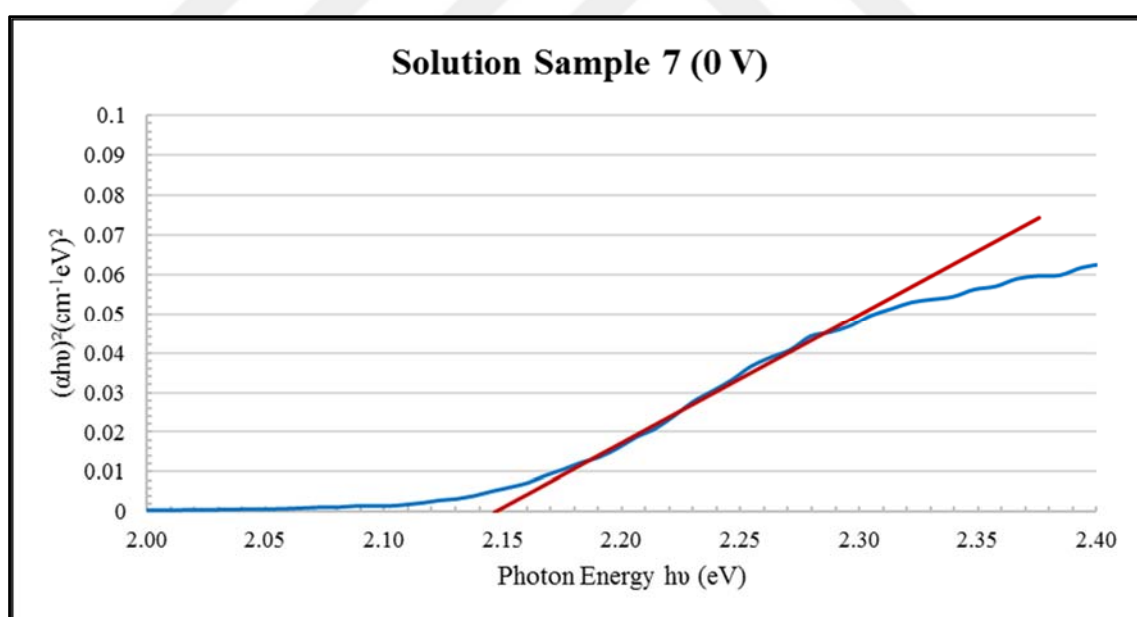


Figure 6.133. Plots of  $(\alpha h\nu)^2$  versus  $h\nu$  for Solution Sample 7 at 0 V.

The last solution sample 7 which has a maximum heat treatment time has maximum particle radius. As the electric field is increased, the band energy decreases, and the particle size increases linearly as shown below.

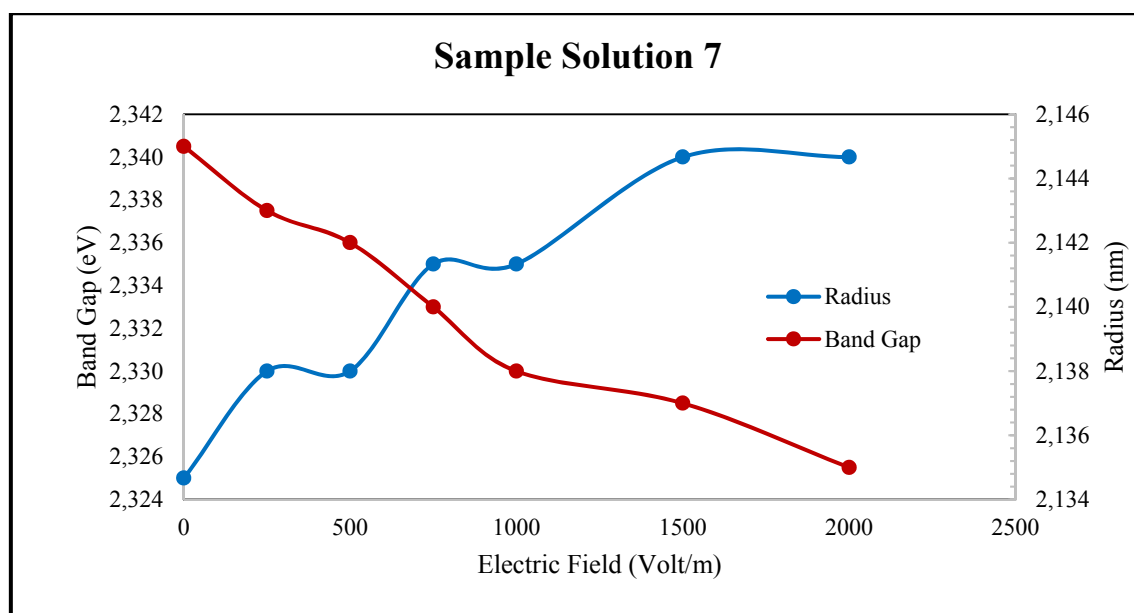


Figure 6.134. Plot of band gap, radius versus applied electric field for solution sample 7, from table above.

Table 6.18. Comparison of Experimental and Theoretical Stark Shift in the Band Gap.

Solid Sample 1			Solid Sample 2		
Applied Field (V)	Experimental (eV)	Theoretical (eV)	Applied Field (V)	Experimental (eV)	Theoretical (eV)
500	0.01	0.01	500	0.03	0.02
1000	0.03	0.06	1000	0.05	0.10
1500	0.05	0.14	1500	0.06	0.24
2000	0.07	0.25	2000	0.06	0.42
2500	0.10	0.40	2500	0.06	0.66
3000	0.10	0.57	3000	0.07	0.95
3500	0.12	0.79			
4000	0.13	1.04			
4500	0.14	1.33			
5000	0.15	1.66			
5500	0.16	2.03			
Solid Sample 3			Solution Sample 1		
Applied Field (V)	Experimental (eV)	Theoretical (eV)	Applied Field (V)	Experimental (eV)	Theoretical (eV)
250	0.007	0.004	500	0.009	0.010
500	0.015	0.016	750	0.012	0.023
1000	0.017	0.064	1000	0.014	0.042
1500	0.018	0.145	1250	0.015	0.065
1750	0.028	0.199	1500	0.022	0.095
			2500	0.030	0.265
Solution Sample 3			Solution Sample 4		
Applied Field (V)	Experimental (eV)	Theoretical (eV)	Applied Field (V)	Experimental (eV)	Theoretical (eV)
250	0.001	0.002	1000	0.030	0.053
500	0.007	0.008			
750	0.017	0.019			
1000	0.023	0.034			
1500	0.036	0.078			
Solution Sample 6			Solution Sample 7		
Applied Field (V)	Experimental (eV)	Theoretical (eV)	Applied Field (V)	Experimental (eV)	Theoretical (eV)
500	0.001	0.010	250	0.002	0.008
1000	0.005	0.039	500	0.003	0.032
1500	0.007	0.089	750	0.005	0.072
2000	0.009	0.159	1000	0.007	0.128
			1500	0.008	0.288
			2000	0.010	0.514

Comparison study on electroabsorption in CdTe quantum structures (both theoretical and experimental) were summarized in Table 6.18. Harmonic oscillator in a uniform electric field problem exact solution was used to determine the theoretical results. According to these results, theoretical values are bigger than experimental measurements. This could be based on the effects of electric field on the electronic structure of a semiconductor QD's inside differs from the one applied to the QDs. In addition to that, polarization and dipole moment changing by the effect of electric field can be the cause for the difference between experimental and theoretical results.



## 7. CONCLUSION AND FUTURE WORK

This thesis has presented a spectroscopic investigation of the properties of aqueous solutions containing QDs and glass samples with QD grown within them and the effect on these properties of high electric fields applied across them. Two different electromodulation effects were studied in the spectra: the quantum Confined Stark Effect (QCSE) and the Franz-Keldysh Effect. Different aspects of the optical and electronic properties of CdSe/ZnS, CdTe nanoparticles were controlled and investigated.

In the preliminary experiments, CdSe/ZnS core shell type quantum dots in aqueous solution were deposited on glass slides using spin coating technique and these nanoparticles were successfully grown inside glass samples. Parameters of the spin coating technique (speed, number of layers and annealing time and temperature) were modified to evaluate the effect on the sample dispersity and quality. It was observed that changing the spin coater speed, affects the dispersion of the QD on the substrate leading to changes in its optical properties means that the cluster of QDs appears as a large particle in absorption spectra, giving rise to shifts in the exciton spectra.

Heat treatment temperature for the various samples was analysed using an absorption spectrometer and showed that the samples had size distributions of 2.1 nm to 2.6 nm. Annealing the quantum dots was found to cause a blue shift in the exciton spectrum, due to migration of QD away from the clusters formed during spinning; this reduces the QD cluster sizes.

AFM analyses were successfully carried out for the samples to view the distribution of the quantum dots on the surface of layered samples. This showed that the distribution of samples depends on number of layers and spin coater speed. Based on trial and error, AFM height profiles reveal that the thin film thickness is very uniform and highly controllable, ranging from 5-7 layers with 500 rpm. Sharp absorption peak optimised at 7 layers with the same peak height most likely due to even sample distribution. (e.g. size distribution is narrow for a single size of particle)



In the main part of this thesis, samples were all prepared in the laboratory. Two types of samples were produced: solid samples and aqueous solution samples. Original methods were successfully developed by trial and error and recorded to synthesize the QDs in solution. The size was well controlled by heat treatment time for both solid and solution samples.

When the temperature was kept constant during the synthesis and the heat treatment time extended, the band gap energy of the particle decreased linearly. This is evidence that infers from Brus equation the size of the particle becomes smaller. Thus optimal heat treatment time and temperatures of the synthesis may allow the particle radius to be tunable.

During the synthesis and preparation of the nanoparticles, temperature measurements were performed with a calibrated platinum resistance (pt-100) thermometer to improve quality and reliability of the measurements.

Particle radii were successfully calculated from the effective mass model by Brus. Nanoparticles size for aqueous samples were changed between 1.925 and 2.395 nm with 6 hours heat treatment, this corresponds to 24.4% increase in particle size. The quantum dots grown in the glass matrix have a range from 1.920 to 2.580 nm equals to 34.4% increase in 9 hours.

As the effect of heat treatment duration on the band energy is analyzed from the absorption spectroscopy measurements. These results show evidence for the absorption wavelength gradually increasing with increasing growth time, explained in terms of red shift.

For the aqueous samples, with increased time of heat treatment the first exciton peak exhibits a red shift and broadening of the excitons peak may be related to the size dispersion of the quantum dots (exciton peaks differs between 460-540 nm). For the aqueous solution samples annealing time changed between 15 minutes to 6 hour, and the band gap changed from 2.552 eV to 2.144 eV, equals a 19% increase in band gap.

For the solid samples, data show the same trend with solution sample. When the growth time was increased from 3 hours to 12 hours, band gap of the samples decreased from 2.56 eV to 2.11 eV, this amounts to approximately 21.3% reduction in the band gap energies.

Spectroscopic absorption peaks were fitted to Gaussian distribution curves using a modelling programme developed in MATLAB. This allowed the extraction of reliable FWHM peaks and accurate calculation of the band gap energies and particle size distribution from spectroscopic measurements.

The repeatability, reproducibility and hysteresis measurements were performed to determine the reliability, validity of the measurements and to determine damage or defect on samples before and after applying the electric field. One reason for the reproducibility measurements made is to investigate whether the optical band energy returned to its original value when we removed the electric field. It seen that all samples have returned to their original values within experimental uncertainty.

Different measurement rigs and techniques were successfully constructed to measure the electro-optical properties of both quantum dots in glass samples and solution samples. The preliminary experiment has been particularly helpful as a guideline for the realization of the main experiments, i.e. the preparation of the test sample, the establishment of experimental setups and conditions to be considered in high electric field applications. All measurements were completed without exposure to electrical breakdown, toxicity of the heavy metals and without degradation of the samples under high dc. voltage.

High voltage applications have been performed for both aqueous and solid samples under a range of high electrical fields to be studied from 0.5 kV/m to 5.5 kV/m. On application of electric field, a blue shift with slightly enhanced optical absorption spectra was observed with increasing electric field. The major electro-optical measurement analysis showed clearly that the increasing electric field causes reduction in band gap energy due to Stark effect which manifests as a spectroscopic red shift.

Quantum confined Stark effect and Franz Keldysh effect were studied for both types of quantum dots by applying high electric field. Presence of the QCSE was distinguished from the Frank-Keldysch effect in the optical absorption spectra obtained. It was found that the QCSE is the dominant effect, but that Franz Keldysh characteristics were still observed. Especillay, for the solution samples, some of the samples show the Franz Keldysh effect, it may be due to larger particles in the solution.

Applied voltage causes the band gap of all the nanoparticles to decrease independent of the matrix they are contained within. This results in an increase in the calculated nanoparticle radius. The band gap shifts due to the Stark effect in solid samples are two times larger than these in aqueous samples. CdTe nanoparticles in solid exhibit Stark shift 7.8% nm while CdTe nanoparticles in aqueous solution shift around 2.4%. This amounts to (8% - 2%) increase in radius for the solid nanoparticle samples and 2.4% - 0.6% for the nanoparticles in solution for a constant applied voltage of 1 kV. This bandgap was observed to decrease as a linear function of the applied dc voltage. This is consistent with the nanoparticles constrained in solids undergoing electric field dependent strain more readily than the relatively unconstrained nanoparticles in solution, in agreement with the literature.

Overall, solution samples change less with applied voltage, since they experience a lower electric field due to their width. Nanoparticles in glass matrices experience a higher electric field, since these samples have smaller physical dimensions of 0.9-1.4 mm, whereas the nanoparticles in solution are within a cell of larger dimension (of width 1 cm).

The electrical permittivity of the samples is a component of the Brus equation and had to be determined based on experimental conditions. The most appropriate method of determining this was found by the Hilbert Transformation of the spectra. Minimum estimated values range from 8.6 F/m to 123.5 F/m. Dielectric constants of the samples were observed to increase in proportion to the growth time during the synthesis. Quantum dots embedded in the glass samples were found to have higher dielectric permittivities than those contained within solution. The determined dielectric permittivity values compared closely with the reference values obtained as a result of the literature review. These findings demonstrate that the electrical permittivity show a close tendency for both solid and aqueous samples.

Without an applied electric field, CdTe nanoparticles synthesised in solution were found to have a narrower size distribution compared to those in glass. An applied electric field causes a decrease in the size distribution of the nanoparticles that amount to approximately 10% for nanoparticles constrained in glass matrices and approximately 15% for nanoparticles in solution. This is related to the fact that nanoparticles in solution may move and the QDs embedded in the glass matrix has interactions and bonds with the other atoms and do not move freely.

Raman spectra peaks of aqueous and solid CdTe semiconductor nanoparticles were observed from 100 to 1000  $\text{cm}^{-1}$  under the same measurement conditions. The low Raman shift regime was investigated and showed three Raman modes observed close to 110, 140 and 160  $\text{cm}^{-1}$ . These Raman modes correspond to the crystalline core and Te defects of the nanoparticles which are at 110  $\text{cm}^{-1}$ . This Raman peak is related to disorder via activated acoustical phonons, second peak 140  $\text{cm}^{-1}$  and 160  $\text{cm}^{-1}$  represents the TO and LO CdTe phonon modes respectively.

Raman spectra peak positions from the solid quantum dots differ somewhat from the solution quantum dots spectrum. In solution samples, acoustic and LO modes are shifted to the upper wavenumber by approximately 10  $\text{cm}^{-1}$ , this extra signal may come from the capping ligand molecule on the CdTe quantum dot.

## **FUTURE WORK**

Use of the semiconductor nanoparticles in biological and medical applications, the toxicity and how the dots are formed have crucial importance. To prepare high quality, desirable and user-friendly nanoparticles, the capping agent (surfactants) can be changed with a reliable and healthy buffer.

QDs characterization can be analysed using the other spectroscopic techniques including, PL, TEM, AFM, Raman and EDX during the application of high electric fields to learn more about the structural, chemical, optical and electrical properties under this unusual condition.

A main problem is electric field breakdown across the samples. It is very important to resolve this problem so that electric fields of much higher values can be applied to samples. Applied voltages of a maximum of 5.5 kV could be applied, However, this was sample dependent, so that in many cases only 1 kV could be applied before electric breakdown. To optimize the applied electric field effect, different types of dielectric materials may be preferred and the sample thickness will be changed.

Different groups III-V semiconductors or II-VI semiconductors quantum dots may be selected to investigate optical and electrical properties under electric fields. The band gap of

the nanoparticles should be modified with the different techniques discussed in this thesis for efficient charge transfer.



## REFERENCES

- 1 . N. S. A. T. Council. The National Nanotechnology Initiative. *Executive Office of The President*. Washington, D.C, 2016.
- 2 . Roco M.C., National Nanotechnology Investment in the FY 2016 Budget. *American Society of Mechanical Engineers*, 2016.
- 3 . Ekimov A. ve Onushchenko A., Quantum Size Effect in Three Dimensional Microscopic Semiconductor Crystals. *Journal of Experimental and Theoretical Physics Letters*. 1981; 34:345.
- 4 . Rossetti R., Nakahara S. ve Brus L., Quantum Size Effects in The Redox Potentials Resonance Raman Spectra. and Electronic Spectra of CdS Crystallites in Aqueous Solution. *Journal of Chemical Physics*. 1983; 79:1086.
- 5 . Brus L., Electron-electron and electron-hole interactions in small semiconductor crystallites: the size dependence of the lowest excited electronic state. *Journal of Chemical Physics*. 1984; 80:4403.
- 6 . Anikeeva P. O., Halpert J. E., Bawendi M. G. and Bulović V., Quantum dot light-emitting devices with electroluminescence tunable over the entire visible spectrum. *Nano Lett*. 2009; 7:2532-6.
- 7 . Huynh W. U., Dittmer J. J. and Alivisatos A. P., Hybrid nanorod-polymer solar cells. 2002; 295:5564, 2425-2427.
- 8 . Michalet X., Pinaud F. F., Bentolila L. A., Tsay J. M., Doose S. , Li J. J., Sundaresan G., Wu A. M., Gambhir S. S. and Weiss S., Quantum dots for live cells, in vivo imaging, and diagnostics. *Science*. 2005; 307:5709, 538-44.
- 9 . Santos A., Miguel A., Tomaz L., Malhó R. and Maycock C. P., The impact of CdSe/ZnS Quantum Dots in cells of *Medicago sativa* in suspension culture. *J Nanobiotechnology*. 2010; 8:24, 6.

10. Yui C., Wei Q., Park H. and Charles M. L., Nanowire Nanosensors for Highly Sensitive and Selective Detection of Biological and Chemical Species. *Science*. 2001; 293:5533, 1289-1292.
11. Zhanga H., Xuab T., Lib C. W. and Yang M., A microfluidic device with microbead array for sensitive virus detection and genotyping using quantum dots as fluorescence labels. *Biosensors and Bioelectronics*. 2010; 25:11, 24.
12. Chukwuocha E. O. and Onyeaju M. C., Simulation of quantum dots (QDs) in the confinement regime. *Int. Journal of Applied Sciences and Engineering Research*. 2012; 1:6, 784-792.
13. Poole C. P. and Owens F. J., *Introduction to Nanotechnology*, New Jersey: Wiley, 2003.
14. Reimann S. M. and Manninen M., Electronic structure of quantum dots. *Reviews of Modern Physics*. 2002; 74:1283-1342.
15. Lacroix L. M., Delpech F., Nayral C., Lachaize S. and Chaudret.B., New generation of magnetic and luminescent nanoparticles for in vivo real-time imaging. *Interface Focus*. 2013; 3:3,1-19.
16. Koole R., Groeneveld E., Vanmaekelbergh D., Meijerink A. and Donega C. M., Size Effects on Semiconductor Nanoparticles. *Nanoparticles*, Springer. 2014; pp. 13-51.
17. Giancoli D. C.. *Physics for Scientists & Engineers*. New Jersey: Pearson. 2009.
18. Ronald C., Lasky U. L. and Osterberg D. P., *Optoelectronics for Data Communication*. California: Academic Press. 1995.
19. Rossetti R. and Brus L., Electron-Hole Recombination Emission as a Probe of Surface-Chemistry in Aqueous Cds Colloids. *J Phys Chem-US*. 1982; 86:23, 4470-4472.

20. Ekimov A. I. and Onuschenko A. A., Interband absorption of light in a semiconductor sphere. *Sov. Phys. Semiconductor*. 1982; 16:775-778.
21. Aldana J., Wang Y. A. and Peng X. G., Photochemical instability of CdSe nanocrystals coated by hydrophilic thiols. *J Am Chem Soc*. 2001; 123:36, 8844-8850.
22. Yu W. W., Qu L. H., Guo W. Z. and Peng X. G., Experimental determination of the extinction coefficient of CdTe, CdSe and CdS nanocrystals. *Chem. Mater*. 2003; 15:2854-2860.
23. Leatherdale C. A., Woo W. K., Mikulec F. V. and Bawendi M. G., On the absorption cross section of CdSe nanocrystal quantum dots. *J Phys Chem B*. 2002; 106:31,7619-7622.
24. Liu X., Tian J., Dai J. and Wang X., Aqueous Synthesis Of Thiol-Capped Cdte Quantum Dots And Its Photoluminescence Enhancement Via Room Temperature Treatment With Alkyl Chain Diamines. *Physica E*. 2014; 57:56-62.
25. Feng L., Kuang H., Yuan X., Huang H., Yi S., Wang T., Deng K., Tang C. and Zeng Y., A novel method for aqueous synthesis of CdTe quantum dots. *Spectrochimica Acta Part A: Molecular and Biomolecular Spectroscopy*. 2014; 123:298-302.
26. Choi S. Y., Shim J. P., Kim D. S., Kim T. and Suh K. S., Aqueous synthesis of CdTe quantum dot using dithiol-functionalized ionic liquid. *Journal of Nanomaterials*. 2012; 6.
27. Bell R. O., Review of Optical Applications of CdTe. *Rev. Phys. Appl*. 1977; 12:2, 391-399.
28. Borchert H., *Solar Cells Based on Colloidal Nanocrystals*. 196, Springer Series in Materials Science.



29. Harris D. K. and Bawendi M. G., Improved Precursor Chemistry for the Synthesis of III-V Quantum Dots. *J Am Chem Soc.* 2012; 134:50, 20211–20213.
30. Hu M. Z. and Zhu T., Semiconductor Nanocrystal Quantum Dot Synthesis Approaches Towards Large-Scale Industrial Production for Energy Applications. *Nanoscale Res Lett.* 2015; 10:469.
31. LaMer V. K. and Dinegar R. H., Theory, Production and Mechanism of Formation of Monodispersed Hydrosols. *J. Am. Chem. Soc.* 1950; 72:11, 4847–4854.
32. O'Brien G., Nanoscale Electronic Properties of Conjugated Polymers and Nanocrystals. *PhD Thesis*, Tyndall National Institute University College Cork, Ireland, 2006.
33. Yükselici M. H. and Allahverdi Ç., Size-dependent photo-induced shift of the first exciton band in CdTe quantum dots in glass prepared by a two-stage heat-treatment process. *Journal of Luminescence.* 2008; 128:537-545.
34. Dunne P. W., Munn A. S., Starkey C. L., Huddle T. A. and Lester E. H., Continuous-Flow Hydrothermal Synthesis for the Production of Inorganic Nanomaterials. *Philos Trans A Math Phys Eng Sci.* 2015; 28:373, 2057.
35. Platt U. and Stutz J., *Differential Optical Absorption Spectroscopy Principles and Applications.* Springer, 2008.
36. Boyd R. W., *Nonlinear Optics.* Burlington: Elsevier, 2008.
37. Larkin P., *Infrared and Raman Spectroscopy: Principles and Spectral Interpretation.* Elsevier, 2011.
38. Feeney M., *Novel Applications of Semiconducting Nanoparticulates.* İstanbul: Ph.D Thesis Yeditepe University, 2011.
39. Montagna M., Characterization of Sol-Gel Derived Materials by Raman and Brillouin Spectroscopies. *Handbook of Sol-Gel Science and Technology:*

*Processing, Characterization and Applications Volume II*, New York, Kluwer Academic, 2004.

40. Kittel C., *Introduction to Solid State Physics Hardcover* 7th ed. Canada: Wiley, 1996.
41. Miller D. A. B., Chemla D. S., Damen T. C., Gossard A. C., Wiegmann W., Wood T. H. and Burrus C. A., Band-Edge Electroabsorption in Quantum Well Structures: The Quantum-Confined Stark Effect. *Phys. Rev. Lett.* 1984; 53:2173.
42. Reed G. T., Mashanovich G., Gardes F. Y. and Thomson D. J.; Silicon optical modulators. *Nature Photonics.* 2010; 4:518-526.
43. Miller D. A. B.; Optics for low-energy communication inside digital processors: quantum detectors, sources, and modulators as efficient impedance converters. *Optics Letters.* 1989; 14:2, 146-148.
44. Bimberg D., Stubenrauch M., Stracke G. and Arsenijevic D., Quantum-dot based distributed feedback lasers and electro-absorption modulators for datacom applications. *Transparent Optical Networks (ICTON).* 2012; 1-4.
45. Murray C. B., Norris D. J. and Bawendi M. G., Synthesis and characterization of nearly monodisperse CdE (E = sulfur, selenium, tellurium) semiconductor nanocrystallites. *J. Am. Chem. Soc.* 1993; 115:19, 8706-8715.
46. Empedocles S. A. and Bawendi M. G., Quantum-confined Stark effect in single CdSe nanocrystallite quantum dots. *Science.* 1997; 278:5346, 2114-2117.
47. Leroux M., Grandjean N., Lügt M., Massies J., Gil B., Lefebvre P. and Bigenwald P., Quantum confined Stark effect due to built-in internal polarization fields in (Al,Ga)N/GaN quantum wells. *Physical Review B.* 1998; 58:20, 1.
48. Phillips C. C., Eccleston R. and Andrews S. R., Theoretical and experimental picosecond photoluminescence studies of the quantum-confined Stark effect in a

- strongly coupled double-quantum-well structure. *Phys Rev B Condens Matter*. 1989 40:14, 9760.
49. Banerjee S. and Shore K. A., Biexcitonic blue Stark shift in semiconductor quantum dots. *Journal of Applied Physics*. 2005; 97:12, 123101(1-5).
  50. Miller D. A. B., Chemla D. S. and Schmitt-Rink S., Relation between electroabsorption in bulk semiconductors and in quantum wells: The quantum-confined Franz-Keldysh effect. *Phys. Rev. B*. 1986; 33:10, 6976-6982.
  51. Keldysh L. V., Behavior of Non-metallic Crystals in Strong Electric Fields. *Soviet Journal of Experimental and Theoretical Physics*. 1958; 6:763.
  52. Miller D. A. B., Chemla D. S. and Schmitt-Rink S., Electroabsorption of highly confined systems: Theory of the quantum-confined Franz-Keldysh effect in semiconductor quantum wires and dots. *Appl. Phys. Lett*. 1988; 52:2154.
  53. Griffiths D. J., *Introduction to Quantum Mechanics*. Cambridge: Cambridge University Press, 1994.
  54. Banfi G. P., Degiorgio V. and Speit B., Neutron Scattering Investigation of the Structure of Semiconductor Doped Glasses. *J. Appl. Phys*. 1993; 74:1.
  55. Moradian R., Elahi M., Hadizadeh A., Roshani M., Taghizadeh A. and Sahraei R., Structural, optical, and electrical properties of thioglycolic acid-capped CdTe quantum dots thin films. *International Nano Letters*. 2013; 1-6.
  56. Feng L., Kuang H., Yuan X., Huang H., Yi S., Wang T., Deng K., Tang C. and Zeng Y., A novel method for aqueous synthesis of CdTe quantum dots. *Spectrochimica Acta Part A: Molecular and Biomolecular Spectroscopy*. 2014; 123:298-302.
  57. Yong K. T., Law W. C., Roy I., Jing Z., Huang H., Swihart M. T. and Prasad P. N., Aqueous phase synthesis of CdTe quantum dots for biophotonics. *Journal of Biophotonics*. 2011; 4:1-2, 9-20.

58. Choi S. Y., Shim J. P., Kim D. S., Kim T. Y. and Suh K. S., Aqueous Synthesis of CdTe Quantum Dot Using Dithiol-Functionalized Ionic Liquid. *Journal of Nanomaterials*. 2012; 1-6.
59. Lajunen L. H. J. and Perämäki P., *Spectrochemical Analysis by Atomic Absorption and Emission*. J. Chem. Educ., 2009.
60. Tauc J., Grigorovici R. and Vancu A., Optical Properties and Electronic Structure of Amorphous Germanium. *Physica Status Solidi*. 1966; 15:2, 627-637.
61. López R. and Gómez R., Band-gap energy estimation from diffuse reflectance measurements on sol-gel and commercial TiO<sub>2</sub>: a comparative study. *Journal of Sol-Gel Science and Technology*. 2012; 61:1, 1-7.
62. *Optical Processes in Semiconductors*, Courier Corporation, 1971.
63. Ghosh B., Hussain S., Ghosh D., Bhar R. and Pal A. K., Studies of CdTe films deposited by pulsed laser deposition technique. *Physica B*. 2012; 407:4214-4220.
64. Brus L., Electronic wave functions in semiconductor clusters: experiment and theory. *J. Phys. Chem.* 1986; 90:12, 2555-2560.
65. Chukwuocha E. O. and Onyeaju M. C., Simulation of quantum dots (QDs) in the confinement regime. *Int. Journal of Applied Sciences and Engineering Research*. 2012; 1:6.
66. Brus L., A simple model for the ionization potential, electron affinity, and aqueous redox potentials of small semiconductor crystallites. *The Journal of chemical physics*. 1983; 79:11, 5566-5571.
67. Castro F. and Nabet B., Numerical computation of the complex dielectric permittivity using Hilbert transform and FFT techniques. *Journal of the Franklin Institute*. 1999; 336B, 53-64.

68. Pesika N. S., Stebe K. J. and Searson P. C., Determination of the Particle Size Distribution of Quantum Nanocrystals from Absorbance Spectra. *Advanced Materials*. 2003; 15:15, 1289–1291.
69. Dzhagan V., Lokteva I., Himcinschi C., Jin X., Kolny-Olesiak J. and Zahn D. R. T., Phonon Raman spectra of colloidal CdTe nanocrystals: effect of size, non-stoichiometry and ligand exchange. *Nanoscale Research Letters*. 2011; 6:79, 1-10.
70. Vodop'yanov L. K., Vinogradov V. S., Mel'nik N. N. and Karczewski G., Raman Scattering in Multilayer Structures with CdTe Quantum Dots in ZnTe. *JETP Letters*. 2003; 77:3, 143-145.
71. Ghosh B., Hussain S., Ghosh D., Bhar R. and Pal A. K., Studies on CdTe Films Deposited by Pulsed Laser Deposition Techniques. *Physica B*. 2012; 407, 4214-4220.
72. Vinogradov V. S., Karczewski G., Kucherenko I. V., Mel'nik N. N. and Fernandez P. Raman Spectra of Structures with CdTe-, ZnTe-, and CdSe-Based Quantum Dots and Their Relation to the Fabrication Technology. *Physics of the Solid State*. 2008; 50:1, 164.
73. Trofimov I. E., Petrov M. V., Balakirev F. F., Milokhin A. E. and Kuzmin V. D., Raman scattering study of strain in  $Zn_xCd_{1-x}Te/CdTe$  superlattices. *Appl. Phys. Lett.* 1992; 61:4, 417-419.
74. Spagnolo V., Scamarcio G., Lugara M. and Righini G. C., Raman scattering in  $CdTe_{1-x}Se_x$  and  $CdS_{1-x}Se_x$  nanocrystals embedded in glass. *Superlattices and Microstructures*. 1994; 16:1, 51-54.
75. Madelung O., Rössler U. and Schulz M., *II-VI and I-VII compounds, semimagnetic compounds*, Berlin: Springer-Verlag, 1999.
76. Adachi S., *Properties of Group-IV, III-V and II-VI Semiconductors*, John Wiley & Sons, 2005.

77. Flytzanis C. and Hutter J., Nonlinear Optics in Quantum Confined Structures. *Contemporary Nonlinear Optics*, Academic Press. 1992; 297-365.
78. Lambropoulos C. P., Karafasoulis K. E., Gnatyuk V. A. and Levytskyi S., Simulation studies of CdTe pixel detectors. *2008 IEEE Nuclear Science Symposium Conference Record*, 2008.
79. Silva E. C. F. and Strauch D., *Landolt-Börnstein Group III: Condensed Matter Semiconductors*, 44, New York: Springer, 2012.
80. Wakaki M., Kudo K. and Shibuya T.. *Physical Properties and Data of Optical Materials*, Boca Raton: CRC Press, 2007.

## APPENDIX A: PUBLICATIONS AND DOCUMENTS

## Spin coated thin film CdSe/ZnS quantum dots for solar cell applications

Melda Patan Alper,<sup>1\*</sup> Rabia Ince<sup>1</sup>, Hikmet Yükselci<sup>2</sup> and Ahmet. T. Ince<sup>1</sup><sup>1</sup>Department of Physics, Yeditepe University, Istanbul 34758, Turkey<sup>1</sup>Department of Physics, Yeditepe University, Istanbul 34758, Turkey<sup>2</sup>Department of Physics, Yıldız Technical University, Istanbul 34220, Turkey

**Abstract**— The characterization of CdSe/ZnS thin films prepared by a spin-coating technique were investigated through optical absorption spectra and is being investigated by atomic force microscope. Thin films were prepared by spin coating CdSe/ZnS liquid samples onto glass substrates as monolayered and multilayered structures. Increase in optical density was observed in the absorption spectra when the number of layers and spin coating setting parameters are modified. The average radius and radius distribution quantum dots were estimated by using the effective mass model in the strong confinement limit.

Thin film quantum dots (QDs) have potential applications as nonlinear optical devices in optoelectronics, fluorescent labels in bioengineering, and window materials in solar cells [1,5]. Thin film QDs were grown on glass slides by spin coating. Their optical and structural properties were studied through optical absorption spectra and AFM.

In this study commercially available core shell type CdSe/ZnS quantum dots in aqueous solution were deposited on glass slides by spin coating. Firstly, all glass slides were cleaned in chromic acid solution for one day, and then washed with distilled water and finally dried. The substrate was first placed on the rotating disk of the spin-coater at 2000 rpm and then CdSe/ZnS solution was dropped on the target substrate every 60 s. For each layer coating 2,5 µl of solution was used, waiting for a minute between consecutive layers so that the thin films could dry, undergoing a phase change to a solid. Finally, multilayered CdSe/ZnS films were obtained for measurements.

The characteristic optical absorption spectra are presented in Figure 1. Figure shows measured optical densities (OD) as a function of wavelength for four typical samples prepared at room temperature.

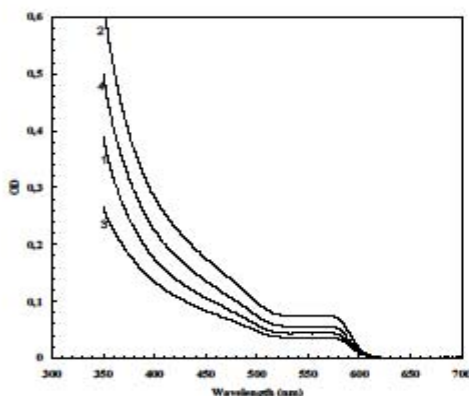


Figure1. Optical absorption spectra for thin film CdSe/ZnS quantum dots. 1→500 rpm, 2→500 rpm, 3→100 rpm and 4→200 rpm.

The observed structure at around 585 nm is due to the production of excitons in the lowest bound state; the asymptotic absorption edge is blue-shifted due to the quantum size effect. Optical absorption spectroscopy is an important tool to understand the behavior of thin films consisting of multilayer structures. The average radius and radius distribution of quantum dots were estimated using the effective mass model in the strong confinement limit. The following relation between the energetic position of first exciton peak and average radius was used.  $E_R$  is the size dependent first exciton transition energy given by,

$$E_R \text{ (eV)} = E_g \text{ (eV)} - \frac{0.14}{R \text{ (nm)}} + \frac{0.356}{\mu [R \text{ (nm)}]^2} \quad \text{Eq. (1)}$$

Where the first term is the bulk band gap of the crystal of  $E_g=1.727$  eV, the second term Coulomb potential energy between an electron and hole, and the third term confinement energy for an electron and a hole. The symbol  $\mu$  is the reduced mass of an electron-hole pair and has a value of 0,106 in units of electron rest mass  $m_0$ , [6]. The average radius of quantum dots was estimated as 2,70 nm employing Eq. (1).

In this presentation optical absorption spectra and AFM images for different thin film samples will be discussed with a view to describing the liquid to solid phase change of quantum dots.

\*Corresponding author: mpatan@yeditepe.edu.tr

[1] Ekimov A.I., Onushchenko A.A. (1981) JETP Lett 34:345

[2] Flytzanis C, Harbe F, Klein MC, Ricard D (1990) Optics in complex systems. SPIE, Bellingham, WA

[3] Jain R, Lin RC (1983) J Opt Soc Am 73:647

[4] Nozik AJ (2002) Physica E 14:115

[5] Chan WCW, Maxwell DJ, Gao X, Bailey RE, Han M, Nie S (2002) Curr Opin Microbiol 13:40

[6] Henneberger, F.; Puls, J.; Spiegelberg, Ch; Schulzgen, A.; Rossman, H.; Jungnickel, V.; Ekimov, A. I. (1991) Semicond Sci Technol 16:A41

Figure A.1. Poster

## Electro-Optical Modulation Characteristic Member Of Group II-VI Semiconductor Nanocrystals

M. PATAN ALPER<sup>1\*</sup>, R.İNCE<sup>1</sup> and H.YÜKSELİCİ<sup>2</sup>

<sup>1</sup> Department of Physics, University of Yeditepe,

<sup>2</sup> Department of Physics, University of Yıldız Technical University,

\*Presenter: mpatan@yeditepe.edu.tr

### Abstract

Electrical and optical properties of Group II-VI semiconductor crystalline substrates have been studied. Electro-modulation and Raman spectroscopy characterization of the various samples have been investigated experimentally. Zn<sub>x</sub>Cd<sub>1-x</sub>Te semiconductor nanocrystals embedded in glass matrixes and their non-linear optical properties under high voltage have been studied by in situ electro-modulation spectroscopy and resonant Raman spectroscopies. In this paper, optical and electrical properties of nanocrystal were described with Franz-Keldysh effect and Quantum Confined Stark Effect (QCSE). The Franz-Keldysh effect occurs in uniform, bulk semiconductors, unlike the quantum confined Stark effect, which requires a quantum well e.g. nanoparticles. The Franz-Keldysh effect usually requires hundreds of volts, whereas quantum confined Stark effect requires voltages an order of magnitude lower [1]. An Airy function includes a "tail" which extends right into the classically forbidden band gap, allowing transitions below the bandgap; this is the Franz-Keldysh effect.

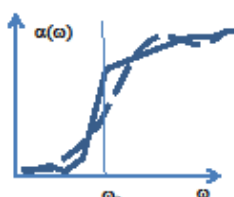


Fig.1 The resulting change in absorption spectrum in Franz-Keldysh effect

Reduction in energy of states due to Stark effect causes red shift. The bandgap is shifted in the quantum confined structure. In addition, electron and hole are forced in opposite directions by the static field; this decreases the overlap of the wave functions in valence and conduction band decreases causing a decrease in absorption.

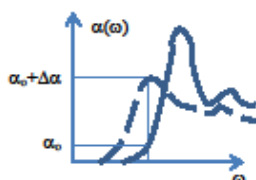


Fig.2 The resulting change in absorption spectrum in QCSE

Excitonic absorption peak remains up to much higher fields than observed for the Stark shift in bulk material. Since the barriers in the quantum well prevent field ionization up to high electric field [2,3,4,5,6,7,8]

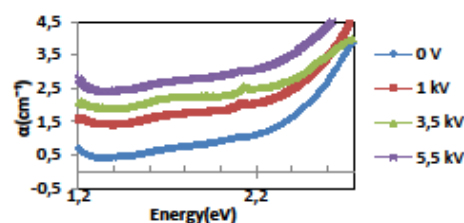



Fig.3 The optical absorption spectra of heat treated sample under different electric field

In the presence of an applied electric field, the change in optical absorption gives a shift. The amount of shift varies from 35meV to 60meV with respect to the applied field. In addition to this along with the red shift the spectrum broadens. According to the experimental results, this red shift may be associated with QCSE in theory.

### 1. References

- [1] Dumas DC, Gallacher K, Rhead S, Myronov M, Leadley DR, Paul DJ, 2014, Ge/SiGe quantum confined Stark effect electro-absorption modulation with low voltage swing at  $\lambda = 1550$  nm, Opt Express, 22, p.19284-92.
- [2] J. S. Weiner et al., Appl. Phys. Lett., 47 (1985) 1148.
- [3] L. V. Keldysh, Behaviour of Non-Metallic Crystals in Strong Electric Fields, J. Exptl. Theoret. Phys. (USSR) 33 (1957) 994-1003, translation: Soviet Physics JETP 6 (1958) 763-770.
- [4] L. V. Keldysh, Ionization in the Field of a Strong Electromagnetic Wave, J. Exptl. Theoret. Phys. (USSR) 47 (1964) 1945-1957, translation: Soviet Physics JETP 20 (1965) 1307-1314.
- [5] R. Williams, Electric Field Induced Light Absorption in CdS, Phys. Rev. 117 (1960) 1487-1490.
- [6] J. I. Pankove, Optical Processes in Semiconductors, Dover Publications Inc. New York (1971).
- [7] H. Haug and S. W. Koch, "Quantum Theory of the Optical and Electronic Properties of Semiconductors", World Scientific (1994).
- [8] C. Kittel, "Introduction to Solid State Physics", Wiley (1996)






YEDITEPE UNIVERSITY

International Conference on Oxide Materials for Electronic Engineering OMEE-2012

### CdTe nanocrystals studied through in-situ electro-modulation spectroscopy

Rabia Inoc<sup>1</sup>, Melda Patan Alper<sup>1</sup>, Hikmet Yükseliç<sup>2</sup>, Asuman Aşkoğlu<sup>1</sup> and Çağdaş Allahverdi<sup>3</sup>  
<sup>1</sup> Department of Physics, Yeditepe University, Atasehir, Istanbul, Turkey  
<sup>2</sup> Department of Physics, Yıldız Technical University, Davutpaşa, Istanbul, Turkey  
<sup>3</sup> Université de Nantes Faculté des Sciences, Nantes, France



#### ABSTRACT

Non-linear optical properties of weakly confined CdTe nanocrystals in a glass matrices were studied by electro-modulation spectroscopy. An as-received color filter glass of thickness 0.8 mm was sandwiched between two indium tin oxide (ITO) covered glass slides help with epoxy. Optical transmission spectra of the samples were recorded under dc high voltage applied to the electrodes. The absorption band is observed to broaden. This is most likely caused by state filling.

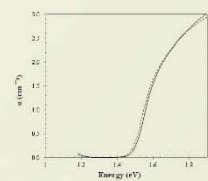


Fig.2. In-situ optical absorption spectra under 5 kV dc applied to the sample (dashed curve) and the spectrum with no field applied (solid curve).

#### INTRODUCTION

CdTe nanocrystals are of special interest due to their potential applications in solar panels for the purpose of increasing light to electric current conversion efficiency [1]. Linear and nonlinear optical properties of Cd chalcogenides including CdSe and CdS have been scrutinized [2-3]. The other less studied member of group II-VI, CdTe has a band gap of around 1.5 eV which is at the optimum value for converting solar energy to electrical energy. The size dependent electro-modulation spectroscopy plays an important role in understanding electronic band structure and the extent to which the band gap energy is modified. In this work, CdTe nanocrystals embedded in glass were characterized by optical absorption spectroscopies. Their non-linear optical properties under high voltage have been studied by in situ electro-modulation spectroscopy.

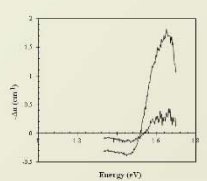


Fig.3. Electro-modulation spectrum for glass doped with CdTe nanocrystals under 3.5 kV and 3.75 kV dc high voltage.

#### EXPERIMENTAL

Commercially available Schott color glass filter RG830 doped with CdTe nanocrystals was used as starting material. The optical absorption spectrum of an as-received glass sample is presented in Fig. 1. The optical absorption edge spectrum for bulk CdTe crystal reported in ref. [4] is shown in the same graph for comparison. The asymptotic absorption edge of 1.44 eV for bulk CdTe is blue shifted by 170 meV for as-received glass doped with CdTe nanocrystals due to confinement of charged particles (electrons and holes). The confinement energy of  $\Delta E = 170$  meV is related to average radius for nanocrystals through the relation,

$$\Delta E = \frac{0.376}{\mu[R(\text{nm})]^2} \quad (1)$$

where  $\mu = 0.106$  is the electron hole reduced mass in unit of electron rest mass. We find an average radius of  $R = 4.57$  nm for the ensemble of nanocrystals.

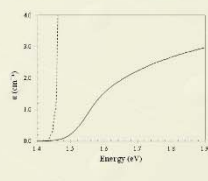


Fig. 1. Optical absorption edge spectra for as-received color glass filter doped with CdTe (solid curve) and for bulk CdTe (dashed curve) obtained by digitizing the curve for 297 K in Fig 5 in ref [4].

An as-received color filter glass was sliced to dimensions of about 10 x 6 x 0.8 mm with a diamond saw. This small sample sandwiched between two ITO (indium-tin-oxide) covered glass slides with epoxy. Optical transmission spectra of the samples were recorded under a high voltage of 5 kV applied to the electrodes. The optical absorption spectra with no electric field (solid curve) and with electric field (dashed curve) applied to the sample are shown in Fig.2. The differential optical absorption coefficient calculated according to,

$$\Delta \alpha = \frac{I_{\text{with field}} - I_{\text{with no field}}}{d} \quad (2)$$

where  $I_{\text{with field}}$  ( $I_{\text{with no field}}$ ) is the transmitted intensity with the field applied (with no field applied).

The electric field strength was changed between 42 kV/cm and 46 kV/cm in Fig.3. The change in absorption  $-\Delta \mu(\omega)$  (with field on)  $-\mu(\omega)$  (with no field) is plotted against energy (electro-modulation spectrum). Asymmetrical shape of the photo-absorption curves shown for two high voltage values applied to the samples is consistent with Fig.3. This means that the applied field produces a red-shift in the asymptotic absorption edge plus bleaching of the absorption. Based on previous studies we presume that the former is due to stark effect while the latter due to state filling.

#### DISCUSSION

A Gaussian absorption band was assumed for the exciton peak in the optical absorption spectrum to explain the observed structure in Fig. 3 [5]. The effect of red shift and broadening with absorption saturation in the Gaussian absorption band on the electro-modulation spectra was shown in Fig. 4 [6,7]. A red shift and a broadening with a decrease in absorption in a Gaussian-like first exciton absorption band correspond to a first derivative and a second derivative line shape respectively in the electro-modulation spectra as seen in Fig. 4 (a) and (b). The former has an asymmetric and the latter a symmetric structure. A mixture of the two structures produces the profile shown in Fig. 4 (c). The structure observed in Fig. 3 is consistent with the structure consisting of a single lobe as observed in Fig. 4 (a). That is why it is reasonable to assume that the applied field causes broadening in optical absorption spectra. The earlier studies on nanometer sized semiconductor-doped glasses show that the state filling is responsible for the positive peak due to the bleaching of the absorption. We presume that dc electric field (causes less perfect overlap of the electron and hole wavefunctions, leading to broadening) modifies recombination of electrons and holes and therefore quantized states are filled. This mechanism results in absorption saturation. The shift was calculated 1.3 meV according to given formula. [8,9]

$$\Delta E(\text{meV}) = -2\lambda \times 10^{-7} M^2 F^2 \left[ \frac{R}{a_{\text{ave}}} (\text{nm}) \right]^4 \quad (3)$$

where M is the translational mass of the electron-hole pair in units of electron rest mass and F is the electric field.

#### CONCLUSION

Electro-modulation spectra show that the exciton band in optical absorption spectra for CdTe nanocrystals embedded in glass whose average radius is about 5 nm (in the medium confinement regime) broadens under a dc high voltage. We presume that state filling is responsible for the observed absorption saturation.

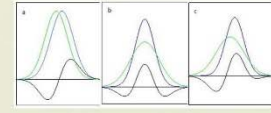


Fig. 4. Schematic plots of differential optical absorption spectra (wavy curve) due to a shift (upper plot), a broadening (center plot) and a shift plus a broadening (lower plot) in a Gaussian absorption band [6].

#### REFERENCES

- [1] P. V. Kamal, "Quantum Dot Solar Cells: Semiconductor Nanocrystals as Light Harvesters" J. Phys. Chem. C 112, 19737, 2008.
- [2] M. G. Beversid, P. J. Carnell, William L. Wilson, and E. Bruji, "Luminescence Properties of CdSe Quantum Crystal Dos: Resonance Between Interior and Surface Localized States." J. Chem. Phys. 96, 840, 1992.
- [3] Y. Hachi, M. C. Khan, D. Richard, C. Flybants, "Photoluminescence study of Schott commercial and experimental CdSe-doped glasses: localization of surface states." J. Non-Cryst. Solids 192, 1993, 1991.
- [4] D. T. F. Marple, Phys. Rev., "Optical absorption edge in CdTe: Experiments", vol 150, no. 2, pp. 728-734, 1988.
- [5] M. H. Yükseliç, Ç. Allahverdi, "Size dependent photo-induced shift of the first exciton band in CdTe quantum dots in glasses prepared by a two stage heat treatment process", J. Lum. 128, 537-545, 2008.
- [6] S. V. Gaponenko, "Optical Properties of Semiconductor Nanocrystals", pp. 148-147, Cambridge University Press, New York, NY 1999.
- [7] P. G. 4 (upper and center) with asthetic norm ref [5].
- [8] F. Henninger, J. Phys. Ch. Solgelberg, A. Ostberg, H. Rosen, V. Janghok, A. I. Barlow, Sensord. Sol Technol. 18 1361
- [9] H. Rosenham, A. Schuzger, F. Henninger, M. Müller Phys. Status Solidi (b) 152 (1990) 287

Figure A.3. Poster

# Certificate of Analysis

SIGMA-ALDRICH®

<b>Product Name</b>	Lumidot™ CdSe/ZnS, 530, core-shell type quantum dots, 5 mg/mL in toluene	
<b>Product Number</b>	694649	
<b>Product Brand</b>	ALDRICH	

TEST	SPECIFICATION	LOT 48397mj RESULTS
<b>Appearance (Color)</b>	Conforms to Requirements Green	Green
<b>Appearance (Form)</b>	Liquid	Liquid
<b>Emission Color</b>	Conforms Green	Conforms
<b>Absorption Max</b>	≈530 nm	510 nm
<b>Emission Wavelength (Peak)</b>	525 - 535 nm	531 nm
<b>Full Width Half Max (FWHM)</b>	≈40 nm	37 nm
<b>Quantum Yield</b>	≈30 %	51 %
<b>Solvent: Toluene</b>	Confirmed	Conforms
<b>Concentration</b>	5 mg/ml	5 mg/ml
<b>Capping Agent: Hexyldecylamine</b>	Confirmed	Conforms
<b>Specification Date:</b>		DEC 2008
<b>Date of QC Release:</b>		DEC 2008
<b>Recommended Retest Date:</b>		APR 2009
<b>Expiry Date:</b>		DEC 01 2013



Barbara Hojzer, Supervisor  
Quality Control  
Milwaukee, Wisconsin, USA

Figure A.4. Certificate of CdSe/ZnS core shell nanoparticles (530 nm)

# Certificate of Analysis


SIGMA-ALDRICH

<b>Product Name</b>	Lumidot™ CdSe, 590, core-type quantum dots, 5 mg/mL in toluene	
<b>Product Number</b>	662607	
<b>Product Brand</b>	ALDRICH	
<b>CAS Number</b>	1306-24-7	
<b>Molecular Formula</b>	CdSe	
<b>Molecular Weight</b>	191.37	

TEST	SPECIFICATION	LOT 74196mj RESULTS
Appearance (Color)	Red	Red
Appearance (Form)	Liquid	Liquid
Wavelength	565 - 575 nm	565 nm
	Absorbance *Supplier Data	
Emission Wavelength	585 - 595 nm	586 nm
	*Supplier Data	
Mass Balance Information	Conforms	Conforms
	5mg in 1ml Toluene *Supplier Data	
Miscellaneous Assay	Conforms	Conforms
	4.0 - 4.3nm	
Specification Date:		SEP 2008
Date of QC Release:		OCT 2008
Expiry Date:		OCT 22 2013



Barbara Hojzer, Supervisor  
Quality Control  
Molecular Biology, St. Louis, MO, USA

Figure A.5. Certificate of CdSe/ZnS core shell nanoparticles (590 nm)



**TÜRKİYE BİLİMSEL VE TEKNOLOJİK ARAŞTIRMA KURUMU**  
**MARMARA ARAŞTIRMA MERKEZİ**  
**KİMYASAL TEKNOLOJİ ENSTİTÜSÜ**

P.K.21, 41470 GEBZE – KOCAELİ  
 T 0 262 677 20 00 F 0 262 641 23 09  
<http://www.mam.tubitak.gov.tr>

**ANALİZ RAPORU**  
 (Endüstriyel Teknik Destek Hizmeti)

Rapor no : 68110102-125.05- 1593-7557  
 Rapor tarihi : 11.11.2015  
 Talep eden : Melda PATAN ALPER  
 Adres : Yeditepe Üniversitesi Fizik Bölümü, 26 Ağustos Yerleşimi İnönü Mah.  
 Kayışdağı Cad. Ataşehir/İstanbul  
 Konusu : Cam numunesinde istenilen analizler

*Bu raporda yer alan sonuçlar, sadece incelenen numunelere aittir.*

Onaylayan


**Pınar AYDIN**  
**Kimyasal Teknoloji Enstitüsü**  
**Endüstriyel Hizmet Sorumlusu**

Bu rapor ve sonuçları talepte bulunan kuruluş ve müşterilerince ticaret ve reklam amaçları ile kullanılamaz. Rapor tamamen veya kısmen çoğaltılamaz/yayınlanamaz. Rapor (\*) işaretli analizler akredite edilmiştir. İmzasız analiz raporları geçersizdir.

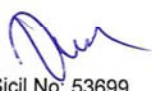

Bu rapor 2 sayfa olup, 2 asıl (1 asıl müşteriye, 1 asıl Enstitü arşivine) olarak hazırlanmıştır.

Sayfa 1/2





**TUBITAK**  
**MAM**

<b>Rapor no</b> : 68110102-125.05- 1593-7557											
<b>Talep eden</b> : Melda PATAN ALPER											
<b>Talep edenin adresi</b> : Yeditepe Üniversitesi Fizik Bölümü, 26 Ağustos Yerleşimi İnönü Mah. Kayışdağı Cad. Ataşehir/İstanbul											
<b>Örnek</b> : Cam	<b>Son kullanım tarihi</b> : -										
<b>Örnek sayısı</b> : 1	<b>Enstitü örnek kayıt no</b> : 15G/822/01										
<b>Örneğin getiriliş şekli</b> : Müşteri tarafından	<b>Kabul tarihi ve saati</b> : 11/11/2015										
<b>Kabul anındaki durumu</b> : Poşet içerisinde	<b>Analiz tarihi</b> : 11/11/2015										
<b>Şahit numune bilgileri</b> : <input type="checkbox"/> Müşteriye iade <input type="checkbox"/> Şahit numune mevcut <input checked="" type="checkbox"/> Şahit numune alınmamıştır											
<p>Yeditepe Üniversitesi Fizik Bölümünden Sn. Melda PATAN ALPER'in 11/11/2015 tarih ve 7112 MAM evrak kayıt numaralı yazıları ile yapılmasını kabul ettiği ve yazılarında "Cam" olarak belirtilen 1 adet örnekte istenilen analizler laboratuvarlarımızdaki ICP Spektrometresi ile yapılmış olup, elde edilen sonuçlar aşağıda verilmiştir.</p> <table border="1" style="width: 100%; border-collapse: collapse; margin-top: 10px;"> <thead> <tr> <th style="text-align: left;">Analizler</th> <th style="text-align: left;">Sonuçlar</th> </tr> </thead> <tbody> <tr> <td>Kadmiyum (Cd)</td> <td>% 0,20</td> </tr> <tr> <td>Tellür (Te)</td> <td>% 0,16</td> </tr> <tr> <td>Çinko (Zn)</td> <td>% 27,10</td> </tr> <tr> <td>Selenyum (Se)</td> <td>% 0,22</td> </tr> </tbody> </table> <p>Bilgilerinize sunulur.</p>		Analizler	Sonuçlar	Kadmiyum (Cd)	% 0,20	Tellür (Te)	% 0,16	Çinko (Zn)	% 27,10	Selenyum (Se)	% 0,22
Analizler	Sonuçlar										
Kadmiyum (Cd)	% 0,20										
Tellür (Te)	% 0,16										
Çinko (Zn)	% 27,10										
Selenyum (Se)	% 0,22										
<b>Açıklamalar:</b>											
<b>Sorumlu İmzalar:</b>											
 Sicil No: 53699	 Sicil No: 51601										
<small>Bu rapor ve sonuçları talepte bulunan kuruluş ve müşterilerince ticaret ve reklam amaçları ile kullanılamaz. Rapor tamamen veya kısmen çoğaltılamaz/yayınlanamaz. Rapor (*) işaretli analizler akredite edilmiştir. İmzasız analiz raporları geçersizdir.</small>											
<small>Bu rapor 2 sayfa olup, 2 asıl (1 asıl müşteriye, 1 asıl Enstitü arşivine) olarak hazırlanmıştır.</small>											
<small>Sayfa 2/2</small>											

P.K.21, 41470 GEBZE – KOCAELİ  
T 0 262 677 20 00 F 0 262 641 23 09  
<http://www.mam.tubitak.gov.tr>

Figure A.6. Analysis report of RG 830 glass sample

Table A.1. Assessment for Control of Substances Hazardous to Health Regulations

<b>Status:</b>	<b>Approved by</b>
Printed on:	10 September 2015 at 12:00
Title of COSHH Form	Effects of electric field on a CdTe quantum dot synthesis in solution
Assessor	ProF. Dr. Rabia INCE. ProF. Dr. Ahmet T. INCE.
Personel Involved (And Status)	Yeditepe Üniversitesi Güvenlik Merkezi 2121. 1278. 1015 İş Sağlığı ve Güvenliği Merkezi 3248. 3249
<b>Chemicals</b>	<b>Precautions</b>
Tellurium (Te)	<ul style="list-style-type: none"> <li>• Toxic if swallowed use suitable respiratory equipment and special filtered mask</li> <li>• Use Rubber gloves</li> <li>• Use Safety glasses.</li> <li>• Wear protective clothing</li> <li>• Storage Keep container tightly closed</li> </ul>
Sodium Borohydride	<ul style="list-style-type: none"> <li>• SMALL FIRE: Use DRY chemical powder. LARGE FIRE: Use water spray or fog.</li> <li>• Keep locked up Keep container dry</li> <li>• Use Splash goggles. Lab coat. Vapor and dust respirator. Boots. Gloves</li> </ul>
Cadmium Chloride	<ul style="list-style-type: none"> <li>• Use safety glasses. Lab coat. Dust respirator. Gloves</li> <li>• Wear suitable protective clothing</li> </ul>
Mercaptopropionic Acid	<ul style="list-style-type: none"> <li>• Reaction with certain metals releases flammable and explosive hydrogen gas.</li> <li>• Work within well-ventilated area</li> <li>• Splash goggles. Gloves.</li> <li>• Use A self contained breathing apparatus</li> <li>• Use an approved/certified respirator</li> </ul>
Cysteine	<ul style="list-style-type: none"> <li>• SMALL FIRE: Use DRY chemical powder. LARGE FIRE: Use water spray. fog or foam. Do not use water jet.</li> <li>• Keep container dry. Keep in a cool place</li> <li>• Splash goggles. Full suit. Dust respirator. Boots. Gloves.</li> <li>• Use a self contained breathing apparatus</li> </ul>

**MATLAB CODE**

```

Ebulk=1.44;
h=6.626e-34;
me=0.11;
mh=0.35;
mo=9.11e-31;
e=1.6e-19;
eps=8.85e-12;
epso=8.72;
r=linspace(5e-9,1e-10,1001);
r=r';
E=Ebulk+((((h^2)/(8*r.^2))*((1/(me*mo))+1/(mh*mo))))
((1.78*e^2)/(4*pi*eps*epso*r))/e;
for i=1:length(E_import)
    r_found(i.)=r(find(abs(E-E_import(i))==min(abs(E-E_import(i)))));
end
    result=[E_import r_found];

```

Figure A.7. Matlab Code to calculate radius from band gap